

Technische Universität Kaiserslautern  
Fachbereich Chemie

**Metal cluster aggregates of the composition  $\text{Fe}_n^{+/-}$ ,  $\text{Co}_n^{+/-}$ ,  $\text{Ni}_n^{+/-}$  and  $[\text{Co}_n\text{M}_m]^{+/-}$  (M: Au, Rh and Pt) as model systems for catalytic C-H activation and structural determination of ionic dicarboxylic acids as model system for intramolecular hydrogen bonding**

Am Fachbereich Chemie der Technischen Universität Kaiserslautern  
zur Erlangung des akademischen Grades „Doktor der Naturwissenschaften“  
genehmigte

Dissertation  
(D386)

vorgelegt von

Dipl.-Chem. Christine Merkert

Betreuer: Prof. Dr. G. Niedner-Schatteburg

Tag der wissenschaftlichen Aussprache: 27. März 2014



Die vorliegende Arbeit wurde in der Zeit von Oktober 2007 bis März 2014 im Fachbereich Chemie der Technischen Universität Kaiserslautern unter der Betreuung von Prof. Dr. G. Niedner-Schatteburg angefertigt.

Datum des Antrags der Eröffnung des Promotionsverfahrens: 27. Juni 2012

Tag der wissenschaftlichen Aussprache: 27. März 2014

Promotionskommission:

Vorsitzender: Prof. Dr. S. Kubik

1. Berichterstatter: Prof. Dr. G. Niedner-Schatteburg

2. Berichterstatter: Prof. Dr. M. Gerhards



Für meine Familie

*Wissenschaft: Es ist nicht ihr Ziel, der unendlichen Weisheit eine Tür zu öffnen,  
sondern eine Grenze zu setzen dem unendlichen Irrtum.*

Bertolt Brecht



## Abbreviations

CLIO	<i>Centre Laser Infrarouge d'Orsay</i>
DAA	Deprotonated Adipic Acid
DDA	Deprotonated Dicarboxylic Acid
DFT	Density Functional Theory
DGA	Deprotonated Glutaric Acid
DMA	Deprotonated Malonic Acid
DSA	Deprotonated Succinic Acid
EPITOPES	Electrons Plus Infrared TO Probe and Elucidate Structure
ESI	Electro Spray Ionization
FEL	Free Electron Laser
FT-ICR	Fourier Transform Ion Cyclotron Resonance
IR-MPD	InfraRed Multi-Photon Dissociation
IVR	Intramolecular Vibrational Redistribution
KDP	Potassium Dihydrogen Phosphate
KTA	Potassium Titanyl Arsenate
KTP	Potassium Titanyl Phosphate
LVAP	Laser Vaporization
MP2	Møller-Plesset perturbation theory second order
MS	Mass Spectrometry
Nd:YAG	Neodymium doped yttrium aluminum garnet
PAA	Protonated Adipic Acid
PDA	Protonated Dicarboxylic Acid
PGA	Protonated Glutaric Acid
PMA	Protonated Malonic Acid
PSA	Protonated Succinic Acid





## Content

1. Introduction, experimental set up and methods	-1-
1.1. General introduction	-1-
1.2. Experimental set up	-3-
1.2.1. Ion generation	-3-
1.2.2. Ion detection	-6-
1.2.3. Free Electron Laser (FEL)	-11-
1.2.4. Optical Parametrical Oscillator / Amplifier (OPO/A)	-13-
1.3. Methods	-15-
1.3.1. InfraRed - Multi Photon Dissociation (IR-MPD)	-15-
1.3.2. Kinetic investigations with neutral reaction gases	-16-
1.3.3. Computational Methods	-17-
1.4. References	-20-
2. IR-MPD spectroscopy of deprotonated and protonated dicarboxylic acids	-27-
2.1. Preamble	-27-
2.2. Spectral fingerprints of proton delocalization in isolated, aliphatic dicarboxylic ions	-28-
2.3. Introduction	-29-
2.4. Experimental and theoretical methods	-32-
2.4.1. IR-MPD spectroscopy and resonant two color IR-MPD spectroscopy	-32-
2.4.2. Ab initio calculations	-34-
2.5. Results and Discussion	-35-
2.5.1. IR-MPD spectra by the FEL	-35-
2.5.2. OPO based IR-MPD spectra	-42-
2.5.3. Calculated structures and calculated spectra	-47-
2.5.4. IR induced fragmentation efficiency	-55-
2.6. Conclusions	-63-
2.7. References	-64-
2.8. Supplement material	-66-
2.9. Comparison of OPO experiments and theory	-70-
2.10. Comparison of experiments performed with the FEL and the OPO set up	-76-
2.11. IR-peak shift of deuterated dicarboxylic acids	-81-
2.12. Estimation of the photon count required to fragment PAA	-86-
2.13. Aromatic dicarboxylic acids	-89-
2.13.1. IR-MPD spectra of protonated aromatic dicarboxylic acids	-90-
2.13.2. IR-MPD spectra of deprotonated aromatic dicarboxylic acids	-92-
2.13.3. Comparison of IR-MPD spectra with simulated IR spectra	-94-
2.14. Summary and conclusions	-100-
2.15. References	-102-
3. H/D isotope effects in the reactions of benzene with iron, cobalt and nickel cluster ions	-103-
3.1. Preamble	-103-
3.2. Introduction	-104-

3.3. Experimental Methods	-106-
3.4. Results and Discussion	-108-
3.4.1. Reactions of iron clusters	-108-
3.4.2. Reactions of cobalt clusters	-110-
3.4.3. Reactions of nickel clusters	-114-
3.4.4. Interpretation of features that are common to iron, cobalt, and nickel cluster cations and anions	-117-
3.4.5. Interpretation of the differences in reactions of iron, cobalt, and nickel cluster cations and anions with benzene and benzene-d6	-119-
3.5. Summary	-121-
3.6. References	-122-
3.7. Supplementary Material	-124-
3.8. Temperature dependent kinetic studies on the reaction of cationic iron clusters with benzene	-128-
3.9. References	-131-
4. H/D isotope effects in the reactions of benzene with cobalt gold and cobalt rhodium bimetallic cluster ions	-133-
4.1. Preamble	-133-
4.2. Introduction	-134-
4.3. Materials and Methods	-136-
4.4. Results and discussions	-138-
4.4.1. Reactions of cobalt gold cluster	-138-
4.4.2. Reaction of cobalt rhodium cluster	-141-
4.4.3. Comparison of the studies on mixed clusters	-146-
4.5. Summary and Conclusions	-150-
4.6. References	-151-
5. Benzene activation and H/D isotope effects in reactions of mixed cobalt platinum clusters: The influence of charge and of composition	-153-
5.1. Preamble	-153-
5.2. Introduction	-154-
5.3. Materials and Methods	-156-
5.4. Results and discussions	-158-
5.5. Summary and Conclusions	-167-
5.6. References	-168-
6. Summary / Zusammenfassung	-171-
6.1. Summary	-171-
6.2. Zusammenfassung	-174-
7. Publications and cotrbutions to conferences	-177-
8. Acknowledgement	-179-
9. Lebenslauf	-181-

# 1. Introduction, experimental set up and methods

## 1.1. General introduction

Mass spectrometry is an important tool in chemistry. The applications of mass spectrometry exceed the pure determination of molecular masses. In analytical chemistry mass spectrometry is applied in proteomics, metabolomics, pollution control, food control, forensic science and many more<sup>1, 2</sup>. The determination of structures is possible by different approaches, e.g. by the detection of fragmentation products after illumination with intensive infrared radiation (IR-MPD) and photoelectron spectroscopy<sup>3</sup>. Other intrinsic molecular properties become available through mass spectrometry as well, e.g. sequencing of proteins via collision induced dissociation (CID)<sup>4-8</sup>, magnetic properties are available by X-ray Magnetic Circular Dichroism (XMCD) measurements<sup>9</sup> and kinetic rate constants by reactivity studies (see chapters 3, 4 and 5)<sup>10-12</sup>. The possibilities of mass spectrometry are virtually unlimited. This work utilizes some of these methods to determine structure and reactivity of selected compounds.

Catalysis is one of the most important topics in chemistry. Understanding the catalytic processes and mechanisms is a great challenge. Catalysis is ubiquitous in our life. In combustion engines platinum serves as catalyst to purify the exhaust fumes. In nature enzymes catalyze most important reactions in metabolism. Enzymes are stabilized by intramolecular hydrogen bonds which in part determine their structures<sup>13</sup>. Thus hydrogen bonding is crucial for their catalytic activity. It causes stabilization of secondary and tertiary structures of e.g. polypeptides and ensures their enzymatic activity. Proton transfer is one of the major mechanisms to activate molecules and to transport chemical energy. It takes place exclusively along hydrogen bonds. To understand hydrogen bonds many investigations have been performed<sup>14</sup>. To identify hydrogen bonds infrared spectroscopy is an important tool<sup>15-23</sup>. Enzymatic mechanisms have been investigated as well<sup>24-28</sup>. Physical chemists started with the investigation of hydrogen bonded dimers<sup>29-31</sup> and clusters<sup>32-34</sup>. Hydrogen bonded species are isolated in the gas phase without environmental interferences in order to simplify the modeling. These investigations are performed with the help of mass spectrometry.

In this work the influence of steric restraints on the proton transfer from one nucleophile carboxyl group to the other is investigated. Therefore we choose dicarboxylic acids as model systems (see chapter 2). Two proton acceptor sites are linked by a flexible alkyl chain. To identify the structures of such species the infrared spectra are recorded with an action spectroscopy method. Here, IR-MPD spectroscopy serves to identify the molecular structures.

## 1. Introduction, experimental set up and methods

---

Mass spectrometry is an important tool not only to identify molecular structures via IR-MPD spectroscopy but also to investigate chemical reactions. In heterogeneous catalysis transition metal surfaces are well known for their catalytic activity. Transition metal cluster may serve as model system for such surfaces. C-H bond activation is one of the most important and often the rate limiting step in many catalytic reactions<sup>35-40</sup>. The catalytic mechanism is often not understood in detail. More than one metal atom (of simple or multiple metals) in the catalytic system can improve the efficiency of the catalytic cycle or vary the resulting reaction products<sup>41-44</sup>. Gas phase investigations supported by quantum mechanical calculations may help to understand elementary steps of these processes in detail<sup>45</sup>. As a model system transition metal clusters are used to investigate various reactions. Differences in reactivity arise with cluster size and charge state. The neutral reaction gas may be adsorbed to the cluster surface. The differences of chemisorption or physisorption are widely discussed<sup>46-62</sup>. Many investigations deal with the reaction of transition metal clusters with benzene<sup>3, 10-12, 63-80</sup>. In our group many experiments centered on the reaction of  $Nb_n^{+/-}$  with benzene. The reaction products are  $[Nb_nC_6]^{+/-}$  and  $[Nb_nC_6H_6]^{+/-}$ , depending on cluster size and charge state<sup>10, 69, 71</sup>. In this work we present results of the reaction of benzene and perdeutero benzene with catalytic transition metals (iron, cobalt and nickel, see chapter 3) and with different cobalt alloys (see chapter 4 ( $Co_nAu_m/Co_nRh_m^{+/-}$ ) and chapter 5 ( $Co_nPt_m^{+/-}$ )).

### 1.2. Experimental set up

Mass spectrometry is an important tool to characterize molecules. In the following the mass spectroscopic methods are describe which are applied to the investigated systems. First the ionization methods are explained followed by the different ways to detect the ions. In the case of action spectroscopy the use of different laser systems is recommended. A more detailed description of the applied mass spectrometers can be found in numerous text books<sup>1,2</sup>.

#### 1.2.1. Ion generation

##### Laser vaporization

Cluster ions are generated by a homebuilt Laser VAPorization source (LVAP)<sup>69, 81, 82</sup>. The second harmonic ( $\lambda = 532$  nm) of a pulsed neodymium doped yttrium aluminum garnet laser (*Innolas Spitlight 200* Nd:YAG laser (Berlin) or a *Continuum Surelite II* (Kaiserslautern)) serves to evaporate metal atoms from a 0.4 – 1.0 mm thick rotating foil. For the generation of mixed clusters alloy foils are prepared by the company *Hauner*. The emerging plasma is cooled by a short transverse gas pulse (40  $\mu$ s, helium, 8 – 15 bar) from a homebuilt piezoelectronic valve<sup>83</sup>. Further cooling arises from the subsequent supersonic expansion through a 20 mm long channel (diameter of 2 mm) into vacuum ( $10^{-6}$  mbar). No additional ionization step is needed. All investigated ions result from the laser generated plasma. After the supersonic expansion the ion beam passes a 1.4 mm skimmer. The cool cluster ions are accelerated to pass an ion beam bender (90°). Electrostatic lenses steer the ion beam into the FT-ICR cell within the high field region of the superconducting magnet (7 T).

The LVAP source consists of a nearly cubic metal block (evaporation block) (1) with two perpendicular drilled holes. Behind the one end a rotating metal target (2) (diameter approximately 12 mm, thickness 0.4 -1.0 mm) is used as cluster material. The rotating metal target can be also moved linearly to achieve a different trace on the circular target. Through the second hole this target is hit by a pulsed laser beam of the frequency doubled laser light of a Nd:YAG laser (see above). The generated metal plasma is s cooled down within the supersonic expansion of a helium gas pulse through the perpendicular drill hole within the evaporation block. This helium pulse is created by a homebuilt piezoelectric valve (5). It allows for the creation of very short (40  $\mu$ s) and sharp helium gas pulses with the helium expanding from 8 to 15 bar into the background pressure within the LVAP source of about  $10^{-6}$  mbar. The metal plasma is cooled down by the supersonic expansion. The evaporation block is followed by the expansion channel (3). Within this 2 mm diameter channel the

## 1. Introduction, experimental set up and methods

---

neutral and ionic metal clusters grow and reach sizes from 2 to approximately 40 atoms. The whole source part is insulated against ground so that a small voltage (up to 10 V) can be applied, the so called source voltage.

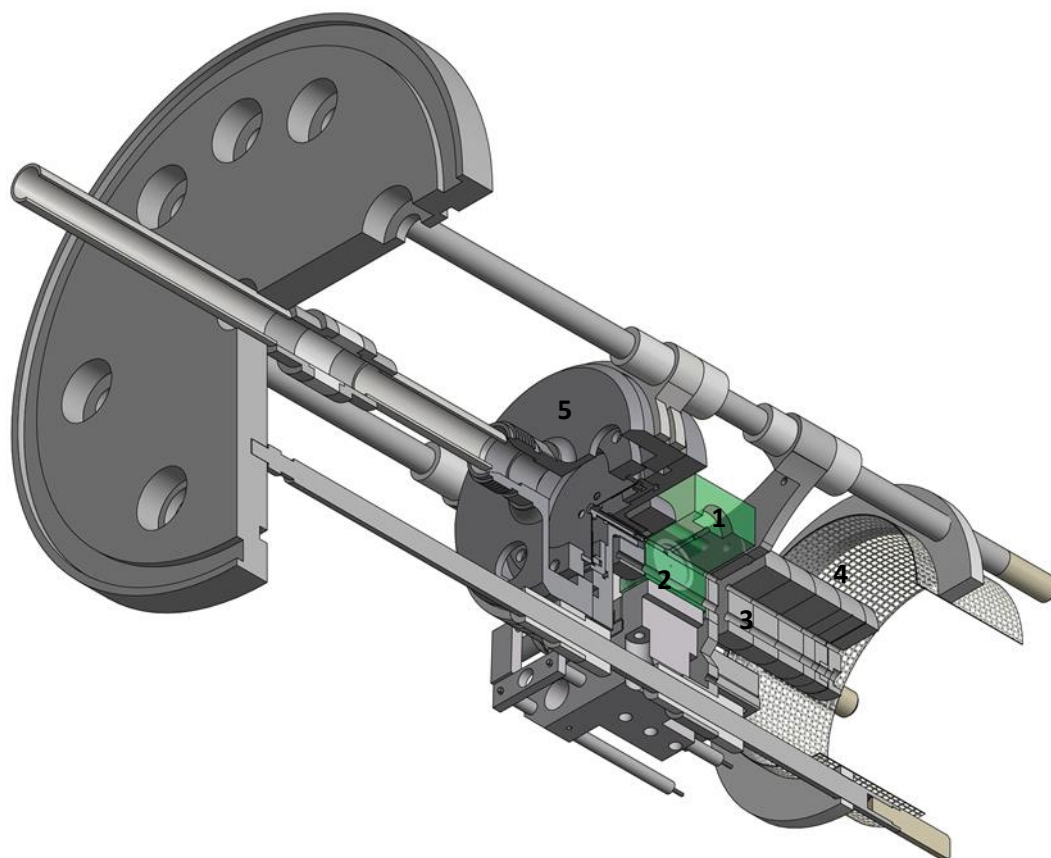


**Figure 1:** Laser VAPorization source. **1:** evaporation block; **2:** rotating metal target; **3** expansion channel; **4** mesh; **5** piezoelectronic valve

The resulting ionic part of the clusters is skimmed by a 1.4 mm skimmer, accelerated to pass the ion bender and transferred into the ICR cell. Ions are stored within this cell. The ions can be exposed to a neutral reaction gas or they can be irradiated with IR light through the entrance within the rear side of the ICR cell before mass detection

### Electrospray Ionization (ESI) source

Fenn *et al.* developed the first application of the electrospray ionization method and was awarded with the Nobel Prize in 2002<sup>84-87</sup>. Initially the ESI process was dedicated to protein analysis and biological applications<sup>88</sup>. Many reviews are released on this topic<sup>89-91</sup> and several edited books cover this topic<sup>92-94</sup>.

The ESI process allows for the transfer of solvated ions to the gas phase. While this process a field gradient of several kV is applied between a capillary tube (comprising the solvated ions) and the entrance of the mass spectrometer allows for a charge accumulation at the liquid surface at the end of the tube. This charge accumulation will break to form highly charged droplets. A nebulizing gas (nitrogen) flows around the tube and assists the creation of a stream of small droplets. Remaining solvent molecules evaporate. This is assisted by a heated drying gas (nitrogen) flowing against the stream of charged droplets. The mechanism of solvent removing and ion release is still discussed<sup>95, 96</sup>. The now naked ions enter the mass spectrometer through a glass capillary with a 0.5 mm diameter and the capillary is 15 - 20 cm long. Both ends are coated with platinum to apply a potential gradient.

### 1.2.2. Ion detection

#### FT-ICR-MS

Fourier transform mass spectrometry uses magnetic field to trap the ions on circular orbits. These kind of ion trap is also referred to a *Penning* trap. To trap the ions the analyzer cell is located within the center of a strong superconducting magnet (typical magnetic field strength of 3 – 15 T). The first description of the cyclotron effect by Ernest Lawrence was awarded with the Nobel prize of Physics in 1939<sup>97</sup>. The application of the *cyclotron* concept to mass spectrometry was first described by Comisaro and Marshall<sup>98,99</sup>. Several reviews on this subject are published<sup>100,101</sup>.

Kinetic measurements require trapped ions in a controlled environment. The Fourier-Transform Ion Cyclotron Resonance (FT-ICR) mass spectrometry provides for such an environment. The ions are trapped in vacuum (around  $10^{-10}$  mbar) and through a leak valve a controlled supply of reaction gas is possible. The experimental set up of the used FT-ICR mass spectrometer is divided in:

1. Ion source: LVAP or ESI
2. Vacuum system and ion transfer optics
3. Analyzer: infinity cell

To transfer the ions into the analyzer cell, ion transfer optics are required. These guide the ions by electric fields. The ions are accelerated to 3.0 keV kinetic energy in order to guide the ions against the magnetic mirror effect<sup>102</sup> into the homogenous high field region of the super conducting magnet (7 T).



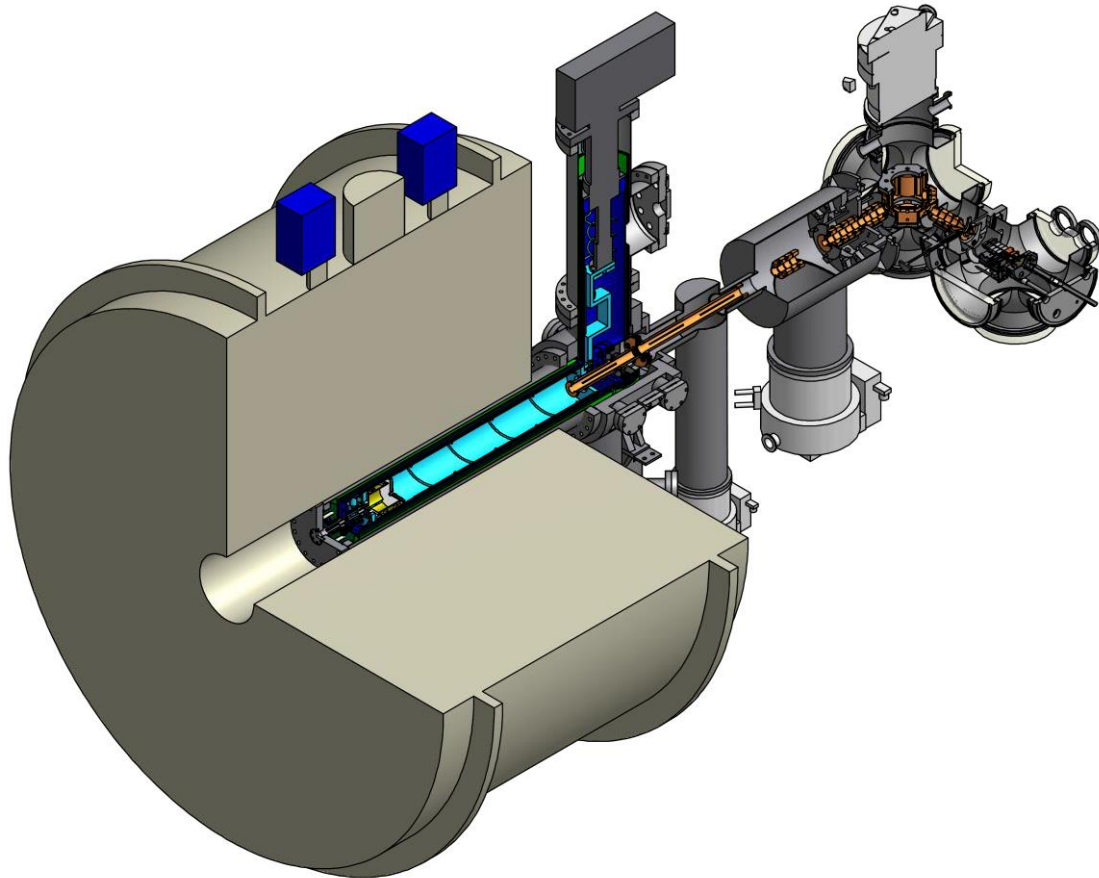


**Figure 2:** Cut through a 3D model of the modified Bruker FT-ICR: Left part: 7 Tesla superconducting magnet with the mass analyzer (infinity cell, yellow). Middle part: Ion transfer optics, vacuum system and cooling system (blue). Right side: External ion sources.

The ion beam enters the analyzer cell - a Bruker “infinity cell”<sup>103</sup>. The trapped ions are excited and detected. With acceleration out of the ion source an ion obtains kinetic energy

$$E_{kin} = zV_{acc} = \frac{1}{2}mv^2 \quad (1)$$

Where  $V_{acc}$  represents the potential difference which defines the acceleration region

$m$  is the mass of the ion

$z$  the charge state of the ion

$v$  represents its velocity

When entering the magnetic field the ion experiences a Lorentz force  $F$  that is perpendicular to the magnetic field  $B$  and the vector of the velocity. The ion is guided on a circular trajectory. The Lorentz force balances the centrifugal force:

$$z v B = \frac{m v^2}{r} \quad (2)$$

## 1. Introduction, experimental set up and methods

---

With this balance the relationship between the  $m/z$  value of an ion and the magnetic field strength is:

$$m/z = r^2 B^2 / 2V_{acc} \quad (3)$$

The infinity cell consists of six plates: two so called trapping plates which are supplied with DC voltage to limit the linear motion of the ion. The other four plates are divided in two groups: the excitation plates and the detection plates both are adjusted parallel to the magnetic field lines.

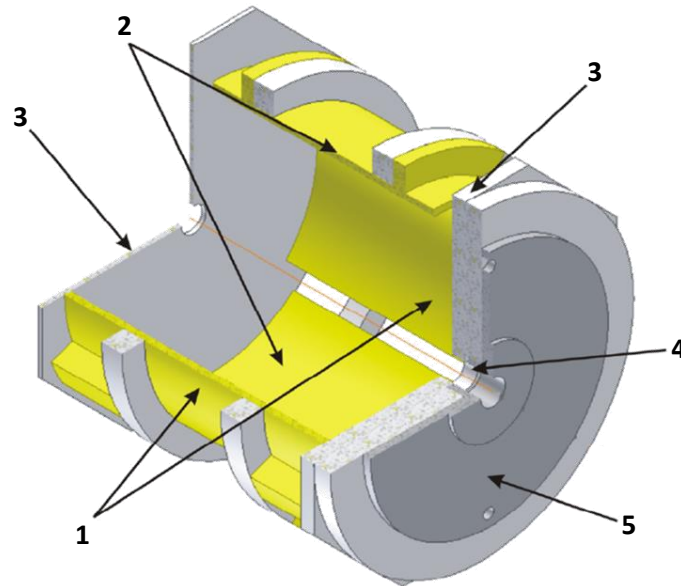


**Figure 3:** The infinity cell of *Bruker*. 1: detection plates, 2 excitation plates, 3 trapping plates, 4 side kick, 5 entrance plate

A trapped ion having a initial velocity  $v$ , will move in a circular path of the radius  $r$

$$r = mv/zB \quad (4)$$

and rotate with a frequency  $\omega_c$ , the so called cyclotron frequency:

$$\omega_c = \frac{2\pi}{\tau} = zB/m \quad (5)$$

The cyclotron frequency  $\omega_c$  is inversely proportional to the mass of an ion. An excitation pulse is applied prior detection, such that all ions absorb energy and then move together coherently on a larger orbit radius.

The motion of the ion in the ICR cell consist of an axial oscillation due to the trapping voltage, a cyclotron motion and a magnetron motion<sup>104</sup>.

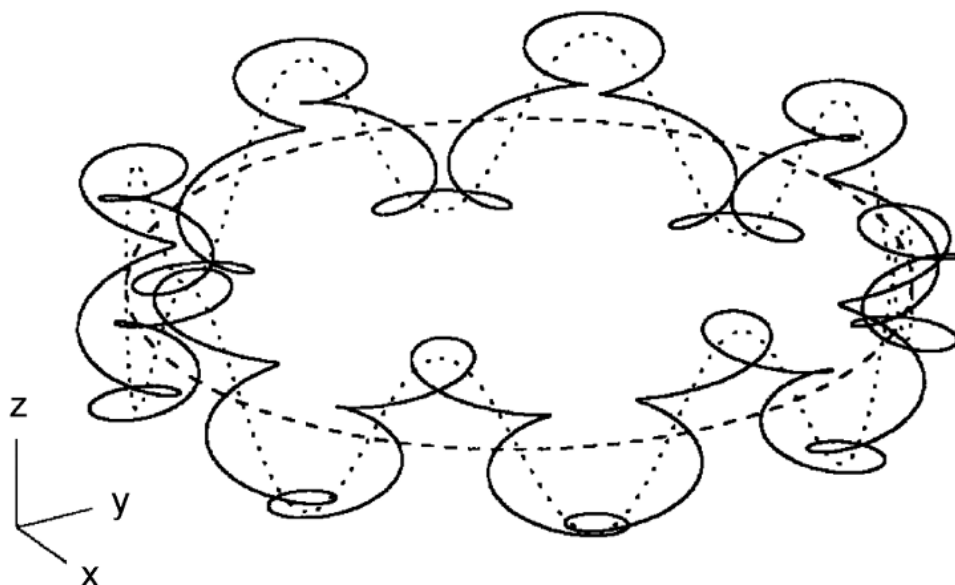


**Figure 4:** Resulting motion of an ion trapped in the ICR cell (*solid*), comprising the three basic oscillations: cyclotron ( $v_c$ ), pure magnetron motion ( $v_m$ ) (*dashed*) and magnetron plus trapping motion ( $v_\tau$ , *dotted*)<sup>105</sup>

Caravetti *et al.* developed a method for enhanced trapping efficiency<sup>103</sup>. A small potential gradient perpendicular to the velocity of the ions converts kinetic energy of the injected ions into cyclotron and magnetron motion perpendicular to the magnetic field.

For kinetic investigations and Infrared MultiPhoton Dissociation (IR-MPD) experiments a *Bruker FT-ICR* mass spectrometer has been used. This mass spectrometer has several modifications. First a window is fixed to the ICR cell to allow IR radiation in the trap and second the analyzer part can be cooled down<sup>106</sup>, this is especially required for XMCD measurements.

### Quadrupol Ion Trap (QIT) mass spectrometry

The FT-ICR mass spectrometry is a rather expensive method to store ions. Another storage possibility that is widely used and cheaper, is the so called *Paul* trap. This trap uses a RF quadrupolar field that traps the ions in three dimensions. The idea was born in 1953 by Paul and Steinwedel<sup>107, 108</sup>. The first commercial mass spectrometer was modified by Stafford *et al.* at the *Finnigan Company* in 1984<sup>109</sup>. The first review on this topic has been published in 1991<sup>110</sup>.

Different ions are present at the same time in the ion trap. To obtain a spectrum they are expelled according to their masses. The trapped ions repel each other. Thus their trajectories expand over the time. To reduce this effect a collision gas (helium) is admitted to the cell. The ion trap consist of a circular electrode (cf. Figure 5, **1** ring electrode) with two ellipsoid caps at the top and the bottom (cf. Figure 5, **2** and **3** entrance and exit cap to the Paul trap). Mass detection is performed by ion ejection out of the trap to a detector device. In most cases a fundamental RF is applied to the ring. The frequency is constant and the amplitude is variable. By stepwise changing the amplitude the ions lose their stable trajectory according to their  $m/z$  value. They are ejected from the cell. Thus the scan of the amplitude equals a scan of a mass spectrum.

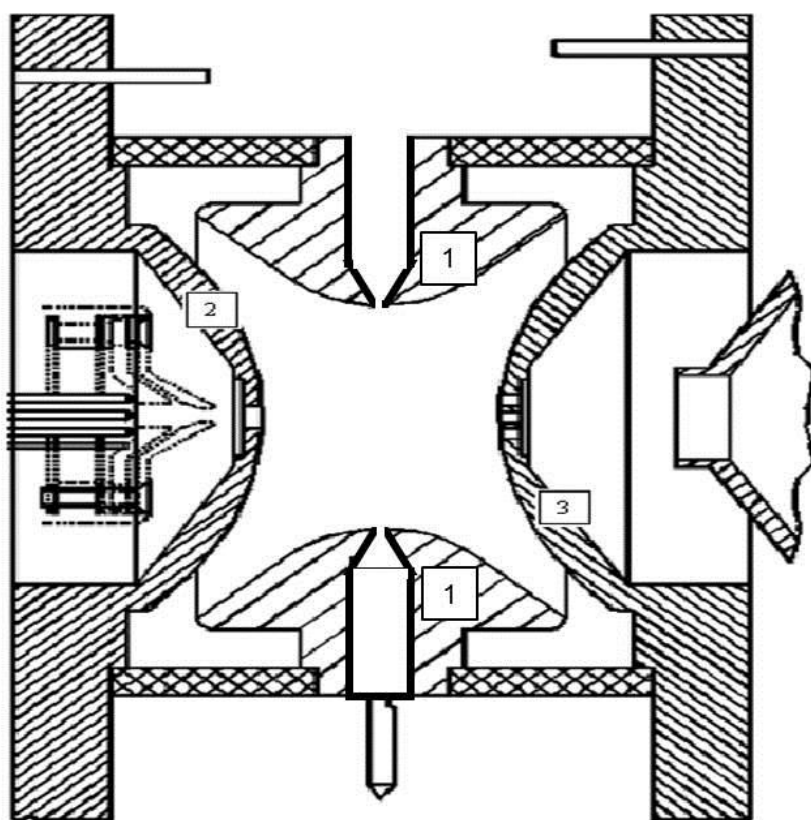


**Figure 5:** Schematic drawing of a Paul trap. **1** the ring electrode with a drilled hole to allow the passage of light for IR-MPD investigations. **2** entrance cap and **3** exit cap

Within this work two commercial mass spectrometers has been used. A *Bruker* amazon SL instrument recorded the Infrared MultiPhoton Dissociation (IR-MPD, see chapter 2) spectra of ionic dicarboxylic acids in Kaiserslautern. The second used Paul trap is also built by *Bruker*, a Esquire 3000+. This instrument recorded the IR-MPD measurements of ionic dicarboxylic acids at the Free Electron Laser CLIO in Orsay, Paris, France (see chapter 2). Both instruments have been modified to allow the passage of infrared light. In the case of the amazon SL two holes are drilled in the ring electrode such that a laser beam can pass the ion trap. In the case of the Esquire 3000+ only one hole is added in the ring electrode.

### 1.2.3. Free Electron Laser (FEL)

IR-MPD spectroscopy requires tunable high power infrared radiation. A light source to fulfill these requirements is a Free Electron Laser. Such a light source is capable of producing tunable, coherent, high power radiation. FEL cover the main part of the spectral range, wavelengths from millimeters to visible and ultraviolet to X-ray radiation are possible<sup>111, 112</sup>. FEL radiation has many applications in the biological and material sciences<sup>113</sup>. The light generation takes place by using a relativistic electron beam as lasing medium. Madey *et al.* established this concept in 1977 of a widely tunable laser using electrons of high energy as active medium instead of crystals as common laser mediums<sup>114</sup>.

The accelerated electron beam is sent through alternating magnetic fields (undulator). The electrons radiate at a resonant wavelength determined solely by the wavelength of the undulator, the magnetic field of the undulator and the electron beam energy whenever they change direction. This radiation is called bremsstrahlung. The wavelength tuning takes place by varying the distance of the gap between a pair of north and south pole magnets. Couprie and Ortega published a review on the characteristics of infrared (IR) to ultraviolet (UV) FELs<sup>115, 116</sup>. In this work the tunable high power infrared light is generated by the FEL CLIO (Centre Laser Infrarouge d'Orsay) in Orsay, Paris, France *Centre Laser Infrarouge d'Orsay*,<sup>115, 117-119</sup>. Providing laser light in the range of 67 - 3333  $\text{cm}^{-1}$  (maximum average power of 40 mJ). Within our European cooperation project EPITOPES (Electrons Plus Ions TO Probe and Elucidate Structure) all measurements using FEL technology have been performed at CLIO (cf. Figure 6) in the wavelength range of 600 - 1800  $\text{cm}^{-1}$ .

## 1. Introduction, experimental set up and methods

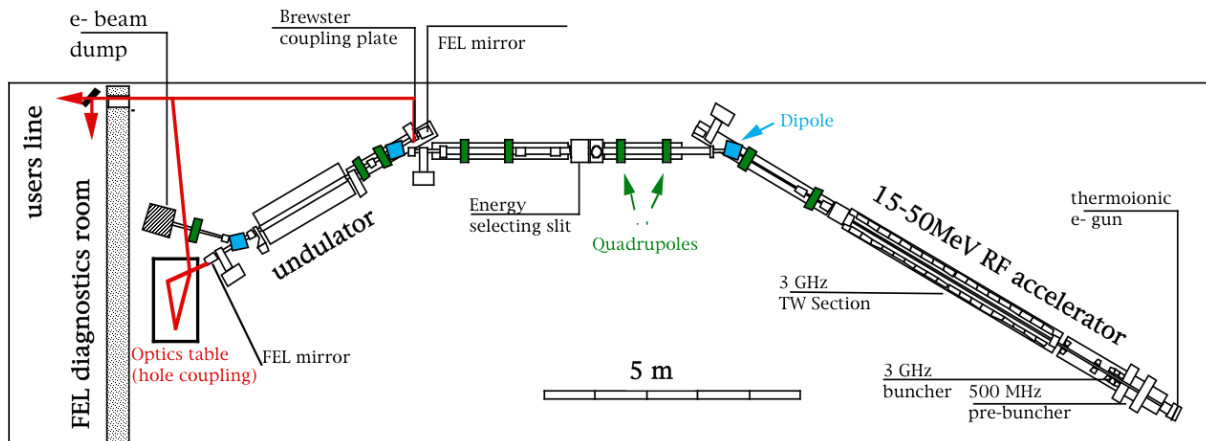


**Figure 6:** Scheme of the CLIO FEL<sup>120</sup>.

At different electron energies continuous tunability is obtained over a spectral range  $\Delta\lambda/\lambda \approx 2.5$  without the need to modify any accelerator settings. The FEL temporal structure consists of macropulses about 8  $\mu\text{s}$  long at a repetition rate of 25 Hz, containing typically 500 micropulses (cf. Figure 7). Each micropulse is a few picoseconds long and separated by 16 ns.

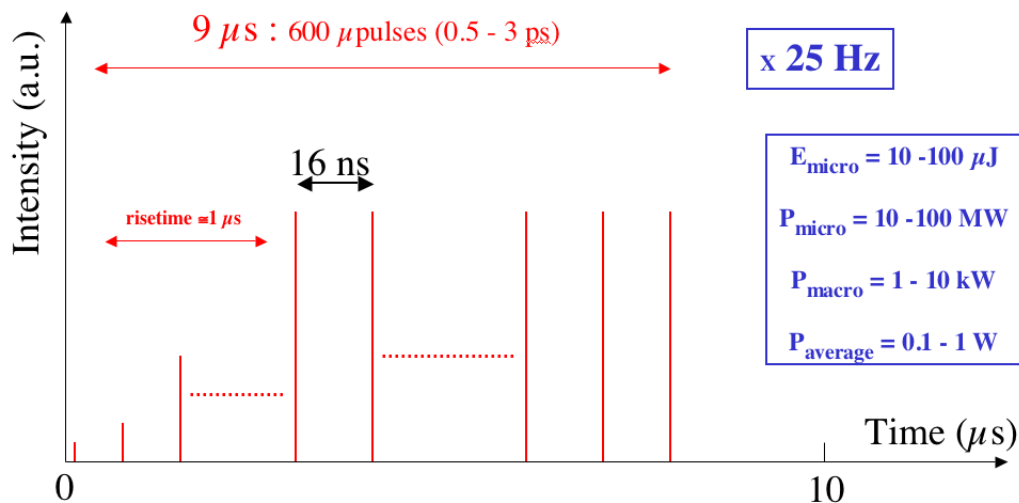


**Figure 7:** Temporal structure of one CLIO macropulse<sup>120</sup>

The intense laser radiation is suitable to probe molecular vibrations of gas phase ions by IRMPD spectroscopy. For this purpose CLIO is coupled to different mass spectrometers: a FT-ICR mass spectrometer and a Paul trap mass spectrometer (see chapter 2).

### 1.2.4. Optical Parametrical Oscillator / Amplifier (OPO/A)

The use of IR light generated by an FEL has many advantages like easy wavelength tuning and high power. This kind of radiation is ideal for IR-MPD spectroscopy (see chapter 2). But disadvantages prevail. An FEL set up is very expensive and the access to these facilities is limited to some weeks a year. Thus, experimental scientists are in need of a tunable light source with enough power to fragment ions.

The idea of such a light source was first mentioned in 1967<sup>121</sup> and first reported in an edited book 1977<sup>122</sup>. This light source is the Optical Parametric Oscillator (OPO) / Amplifier (OPA). This Laser set up is available in sizes that fit easily on a table set up. The laser light is generated by a frequency fixed polarized pump laser. The pump laser beam is split by a nonlinear crystal into a signal wave and an idler wave. The wavelength of these new beams depends on the refraction index of the crystal. The refractive index of a nonlinear crystal depends on the angle of the incident light beam and the crystal and the crystal temperature. For spectroscopy high spectral resolution is required. To reach a better resolution the bandwidth of the pump laser should be as small as possible. The usage of seeded pump lasers fulfills this requirement<sup>123</sup>. In seeded lasers a second weak laser beam is injected in the cavity of the pump laser and thus the wavelength of the seeded laser defines one favored oscillation in the pump laser cavity. Another possibility to refine the bandwidth of the OPO / OPA system is the installation of a grating within the OPO cavity.

Within this work OPO/OPA systems of Dean Guyer's company *Laservision* have been used: As a pump laser beam serves Nd:YAG lasers with an output wavelength of 1064 nm. The pump beam is injected to the OPO/OPA set up by two steering mirrors and then divided into two separated beam lines (cf. Figure 8). One third of the laser power is directed to the OPO resonator. This part of the light passes a potassium dihydrogen phosphate (KDP) crystal that doubles the frequency of the light to 532 nm. The now visible green light enters the OPO resonator consisting of a converging potassium titanyl phosphate (KTP) crystal. According to the angle between the light and the crystal, each photon is converted into one signal (signal 1) and one idler photon (idler 1). The idler 1 photon is directed to the OPA stage. This stage comprises of four potassium titanyl arsenate (KTA) crystals. The idler 1 photon is recombined with the residual two thirds of the 1064 nm pump beam. In the OPA process a signal (signal 2) and an idler beam (idler 2) is generated. The signal 2 beam possesses the same frequency as idler 1.

## 1. Introduction, experimental set up and methods

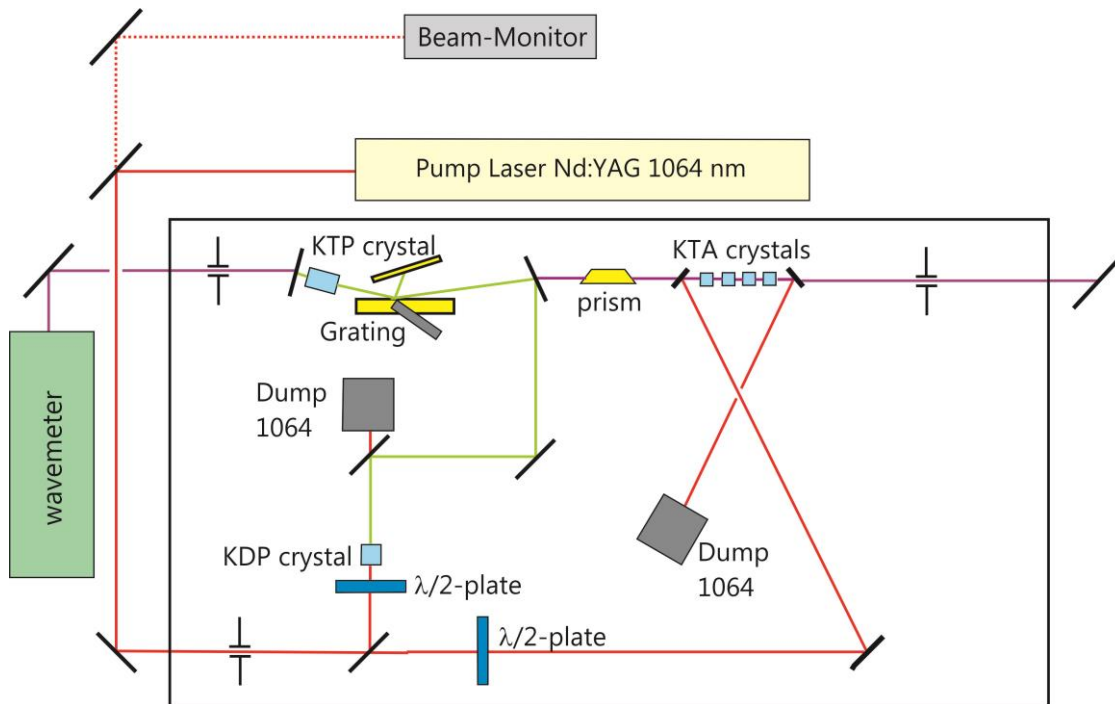


**Figure 8:** Set up of the OPO/OPA system.

A filter separates the signal 2 and idler 2 beam before either the idler 2 beam ( $2200 - 4700 \text{ cm}^{-1}$ ) or the signal 2 beam ( $4700 - 7400 \text{ cm}^{-1}$ ) is directed to the experiment. In addition to this, a Difference Frequency Mixing (DFM) crystal ( $\text{AgGaSe}_2$ ) is able to recombine the signal 2 and idler 2 beam to cover a wavelength range between  $800$  and  $2200 \text{ cm}^{-1}$ . The laser power of the OPO system is up to  $15 \text{ mJ}$ . This is nearly comparable with the FEL. When using the DFM stage, the power is much lower (approximately  $2 - 3 \text{ mJ}$ ).

In this work, two different combinations of Nd:YAG pump lasers and Dean Guyer OPO/OPA systems were used: a Continuum PowerLite 8000 with a narrowband OPO/OPA system and a seeded Continuum PowerLite 8000 laser with a broadband OPO/OPA system.



### 1.3. Methods

#### 1.3.1. InfraRed - Multi Photon Dissociation (IR-MPD)

In the gas phase the measurement of absorption spectra is difficult or impossible due to the low ion density. To solve this problem an action spectroscopy method is applied. InfraRed - Multi Photon Dissociation (IR-MPD) spectroscopy is an approach to obtain IR spectra of molecules in the gas phase<sup>3, 124</sup>. This method was first described by Lee *et al.* in 1977 and Beauchamp *et al.* used this method on biologically relevant molecules in 1978 to induce the fragmentation by irradiating and thus heating the trapped ions with infrared light<sup>125</sup>. The use of CO<sub>2</sub> lasers in combination with FT-ICR instruments to perform IR-MPD became a widely used technique especially for biological sequencing<sup>126</sup>. The use of Paul trap mass spectrometers with their high gas load and thus rethermalization of the irradiated ion was established shortly after<sup>127, 128</sup>.

To perform IR-MPD spectroscopy, the ions are transferred to an ion trap (see chapter 1.2.2) and then radiated with IR photons. If the wavelength of the photons is in resonance with a vibrational mode of the ions, the ion absorbs the light and gains energy. This energy is redistributed due to internal vibrational relaxation (IVR) into all accessible modes of the ion. How the fragmentation takes place is still discussed. Two models have been debated: In the first model, the dissociation of the ions occurs by absorption of multiple photons adding their energy into one mode and further absorption takes place in the next excited state. The fragmentation takes place by ladder climbing. The second model assumes that absorption of photons into the ground state of one mode increases the energy of the ion which is redistributed into the rest of the molecule (IVR: intramolecular vibrational redistribution) and thus the ground state is repeatedly pumped. Depending on the photon energy the absorption of up to 100 photons can be necessary before fragmentation occurs<sup>129</sup>. The second model seems more reasonable. In the first model anharmonicity reduces the energy uptake as soon as higher states are reached. The fragmentation does not always occur in the mode which is pumped, often the path with the lowest fragmentation energy is experimentally observed. Many publications deal with the dynamics of the energy transfer and fragmentation process of Collision Induced Dissociation (CID)<sup>130</sup> and IR-MPD<sup>131, 132</sup> often combining theoretical investigations of the RRKM (Rice-Ramsberger-Kassel-Markus) theory of collision less dissociation<sup>133-140</sup>. A large variety of neutral and ionic systems has been investigated by IRMPD before<sup>111, 141-148</sup>.

Since IR-MPD spectroscopy is an action spectroscopy a limiting factor of this method is that the obtained spectra only mimic the (calculated) absorption spectra. The calculated intensity does not

necessary relate to the observed fragmentation efficiency. Furthermore, it is possible that absorption does not lead to fragmentation in some vibrational modes. These are called “dark modes”.

A further development on IR-MPD spectroscopy is the two color IR-MPD spectroscopy<sup>149</sup>. Sometimes the energy of the OPO/OPA laser system is not sufficient for fragmentation, especially while using the DFM stage (see chapter 1.2.4). While recording IR spectra in this energy range, it might happen that repeated photon absorption into a vibrational mode does not lead to fragmentation. This can be overcome by post heating an irradiated molecule with a second laser pulse, whose wavelength is set to a known band of the system, e.g. in the OH stretching and thus heating the trapped ions with infrared light. Within the two-color investigations reported in this thesis, the broadband system was used for scanning and the narrowband system for probing.

### 1.3.2. Kinetic investigations with neutral reaction gases

In our research group we are interested in the reactivity of cluster ions with neutral reaction gases<sup>10</sup>. We are using mass spectrometry to investigate isolated ions. The ions are generated with the LVAP or the ESI source (see chapter 1.2.3.), respectively and then transferred into the ICR cell within the high field region of the superconducting magnet (see chapter 1.2.2.). Since the pressure is very low in the ICR cell we can add a neutral reaction gas. A reaction can be proven by appearance of additional masses in the mass spectrum and simultaneous decrease of the intensity of the former *parent* ion. Multiple mass spectra are recorded while varying the *reaction delay* (the time between the entering of the ions into the ICR cell and their mass detection). In the time dependent mass spectra the different reaction products are identified. The reaction gas is apparent in excess and constantly added to the ICR cell, the relative intensities of the identified mass peaks can be plotted and fitted as *pseudo first order* kinetics.

$$v = -\frac{d[Int]}{dt} = k \cdot [Int] \quad (6)$$

The interpretation of the resulting rate constants is executed by the comparison of the values obtained by different molecules. In this work we investigated the reaction of benzene and perdeutero benzene with different transition metal complexes and mixed transition metal complexes.

### 1.3.3. Computational methods

The computational prediction of molecular structures and vibrational spectra plays a important role in chemistry. In the last years many improvements contributed to the exact simulation of molecular properties. Especially density functional theory (DFT) is widely used. This theory is developed by Hohenberg und Kohn in 1964<sup>150</sup>. DFT calculations determine a molecule's ground state energy by performing calculations using the electron density (short lecture see Ref.<sup>151</sup>): During the calculations the molecular geometry is energy optimized until within given convergence criteria the lowest energy is reached. To find the global minimum, many calculation with different start geometries have to be performed. From the geometries the characteristic bond lengths and angels are extracted from the calculated geometries. Vibrational spectra can be simulated. These simulated vibrational spectra serve to identify the molecular structure by comparison with the experimental IR-MPD spectra (see chapter 2).

The Hohenberg-Kohn-Theorem<sup>150</sup> claims that the ground state of a system of N electrons does have a unique position dependent electron density and all molecular properties are functionals of this electron density. Thus it is not necessary to solve the Schrödinger equation for the whole system. The system is described by the Kohn-Sham equations<sup>152</sup> which treat all N electrons separately generating the same density as the complete molecule with interacting electrons. Therefore the Kohn-Sham wavefunction is a single Slater determinant constructed from a set of orbitals that are the lowest energy solution to

$$\left(-\frac{\hbar}{2m}\nabla^2 + V_{eff}(r)\right)\Phi_i(r) = \epsilon_i\Phi_i(r) \quad (7)$$

With  $\epsilon_i$  being the orbital energy of the corresponding Kohn-Sham orbital.

The density of the whole system is

$$\rho(r) = \sum_i^N |\Phi_i(r)|^2 \quad (8)$$

And the total energy of the system is obtained by

$$E[\rho] = T_s[\rho] + \int dr V_{ext}(r)\rho(r) + V_H[\rho] + E_{XC}[\rho] \quad (9)$$

With

$T_s[\rho]$	Kohn-Sham kinetic energy
$V_{ext}(r)$	external potential interaction (electron-nuclei interaction)

## 1. Introduction, experimental set up and methods

---

$V_H(r)$	Coulomb energy
$E_{XC}[\rho]$	exchange-correlation (XC) energy

To perform DFT calculation the choice of the basis set and the choice of the functional used in the term of exchange correlation energy is crucial. To approaches to determine the XC term exists: the local density approximation (LDA) and the generalized gradient approximation (GGA). Very popular is also the use of hybrid methods combining GGA methods with partially calculating exchange energy according to the Hartree-Fock-method<sup>153-155</sup>. The results are more precise while a longer calculation time is recommended. Within this work, energetic and structural calculations have been performed on DFT level before the obtained results are used in MP2 (Møller-Plesset perturbation theory second order) calculations. MP2 is a post-Hartree-Fock method improving the Hartree-Fock method by adding electron correlation effects<sup>156-159</sup>. Møller and Plesset proposed the MP2 method in 1934 by<sup>160</sup>. The perturbation treatment of atoms and molecules in which the unperturbed wave function is the Hartree-Fock function and as a non-iterative correction higher excitations are added, based on the so-called many body perturbation theory<sup>161</sup>.

The perturbation  $\hat{H}'$  is the difference between the true molecular Hamiltonian  $\hat{H}$  and  $\hat{H}^0$  (the Hamiltonian of the HF equation). The Møller-Plesset (MP) unperturbed Hamiltonian is taken as the sum of one-electron Fock operators  $f$  and a parameter  $\lambda$  is introduced, which leads to a unperturbed system for  $\lambda = 0$  and a fullyturned on perturbation for  $\lambda = 1$ .

$$\hat{H} = \hat{H}^0 + \lambda\hat{H}' \quad (10)$$

The Schrödinger equation for a perturbed state is then

$$\hat{H}\psi_n = (\hat{H}^0 + \lambda\hat{H}')\psi_n = E_n\psi_n \quad (11)$$

With

$\psi_n$  perturbed wavefunction

$E_n$  energy of the System

Inserting a Taylor series for  $\psi_n$  and after serveral transformations the desired expression for the energy of the perturbed system  $E_n^{(2)}$  is achieved.

$$E_n^{(2)} = \sum_{m \neq n} \frac{|\langle \Psi_m^0 | \hat{H}' | \Psi_n^0 \rangle|^2}{E_n^{(0)} - E_m^{(0)}} \quad (12)$$

By now we are able to determine the second-order correction to the energy that depends only on the wavefunctions of the undisturbed system in the ground state. For determination of the third-order correction it is necessary to know the first perturbed wavefunction  $\Psi_m^1$ . Thus the calculation becomes more complicated. The second-order Møller-Plesset perturbation theory (MP2) method includes correlation and is size consistent. Besides these advantages of this method, calculations exhibit relative high computational costs and, as this method is not variational, the risk persists that the calculated energy is below the true energy. All calculation presented in this work are performed with the TURBOMOLE<sup>162</sup> program or the GAUSSIAN 09 program<sup>163</sup>.

### 1.4. References

1. E. S. de Hoffmann, V., *Mass Spectrometry: Principles and Applications*, John Wiley & Sons Ltd., Chichester, West Sussex, England, 2007.
2. J. H. Gross, *Massenspektrometrie: Ein Lehrbuch*, Springer Spektrum, Berlin Heidelberg, 2013.
3. R. C. Dunbar, *International Journal of Mass Spectrometry*, 2000, **200**, 571-589.
4. K. Levsen and H. Schwarz, *Angewandte Chemie*, 1976, **88**, 589-599.
5. R. G. Cooks, *J. Mass Spectrom.*, 1995, **30**, 1215-1221.
6. E. de Hoffmann, *J. Mass Spectrom.*, 1996, **31**, 129-137.
7. A. K. Shukla and J. H. Futrell, *J. Mass Spectrom.*, 2000, **35**, 1069-1090.
8. K. R. Jennings, *International Journal of Mass Spectrometry*, 2000, **200**, 479-493.
9. S. Peredkov, M. Neeb, W. Eberhardt, J. Meyer, M. Tombers, H. Kampschulte and G. Niedner-Schatteburg, *Phys. Rev. Lett.*, 2011, **107**, 233401.
10. B. Pfeffer, S. Jaberg and G. Niedner-Schatteburg, *Journal of Chemical Physics*, 2009, **131**.
11. M. Tombers, L. Barzen and G. Niedner-Schatteburg, *The Journal of Physical Chemistry A*, 2012, **117**, 1197-1203.
12. L. Barzen, M. Tombers, C. Merkert, J. Hewer and G. Niedner-Schatteburg, *International Journal of Mass Spectrometry*, 2012, **330**, 271-276.
13. L. Stryer, Berg, Jeremy M., Tymoczko, John L., *Biochemie*, Springer Spectrum, 2013.
14. T. Steiner, *Angewandte Chemie-International Edition*, 2002, **41**, 48-76.
15. S. J. Grabowski, *Hydrogen Bonding - New Insights*, Springer, Dordrecht, Netherlands, 2006.
16. S. Scheiner, *Hydrogen Bonding: A Theoretical Perspective*, University Press, Oxford, 1997.
17. U. Buck and F. Huisken, *Chem. Rev.*, 2000, **100**, 3863-3890.
18. N. J. Singh, A. C. Olleta, A. Kumar, M. Park, H. B. Yi, I. Bandyopadhyay, H. M. Lee, P. Tarakeshwar and K. S. Kim, *Theor. Chem. Acc.*, 2006, **115**, 127-135.
19. H. M. Lee, S. B. Suh, J. Y. Lee, P. Tarakeshwar and K. S. Kim, *Journal of Chemical Physics*, 2000, **112**, 9759-9772.
20. H. M. Lee, S. B. Suh, P. Tarakeshwar and K. S. Kim, *Journal of Chemical Physics*, 2005, **122**, 6.
21. G. Gilli and P. Gilli, *Journal of Molecular Structure*, 2000, **552**, 1-15.
22. V. Bertolasi, P. Gilli, V. Ferretti and G. Gilli, *Chemistry-a European Journal*, 1996, **2**, 925-934.
23. W. W. Cleland and M. M. Kreevoy, *Science*, 1994, **264**, 1887-1890.
24. H. S. Cho, N. C. Ha, G. Choi, H. J. Kim, D. Lee, K. S. Oh, K. S. Kim, W. Lee, K. Y. Choi and B. H. Oh, *Journal of Biological Chemistry*, 1999, **274**, 32863-32868.
25. P. A. Frey, S. A. Whitt and J. B. Tobin, *Science*, 1994, **264**, 1927-1930.
26. K. S. Kim, K. S. Oh and J. Y. Lee, *Proceedings of the National Academy of Sciences of the United States of America*, 2000, **97**, 6373-6378.
27. J. Lin and P. A. Frey, *Journal of the American Chemical Society*, 2000, **122**, 11258-11259.
28. K. S. Kim, D. W. Kim, J. Y. Lee, P. Tarakeshwar and K. S. Oh, *Biochemistry*, 2002, **41**, 5300-5306.
29. J. R. Roscioli, L. R. McCunn and M. A. Johnson, *Science*, 2007, **316**, 249-254.
30. T. Pankewitz, A. Lagutschenkov, G. Niedner-Schatteburg, S. S. Xantheas and Y. T. Lee, *Journal of Chemical Physics*, 2007, **126**.
31. K. R. Asmis, N. L. Pivonka, G. Santambrogio, M. Brummer, C. Kaposta, D. M. Neumark and L. Woste, *Science*, 2003, **299**, 1375-1377.
32. J. C. Jiang, Y. S. Wang, H. C. Chang, S. H. Lin, Y. T. Lee and G. Niedner-Schatteburg, *Journal of the American Chemical Society*, 2000, **122**, 1398-1410.
33. N. I. Hammer, E. G. Diken, J. R. Roscioli, M. A. Johnson, E. M. Myshakin, K. D. Jordan, A. B. McCoy, X. Huang, J. M. Bowman and S. Carter, *Journal of Chemical Physics*, 2005, **122**, 10.
34. R. W. Larsen, P. Zielke and M. A. Suhm, *Journal of Chemical Physics*, 2007, **126**.
35. F. W. Patureau, J. Wencel-Delord and F. Glorius, *Aldrichimica Acta*, 2012, **45**, 31-41.

## 1. Introduction, experimental set up and methods

---

36. F. W. Patureau, T. Besset, R. Fröhlich and F. Glorius, *Comptes Rendus Chimie*, 2012, **15**, 1081-1085.
37. J. Wencel-Delord, C. Nimphius, F. W. Patureau and F. Glorius, *Chemistry – An Asian Journal*, 2012, **7**, 1208-1212.
38. J. Wencel-Delord, C. Nimphius, F. W. Patureau and F. Glorius, *Angewandte Chemie International Edition*, 2012, **51**, 2247-2251.
39. G. Altenhoff, R. Goddard, C. W. Lehmann and F. Glorius, *Angewandte Chemie International Edition*, 2003, **42**, 3690-3693.
40. S. Würtz, C. Lohre, R. Fröhlich, K. Bergander and F. Glorius, *Journal of the American Chemical Society*, 2009, **131**, 8344-8345.
41. R. D. Adams and F. A. Cotton, *Catalysis by di- and polynuclear metal cluster complexes*, Wiley-VCH, 1998.
42. M.-L. Louillat and F. W. Patureau, *Organic Letters*, 2012, **15**, 164-167.
43. H. M. L. Davies and J. R. Manning, *Nature*, 2008, **451**, 417-424.
44. G. M. Sammis, H. Danjo and E. N. Jacobsen, *Journal of the American Chemical Society*, 2004, **126**, 9928-9929.
45. M. Arndt, K. S. M. Salih, A. Fromm, L. J. Goossen, F. Menges and G. Niedner-Schatteburg, *Journal of the American Chemical Society*, 2011, **133**, 7428-7449.
46. C. S. Yeh, Y. G. Byun, S. Afzaal, S. Z. Kan, S. Lee, B. S. Freiser and P. J. Hay, *Journal of the American Chemical Society*, 1995, **117**, 4042-4048.
47. Y. G. Byun, S. Z. Kan, S. A. Lee, Y. H. Kim, M. Miletic, R. E. Bleil, S. Kais and B. S. Freiser, *The Journal of Physical Chemistry*, 1996, **100**, 6336-6341.
48. M. R. Zakin, R. O. Brickman, D. M. Cox and A. Kaldor, *The Journal of Chemical Physics*, 1988, **88**, 6605-6610.
49. J. L. Elkind, F. D. Weiss, J. M. Alford, R. T. Laaksonen and R. E. Smalley, *Journal of Chemical Physics*, 1988, **88**, 5215-5224.
50. R. S. Walters, T. D. Jaeger and M. A. Duncan, *The Journal of Physical Chemistry A*, 2002, **106**, 10482-10487.
51. P. J. Brucat, C. L. Pettiette, S. Yang, L. S. Zheng, M. J. Craycraft and R. E. Smalley, *The Journal of Chemical Physics*, 1986, **85**, 4747-4748.
52. M. P. Irion, *Int. J. Mass Spectrom. Ion Process.*, 1992, **121**, 1-47.
53. P. B. Armentrout, *Annual Review of Physical Chemistry*, 2001, **52**, 423-461.
54. M. B. Knickelbein, *Annual Review of Physical Chemistry*, 1999, **50**, 79-115.
55. J. Harris and S. Andersson, *Phys. Rev. Lett.*, 1985, **55**, 1583-1586.
56. J. S. Pilgrim, L. R. Brock and M. A. Duncan, *The Journal of Physical Chemistry*, 1995, **99**, 544-550.
57. A. Bérces, P. A. Hackett, L. Lian, S. A. Mitchell and D. M. Rayner, *The Journal of Chemical Physics*, 1998, **108**, 5476-5490.
58. K. Eller and H. Schwarz, *Chem. Rev.*, 1991, **91**, 1121-1177.
59. U. Achatz, C. Berg, S. Joos, B. S. Fox, M. K. Beyer, G. Niedner-Schatteburg and V. E. Bondybey, *Chem. Phys. Lett.*, 2000, **320**, 53-58.
60. G. Albert, C. Berg, M. Beyer, U. Achatz, S. Joos, G. Niedner-Schatteburg and V. E. Bondybey, *Chem. Phys. Lett.*, 1997, **268**, 235-241.
61. R. L. Whetten, D. M. Cox, D. J. Trevor and A. Kaldor, *Phys. Rev. Lett.*, 1985, **54**, 1494-1497.
62. J. Ho, L. Zhu, E. K. Parks and S. J. Riley, *Journal of Chemical Physics*, 1993, **99**, 140-147.
63. T. D. Jaeger, D. van Heijnsbergen, S. J. Klippenstein, G. von Helden, G. Meijer and M. A. Duncan, *Journal of the American Chemical Society*, 2004, **126**, 10981-10991.
64. D. van Heijnsbergen, T. D. Jaeger, G. von Helden, G. Meijer and M. A. Duncan, *Chem. Phys. Lett.*, 2002, **364**, 345-351.
65. H. P. Fritz, W. Lüttke, H. Stammreich and R. Forneris, *Spectrochimica Acta*, 1961, **17**, 1068-1091.
66. G. M. Koretsky and M. B. Knickelbein, *Chem. Phys. Lett.*, 1997, **267**, 485-490.

## 1. Introduction, experimental set up and methods

---

67. N. R. Walker, R. S. Walters and M. A. Duncan, *New Journal of Chemistry*, 2005, **29**, 1495-1503.
68. M. R. Zakin, D. M. Cox and A. Kaldor, *The Journal of Physical Chemistry*, 1987, **91**, 5224-5228.
69. C. Berg, T. Schindler, G. Niedner-Schatteburg and V. E. Bondybey, *J. Chem. Phys.*, 1995, **102**, 4870-4884.
70. M. R. Zakin, R. O. Brickman, D. M. Cox and A. Kaldor, *The Journal of Chemical Physics*, 1988, **88**, 5943-5947.
71. C. Berg, M. Beyer, U. Achatz, S. Joos, G. Niedner-Schatteburg and V. E. Bondybey, *Journal of Chemical Physics*, 1998, **108**, 5398-5403.
72. C. Berg, M. Beyer, T. Schindler, G. Niedner-Schatteburg and V. E. Bondybey, *Journal of Chemical Physics*, 1996, **104**, 7940-7946.
73. C. Berg, T. Schindler, M. Kantlehner, G. Niedner-Schatteburg and V. E. Bondybey, *Chemical Physics*, 2000, **262**, 143-149.
74. M. Gerhards, O. C. Thomas, J. M. Nilles, W. J. Zheng and K. H. Bowen, *Journal of Chemical Physics*, 2002, **116**, 10247-10252.
75. S. Jaberg, TU Kaiserslautern, 2008.
76. B. Pfeffer, TU Kaiserslautern, 2008.
77. V. E. Bondybey and M. K. Beyer, *Journal of Physical Chemistry A*, 2001, **105**, 951-960.
78. H. T. Liu, S. T. Sun, X. P. Xing and Z. C. Tang, *Rapid Communications in Mass Spectrometry*, 2006, **20**, 1899-1904.
79. D. Majumdar, S. Roszak and K. Balasubramanian, *The Journal of Chemical Physics*, 2001, **114**, 10300-10310.
80. K. Béchamp, M. Levesque, H. Joly and L. Manceron, *The Journal of Physical Chemistry A*, 2006, **110**, 6023-6031.
81. S. Maruyama, L. R. Anderson and R. E. Smalley, *Review of Scientific Instruments*, 1990, **61**, 3686-3693.
82. T. G. Dietz, M. A. Duncan, D. E. Powers and R. E. Smalley, *Journal of Chemical Physics*, 1981, **74**, 6511-6512.
83. D. Proch and T. Trickl, *Review of Scientific Instruments*, 1989, **60**, 713-716.
84. M. Yamashita and J. B. Fenn, *J. Phys. Chem.*, 1984, **88**, 4671-4675.
85. M. Mann, C. K. Meng and J. B. Fenn, *Anal. Chem.*, 1989, **61**, 1702-1708.
86. J. B. Fenn, M. Mann, C. K. Meng, S. F. Wong and C. M. Whitehouse, *Science*, 1989, **246**, 64-71.
87. M. Yamashita and J. B. Fenn, *J. Phys. Chem.*, 1984, **88**, 4451-4459.
88. J. A. Loo, H. R. Udseth and R. D. Smith, *Anal. Biochem.*, 1989, **179**, 404-412.
89. J. F. de la Mora, G. J. Van Berkel, C. G. Enke, R. B. Cole, M. Martinez-Sanchez and J. B. Fenn, *J. Mass Spectrom.*, 2000, **35**, 939-952.
90. N. B. Cech and C. G. Enke, *Mass Spectrom. Rev.*, 2001, **20**, 362-387.
91. T. C. Rohner, N. Lion and H. H. Girault, *Phys. Chem. Chem. Phys.*, 2004, **6**, 3056-3068.
92. A. P. Snyder, ed., *Biochemical and biotechnological applications of electrospray mass spectrometry*, Wiley, 1996.
93. R. B. Cole, ed., *Electrospray ionization mass spectrometry: fundamentals instrumentation, and applications*, Wiley, 1997.
94. R. B. Cole, Wiley, 2011.
95. P. Kebarle and L. Tang, *Anal. Chem.*, 1993, **65**, A972-A986.
96. A. Gomez and K. Q. Tang, *Phys. Fluids*, 1994, **6**, 404-414.
97. E. O. Lawrence and D. Cooksey, *Phys. Rev.*, 1936, **50**, 1131-1140.
98. Comisaró.Mb and A. G. Marshall, *Chem. Phys. Lett.*, 1974, **25**, 282-283.
99. Comisaró.Mb and A. G. Marshall, *Chem. Phys. Lett.*, 1974, **26**, 489-490.
100. I. J. Amster, *J. Mass Spectrom.*, 1996, **31**, 1325-1337.
101. A. G. Marshall, C. L. Hendrickson and G. S. Jackson, *Mass Spectrom. Rev.*, 1998, **17**, 1-35.
102. J. D. Jackson, *Klassische Elektrodynamik*, de Gruyter, Berlin, New York, 1983.
103. P. Caravatti and M. Allemann, *Org. Mass Spectrom.*, 1991, **26**, 514-518.



104. L. S. Brown and G. Gabrielse, *Rev. Mod. Phys.*, 1986, **58**, 233-311.
105. L. Schweikhard, J. Ziegler, H. Bopp and K. Lützenkirchen, *Int. J. Mass Spectrom. Ion Process.*, 1995, **141**, 77-90.
106. S. Peredkov, A. Savci, S. Peters, M. Neeb, W. Eberhardt, H. Kampschulte, J. Meyer, M. Tombers, B. Hofferberth, F. Menges and G. Niedner-Schatteburg, *Journal of Electron Spectroscopy and Related Phenomena*, 2011, **184**, 113-118.
107. W. Paul and H. Steinwedel, *Z. Naturforsch. Sect. A-J. Phys. Sci.*, 1953, **8**, 448-450.
108. *US Pat.*, 1960.
109. G. C. Stafford, P. E. Kelley, J. E. P. Syka, W. E. Reynolds and J. F. J. Todd, *Int. J. Mass Spectrom. Ion Process.*, 1984, **60**, 85-98.
110. J. F. J. Todd, *Mass Spectrom. Rev.*, 1991, **10**, 3-52.
111. W. B. Colson, E. D. Johnson, M. J. Kelley and H. A. Schwettman, *Phys. Today*, 2002, **55**, 35-41.
112. H. P. Freund and G. R. Neil, *Proc. IEEE*, 1999, **87**, 782-803.
113. G. S. Edwards, S. J. Allen, R. F. Haglund, R. J. Nemanich, B. Redlich, J. D. Simon and W. C. Yang, *Photochem. Photobiol.*, 2005, **81**, 711-735.
114. D. A. G. Deacon, L. R. Elias, J. M. J. Madey, G. J. Ramian, H. A. Schwettman and T. I. Smith, *Phys. Rev. Lett.*, 1977, **38**, 892-894.
115. M. E. Couprie and J. M. Ortega, *Analisis*, 2000, **28**, 725-736.
116. J. J. Valle, J. R. Eyler, J. Oomens, D. T. Moore, A. F. G. van der Meer, G. von Helden, G. Meijer, C. L. Hendrickson, A. G. Marshall and G. T. Blakney, *Rev. Sci. Instrum.*, 2005, **76**.
117. R. Prazeres, F. Glotin, C. Insa, D. A. Jaroszynski and J. M. Ortega, *Eur. Phys. J. D*, 1998, **3**, 87-93.
118. R. Prazeres, F. Glotin, J. M. Ortega, C. Rippon, R. Andouart, J. M. Berset, E. Arnaud and R. Chaput, *Nucl. Instrum. Methods Phys. Res. Sect. A-Accel. Spectrom. Dect. Assoc. Equip.*, 2000, **445**, 204-207.
119. J. M. Ortega, J. M. Berset, R. Chaput, F. Glotin, G. Humbert, D. Jaroszynski, P. Joly, B. Kergosien, J. Lesrel, O. Marcouille, A. Peremans, R. Prazeres and A. Tadjeddine, *Nucl. Instrum. Methods Phys. Res. Sect. A-Accel. Spectrom. Dect. Assoc. Equip.*, 1996, **375**, 618-625.
120. Centre Laser Infrarouge d'Orsay, [http://clio.lcp.u-psud.fr/clio\\_eng/laserSR.html](http://clio.lcp.u-psud.fr/clio_eng/laserSR.html),.
121. S. E. Harris, M. K. Oshman and R. L. Byer, *Phys. Rev. Lett.*, 1967, **18**, 732-&.
122. R. L. Byer, ed., *Nonlinear optics Edited by P.G. Harper*, B.S. Wherrett Academic Press, Academic, 1977.
123. J. G. Haub, M. J. Johnson, B. J. Orr and R. Wallenstein, *Appl. Phys. Lett.*, 1991, **58**, 1718-1720.
124. M. A. Duncan, *International Journal of Mass Spectrometry*, 2000, **200**, 545-569.
125. R. L. Woodin, D. S. Bomse and J. L. Beauchamp, *Journal of the American Chemical Society*, 1978, **100**, 3248-3250.
126. D. P. Little, J. P. Speir, M. W. Senko, P. B. Oconnor and F. W. McLafferty, *Anal. Chem.*, 1994, **66**, 2809-2815.
127. J. S. Brodbelt and J. J. Wilson, *Mass Spectrom. Rev.*, 2009, **28**, 390-424.
128. Y. Hashimoto, H. Hasegawa and L. Waki, *Rapid Communications in Mass Spectrometry*, 2004, **18**, 2255-2259.
129. J. Oomens, A. J. A. van Rooij, G. Meijer and G. von Helden, *Astrophysical Journal*, 2000, **542**, 404-410.
130. J. Laskin and J. H. Futrell, *Mass Spectrom. Rev.*, 2003, **22**, 158-181.
131. J. Roithova, *Chemical Society Reviews*, 2012, **41**, 547-559.
132. J. Oomens, B. G. Sartakov, G. Meijer and G. Von Helden, *International Journal of Mass Spectrometry*, 2006, **254**, 1-19.
133. J. G. Black, E. Yablonovitch, N. Bloembergen and S. Mukamel, *Phys. Rev. Lett.*, 1977, **38**, 1131-1134.
134. W. H. Green, C. B. Moore and W. F. Polik, *Annual Review of Physical Chemistry*, 1992, **43**, 591-626.

## 1. Introduction, experimental set up and methods

---

135. K. K. Lehmann, G. Scoles and B. H. Pate, *Annual Review of Physical Chemistry*, 1994, **45**, 241-274.
136. Rynbrand.Jd and Rabinovi.Bs, *J. Phys. Chem.*, 1971, **75**, 2164-&.
137. S. H. P. Bly, L. W. Dickson, Y. Nomura, J. C. Polanyi, I. W. M. Smith, P. N. Clough, M. Kneba, U. Wellhausen, J. Wolfrum, P. E. Siska, R. J. Wolf, C. S. Sloane, W. L. Hase, L. Holmlid, K. Rynefors, K. Luther, M. Quack, K. Freed, W. M. Jackson, R. Naaman, R. N. Zare, G. Hancock, R. Walsh, J. Troe, D. M. Lubman, G. Atkinson, D. W. Setser, M. R. Levy, M. Mangir, H. Reisler, M. H. Yu, C. Wittig, C. M. Miller, F. M. G. Tablas, M. N. R. Ashfold, A. J. Roberts, I. Veltman, A. Durkin, D. J. Smith, R. Grice, D. R. Herschbach, G. M. McClelland and K. L. Kompa, *Faraday Discussions of the Chemical Society*, 1979, **67**, 221-254.
138. O. K. Rice and H. C. Ramsperger, *Journal of the American Chemical Society*, 1927, **49**, 1617-1629.
139. L. S. Kassel, *J. Phys. Chem.*, 1928, **32**, 1065-1079.
140. L. S. Kassel, *J. Phys. Chem.*, 1928, **32**, 225-242.
141. J. Lemaire, P. Boissel, M. Heninger, G. Mauclaire, G. Bellec, H. Mestdagh, A. Simon, S. L. Caer, J. M. Ortega, F. Glotin and P. Maitre, *Phys. Rev. Lett.*, 2002, **89**.
142. B. Chiavarino, M. E. Crestoni, S. Fornarini, J. Lemaire, L. Mac Aleese and P. Maitre, *Chemphyschem*, 2004, **5**, 1679-1685.
143. B. Chiavarino, M. E. Crestoni, S. Fornarini, J. Lemaire, L. Mac Aleese and P. Maitre, *Chemphyschem*, 2005, **6**, 437-440.
144. B. Chiavarino, M. E. Crestoni, S. Fornarini, J. Lemaire, P. Maitre and L. MacAleese, *Journal of the American Chemical Society*, 2006, **128**, 12553-12561.
145. R. C. Dunbar, D. T. Moore and J. Oomens, *Journal of Physical Chemistry A*, 2006, **110**, 8316-8326.
146. O. Dopfer, J. Lemaire, P. Maitre, B. Chiavarino, M. E. Crestoni and S. Fornarini, *International Journal of Mass Spectrometry*, 2006, **249**, 149-154.
147. L. MacAleese and P. Maitre, *Mass Spectrom. Rev.*, 2007, **26**, 583-605.
148. D. T. Moore, J. Oomens, J. R. Eyler, G. von Helden, G. Meijer and R. C. Dunbar, *Journal of the American Chemical Society*, 2005, **127**, 7243-7254.
149. Y. Nosenko, F. Menges, C. Riehn and G. Niedner-Schatteburg, *Phys. Chem. Chem. Phys.*, 2013, **15**, 8171-8178.
150. P. Hohenberg and W. Kohn, *Phys. Rev.*, 1964, **136**, B864-B871.
151. K. Capelle, *Brazilian Journal of Physics*, 2006, **36**, 1318-1343.
152. W. Kohn and L. J. Sham, *Phys. Rev.*, 1965, **140**, A1133-A1138.
153. S. Grimme, *Journal of Computational Chemistry*, 2004, **25**, 1463-1473.
154. S. Grimme, *Journal of Computational Chemistry*, 2006, **27**, 1787-1799.
155. S. Grimme, *The Journal of Chemical Physics*, 2006, **124**, -.
156. M. J. Frisch, M. Head-Gordon and J. A. Pople, *Chem. Phys. Lett.*, 1990, **166**, 275-280.
157. M. J. Frisch, M. Head-Gordon and J. A. Pople, *Chem. Phys. Lett.*, 1990, **166**, 281-289.
158. M. Head-Gordon, J. A. Pople and M. J. Frisch, *Chem. Phys. Lett.*, 1988, **153**, 503-506.
159. S. Sæbø and J. Almlöf, *Chem. Phys. Lett.*, 1989, **154**, 83-89.
160. C. Møller and M. S. Plesset, *Phys. Rev.*, 1934, **46**, 618-622.
161. I. N. Levine, *Quantum chemistry*, Boston: Allyn and Bacon, Boston, 1991.
162. R. Ahlrichs, M. Bar, M. Haser, H. Horn and C. Kolmel, *Chem. Phys. Lett.*, 1989, **162**, 165-169.
163. G. W. T. M. J. Frisch, H. B. Schlegel, G. E. Scuseria, M. A. Robb, J. R. Cheeseman, G. Scalmani, V. Barone, B. Mennucci, G. A. Petersson, H. Nakatsuji, M. Caricato, X. Li, H. P. Hratchian, A. F. Izmaylov, J. Bloino, G. Zheng, J. L. Sonnenberg, M. Hada, M. Ehara, K. Toyota, R. Fukuda, J. Hasegawa, M. Ishida, T. Nakajima, Y. Honda, O. Kitao, H. Nakai, T. Vreven, J. A. Montgomery, Jr., J. E. Peralta, F. Ogliaro, M. Bearpark, J. J. Heyd, E. Brothers, K. N. Kudin, V. N. Staroverov, R. Kobayashi, J. Normand, K. Raghavachari, A. Rendell, J. C. Burant, S. S. Iyengar, J. Tomasi, M. Cossi, N. Rega, J. M. Millam, M. Klene, J. E. Knox, J. B. Cross, V. Bakken, C. Adamo, J. Jaramillo, R. Gomperts, R. E. Stratmann, O. Yazyev, A. J. Austin, R. Cammi, C. Pomelli, J. W. Ochterski, R.

## 1. Introduction, experimental set up and methods

---

L. Martin, K. Morokuma, V. G. Zakrzewski, G. A. Voth, P. Salvador, J. J. Dannenberg, S. Dapprich, A. D. Daniels, Ö. Farkas, J. B. Foresman, J. V. Ortiz, J. Cioslowski, and D. J. Fox, Gaussian, Inc., Wallingford CT, 2009.



### 2. IR-MPD spectroscopy of deprotonated and protonated dicarboxylic acids

#### 2.1. Preamble

This work has been dedicated for publication at the Journal *Physical Chemistry Chemical physics* with the title: *Spectral fingerprints of proton delocalization in isolated dicarboxylic ions*. The text of the publication was mainly written by me. Measurements and data evaluation were done by Fabian Menges, Lars Barzen and me. Structural and energetic calculations were made by Anita Röthke and me.

### 2.2. Spectral fingerprints of proton delocalization in isolated, aliphatic dicarboxylic ions

#### Abstract

The dicarboxylic acids  $\text{HOOC}-(\text{CH}_2)_n-\text{COOH}$ , ( $n = 1, \dots, 5$ ) reveal protonated cations and deprotonated anions in acidic and basic aqueous media, respectively. We utilized ElectroSpray Ionization (ESI) and isolated such ions. InfraRed MultiPhoton Dissociation (IR-MPD) reveals fragmentation yield mass spectra with anhydride fragment cations and decarboxylated anions dominating, respectively. Optical IR-MPD spectra arose from tuning the IR photon source, which was either a Free Electron Laser (FEL) or an Optical Parametric Oscillator (OPO). Two color enhancement in the IR-MPD spectra arises through application of a second pulse of IR photons when tuned into resonance with an IR active vibrational band. Interpretation of recorded spectra occurred in conjunction with DFT calculations. Reflecting the limitations of the harmonic approximation in calculated spectra, we find good agreement in the spectral features of the FEL mediated and OPO mediated one and two color IR-MPD spectra, subtle differences prevailing. We confirm hydrogen bonded cyclic structures for all parent ions while fragments open up in part. Future experiments with actively cooled ions will start to elucidate the localization of the hydrogen bonding protons under the steric constraints of the cyclic structures.

**Keywords:** Dicarboxylic acids, Hydrogen bonding, IR multiphoton dissociation

### 2.3. Introduction

Hydrogen bonding is ubiquitous in nature. Hydrogen bonding causes stabilization of secondary and tertiary structures of e.g. polypeptides and ensures their enzymatic activity. Proton transfer is one of the major mechanisms to activate molecules and to transport chemical energy. It takes place exclusively along hydrogen bonds. Spectra of OH stretching vibrations have provided crucial information of such hydrogen bonding networks within molecules and amongst them, e.g. in cluster systems<sup>1-6</sup>. The infrared (IR) OH stretching frequencies in the O-H...O hydrogen bond system tend to be considerably red shifted as they involve strong hydrogen bonding<sup>7,8</sup>. If the O-H...O moiety is either positively or negatively charged, this charged hydrogen bond is even stronger with a shorter O...O distance (2.4 - 2.6 Å), a so called short strong hydrogen bond<sup>9</sup>. Accordingly, the presence of an oxyanion often lowers the activation barriers in various enzymatic mechanisms drastically<sup>10-14</sup>. Early classifications of hydrogen bonding in aqueous acids distinguish two major cases. Historically first, the Eigen cation motif  $\text{H}_3\text{O}^+_{(\text{aq})}$  assumes excess proton localization at a single site. Hydrogen bonding is asymmetric (OH...O).<sup>15</sup> Subsequent proposition<sup>16</sup> and spectroscopic evidence<sup>17</sup> reveal proton delocalization amongst two acceptor sites – the so called Zundel cation  $\text{H}_5\text{O}_2^+$  – once the hydration environment becomes symmetric. Both motifs interchange swiftly through the Grothuss mechanism that leads to high proton conductivity in water. Note that the net proton transfer involves solvent rearrangements up to the second solvation shell<sup>18</sup>. Vibrational predissociation spectroscopy of protonated water clusters reveals the coexistence of both structural motifs in the gas phase<sup>19</sup>. It remains open, however, what happens if the free relaxation of O...O distances along the proton transferring hydrogen bond is made subject of sterical hindrance beyond solvation.

The potential energy hyper surface along the internal proton-transfer coordinate, that enables the proton motion between two oxygen atoms of the hydrogen bond, is often very flat. The “standard” normal mode analysis (in harmonic approximation) is questionable. Any meaningful frequency analysis would need to take account of this situation. Most advanced approaches such as multiconfigurational time-dependent Hartree (MCTDH) apply to small species only, such as  $\text{H}_5\text{O}_2^+$ <sup>20</sup>. Large anharmonic effects and complex coupling of vibrational modes prevail.

Understanding the quantum structure of the intermolecular hydrogen bonding is crucial to predict vibrational spectra. Studies of proton bound dimers reveal that the red shift of the OH stretching vibration and the form of the one dimensional potential for the shared proton motion depends on the proton affinity<sup>21</sup>.

## 2. IR-MPD spectroscopy of deprotonated and protonated dicarboxylic acids

---

We chose to investigate two proton acceptor sites linked by a flexible alkyl chain. This is a systematic study on the homologous row of dicarboxylic acids ( $\text{HOOC}-(\text{CH}_2)_n-\text{COOH}$ ,  $n$  number of  $\text{CH}_2$ -groups). Protonated and deprotonated dicarboxylic acids form cyclic structures with an intramolecular hydrogen bond in the gas phase. There are some steric restraints on proton transfer from one nucleophile carboxyl group to the other. The resulting minimum structure is dependent on the ring strain.

Dicarboxylic acids by themselves have been an interesting topic of research. Since the 1960s scientist discuss that dicarboxylic acids form intramolecular hydrogen bonding. The first evidence was found by Haslam *et al*<sup>22</sup>. They determined the rate constants for the rapid abstraction of a proton from the mono anion of alkyl substituted succinic acid ( $n = 3$ ). NMR investigations of mono anions of succinic acid, maleic acid ( $\text{C}_2\text{H}_2(\text{COOH})_2$ ) and phthalic acid ( $\text{C}_6\text{H}_4(\text{COOH})_2$ ) show that these mono anions exist as two equilibrating tautomers in aqueous solution but as a single symmetric isomer in a nonpolar solvent<sup>23</sup>. The gas-phase acidities of dicarboxylic acids ( $n = 0 - 8$ ) were estimated by applying an "extended kinetic method"<sup>24</sup>. Suberic ( $n = 6$ ) and pimelic ( $n = 5$ ) acid have the highest acidities in this series. The acidity increases with alkyl chain length and thus with ring size. Studies in the solid phase reveal inter anion hydrogen bonding interactions between mono-deprotonated polycarboxylic acid and zwitterionic molecules<sup>25</sup>. Charge localisation onto the deprotonated carboxylate groups is seen as a mean of exploiting the stabilising contribution of dipole-dipole interactions in conjunction with charge-assisted  $\text{O-H}\cdots\text{O}$  interactions. Few cases of nearly symmetric  $\text{O-H}\cdots\text{O}$  interactions are identified. Woo *et al.*<sup>26</sup> recorded photoelectron spectra of singly charged dicarboxylate anions ( $n = 1-10$ ) at room temperature and at 70 K in the gas phase. The mono anions form cyclic structures due to strong intramolecular hydrogen bonding. Electron binding energies depend on the chain length, reflecting the different  $\text{O-H}\cdots\text{O}$  bond strengths as a result of strain in the cyclic conformation. There is a minimum in binding energy for the mono anion of pimelic acid ( $n = 5$ ), this indicates that the intramolecular hydrogen bond is the weakest. The formed ten-membered ring is the most strained among all of the investigated dicarboxylic anions. Vibrational predissociation spectroscopy of the mono dicarboxylate anion of dodecanedioic acid indicates that the monoanion form a cyclic structure through the formation of an intramolecular hydrogen bond<sup>27</sup>.

Density functional calculations of neutral dicarboxylic acids  $\text{HOOC}-(\text{CH}_2)_n-\text{COOH}$  ( $n = 1 - 4$ ) reveal cyclic structures and intramolecular hydrogen bonding as well<sup>28</sup>. Car-Parrinello molecular dynamics (CPMD) simulations indicate that the proton transfer occurs by multistep chiral transformation in protonated (PAA) and deprotonated adipic acid (DAA) ( $n = 4$ )<sup>29</sup>. The lowest energy structure of PAA is predicted to have Zundel like symmetric hydrogen bonding, whereas that of DAA has Eigen-like



## 2. IR-MPD spectroscopy of deprotonated and protonated dicarboxylic acids

---

asymmetric hydrogen bonding. Direct proton transfer between the two proton acceptor sites is unfavorable. Instead chiral transformation is possible by subsequent backbone twisting through stepwise proton transfer along multistep intermediate structures, which are Zundel-like ion for PAA and Eigen-like for DAA.

In contrast direct proton transfer is feasible in the amine analogue of PAA ( $\text{Me}_2\text{N}-(\text{CH}_2)_4-\text{NMe}_2$ ). The NHN angle is nearly linear and the barrier for the proton transit from one nitrogen to the other is low<sup>30</sup>. The IR-MPD spectrum reveals a band at  $530\text{ cm}^{-1}$  which is assigned to the asymmetric stretch of the bridging proton between the two nitrogen atoms.

The effect of this steric constraint has been investigated by IR-MPD spectroscopy, inelastic neutron scattering and high pressure Raman spectroscopy of  $\text{Me}_2\text{N}-(\text{CH}_2)_4-\text{NMe}_2$  and of  $\text{Me}_2\text{N}-(\text{CH}_2)_3-\text{NMe}_2$ <sup>30</sup>.

Here we chose to investigate the dicarboxylic acids by infrared multi photon dissociation (IR-MPD) spectroscopy<sup>31</sup>. The ions of interest are transferred to an ion trap (in this paper a Penning trap/ ion cyclotron resonance trap or a Paul trap respectively). Trapped ions are irradiated with IR photons generated by Free Electron Laser (FEL) or by optical parametrical oscillator/amplifier (OPO/A, LaserVision). If the wavelength of the photons is in resonance with a vibrational mode of the ion, the photon is absorbed and the energy of the ion increases. Due to internal vibrational relaxation (IVR), the additional energy can be distributed into all accessible modes of the ion and eventually induce fragmentation to record.

### 2.4. Experimental and theoretical methods

#### 2.4.1 IR-MPD spectroscopy and resonant two color IR-MPD spectroscopy

IR-MPD spectroscopic measurements of protonated and deprotonated dicarboxylic acids in the range of 1100-2400  $\text{cm}^{-1}$  were performed employing the Free Electron Laser (FEL) "CLIO" in Orsay as described elsewhere<sup>32</sup>. The ions were trapped either by a Paul ion trap (Bruker, Esquire 3000+) or by a Penning trap (7.05 T Fourier Transform Ion Cyclotron Resonance (FT-ICR) mass spectrometer/ Bruker, Apex Qe hybrid). In addition resonant two color IR-MPD measurements of aliphatic protonated and deprotonated species were performed using two tunable infrared laser systems (Laser Vision). The experimental setup is described elsewhere<sup>33</sup>.

Ion generation took place from aqueous samples by electrospray ionization (ESI) using equivalent ion sources. The dicarboxylic acids were obtained from Sigma Aldrich and used without further purification. A  $1 \cdot 10^{-4}$  mol/l solution of dicarboxylic acids in methanol: water (1:1) and 1% formic acid was sprayed at a flow rate of 150  $\mu\text{L/h}$ , a spray voltage of 4000 V, and a drying gas temperature of 150 °C.

Fourier Transform Ion Cyclotron Resonance Mass Spectrometry (FT-ICR-MS) was performed with an Apex Qe hybrid 7.05 T FT-ICR mass spectrometer equipped with a quadrupole-hexapole interface between the ion source and the ICR cell. In the quadrupole mass filter selected ions were accumulated in a pressurized linear hexapole trap for thermalisation. In the hexapole trap the mass selected ions undergo multiple collisions with argon buffer gas atoms. The thermalized ions were pulse extracted from the hexapole trap and transferred to the ICR cell. The background pressure in the ICR cell was lower than  $10^{-9}$  mbar. The laser entered the cell through a 3.45 mm diameter aperture. The IR light traverses the ICR cell along the axis of the magnet in a single pass configuration. The laser beam is focused with a 2 m focal mirror. After a defined irradiation time with the FEL the ions fragment as a function of the wavelength. The beam position was tuned in order to maximize the fragmentation efficiency. All operations were performed using the Bruker Apex control software<sup>34</sup>. FEL based IR-MPD spectra of Protonated Dicarboxylic Acids (PDAs) and Deprotonated Dicarboxylic Acids (DDAs) of the same chain length  $n$  were recorded within single beam time weeks at CLIO, while the data taking of different chain lengths  $n = 1, \dots, 5$  stretched out over multiple years.

In the case of the spectra generated with a Paul trap, the standard Bruker software controls the multistep mass spectrometry experiment and records the data. Parent ions were mass selected and the irradiation time of the ions in the trap was controlled using the MS2 step where the excitation

## 2. IR-MPD spectroscopy of deprotonated and protonated dicarboxylic acids

---

amplitude was set to zero. The associated output trigger was used to control the optical shutter, which was opened for a controlled number of IR pulses. The IR FEL laser beam was focused at the center of the ion trap using a 500 mm ZnSe focal lens. A 0.7 mm hole drilled in the ring electrode of the ion trap allows for the optical access to the center of the ion trap. The beam position was tuned in order to maximize the fragmentation efficiency<sup>35</sup>.

Resonant two color IR-MPD measurements were performed using a modified Paul Trap mass spectrometer (Bruker, amaZonSL) in Kaiserslautern. The parent ions were mass selected and stored in the Paul trap. The trapped ions are irradiated by two tunable IR-lasers for one irradiation time. After this irradiation time the fragment ions were detected. Laser pulse scheme: First a tunable pump laser irradiates the ions. After a delay time of 100 ns a second laser is used on a resonant wavelength to facilitate the fragmentation of the parent ion. Thus it is possible to obtain spectra in the fingerprint region with a table top tunable OPO laser system which are comparable to the spectra obtained by the high power FEL.

IR-MPD spectra were obtained at either instrument by recording the signal intensity of parent and fragment ions while the wavelength is varied. We define the fragmentation efficiency frag. eff. as

$$frag. eff. = \frac{\sum_i I_{frag,i}(\tilde{\nu})}{\sum_i I_{parent,i}(\tilde{\nu}) + \sum_i I_{frag,i}(\tilde{\nu})} \quad (1)$$

where  $I_{parent,i}(\tilde{\nu})$  and  $I_{frag,i}(\tilde{\nu})$  are the intensities of the  $i^{\text{th}}$  parent ion and of the  $i^{\text{th}}$  fragment ion.

The CLIO IR FEL provides for typical average powers of  $\sim 500$  mW around  $1000 \text{ cm}^{-1}$ , 600 mW near  $1300 \text{ cm}^{-1}$  and 200 mW near  $2000 \text{ cm}^{-1}$  at the user Table. IR photodissociation experiments, however, were performed with an attenuated IR-beam ( $\sim 10$  dB per attenuator) in order to avoid saturation. Laser wavelength profile was monitored with a monochromator associated with a pyroelectric detector.

### 2.4.2 Ab initio calculations

All calculations were performed at the second order Møller-Plesset<sup>36</sup> perturbation theory (MP2) level with Dunning's<sup>37</sup> correlation-consistent basis set of double- $\zeta$  quality (cc-pVDZ). Based on the calculated equilibrium structure of the respective dicarboxylic acid at zero Kelvin, potential energy curves are obtained by parametrical variation of the initially shortest O-H distance in the equilibrium structure. All other coordinates are free to relax in course of geometry optimization. The energy of the equilibrium structure is arbitrarily set to zero and all other values are given relative to it. With exception of the equilibrium structures and some local minima, all other structures are not stationary points. Therefore the relative  $\Delta E$  values are not corrected by zero point energy (ZPE). All calculations were performed by the TURBOMOLE 5.9 program package<sup>38</sup>.

### 2.5 Results and Discussion

#### 2.5.1 IR-MPD spectra by the FEL

##### Protonated dicarboxylic acids (PDA)

The obtained experimental IR-MPD spectra of the cationic species  $n=1 - 5$  (Fig. 1 a - e) reveal strong bands throughout the investigated energy range. A spectrum of the protonated oxalic acid ( $C_2O_4H_3^+$ ) could not be recorded under the conditions used. This is most likely due to high ionization barriers and/ or dissociation enthalpies. Dehydration appears to be the main fragmentation process. At higher photon flux also the loss of carbon dioxide to a smaller extent was detected.

**Table 1:** Abbreviations

---

name	alkyl chain length	protonated	deprotonated
malonic acid	$n = 1$	PMA	DMA
succinic acid	$n = 2$	PSA	DSA
glutaric acid	$n = 3$	PGA	DGA
adipic acid	$n = 4$	PAA	DAA
pimelic acid	$n = 5$	PPA	DPA

---

Calculated potential energy curves (MP2/cc-pVDZ) obtained by freezing the shorter O-H distance ( $d_1$ ) while all other coordinates are freely optimized (insets to Fig. 1 a - e). The potential energy curve  $V(d_1)$  is parameterized by the O-H distances within the O-H $\cdots$ O bond with all other nuclear coordinates relaxed. In most cases  $V(d_1)$  has a quartic form. It becomes more harmonic for PAA ( $n = 4$ ).

## 2. IR-MPD spectroscopy of deprotonated and protonated dicarboxylic acids

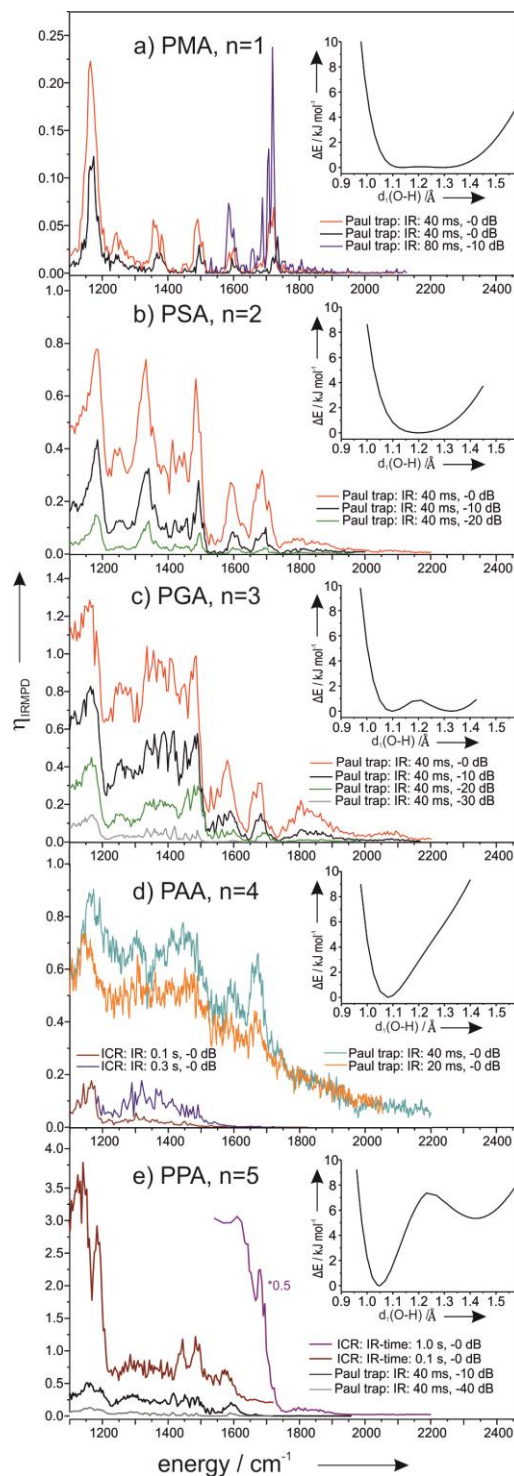


**Figure 1:** IR-MPD spectra of PDAs recorded by FEL and calculated potential energy curves (MP2/cc-pVDZ). The O-H distance is frozen while all other coordinates are freely optimized. The main fragment in the case of protonated acids is the elimination of water. The potential energy curve has a quartic form and becomes more harmonic for PAA.

## 2. IR-MPD spectroscopy of deprotonated and protonated dicarboxylic acids

---

**Protonated malonic acid, PMA (n = 1):** (Fig. 1a) The vibrational spectrum reveals six narrow bands at 1160, 1250, 1365, 1495, 1590 and 1720  $\text{cm}^{-1}$ . The bands at 1160  $\text{cm}^{-1}$  and 1720  $\text{cm}^{-1}$  in PMA exhibit a fivefold stronger intensity than the bands at 1250, 1365, 1495 and 1590  $\text{cm}^{-1}$  which exhibit about the same height. The observed bands have FWHM between 20 and 40  $\text{cm}^{-1}$ .

**Protonated succinic acid, PSA (n = 2):** (Fig. 1b) The IR-MPD spectrum shows six bands at 1180, 1250, 1335, 1490, 1595 and 1690  $\text{cm}^{-1}$ . These bands are significantly broader than those of PMA (n = 1). The half width varies between 35 and 60  $\text{cm}^{-1}$ . The bands at 1180, 1335 and 1490  $\text{cm}^{-1}$  have similar intensities while the bands at 1595 and 1690  $\text{cm}^{-1}$  are reduced by a factor of 2.5. There is a very broad band was observed around 1800  $\text{cm}^{-1}$  which is absent in PMA. The band with the highest observed frequency (1690  $\text{cm}^{-1}$ ) shifts to the red compared to the spectra of PMA (1720  $\text{cm}^{-1}$ ).

**Protonated glutaric acid, PGA (n = 3):** (Fig. 1c) The band pattern of PGA resembles that of PSA. Bands are significantly broad, however. There is a particularly strong absorption at 1165  $\text{cm}^{-1}$ . The very broad band at 1800  $\text{cm}^{-1}$  gained further intensity as compared to PSA.

**Protonated adipic acid, PAA (n = 4):** (Fig. 1d) The IR-MPD spectrum reveals a broad band at 1160  $\text{cm}^{-1}$  and a group of broader absorptions between 1220 and 1520  $\text{cm}^{-1}$ . A weak band appears at 1675  $\text{cm}^{-1}$  which is only visible with higher photon flux e.g. longer irradiation times.

**Protonated pimelic acid, PPA (n = 5):** (Fig 1e) The IR-MPD spectrum reveals a very intense broad band around 1160  $\text{cm}^{-1}$  and likely below which is outside the present investigation window. All other recorded PPA bands seem to diminish relative to corresponding PGA bands. In particular the broad PPA feature around 1800  $\text{cm}^{-1}$  vanishes in PGA, except at highest IR photon flux and exposure, namely at application of numerous laser pulses.

IR-MPD spectra of the smaller dicarboxylic acids (n = 1, 2) exhibit narrow bands. Spectra of the higher homologues (n = 3 - 5) reveal increasing broadening. This is attributed to an increasing length of the bridging alkyl chain which enables an increase in numbers and population of low lying isomers. The need for further investigation of cold ions at well-defined temperatures is obvious.

The highest observed fragmentation efficiency in the IR-MPD spectra by FEL of PDAs (n = 1 - 5) increases with the alkyl chain length: It is 0.20 for the protonated malonic acid (PMA, n = 1), 0.55 for PSA and 0.73 for PGA. A more quantitative evaluation is hampered by the variation of experimental conditions as of now.

## 2. IR-MPD spectroscopy of deprotonated and protonated dicarboxylic acids

---

The lack of narrow spectral bands points to strong intra mode coupling which is most likely due to the proton involving modes. The spectral features are similar for all investigated PDAs. Further interpretation arises by comparison to spectra of deprotonated dicarboxylic acids, by inspection of OPO/OPA based spectra and by reference to ab initio spectra (cf. below) and to the computed potential curves (insets to Fig. 1).

### Deprotonated Dicarboxylic Acids, DDAs

We recorded IR-MPD spectra by FEL of the deprotonated dicarboxylic acids ( $n = 1 - 5$ ) by reversing ESI polarity while all other parameters were kept the same as in the experiment with PDAs (fig 2). The dominating dissociation pathway is decarboxylation ( $\text{CO}_2$ ). The strongest band arises around  $1100 \text{ cm}^{-1}$ . It does not correspond to an a priori "obvious" vibrational mode. Because of its strength it may relate to a proton motion along an ionic hydrogen bond as e.g. possible in cyclic forms of protonated dicarboxylic acids. The successively broadened features in the range of  $1250 - 1500 \text{ cm}^{-1}$  largely coincide with the textbook frequency range of known  $\text{CH}_2$  bending and wagging frequencies ( $1370 - 1470 \text{ cm}^{-1}$ ). Some charge induced red shifts seem reasonable. The persistent  $1580 - 1620 \text{ cm}^{-1}$  band puts one in mind of conjugated CO stretching vibrations in carboxylate salts. The  $1720 \text{ cm}^{-1}$  band of DMA redshifts with increasing alkyl chain length via  $1690 \text{ cm}^{-1}$  (DSA),  $1680 \text{ cm}^{-1}$  (DGA) to  $1660 \text{ cm}^{-1}$  in DAA and  $1590 \text{ cm}^{-1}$  DPA. It coincides with the known range of non-conjugated CO stretching modes in anhydrides.



## 2. IR-MPD spectroscopy of deprotonated and protonated dicarboxylic acids

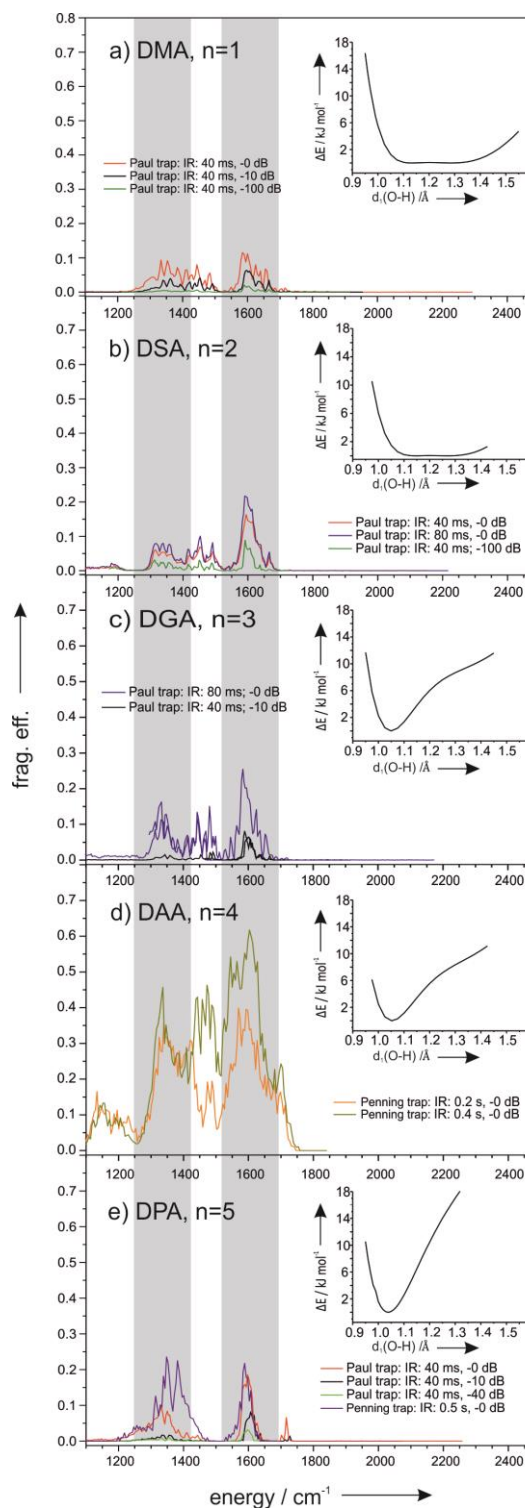


**Figure 2:** IR-MPD spectra of DDAs recorded by FEL and calculated potential energy curves (MP2/cc-pVDZ). The O-H distance is frozen while all other coordinates are freely optimized. The main fragment in the case of deprotonated acids is the elimination of carbon dioxide. Grey areas emphasize the common band structure.

## 2. IR-MPD spectroscopy of deprotonated and protonated dicarboxylic acids

---

**Deprotonated malonic acid, DMA (n = 1):** (Fig. 2 a) In the range of 1250 - 1500  $\text{cm}^{-1}$  the spectrum is much less structured than that of PMA. The Fragmentation yield below 1250  $\text{cm}^{-1}$  declines. A discernible band occurs around 1620  $\text{cm}^{-1}$ . A very weak band arises at 1664  $\text{cm}^{-1}$ . The overall fragmentation efficiency is comparable to that of PMA.

**Deprotonated succinic acid, DSA (n = 2):** (Fig. 2b) The IR-MPD spectrum of deprotonated succinic acid, DSA (n = 2) reveals a narrow band at 1665  $\text{cm}^{-1}$  and broad features in the range of 1250 - 1500  $\text{cm}^{-1}$  such as DMA. There is some weak band at 1180  $\text{cm}^{-1}$ .

**Deprotonated glutaric acid, DGA (n = 3):** (Fig. 2c) The recorded IR-MPD spectrum suffers from bad signal-to-noise ratio. It largely resembles that of DMA.

**Deprotonated adipic acid, DAA (n = 4):** (Fig. 2d) All bands in the spectrum are broad. The IR-MPD spectra stem from the FT-ICR-MS trap. All other spectra (n = 1 - 3 and 5) originate from Paul trap measurements. Fragmentation yields are significantly lower. This likely originates from the use of varying instrumentation rather than from the variation of the investigated species. Cross features of previous spectra repeat in DAA with additional weak bands around 1150 - 1200  $\text{cm}^{-1}$  and 1720  $\text{cm}^{-1}$ .

**Deprotonated pimelic acid, DPA (n = 5):** (Fig. 2e) The IR-MPD spectrum reveals a 1620  $\text{cm}^{-1}$  band as in all other cases and some weak 1720  $\text{cm}^{-1}$  feature. Most notably, the featureless gap to the red of the 1620  $\text{cm}^{-1}$  band is significantly broader than in all other observed cases. What used to be a broad 1250 - 1500  $\text{cm}^{-1}$  absorption in DMA and DSA shrinks (and shifts) to a 1200 - 1450  $\text{cm}^{-1}$  band in DPA. There is no indication of absorption/fragmentation at photon energies below 1200  $\text{cm}^{-1}$ .

It is interesting to note that the band below 1200  $\text{cm}^{-1}$  occur exclusively for the even numbered deprotonated carboxylic species (n = 2 and 4). In contrast to the protonated acids the efficiency of the fragmentation remains nearly constant. The weak band with the highest observed frequency shifts to the blue with more bridging  $\text{CH}_2$ -groups (see Tab. 2).

Comparison of the IRMPD efficiencies of the protonated and deprotonated species reveals that the protonated species require less accumulated energy for fragmentation than the deprotonated acids (see below).

## 2. IR-MPD spectroscopy of deprotonated and protonated dicarboxylic acids

---

**Table 2:** Frequencies of the strong carbonyl bands in DDAs (n = 1 - 5)

DDA		frequency / $\text{cm}^{-1}$	shift / $\text{cm}^{-1}$
DMA	(n=1)	1665	0
DSA	(n=2)	1665	0
DGA	(n=3)	1665	0
DAA	(n=4)	1700	35
DPA	(n=5)	1715	50

---

### 2.5.2 OPO based IR-MPD spectra

The above discussed FEL based IR-MPD spectra provide a reasonable overview over the IR active vibrations in protonated and deprotonated dicarboxylic acids,  $n = 1 - 5$ . Some spectra, in particular, those of PAA and DAA recorded earlier, suffer from bad S/N. Recording of IR-MPD spectra in the OH stretching region had not been possible at that time either. We therefore decided to utilize meanwhile available, efficient OPO/OPA and DFM (difference frequency mixing) technique to re-record selected spectra and to extend the wavelength range considerably.

#### OPO/OPA based IR-MPD spectra of PDAs:

By OPO/OPA-DFM recorded one and two color IR-MPD spectra of PDAs ( $n = 1 - 4$ ) (Fig. 3) confirm nicely the spectral features of the FEL based spectra (Fig. 1). The spectral features of protonated malonic acid, PMA,  $n = 1$ , are sharp. The IR bands of the higher homologues ( $n = 2,3,4$ ) grow successively broader. All spectra reveal a band below  $1200 \text{ cm}^{-1}$  except the spectra of PMA. There are two distinct bands at approximately  $1600$  and  $1700 \text{ cm}^{-1}$ . Surprisingly, these exhibit with reverse intensities as compared to the FEL spectra. Intensity issues may relate to power fluctuations of either photon sources. With increasing number of bridging  $\text{CH}_2$ -groups the fragmentation efficiency rises comparable to the experiment recorded with the FEL. Measurements of the region between  $2500$  and  $4000 \text{ cm}^{-1}$  reveal a single OH stretching vibration at  $3500 - 3550 \text{ cm}^{-1}$ . This band shifts to the blue with increasing  $n$  (cf. Tab. 3). The weak bands around  $2950 \text{ cm}^{-1}$  are assigned to CH stretching vibrations. Two color IR-MPD is applied in order to enhance fragmentation yields beyond those of one color experiments as shown before<sup>33</sup>. Surprisingly, the present two color IR-MPD spectra reveal little to no enhancement with respect to the one color fragmentation yields (cf. Fig.3). This likely points to low fragmentation enthalpies and/or high absorption and relaxation rates.

There is little to no difference between the one color and two color IR-MPD scheme. The probe laser is set to two fixed photon energies ( $3535$  and  $2960 \text{ cm}^{-1}$ ) in the case of PAA ( $n = 4$ ). Regardless of which band is pumped the spectra of PAA do not distinguish. It is noteworthy that the PAA ( $n = 4$ ) spectrum of OPO/OPA based recordings fits nicely to the other spectra of the series.

## 2. IR-MPD spectroscopy of deprotonated and protonated dicarboxylic acids

---

**Table 3:** observed frequencies of OH stretching and CH stretching modes in PDAs ( $n = 1 - 4$ )

---

PDA	alkyl chain length $n$	vibrational mode	Frequency / $\text{cm}^{-1}$	fragmentation efficiency $\eta_p^{(n)}$
PMA	1	$\nu_s(\text{OH})$	3500	0.56
		$\nu_s(\text{CH})$	2945	0.04
PSA	2	$\nu_s(\text{OH})$	3530	0.56
		$\nu_s(\text{CH})$	2940; 3000	0.03
PGA	3	$\nu_s(\text{OH})$	3520	0.55
		$\nu_s(\text{CH})$	2970; (3025)	0.01; (0.007)
PAA	4	$\nu_s(\text{OH})$	3535	0.81
		$\nu_s(\text{CH})$	2965	0.03

---

## 2. IR-MPD spectroscopy of deprotonated and protonated dicarboxylic acids

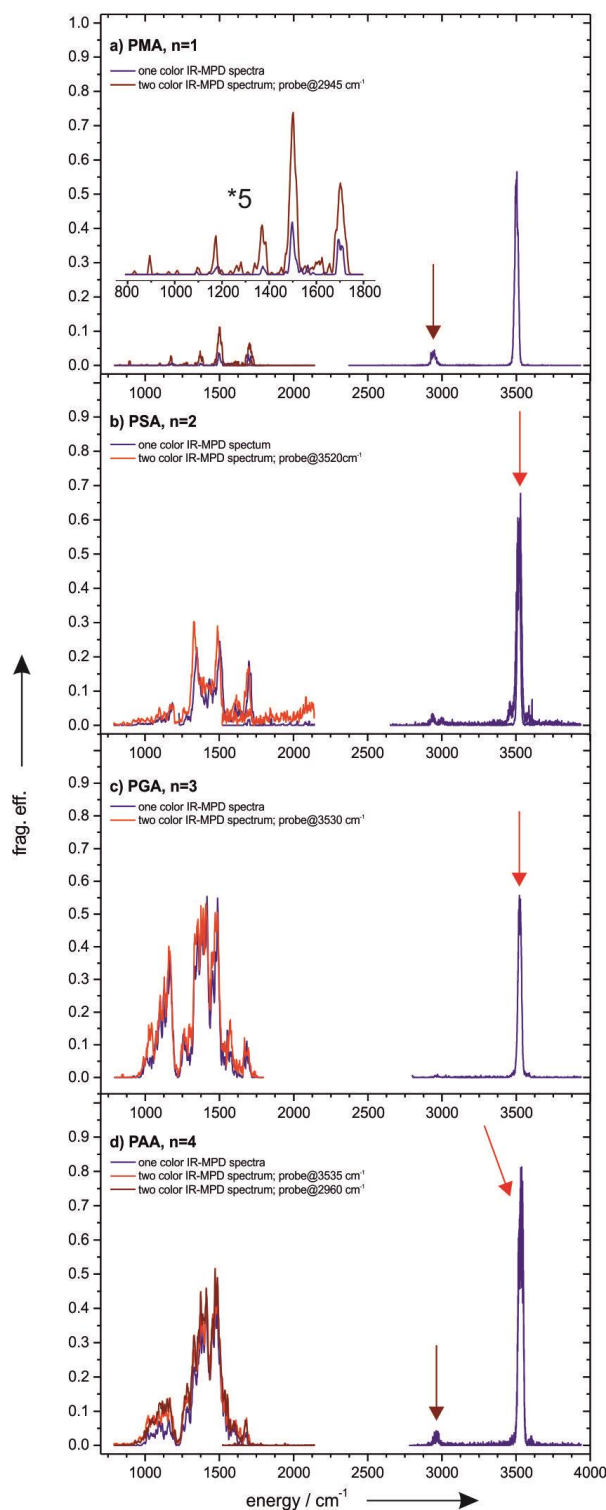


**Figure 3:** One color (blue) and two color (red and brown) IR-MPD spectra by OPO/OPA laser of PDAs (a) PMA ( $n=1$ ), (b) PSA ( $n=2$ ), (c) PGA ( $n=3$ ), and (d) PAA ( $n=4$ ). Red and brown arrows indicate the frequency of photons from the second OPO/OPA laser (probe). There is small enhancement of fragmentation yield by application of the two color IR-MPD scheme. For enlarged plots of the fingerprinting range see Fig. S1 in the supplement.

## OPO/OPA based IR-MPD spectra of DDAs:

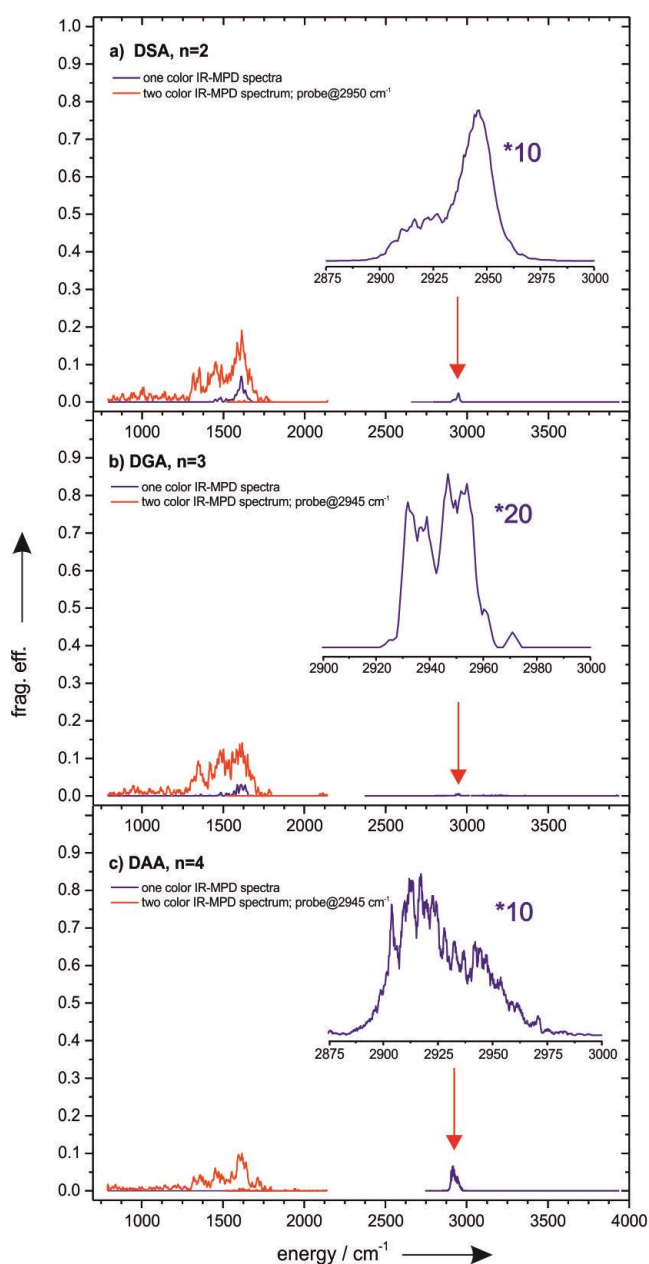


**Figure 4:** One color (blue) and two color (red) IR-MPD spectra by OPO/OPA laser of deprotonated dicarboxylic acids (a) DSA ( $n = 2$ ), (b) DGA ( $n = 3$ ), and (c) DAA ( $n = 4$ ). The weak bands about  $3000 \text{ cm}^{-1}$  are enlarged by the depicted factor. Red arrows indicate the frequency of photons from the second OPO/OPA laser (probe). There is significant enhancement of fragmentation yield by application of the two color IR-MPD scheme. For enlarged plots of the fingerprinting range see Fig. S2 in the supplement.

## 2. IR-MPD spectroscopy of deprotonated and protonated dicarboxylic acids

---

DDAs ( $n = 2 - 4$ ) yield OPO/OPA based IR-MPD spectra (Fig. 4) that provide for low fragmentation yields - even lower than obtained when utilizing the FEL light source (cf. Fig. 2). There are no OH stretching bands and the CH stretching bands are very weak. The absence of a free OH stretching vibration indicates that there is a strong intramolecular hydrogen bond with a strong red shift of the OH stretching bond. When utilizing the latter bands to pump our two colors enhancing scheme, the fragmentation yield rises significantly. We reach yields that are on the order of those in the FEL spectra. Strong two color effect of DDAs (other than in PDAs) is noticed and will be discussed in the following (cf. sec. 2.5.4.)



### 2.5.3 Calculated structures and calculated spectra

We optimized geometries of the PDAs,  $n = 0, \dots, 6$  (Fig. 5.) and of the deprotonated ones, DDAs,  $n = 0, \dots, 6$  (Fig.6).

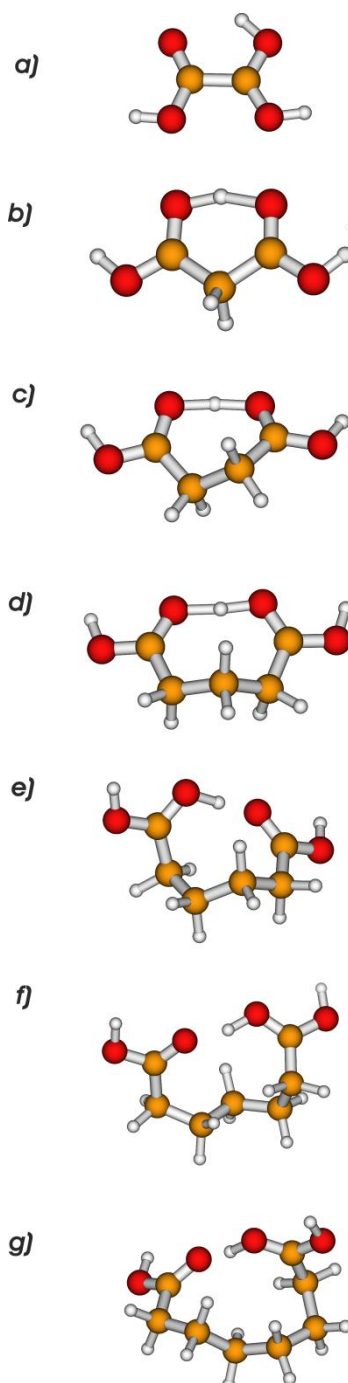


**Figure 5:** Calculated minimum energy structures of PDAs (MP2/cc-pVDZ). (a) Protonated oxalic acid (POA),  $n = 0$ ; (b) Protonated malonic acid (PMA),  $n = 1$ ; (c) Protonated succinic acid (PSA),  $n = 2$ ; (d) Protonated glutaric acid (PGA),  $n = 3$ ; (e) Protonated adipic acid (PAA),  $n = 4$ ; (f) Protonated pimelic acid (PPA),  $n = 5$ ; (g) Protonated suberic acid (PSuA),  $n = 6$ .

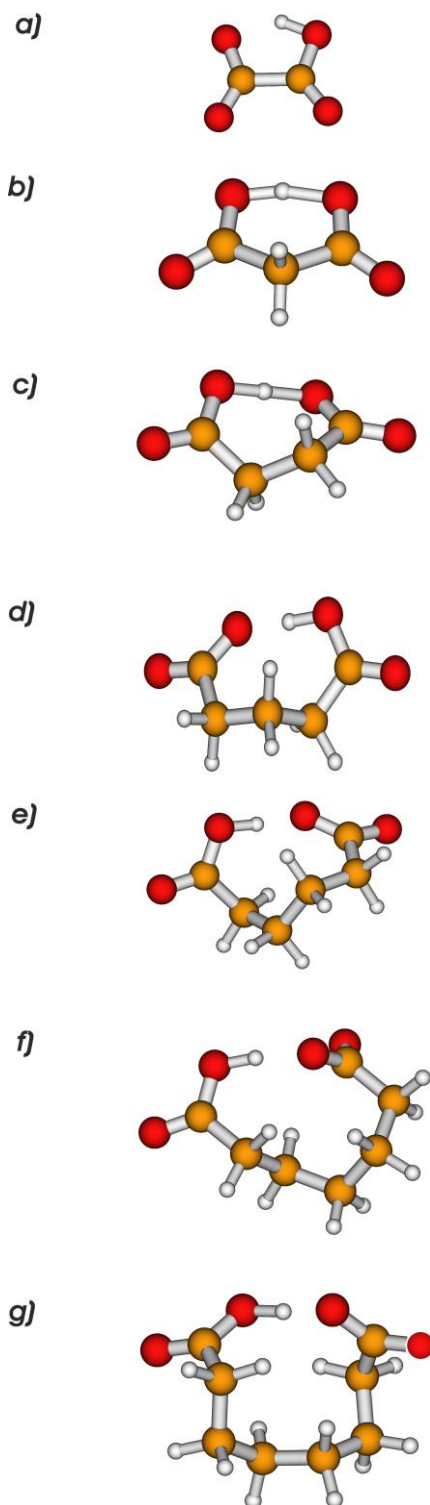


**Figure 6:** Calculated minimum energy structures of DDAs (MP2/cc-pVDZ). (a) Deprotonated oxalic acid (DOA),  $n = 0$ ; (b) deprotonated malonic acid (DMA),  $n = 1$ ; (c) deprotonated succinic acid (DSA),  $n = 2$ ; (d) deprotonated glutaric acid (DGA),  $n = 3$ ; (e) deprotonated adipic acid (DAA),  $n = 4$ ; (f) deprotonated pimelic acid (DPA),  $n = 5$ ; (g) deprotonated suberic acid (DSuA),  $n = 6$ .

## 2. IR-MPD spectroscopy of deprotonated and protonated dicarboxylic acids

Protonated and deprotonated oxalic acid, POA and DOA ( $n = 0$ ) reveal no internal hydrogen bond ( $O\cdots H$  distance  $\geq 1.6$  Å). All other calculated species do reveal hydrogen bridged cyclic structure with  $O-H\cdots O$  bond distances of 1.2 - 1.4 Å (PDAs) and of 1.3 - 1.5 Å (DDAs). Min et al.<sup>29</sup> had shown how the backbone conformation determines the asymmetry of the ionic hydrogen bond in the case of PAA and DAA ( $n = 4$ ). Multiple “Eigen type” and “Zundel type” conformers coexist. It is most likely that larger PDAs and DDAs ( $n > 4$ ) exhibit a similar coexistence of multiple hydrogen bonding conformers. This is not so obvious for smaller PDAs and DDAs ( $n < 4$ ). Short alkyl chains may cause higher ring strain. This would become apparent by bending the hydrogen bond into nonlinear conformations. Indeed, this effect persists (Fig. 7). Oxalic ( $n = 0$ ) and malonic acid ( $n = 1$ ) ions reveal  $O-H\cdots O$  angles far from linear. Succinic acid ( $n = 2$ ) ions and all larger ones seem to allow for relaxed ring conformations that enable linear hydrogen bonds, and for some proton disorder along the bond as well. We refrain from a focused interpretation of further details of calculated conformers (cf. supplement material). An exhaustive investigation of the full conformation space in the larger PDAs and DDAs is beyond the scope of the present study (see ref<sup>29</sup> for a conceivable approach).

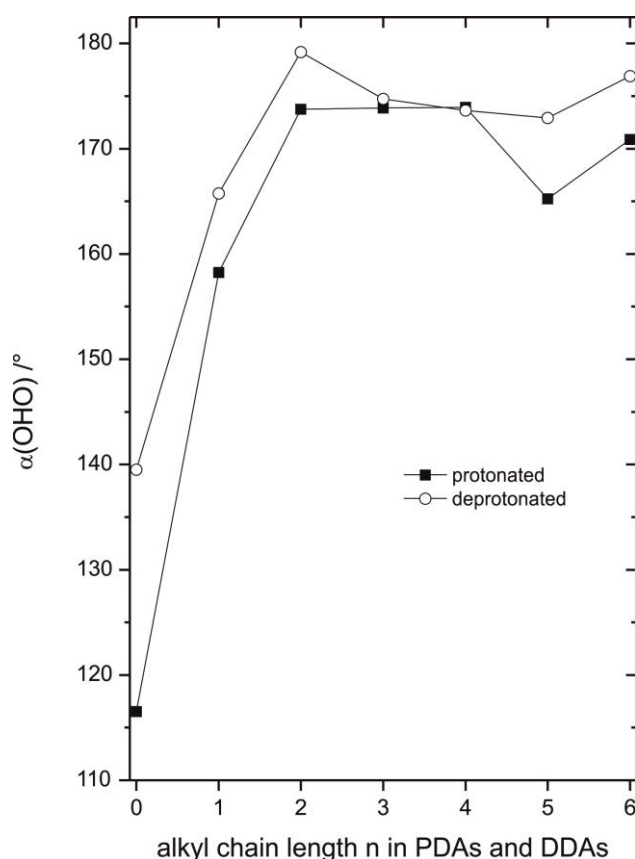


**Figure 7:**  $O-H\cdots O$  angle in PDAs and DDAs as function of alkyl chain length  $n$ . The longer the alkyl chain the more linear the hydrogen bond becomes. Considerable ring strain at  $n = 0$  and  $n = 1$  forces the hydrogen bonds to become nonlinear and weaker.

## 2. IR-MPD spectroscopy of deprotonated and protonated dicarboxylic acids

---

Given the prevailing large anharmonicities along the hydrogen bond it is self-evident that harmonic normal mode analysis by standard ab initio based procedures is doomed to fail in principle. Perturbative lump sum linear scaling corrections are inappropriate. Their application would lead to false predictions. Nevertheless, it is an open question whether all of the calculated force constants are false. It is conceivable that some part of the force constant matrix (e.g. a few normal modes involving O-H...O motions) decouples from the remainders (e.g. motions within carboxylic and alkylic parts of the PDA and DDA ions). If such a case prevails part of the calculated modes would find correspondence in experimental IR-MPD bands while others – the highly anharmonic ones – would suffer from systematically false predictions that do not relate to any experimental evidence. In this regard it might become valuable to evaluate ab initio based normal mode predictions while keeping the apparent limitations of harmonic analysis and linear scaling corrections in mind.

### Comparison of the experimental and the calculated IR spectra for small dicarboxylic acids (n = 1,2)

The calculated spectrum of PMA (n = 1) (Fig. 8) comprises of seven IR active bands in the fingerprint range of 1100 - 2000  $\text{cm}^{-1}$  while the experimental spectrum reveals six bands that coincide in part (Fig. 8a) and b)). Five out of seven calculated bands involve little to no motion of the O-H...O bridging proton. These bands originate from  $\text{CH}_2$  wagging motions (1100 – 1300  $\text{cm}^{-1}$ ) and from asymmetric and symmetric CO stretching motions (1504 and 1734  $\text{cm}^{-1}$ ). These are five calculated absorption bands nicely coincide with the experimental bands (marked in color in Fig 8a). The two calculated bands at 1672 and 1821  $\text{cm}^{-1}$  originate from the O-H...O bridging proton motion perpendicular and parallel to the hydrogen bond, respectively. Most likely they do not relate to any recorded IR-MPD bands. We find in PMA (n = 1) the above outlined scenario: scaled harmonic calculation fails to describe highly anharmonic modes. Nevertheless, the remainder of modes may well be treated this way. It seems as if the vibrational phase space largely decouples into two subspaces with little - or at least reduced- interaction. It is worthwhile to continue inspection of other cases beyond PMA (n = 1).

## 2. IR-MPD spectroscopy of deprotonated and protonated dicarboxylic acids

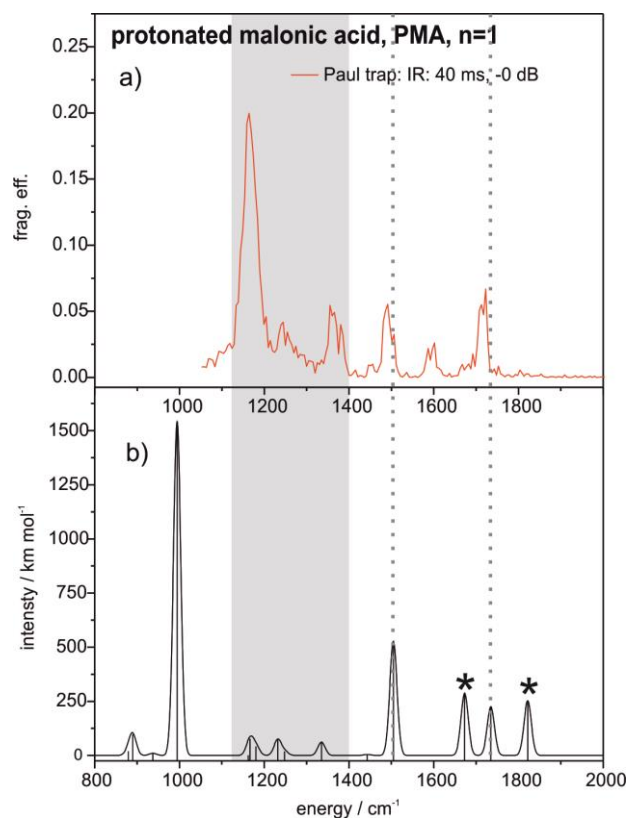


**Figure 8:** (a) IR-MPD spectrum of protonated malonic acid, PMA ( $n=1$ ); (b) calculated infrared spectrum (MP2/cc-pVDZ, scaled with 0.956). The grey shaded area indicates the region where the  $\text{CH}_2$  wagging vibrations occur. The grey dotted lines assign the CO Stretching motions. The star marks the vibrations that originate from the O-H $\cdots$ O bridging proton motion.

The calculated and linearly scaled IR absorption spectrum of DMA ( $n = 1$ ) comprises of six bands in the fingerprinting region of  $1100 - 2000 \text{ cm}^{-1}$ . Weak C-C stretching and wagging modes below  $1400 \text{ cm}^{-1}$  and medium to weak carbonyl stretching modes at  $1688$ ,  $1745$  and  $1836 \text{ cm}^{-1}$  are more or less compatible with the recorded IR-MPD spectrum which suffers from seeming inferior statistics, however. The calculations reveal a sole O-H $\cdots$ O bridging proton motion at  $1441 \text{ cm}^{-1}$ . It does not coincide with recorded IR-MPD features. Most likely, linear scaling for anharmonicity fails in this case. The actual O-H $\cdots$ O stretching and bending modes likely shift much more to the red and thus fall outside of the recorded frequency range.

## 2. IR-MPD spectroscopy of deprotonated and protonated dicarboxylic acids

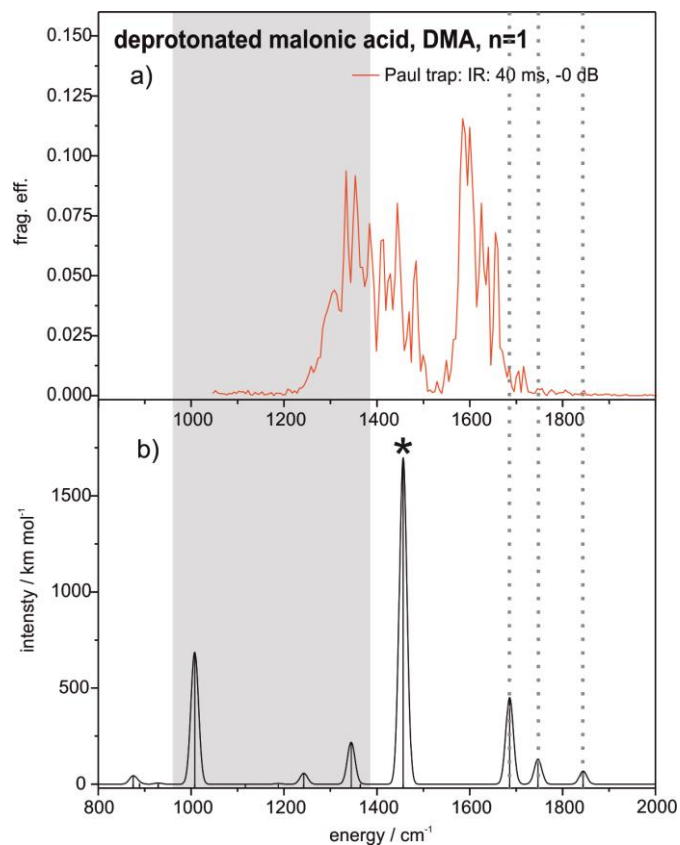


**Figure 9:** (a) IR-MPD spectrum of deprotonated malonic acid, DMA ( $n=1$ ); (b) calculated IR spectrum (MP2/cc-pVDZ, scaled with 0.956). The grey shaded area indicates the region where the  $\text{CH}_2$  wagging vibrations occur. The grey dotted lines assign the CO stretching motions. The star marks the vibrations that originate from the O-H $\cdots$ O bridging proton motion.

## 2. IR-MPD spectroscopy of deprotonated and protonated dicarboxylic acids

The experimental spectrum of PSA ( $n = 2$ ) (Fig. 10) comprises of six bands in the fingerprint range of  $1100 - 2000 \text{ cm}^{-1}$  while the calculated spectrum reveals eight bands that coincide in part (Fig. 8a) and b)). The symmetric and asymmetric CO stretching motions (marked with grey dotted lines) involve little to no motion of the O-H...O bridging proton. In the grey shaded area six bands occur that originate from  $\text{CH}_2$  wagging motions ( $1100 - 1400 \text{ cm}^{-1}$ ). These are six calculated absorption bands nicely coincide with the experimental, broad bands. It is possible that more than one minimum structure contributes to the experimental room temperature spectra. This leads to a broadening of the observed bands. The two calculated bands at  $1728$  and  $878 \text{ cm}^{-1}$  originate from the O-H...O bridging proton motion perpendicular and parallel to the hydrogen bond, respectively. Most likely they do not relate to any recorded IR-MPD bands. We find in PSA ( $n = 2$ ) the above outlined scenario: scaled harmonic calculation fails to describe highly anharmonic modes. Nevertheless, the remainder of modes may well be treated this way. As in PMA, it also seems as if the vibrational phase space largely decouples into two subspaces with little - or at least reduced- interaction.

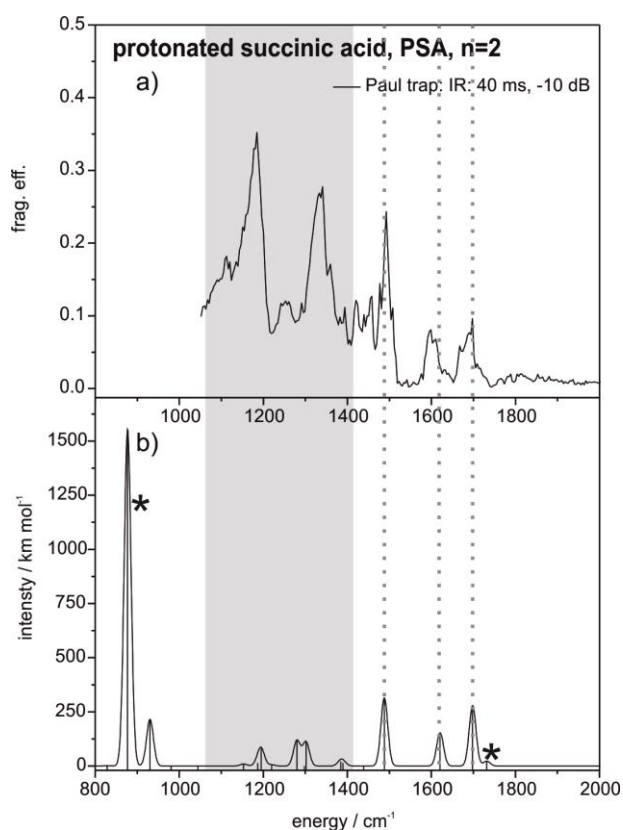


**Figure 10:** (a) IR-MPD spectrum of protonated succinic acid, PSA ( $n=2$ ); (b) calculated infrared spectrum (MP2/cc-pVDZ, scaled with 0.956). The grey shaded area indicates the region where the  $\text{CH}_2$  wagging vibrations occur. The grey dotted lines assign the CO Stretching motions. The star marks the vibrations that originate from the O-H...O bridging proton motion.

## 2. IR-MPD spectroscopy of deprotonated and protonated dicarboxylic acids

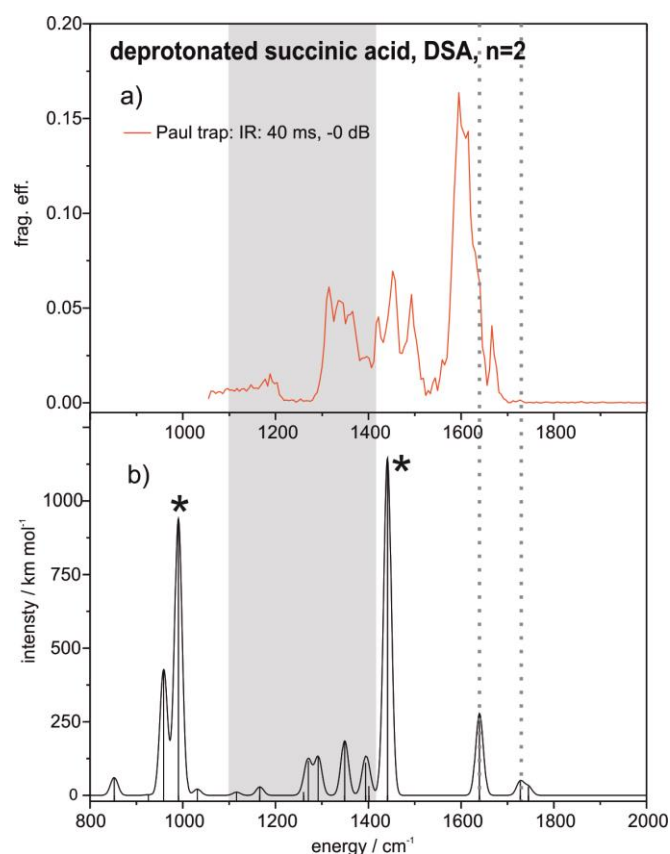


**Figure 11:** (a) IR-MPD spectrum of deprotonated succinic acid, DSA ( $n=2$ ); (b) calculated IR spectrum (MP2/cc-pVDZ, scaled with 0.956). The grey shaded area indicates the region where the  $\text{CH}_2$  wagging vibrations occur. The grey dotted lines assign the CO stretching motions. The star marks the vibrations that originate from the O-H $\cdots$ O bridging proton motion.

The calculated and linearly scaled IR absorption spectrum of DSA ( $n = 2$ ) comprises of various bands in the fingerprinting region of 1100 - 2000  $\text{cm}^{-1}$ . Weak C-C stretching and wagging modes below 1400  $\text{cm}^{-1}$  and medium to weak carbonyl stretching modes at 1688, 1745 and 1836  $\text{cm}^{-1}$  are more or less compatible with the recorded IR-MPD spectrum which suffers from seeming inferior statistics, however. The calculations reveal a sole O-H $\cdots$ O bridging proton motion at 1441  $\text{cm}^{-1}$ . It does not coincide with recorded IR-MPD features. Most likely, linear scaling for anharmonicity fails in this case. The actual O-H $\cdots$ O stretching and bending modes likely shift much more to the red and thus fall outside of the recorded frequency range.

It has been predicted before that proton delocalization along the hydrogen bond of PAA and DAA ( $n = 4$ ) complicates vibrational spectra and leads to temperature dependent broadening<sup>29</sup>. The recorded IR-MPD spectra of PAA and DAA are in line with that prediction. Spectra of smaller PDAs and DDAs ( $n < 4$ ) comprise of sharper bands. Spectral features of larger PDAs and DDAs are comparable to those of the  $n = 4$  case. It is likely -though not proven - that this relates to the onset of



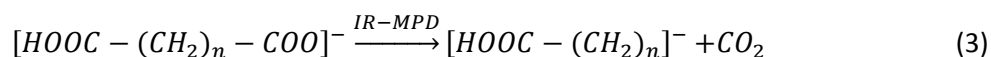
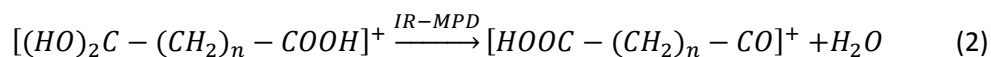
## 2. IR-MPD spectroscopy of deprotonated and protonated dicarboxylic acids

---

proton delocalization along the hydrogen bond which is known to induce strong anharmonic coupling to other vibrational modes.

### 2.5.4 IR induced fragmentation efficiency

IR-MPD investigations provide for further insight beyond the spectral information of frag. eff. (see eq. 1). Conservation of total mass and of chemical composition in the course of the IR-MPD process allows determining the mass and the composition of the corresponding ionic and neutral fragments. The evaluation of the present IR-MPD data reveals a predominant water loss in PDAs and a predominant loss of carbon dioxide in DDAs:



Other fragmentation channels are minor and sum up to less than 5% of the total fragmentation efficiency. We define total integral fragmentation efficiencies  $\eta_{p,d}^{(n)}$  of PDAs (index  $p$  for protonated) and DDAs (index  $d$  for deprotonated) of alkyl chain length  $n$  as follows:

$$\eta_p^{(n)} = \int_{\tilde{\nu}} frag. eff.^{(n)}(\tilde{\nu}) d\tilde{\nu} \quad (4)$$

and

$$\eta_d^{(n)} = \int_{\tilde{\nu}} frag. eff.^{(n)}(\tilde{\nu}) d\tilde{\nu} \quad (5)$$

The integration runs over all recorded frequencies, which is  $1100 \text{ cm}^{-1} < \tilde{\nu} < 2000 \text{ cm}^{-1}$ . The recorded spectra are not normalized to the laser power. Since IR-MPD is a multiphoton process the correlation between laser power and fragmentation efficiency is unknown and depends on multiple factors. Obviously, these limitations render the obtained values of  $\eta_d^{(n)}$  and  $\eta_p^{(n)}$  (Tab. 4 and Fig. 14) qualitative.

## 2. IR-MPD spectroscopy of deprotonated and protonated dicarboxylic acids

**Table 4:** Relative fragmentation efficiencies  $\eta_p^{(n)}$  (of PDA) and  $\eta_d^{(n)}$  (of DDA) as a function of the the alkyl chain length  $n$ . (data of Fig. 14)

DCA	n	$\eta_p^{(n)}$ (FEL)	$\eta_p^{(n)}$ (OPO, 1 color)	$\eta_p^{(n)}$ (OPO, 2 color)	$\eta_d^{(n)}$ (FEL)	$\eta_d^{(n)}$ (OPO, 1 color)	$\eta_d^{(n)}$ (OPO, 2 color)
MA	1	18	1.7	8.0	18	—	—
SA	2	183	32	57	19	3.5	37
GA	3	179	110	136	3.1	2.0	36
AA	4	—	78	102	—	0.1	19
PA	5	94	—	—	3.9	—	—

The “—” indicates missing experimental data due to different reasons:

MA: mass of fragments below the detection limit

AA: no comparable experimental conditions

PA: no OPO measurements

For all PDAs, and in total, FEL mediated fragmentation  $\eta_{p,FEL}^{(n)}$  is most efficient. For all DDAs but DMA ( $n=1$ ), FEL mediated fragmentation  $\eta_{d,FEL}^{(n)}$  is at least an order of magnitude less efficient. OPO based one color fragmentation of PDAs,  $\eta_{p,OPO,1color}^{(n)}$  and of DDAs,  $\eta_{d,OPO,1color}^{(n)}$ , are seemingly less efficient than the FEL mediated fragmentations and OPO based two color fragmentation of DDAs,  $\eta_{d,OPO,2color}^{(n)}$  are more efficient than the FEL mediated fragmentations, respectively. Application of a second OPO pulse enables an enhancement of the two color fragmentation of PDAs,  $\eta_{p,OPO,2color}^{(n)}$  and of DDAs,  $\eta_{d,OPO,2color}^{(n)}$ . The enhancement factor is 1.3 - 4.7 for PDAs and 10.6 - 190 for DDAs, when changing from one color to two color fragmentation (cf. grey shaded areas in

## 2. IR-MPD spectroscopy of deprotonated and protonated dicarboxylic acids

Fig. 14). For all applied probing schemes and alkyl chain lengths  $n$ , but  $n = 1$ ,  $\eta_p^{(n)} > \eta_d^{(n)}$ . The interpretation of these findings benefits from the knowledge of dissociation enthalpies of PDAs,  $\Delta_{\text{diss}}H_p^{(n)}$ , and of DDAs,  $\Delta_{\text{diss}}H_d^{(n)}$ .

All calculated dissociation enthalpies of PDAs are smaller than those of DDAs,  $\Delta_{\text{diss}}H_p^{(n)} < \Delta_{\text{diss}}H_d^{(n)}$ ,  $n \leq 4$  (Tab.5). This supports  $\eta_p^{(n)} > \eta_d^{(n)}$  nicely. Dissociation enthalpies of PMA ( $n = 1$ ) and DMA ( $n = 1$ ) are close to each other,  $\Delta_{\text{diss}}H_p^{(1)} \sim \Delta_{\text{diss}}H_d^{(1)}$ . So are the corresponding fragmentation efficiencies,  $\eta_{p,FEL}^{(1)} \sim \eta_{d,FEL}^{(1)}$ . PDAs with longer alkyl chains ( $n \geq 2$ ) can form protonated cyclic anhydride structures with the emerging water molecule coordinated prior to evaporation (cf. Fig. 12 ( $n = 4$ )). The concomitant stabilization is considerable. It lowers dissociation enthalpies of the cyclic PDAs into cyclic fragments,  $\Delta_{\text{diss}}H_p^{(3,4)}$ , by - 58 and - 85 kJ/mol with respect to open fragment structures, respectively. In DDAs the difference is even larger in the case of  $n = 3$  (+ 138 kJ/mol), but of comparable magnitude in the case of  $n = 4$  (+ 43 kJ/mol). Finally, it is worth mentioning that the open DMA-CO<sub>2</sub> fragment possesses significantly higher stability than other DDA-CO<sub>2</sub> fragments which shows in the low value of  $\Delta_{\text{diss}}H_d^{(1)} = + 190$  kJ/mol.

**Table 5:** Calculated dissociation enthalpies  $\Delta_d H^{0K}$  (MP2/ cc-pVDZ). Values in kJ/mol hold for the lowest accessible dissociation channels, not taking likely activation barriers into account. Note that a resonant IR excitation by a single photon per molecule of e.g. a carbonyl band at 1700 cm<sup>-1</sup> corresponds to an energy gain of 21 kJ/mol.

		PDA - H <sub>2</sub> O			DDA - CO <sub>2</sub>			
		cyclic	open		cyclic	open		
$n = 1$	open	PMA	—	+ 180	open	DMA	—	+ 190
$n = 2$	cyclic	PSA	+ 150	+ 196	cyclic	DSA	—	+335
$n = 3$	cyclic	PGA	+ 142	+ 200	cyclic	DGA	+ 189	+ 327
$n = 4$	cyclic	PAA	+ 157	+ 242	cyclic	DAA	+ 199	+ 242

We calculated the fragmentation of the  $n = 4$  case in more detail (see Fig. 12 and Fig. 13). PAA can form protonated cyclic anhydride structures with coordinated water molecule (blue arrows). In PAA this structure is only 58 kJ/mol higher in energy than the calculated minimum structure. This

## 2. IR-MPD spectroscopy of deprotonated and protonated dicarboxylic acids

corresponds to three IR photons at  $1700\text{ cm}^{-1}$ . The dehydration via an open structure is much higher in energy (red arrows). Due to the alkyl chain, an intramolecular condensation path resulting in formation of a corresponding anhydride aids the elimination of water and thus, avoiding destabilized intermediates resulting in a slow fragmentation mechanism.

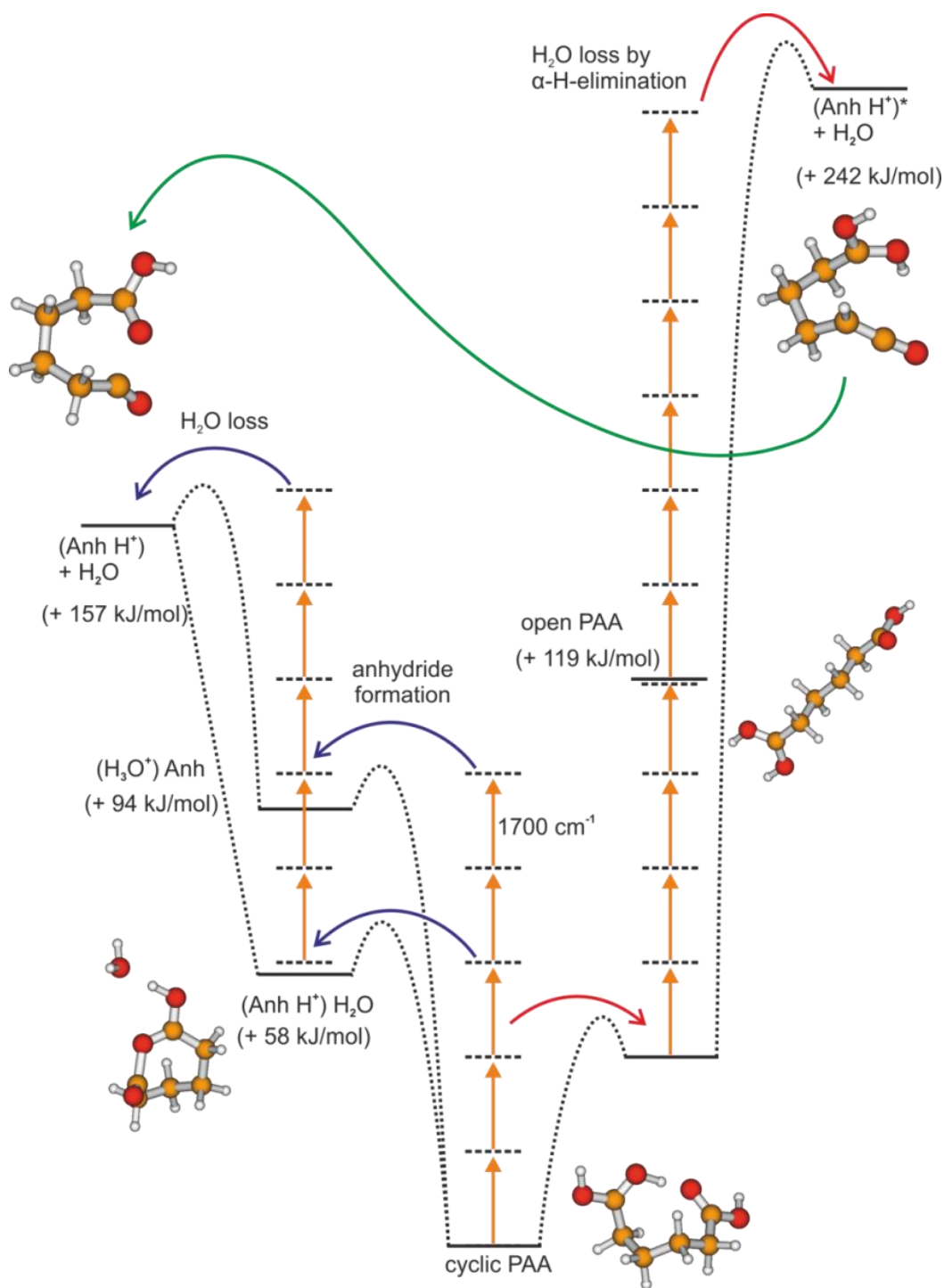


**Figure 12:** Computed fragmentation path of PAA ( $n = 4$ ). In PAA two possible paths of fragmentation have been calculated.

## 2. IR-MPD spectroscopy of deprotonated and protonated dicarboxylic acids

---

In DAA the loss of carbon dioxide is feasible but in comparison with PAA more laborious. The formation of a cyclic anhydride structure is not possible. This coincides with the observation in our experiments. The fragmentation efficiency of protonated species is higher than in deprotonated species.

Calculating the fragments of DAA ( $n = 4$ ) reveals that the fragmentation of carbon dioxide leads to a reaction product which is 150 kJ/mol higher in energy than the calculated minimum structure of DAA. One possible calculated reaction coordinate needs 200 kJ/mol for fragmentation. This is comparable to the needed energy of DMA and DGA. The reaction mechanism seems to be the same. At first glance there is a disagreement between this theoretical result and our experiments (see Tab. 4). Here the fragmentation efficiency decreases for DDAs with rising alkyl chain. To explain this discrepancy we have to take in account that we only calculated the products of fragmentation (cf. Tab 4). There is no transition states calculated. The decrease of fragmentation efficiency may be due to activation barriers. DDAs can fragment directly but higher fragmentation energy is needed. The elimination of carbon dioxide occurs on a direct fragmentation path while the fragmentation of PDAs needs a rearrangement of the molecular structure prior fragmentation. Thus, the spectra of DDAs are more affected by the use of a second resonant IR laser. This corresponds to our experimental findings.

## 2. IR-MPD spectroscopy of deprotonated and protonated dicarboxylic acids

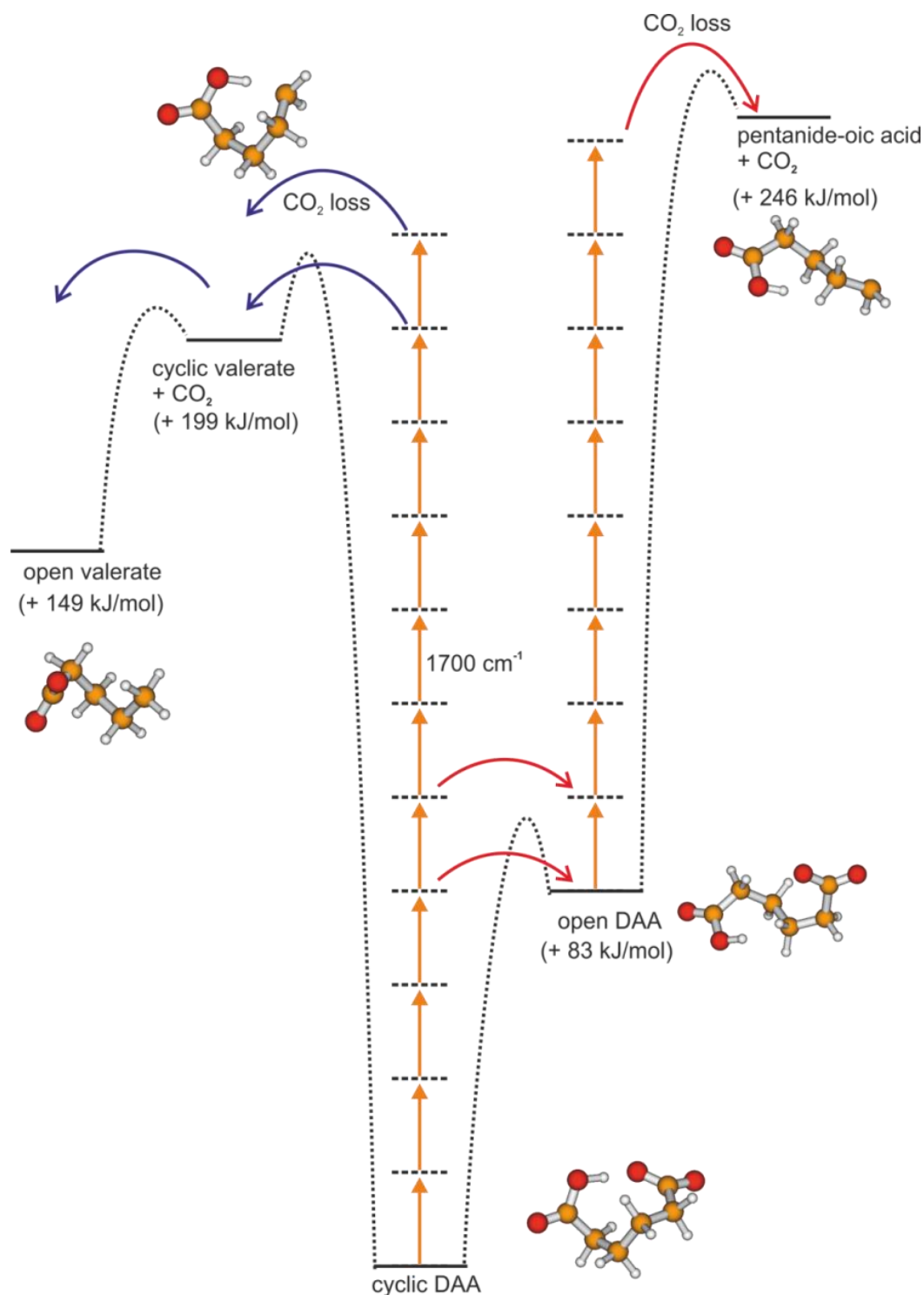


**Figure 13:** Computed fragmentation path of DAA ( $n = 4$ ). In DAA two possible paths of fragmentation have been calculated.

PMA and DMA ( $n = 1$ ) both fragment with comparable efficiency while for dicarboxylic acids with a longer alkyl chain ( $n \geq 2$ ) the ratio  $\eta_d^{(n)}/\eta_p^{(n)}$  decreases drastically. We calculated the emerging fragments to comprehend this observation. Both species need at least 180 kJ/mol to fragment. This

## 2. IR-MPD spectroscopy of deprotonated and protonated dicarboxylic acids

corresponds to nine photons with a photon energy of  $1700\text{ cm}^{-1}$  ( $= 21\text{ kJ/mol}$ ). The cyclic anhydride structure of PMA is a four membered ring which possess considerable ring strain. This cyclic anhydride structure is not stable. PMA needs more energy to eliminate water than dicarboxylic acids with a longer alkyl chain (cf. S3 and S4 in the supplement material). The resulting dehydrated species undergoes tautomerization. Both tautomer structures are separated by  $8\text{ kJ/mol}$ . In DMA ( $n = 1$ ) at least ten photons are required to eliminate carbon dioxide. This processes lead to two tautomer structures which are separated by  $119\text{ kJ/mol}$ . This fragmentation process needs nearly the same energy as the fragmentation of PMA ( $n = 1$ ). Thus, the calculations are in good agreement with our experiments.

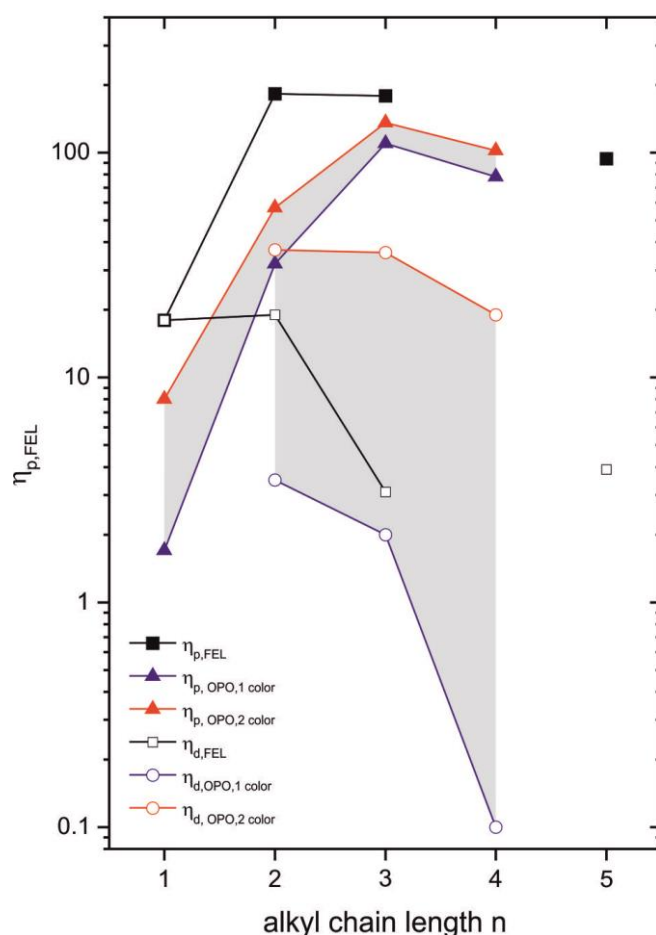


**Figure 14:** Fragmentation efficiencies  $\eta_p^{(n)}$  (of PDA, filled symbols) and  $\eta_d^{(n)}$  (of DDA, open symbols) as a function of the the alkyl chain length  $n$ .

The two color effect need a dedicated explanation. Two color IR-MPD spectroscopy in the fingerprint range with the OPO laser system leads only to little amplification of the bands in the PDAs (cf. Fig.

## 2. IR-MPD spectroscopy of deprotonated and protonated dicarboxylic acids

---

14). The spectra of DDAs are more affected by the use of a second resonant IR laser. The elimination of carbon dioxide occurs on a direct fragmentation path while the fragmentation of PDAs needs a rearrangement of the molecular structure prior to fragmentation. We see in general an enhancement of weak modes. This seems to relate to the IR strength in a nonlinear way. It is not specific to particular types of modes.

The adipin case and the other computed values of the dissociation enthalpies are well compatible with the observed fragmentation efficiencies. Nevertheless, there is no one-to-one correlation. Other factors contribute, just to name five of these: (1) Density of states (DOS), (2) entropy gain in forming open fragment structures, (3) barriers towards reorganization, (4) anharmonicities and (5) nonlinear power effects.

(1) Density of states: The small DCAs ( $n = 1$  and  $2$ ) provide for low DOS values. This renders IR-MPD less efficient the smaller the DAs. The DOS increasing with  $n$  may account for the observed rise with  $n$  by more than one magnitude of the fragmentation efficiencies  $\eta_{p,OPD}^{(1,2)}$  in PDAs – a small rise in  $\Delta_{\text{diss}}H_p^{(2)} > \Delta_{\text{diss}}H_p^{(1)}$  counteracting less.

It looks as if the rise of DOS from  $n=1$  to  $n=2$  in DDAs causes an effect on  $\eta_{p,FEL}^{(1,2)}$  that is balanced by the counteracting rise of  $\Delta_{\text{diss}}H_d^{(2)} \gg \Delta_{\text{diss}}H_d^{(1)}$ .

(2) entropy gain in forming open fragment structures

(3) barriers towards reorganization: Our calculations of the fragment structures do not cover the barriers of reorganisation

(4) anharmonicities: cause a walk off in excited Eigen states that works against resonant multiphoton excitation and thereby reduces fragmentation efficiency

(5) nonlinear power effects: at high photon fluxes non resonant multiphoton excitations start to contribute.

It would be beyond the scope of the present study to provide a full coverage of the influence on the recorded fragmentation efficiencies of all of the listed factors. It is worthwhile, however, to consider subsequent work into that direction.



### 2.6 Conclusions

IR-MPD spectra of PDAs and DDAs ( $n = 1 - 5$ ) has been recorded in the CO stretching region and in the O-H stretching region. The longer the alkyl chain, the more flexible is the backbone, the more structures contribute to the spectra. This leads to a broadening in the recorded room temperature spectra.

The quantum chemical calculations on MP2 level of theory with a double  $\zeta$  basis show that ionic dicarboxylic acids form cyclic structures with an intramolecular hydrogen bond in the gas phase. The potential energy surface along the proton transfer mode varies in the homologous row with the ring size. Small dicarboxylic acids have a potential energy surface with a quartic shape. They have a Zundel like structure. Dicarboxylic acids with a longer  $\text{CH}_2$  backbone have a narrower surface. They form structures with an Eigen like structure where the proton is not symmetrically shared.

The different fragmentation behavior corresponds to the calculated fragmentation paths. The fragmentation efficiency is higher in PDAs. PDAs with  $n \geq 2$  can form protonated anhydride structures with coordinated water. This reorganization facilitates the elimination of water. DDAs can fragment directly but higher fragmentation energy is needed.

The enhancement of a second IR laser is stronger in DDAs. The elimination of carbon dioxide occurs on a direct fragmentation path while the fragmentation of PDAs needs a rearrangement of the molecular structure prior to fragmentation. Thus, the spectra of DDAs are more affected by the use of a second resonant IR laser. This corresponds to our experimental findings.

### Acknowledgment

This work was supported by the German research foundation DFG within the transregional collaborative research center SFB/TRR 88 "Cooperative effects in homo and heterometallic complexes" (3MET.de), by the Carl-Zeiss Foundation, and by the state research center OPTIMAS. We benefitted from inspiring discussions with Marc Prosenc and Mark Johnson.

### 2.7 References

1. S. J. Grabowski, *Hydrogen Bonding - New Insights*, Springer, Dordrecht, Netherlands, 2006.
2. S. Scheiner, *Hydrogen Bonding: A Theoretical Perspective*, University Press, Oxford, 1997.
3. U. Buck and F. Huisken, *Chem. Rev.*, 2000, **100**, 3863-3890.
4. N. J. Singh, A. C. Olleta, A. Kumar, M. Park, H. B. Yi, I. Bandyopadhyay, H. M. Lee, P. Tarakeshwar and K. S. Kim, *Theor. Chem. Acc.*, 2006, **115**, 127-135.
5. H. M. Lee, S. B. Suh, J. Y. Lee, P. Tarakeshwar and K. S. Kim, *Journal of Chemical Physics*, 2000, **112**, 9759-9772.
6. H. M. Lee, S. B. Suh, P. Tarakeshwar and K. S. Kim, *Journal of Chemical Physics*, 2005, **122**, 6.
7. G. Gilli and P. Gilli, *Journal of Molecular Structure*, 2000, **552**, 1-15.
8. V. Bertolasi, P. Gilli, V. Ferretti and G. Gilli, *Chemistry-a European Journal*, 1996, **2**, 925-934.
9. W. W. Cleland and M. M. Kreevoy, *Science*, 1994, **264**, 1887-1890.
10. H. S. Cho, N. C. Ha, G. Choi, H. J. Kim, D. Lee, K. S. Oh, K. S. Kim, W. Lee, K. Y. Choi and B. H. Oh, *Journal of Biological Chemistry*, 1999, **274**, 32863-32868.
11. P. A. Frey, S. A. Whitt and J. B. Tobin, *Science*, 1994, **264**, 1927-1930.
12. K. S. Kim, K. S. Oh and J. Y. Lee, *Proceedings of the National Academy of Sciences of the United States of America*, 2000, **97**, 6373-6378.
13. J. Lin and P. A. Frey, *Journal of the American Chemical Society*, 2000, **122**, 11258-11259.
14. K. S. Kim, D. W. Kim, J. Y. Lee, P. Tarakeshwar and K. S. Oh, *Biochemistry*, 2002, **41**, 5300-5306.
15. M. Eigen, *Angewandte Chemie-International Edition*, 1963, **75**, 489-&.
16. G. Zundel and H. Metzger, *Zeitschrift Fur Physikalische Chemie-Frankfurt*, 1968, **58**, 225-&.
17. N. I. Hammer, E. G. Diken, J. R. Roscioli, M. A. Johnson, E. M. Myshakin, K. D. Jordan, A. B. McCoy, X. Huang, J. M. Bowman and S. Carter, *Journal of Chemical Physics*, 2005, **122**, 10.
18. G. Niedner-Schatteburg, *Angewandte Chemie-International Edition*, 2008, **47**, 1008-1011.
19. J. C. Jiang, Y. S. Wang, H. C. Chang, S. H. Lin, Y. T. Lee and G. Niedner-Schatteburg, *Journal of the American Chemical Society*, 2000, **122**, 1398-1410.
20. O. Vendrell, F. Gatti and H. D. Meyer, *Angewandte Chemie-International Edition*, 2007, **46**, 6918-6921.
21. J. R. Roscioli, L. R. McCunn and M. A. Johnson, *Science*, 2007, **316**, 249-254.
22. J. L. Haslam, E. M. Eyring, W. W. Epstein, R. P. Jensen and C. W. Jaget, *Journal of the American Chemical Society*, 1965, **87**, 4247-&.
23. C. L. Perrin and J. D. Thoburn, *Journal of the American Chemical Society*, 1992, **114**, 8559-8565.
24. M. R. Kumar, S. Prabhakar, V. Nagaveni and M. Vairamani, *Rapid Communications in Mass Spectrometry*, 2005, **19**, 1053-1057.
25. D. Braga, J. J. Novoa and F. Grepioni, *New Journal of Chemistry*, 2001, **25**, 226-230.
26. H. K. Woo, X. B. Wang, K. C. Lau and L. S. Wang, *Journal of Physical Chemistry A*, 2006, **110**, 7801-7805.
27. M. Z. Kamrath, R. A. Relph, T. L. Guasco, C. M. Leavitt and M. A. Johnson, *International Journal of Mass Spectrometry*, 2011, **300**, 91-98.
28. T. H. Nguyen, D. E. Hibbs and S. T. Howard, *Journal of Computational Chemistry*, 2005, **26**, 1233-1241.

## 2. IR-MPD spectroscopy of deprotonated and protonated dicarboxylic acids

---

29. S. K. Min, M. Park, N. J. Singh, H. M. Lee, E. C. Lee, K. S. Kim, A. Lagutschenkov and G. Niedner-Schatteburg, *Chemistry-a European Journal*, 2010, **16**, 10373-10379.
30. G. J. O. Beran, E. L. Chronister, L. L. Daemen, A. R. Moehlig, L. J. Mueller, J. Oomens, A. Rice, D. R. Santiago-Dieppa, F. S. Tham, K. Theel, S. Yaghmaei and T. H. Morton, *Phys. Chem. Chem. Phys.*, 2011, **13**, 20380-20392.
31. R. C. Dunbar, *International Journal of Mass Spectrometry*, 2000, **200**, 571-589.
32. R. Prazeres, F. Glotin, C. Insa, D. A. Jaroszynski and J. M. Ortega, *Eur. Phys. J. D*, 1998, **3**, 87-93.
33. Y. Nosenko, F. Menges, C. Riehn and G. Niedner-Schatteburg, *Phys. Chem. Chem. Phys.*, 2013, **15**, 8171-8178.
34. J. M. Bakker, T. Besson, J. Lemaire, D. Scuderi and P. Maitre, *Journal of Physical Chemistry A*, 2007, **111**, 13415-13424.
35. D. Scuderi, C. F. Correia, O. P. Balaj, G. Ohanessian, J. Lemaire and P. Maitre, *Chemphyschem*, 2009, **10**, 1630-1641.
36. C. Moller and M. S. Plesset, *Phys. Rev.*, 1934, **46**, 0618-0622.
37. T. H. Dunning, *Journal of Chemical Physics*, 1989, **90**, 1007-1023.
38. R. Ahlrichs, M. Bar, M. Haser, H. Horn and C. Kolmel, *Chem. Phys. Lett.*, 1989, **162**, 165-169.

## 2.8 Supplement material

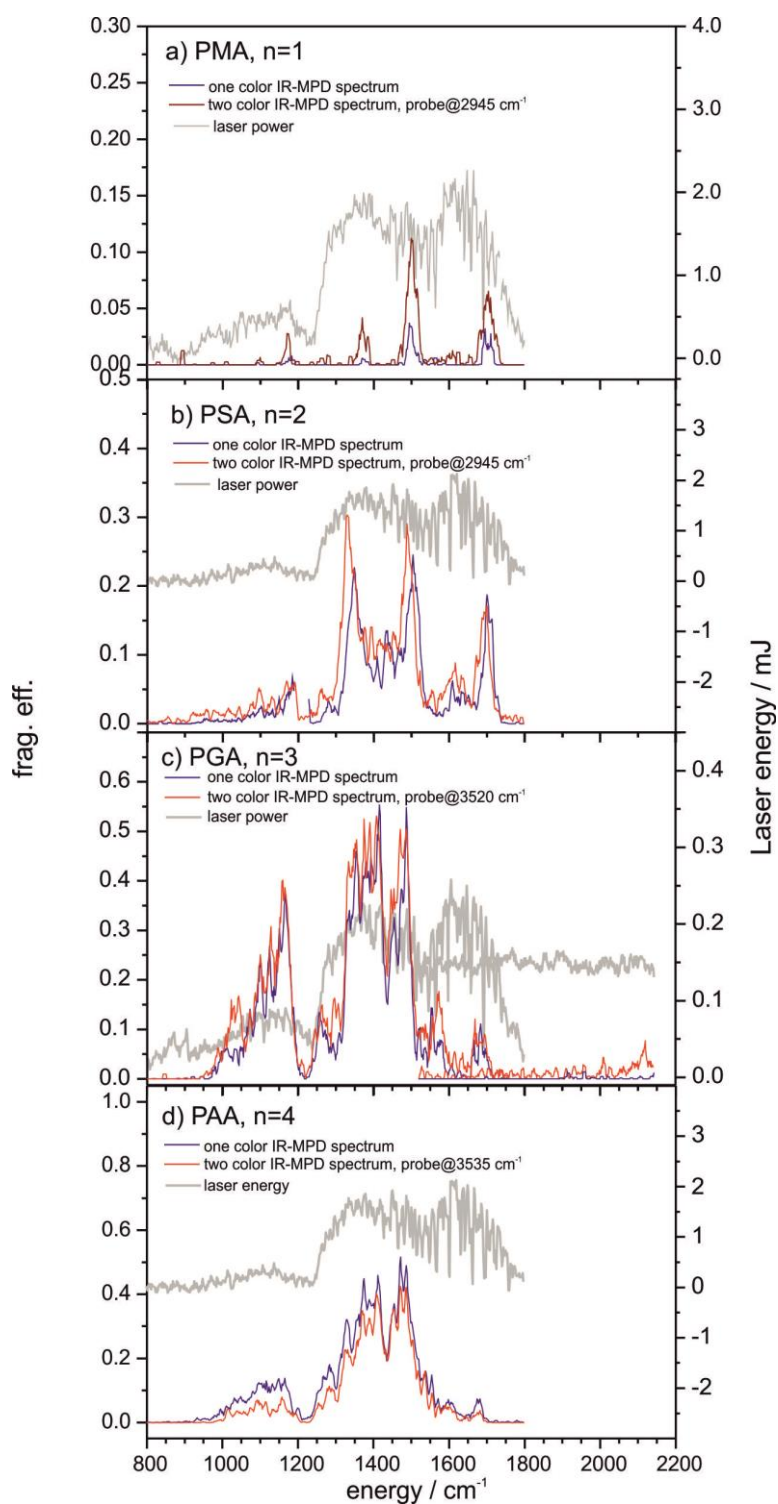


**Figure S1:** Enlarged plots of the fingerprint region of PDAs. One color (blue) and two color (red and brown) IR-MPD spectra by OPO/OPA laser of PDAs (a) PMA ( $n = 1$ ), (b) PSA ( $n = 2$ ), (c) PGA ( $n = 3$ ), and (d) PAA ( $n = 4$ ).

## 2. IR-MPD spectroscopy of deprotonated and protonated dicarboxylic acids

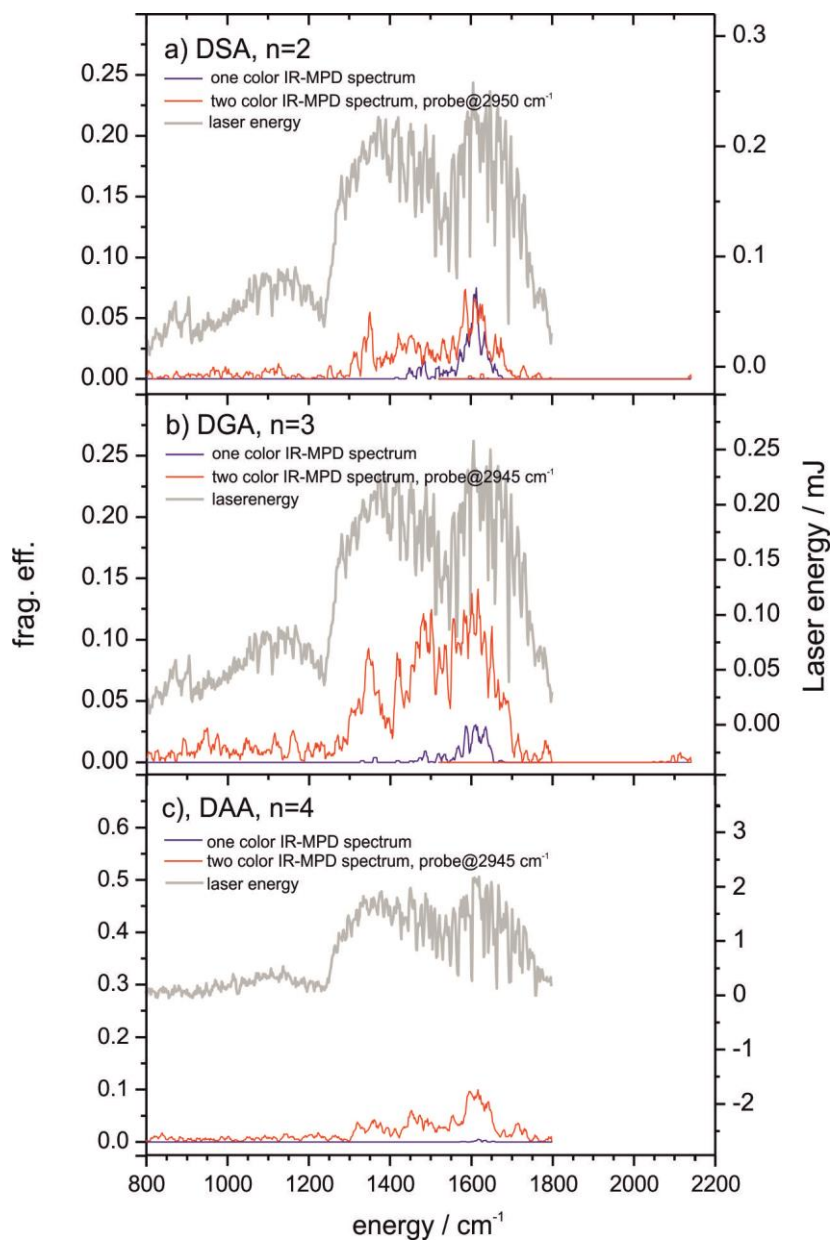


**Figure S2:** Enlarged plots of the fingerprint region of DDAs. One color (blue) and two color (red) IR-MPD spectra by OPO/OPA laser of deprotonated dicarboxylic acids (a) DSA ( $n = 2$ ), (b) DGA ( $n = 3$ ), and (c) DAA ( $n = 4$ ).

## 2. IR-MPD spectroscopy of deprotonated and protonated dicarboxylic acids

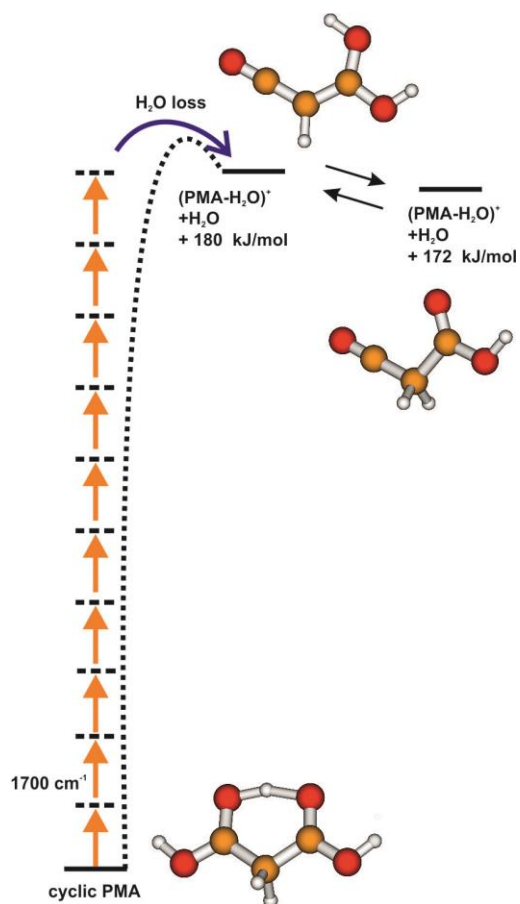


**Figure S3:** Computed fragmentation path of PMA ( $n = 1$ ). For PMA the H<sub>2</sub>O loss dominates. After fragmentation the fragment stabilizes by tautomerization.

## 2. IR-MPD spectroscopy of deprotonated and protonated dicarboxylic acids

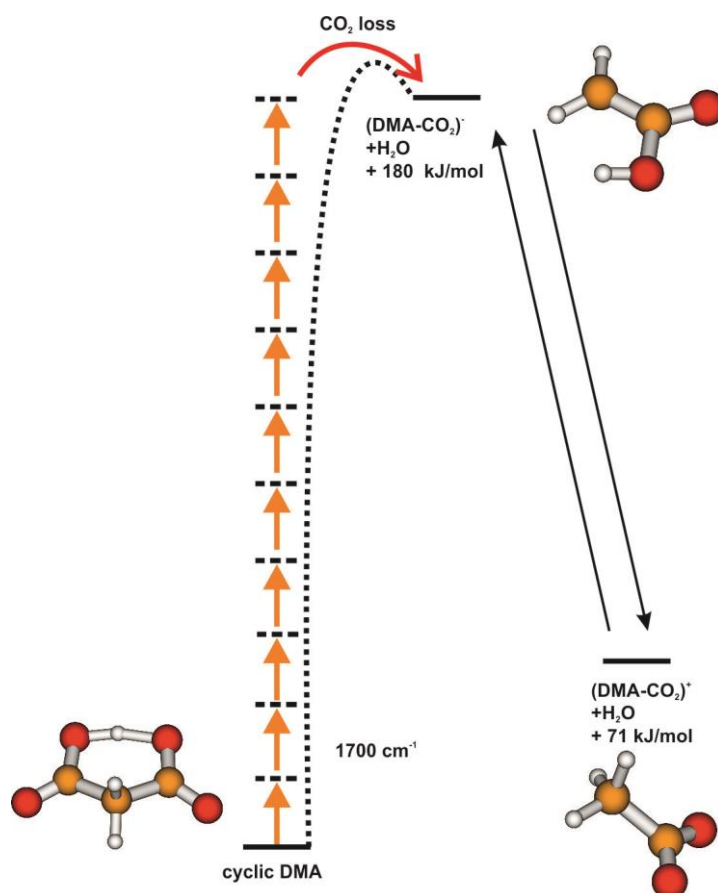


**Figure S4:** Computed fragmentation path of DMA ( $n = 1$ ). For DMA the  $\text{CO}_2$  loss dominates. After fragmentation the fragment stabilizes by tautomerization.

### 2.9. Comparison of OPO experiments and theory

IR-MPD and MP2 calculations on PDAs and DDAs have been performed<sup>1</sup>. In chapter 2.1 we compare the smaller dicarboxylic acids with the experiments obtained by the CLIO FEL set up. This comparison is more difficult for higher dicarboxylic structures because at room temperature many conformer structures contribute to the infrared spectrum. Nevertheless here we will compare the calculated infrared spectra of the minimum structure of higher dicarboxylic acids with experimental spectra performed with the OPO set up in Kaiserslautern. It is important to remember that many structures contribute to the room temperature spectra and the bands are broadened. The longer the alkyl chain the more flexible the structure becomes the more conformers contribute to the room temperature spectrum. Here only one calculated minimum structure is shown. The conformer spectra are often similar because they all show the same proton bridged motif. K.S Kim *et al.* performed Car-Parrinello molecular dynamics (CPMD) simulations. The results indicate that the proton transfer occurs by multistep chiral transformation in protonated (PAA) and deprotonated adipic acid (DAA) ( $n=4$ )<sup>2</sup>. The lowest energy structure of PAA is predicted to have Zundel like symmetric hydrogen bonding, whereas that of DAA has Eigen-like asymmetric hydrogen bonding. Direct proton transfer between the two proton acceptor sites is unfavorable. Instead chiral transformation is possible by subsequent backbone twisting through stepwise proton transfer along multistep intermediate structures, which are Zundel-like ion for PAA and Eigen-like for DAA.<sup>2</sup> To eliminate the problem of many contributing conformers it is necessary to measure the IR-MPD spectra of the cold species. These measurements are planned. Up to now only spectra of the room temperature species were possible.



## 2. IR-MPD spectroscopy of deprotonated and protonated dicarboxylic acids

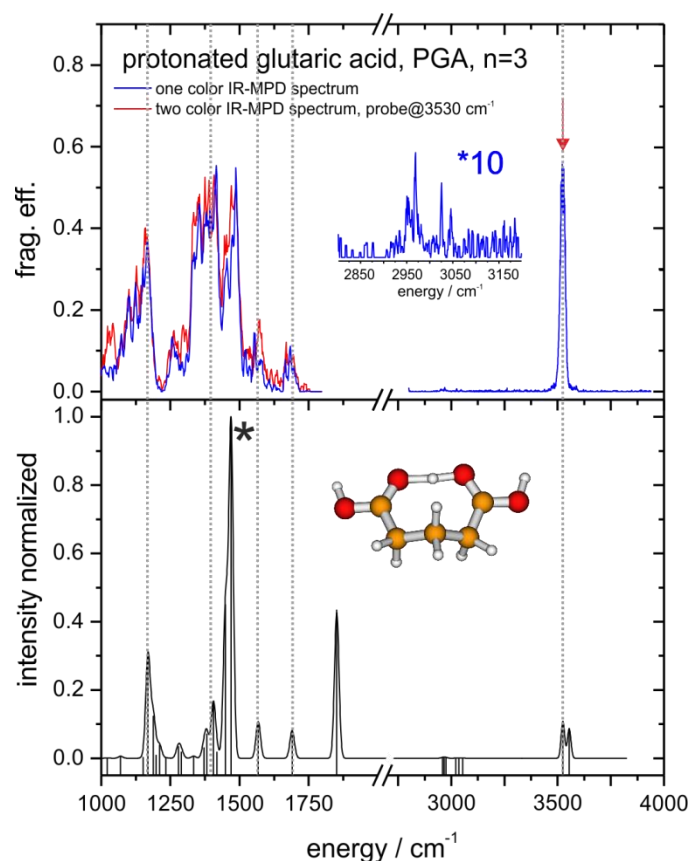


**Figure 15:** The IR-MPD spectrum of PGA ( $n = 3$ ) (top), the inset shows the blow-up of the CH stretching region. The theoretical spectrum is calculated on MP2 level of theory with a double  $\zeta$  basis and scaled by 0.956.

The experimental spectrum of PGA ( $n = 3$ ) (cf. Fig. 15, top) comprises of one strong OH stretching band at  $3525 \text{ cm}^{-1}$  and six broad bands in the fingerprint range of  $1000 - 2000 \text{ cm}^{-1}$ . The strongest band marked by a star arises from the bridging proton motion. Many conformers contribute to the observed spectrum. Hence, the observed bands are broadened and a comparison of experimental and calculated spectra is difficult. Nevertheless, part of the bands coincides nicely with the experimental bands (dotted lines). The band at  $3525 \text{ cm}^{-1}$  arises from the free OH stretching motion. In the experimental spectra only one band arises in this region. This experimental band is about  $25 \text{ cm}^{-1}$  broad. In the calculation these two bands are separated only by  $30 \text{ cm}^{-1}$  that leads to one observed band in the experimental spectrum. The excess proton is located in a proton bridge. We expect a considerable red shift and broadening of the OH stretching frequency which is not observed or identified in the experimental spectra. In the calculated spectrum the bands with the strongest intensity originate from the movement of the bridging proton (star). At  $1851 \text{ cm}^{-1}$  the proton transfer mode is predicted. This is calculated in harmonic approximation and this band may shift further to the red. The anharmonicity of these proton movements is very strong and harmonic approximation is doomed to fail. The symmetric and asymmetric CO stretching bands at  $1565$  and  $1690 \text{ cm}^{-1}$  are in

## 2. IR-MPD spectroscopy of deprotonated and protonated dicarboxylic acids

good agreement with the experiment. The motion of the bridging proton is uncoupled to these modes. The CH stretching vibrations are very weak in both calculation and experiment.

In the experimental spectra the two color effect is minor which is expected. In chapter 2.5.4 the fragmentation path of the PDAs proceeds via a protonated anhydride with a coordinated water molecule. This anhydride formation prior the fragmentation leads to a slow fragmentation process which is not affected by a second IR photon.

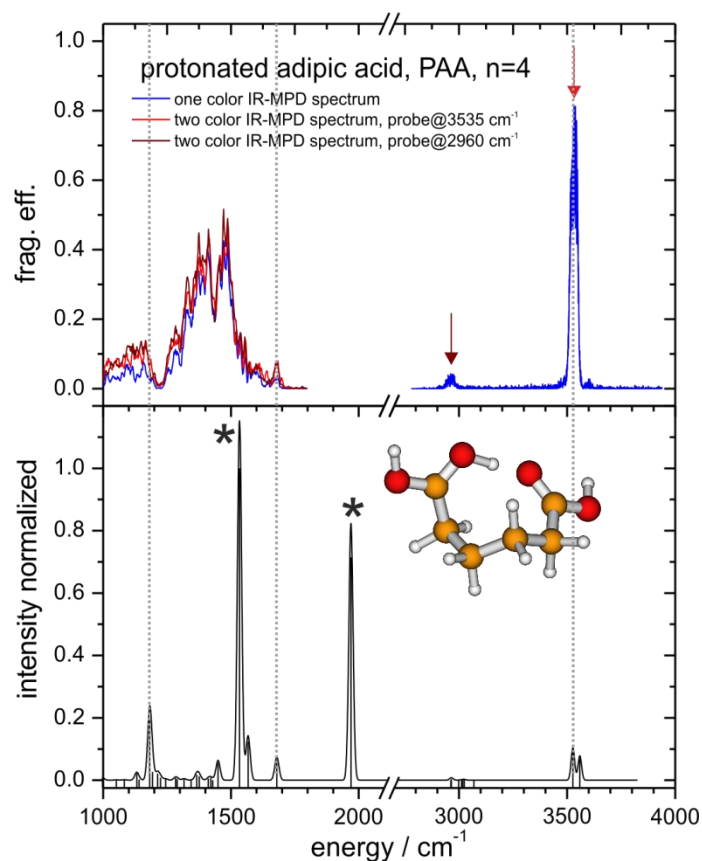


**Figure 16:** The IR-MPD spectrum of PAA ( $n = 4$ ) (top), the inset shows the blow-up of the CH stretching region. The theoretical spectrum is calculated on MP2 level of theory with a double  $\zeta$  basis and scaled by 0.956.

The experimental spectrum (cf. Fig. 16; top) comprises of a strong band in the OH stretching region and a broad small band in the CH stretching region. In the fingerprint range small sharp band is found which is assigned to a CO stretching motion. Further bands interfere with each other. Only two very broad absorptions remain. In the calculated spectrum two bands separated by  $32 \text{ cm}^{-1}$  are assigned to the two free OH stretching vibrations. These two modes lead to one observed OH stretching band in the experimental spectra. The comparison of the observed and calculated CH stretching frequencies is difficult. The bands are broadened. To gain further insight in this very flexible PAA spectrum IR-MPD experiments at low temperature are necessary. There are more CH stretching frequencies calculated than seen in the experiment. IR-MPD spectroscopy is an action spectroscopy

## 2. IR-MPD spectroscopy of deprotonated and protonated dicarboxylic acids

and dark bands are possible. The calculated asymmetric CO stretching mode is in good agreement with the experimental spectra (cf. Fig. 16, dotted line). The proton transfer mode is calculated to appear at  $1970\text{ cm}^{-1}$  marked by a star. As mentioned before, this band is probably considerably red shifted and broadened. The calculated band with the highest intensity results from a CO stretching vibration coupled to the movement of the bridging proton. An assignment of all observed bands is not possible. The experimental spectrum is too broad.  $\text{CH}_2$  bending motions are observed in the region below  $1400\text{ cm}^{-1}$ . As explained before, the two color effect is minor in the spectrum of PAA due to the slow fragmentation path.

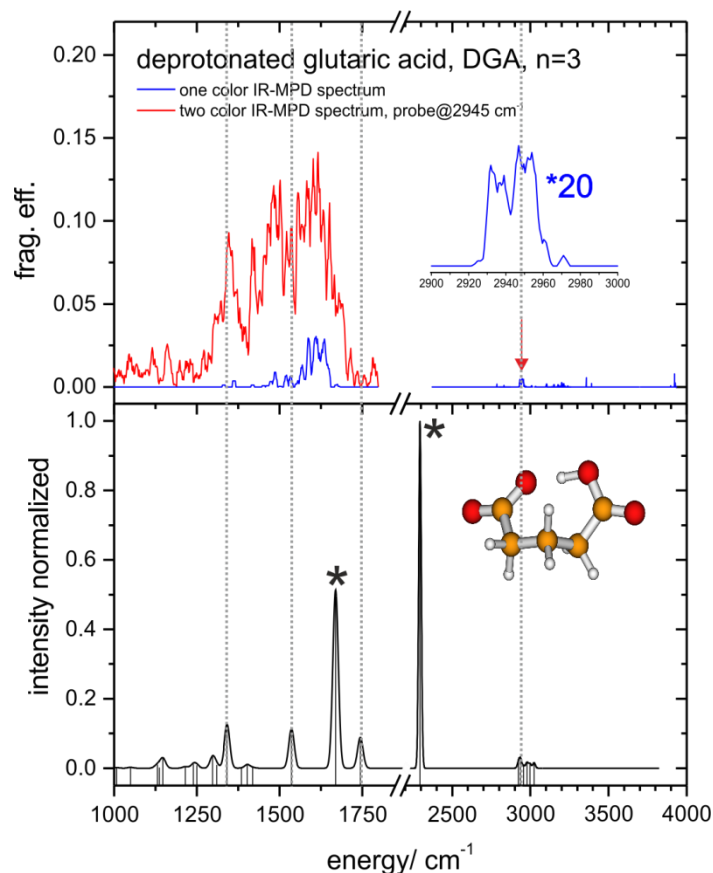


**Figure 17:** The IR-MPD spectrum of DGA ( $n = 3$ ) (top), the inset shows the blow-up of the CH stretching region. The theoretical spectrum is calculated on MP2 level of theory with a double  $\zeta$  basis and scaled by 0.956.

The experimental spectra of DDAs are broader than the spectra of PDAs. The experimental spectrum of DGA ( $n = 3$ ) comprises one very broad absorption in the range of  $1000 - 1800\text{ cm}^{-1}$  (cf. Fig. 17) and two very weak bands in the CH stretching region. There is no band in the free OH stretching region. This leads to the conclusion that the OH group forms a hydrogen bond. The resulting vibrational mode shifts to the red. In the calculated spectrum (cf. Fig. 17, bottom) OH stretching band occurs at  $2300\text{ cm}^{-1}$ . Around this region the laser power of the OPO system is too low for our action spectroscopy. Furthermore, we expect that the red shift of the bridged hydrogen bond is

## 2. IR-MPD spectroscopy of deprotonated and protonated dicarboxylic acids

considerably higher. The harmonic approximation is doomed to fail. The anharmonicity in this system is high. The experimental spectrum with only one IR laser shows a broad absorption around  $1600\text{ cm}^{-1}$ . The two color IR-MPD method has a strong influence on the experimental results. In contrast to the PDAs the DDAs fragment via a direct fragmentation path. No rearrangement of the molecular structure (as anhydride formation in PDAs) is necessary. Thus the second IR pulse has a great influence in the experimental spectra. Three broad structures become apparent in the fingerprint region. The weak absorption around  $1770\text{ cm}^{-1}$  is assigned to a CO stretching vibration.  $\text{CH}_2$  bending motions occur around  $1300\text{ cm}^{-1}$ . These bands arise also in the calculated spectrum. The bands including the bridging proton movement (star) cannot be assigned unambiguously to the bands in the experimental spectrum.

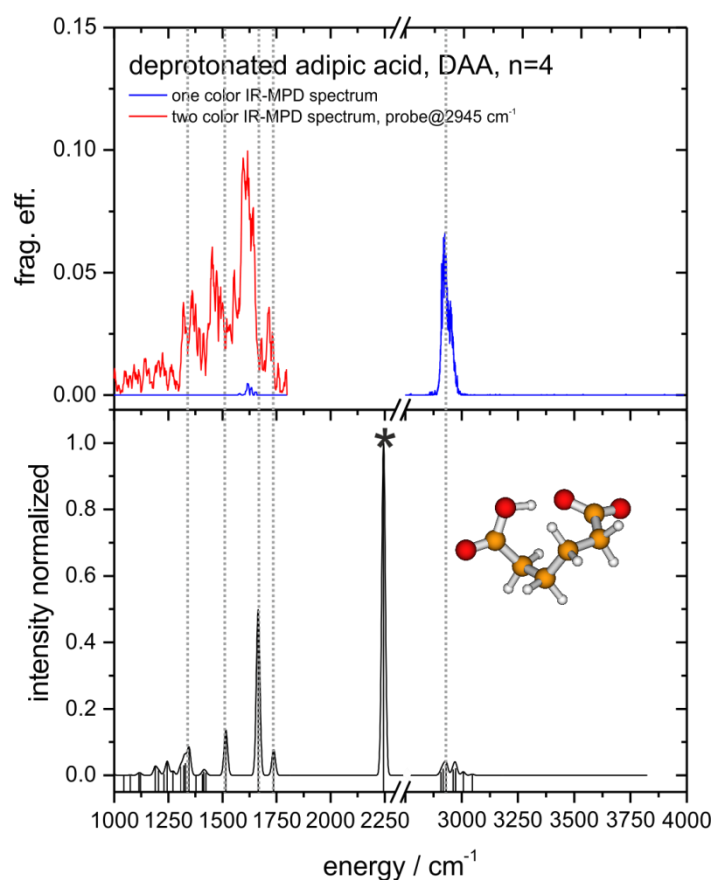


**Figure 18:** The IR-MPD spectrum of DGA ( $n = 4$ ) (top), the inset shows the blow-up of the CH stretching region. The theoretical spectrum is calculated on MP2 level of theory with a double  $\zeta$  basis and scaled by 0.956.

The same considerations are valid in the DAA ( $n = 4$ ) case (cf. Fig. 18). In the experimental spectra no free OH stretching band occurs which leads to the conclusion that the calculated cyclic minimum structure is correct. The intramolecular hydrogen bond exists. The bridging proton vibrations shift to the red and the resulting bands are broadened. The unambiguous assignment of these bands in the experimental spectra not possible. Harmonic calculations are doomed to fail. The predicted red

## 2. IR-MPD spectroscopy of deprotonated and protonated dicarboxylic acids

---

shift is probably stronger than expected and the proton motion may couple to other vibrational modes preventing the normal mode approximation. In the fingerprint region only one broad band is observed. The spectrum gains information using the second IR laser. Four broad absorptions arise. The modes around  $1300\text{ cm}^{-1}$  relate to  $\text{CH}_2$  bending vibrations. CO stretching vibrations assign to the two bands at  $1600\text{ cm}^{-1}$  and  $1745\text{ cm}^{-1}$ . All bands are broad and a superposition of several isomers is likely.

Deprotonated dicarboxylic acids have a much lesser fragmentation efficiency than protonated species. The two color effect is more visible for deprotonated species and minor in protonated species with an exception, protonated malonic acid. Different fragmentation mechanisms are responsible for this effect (cf. chapter 2.5.4). PDAs fragment via water loss and DDAs lose carbon dioxide. While the fragmentation of PDAs needs a rearrangement of the molecular structure, DDAs fragment directly. Therefore the second IR laser pulse is more effective to fragment the DDAs. The anhydride formation in PMA is not possible and this acid fragments directly.

The experimental spectra of the higher protonated species are not as broad as the deprotonated spectra. The interpretation of the deprotonated spectra is more complicated. The most important spectral feature which all investigated deprotonated species have in common is the missing free OH stretching motion which is a strong indication of a proton bridged cyclic structure.

## 2. IR-MPD spectroscopy of deprotonated and protonated dicarboxylic acids

---

### 2.10. Comparison of experiments performed with the FEL and the OPO set up

Experiments were performed with different set ups under different experimental conditions. The time for experiments at the CLIO set up is limited. Thus the experiments with the FEL were performed over various beam times. The extent of experiments done with the FEL set up is not possible in one beam time. It is necessary to accumulate the experimental data. This is one disadvantage of the FEL set up. On the other side there is no table top laser system that has so much laser power as a FEL. Since IR-MPD spectroscopy is an action spectroscopy in the need of laser power to yield fragmentation the high laser power of a FEL is a great advantage.

The experimental set up with an OPO system is accessible the whole time. The available laser power is much less than with a FEL. The question is: does this laser energy suffice to fragment our analytes and do we obtain comparable results? Therefore we compare the experiments performed by the experimental set up with the FEL in Paris (CLIO) with the experiments performed with the OPO set up in Kaiserslautern.

The PDAs are easy to fragment (cf. chapter 2.5.4). Both experiments yield the same fragmentation products. The dehydrogenation of protonated dicarboxylic acids is dominant and all other fragmentation products are minor. The smallest studied dicarboxylic acid is malonic acid. The experimental spectra of PMA ( $n = 1$ ) exhibit the narrowest bands in the studied row of dicarboxylic acids. The fragmentation efficiencies in the PMA spectra are low in both experiments (see Table 6). Two weak bands arise in the FEL experiment at 1565 and 1265  $\text{cm}^{-1}$ . These bands are absent in the one color IR-MPD spectrum and appear only in the two color IR-MPD spectrum. The laser power of the OPO does not suffice to fragment our analyte molecule. The second IR laser is needed to fragment.

The sharpest bands in IR-MPD spectra possesses PMA ( $n = 1$ ). The longer the  $\text{CH}_2$  chain the more conformers contribute to the room temperature spectrum the broader the bands arise in the spectrum. This corresponds to all experimental spectra (cf. Fig. 19). The IR-MPD spectra of PAA ( $n = 4$ ) are the broadest. Single bands are no longer specifiable. To overcome this problem it is necessary to study these species in a cold ion trap. This experiment is in preparation in our laboratory in Kaiserslautern. Here the isolated ionic species will be cooled in a cold hexapole for precooling and after that the ions are transferred in the cooled ICR cell. This cell is cool able up to 10 K and already in use. The IR-MPD spectra of both set ups appear to be in good agreement. The differences in the fragmentation efficiencies result from the different laser energies.

## 2. IR-MPD spectroscopy of deprotonated and protonated dicarboxylic acids

**Table 6:** fragmentation efficiencies of PMA in different experiments

energy (OPO, one color)  / $\text{cm}^{-1}$	frag. eff. (one color)	energy (OPO, two color)  / $\text{cm}^{-1}$	frag. eff. two color	energy (FEL)  / $\text{cm}^{-1}$	frag. eff. (FEL)
1695	0.03	1700	0.07	1715	0.07
		1565	0.006	1565	0.02
1495	0.04	1500	0.11	1490	0.06
1370	0.006	1370	0.04	1365	0.05
		1265	0.006	1220	0.4
1180	0.008	1175	0.03	1165	0.2

The comparison between the two experiments facilitates the different presentation (cf. Fig. 20). Here columns represent the IR-MPD bands. The width of the columns corresponds to the average FWHM in the IR-MPD spectra. It is remarkable that the band position is reproducible in all experiments. Different set ups lead to the same result. The differences in laser energy explain the differences in the fragmentation efficiencies. Thus both experimental set ups provides comparable IR-MPD spectra. Since the FEL beam time is limited the same IR-MPD spectra are obtained by the Kaiserslautern table top set up. The FEL has more energy in the frequency range below  $1000 \text{ cm}^{-1}$  than an OPO laser. For measurements below  $1000 \text{ cm}^{-1}$  a FEL is needed for fragmentation.

## 2. IR-MPD spectroscopy of deprotonated and protonated dicarboxylic acids

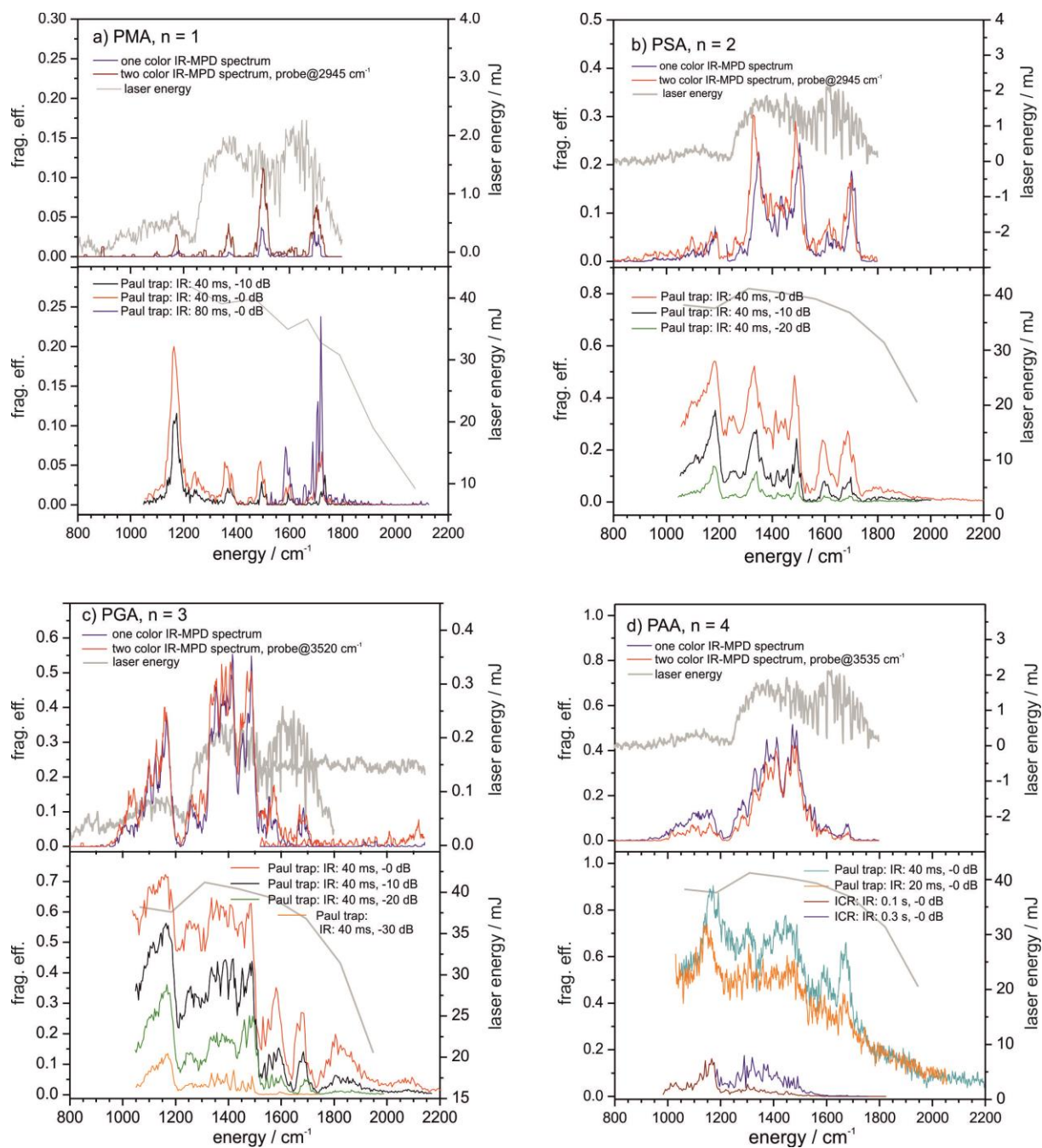


**Figure 19:** comparison of OPO (top) and FEL (bottom) IR-MPD spectra of PDAs, a) PMA, b) PSA, c) PGA and d) PAA. Laser energy curves are depicted in grey.



## 2. IR-MPD spectroscopy of deprotonated and protonated dicarboxylic acids

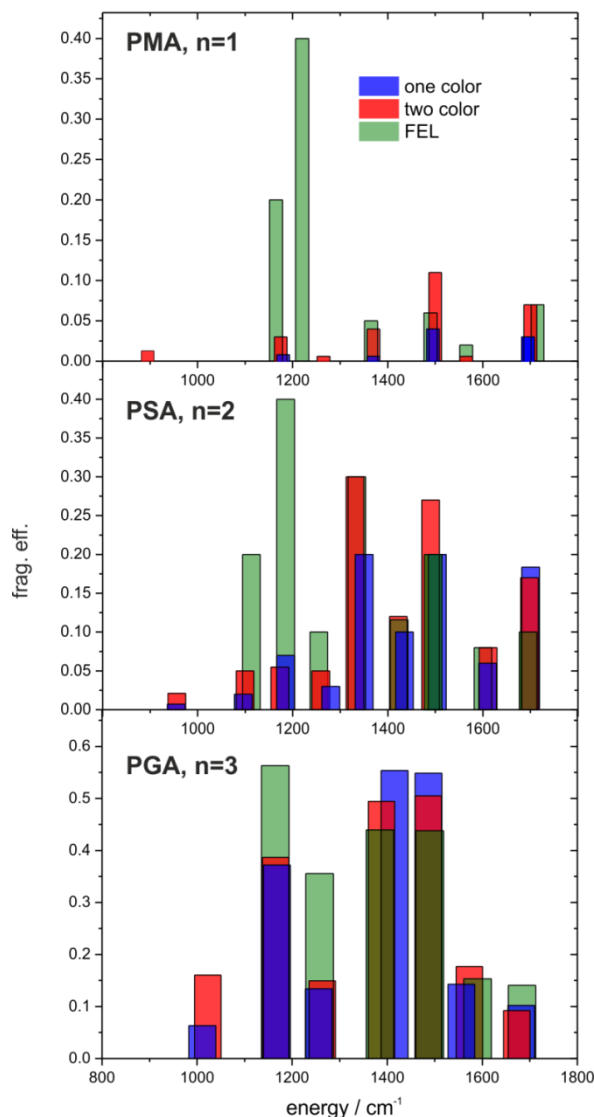


**Figure 20:** Comparison of all experiments of small dicarboxylic acids. The width of the columns indicates the average half width full maximum of the observed bands. For higher dicarboxylic acids the bands are too broad. Blue columns represent the one color IR-MPD experiment, the red ones the two color IR-MPD experiment and green columns represent the FEL experiments.

In the case of DDAs the results are similar. The IR-MPD spectra are broader than the PDA spectra. DDAs lose carbon dioxide as main fragmentation product. In case of DMA ( $n = 1$ ) this fragmentation process leads to products below the detection limit of the Paul trap. An IR-MPD spectrum of DMA is not possible with the Paul trap in Kaiserslautern. Here the FT-ICR mass spectrometer is a valid substitution of the Paul trap.

## 2. IR-MPD spectroscopy of deprotonated and protonated dicarboxylic acids

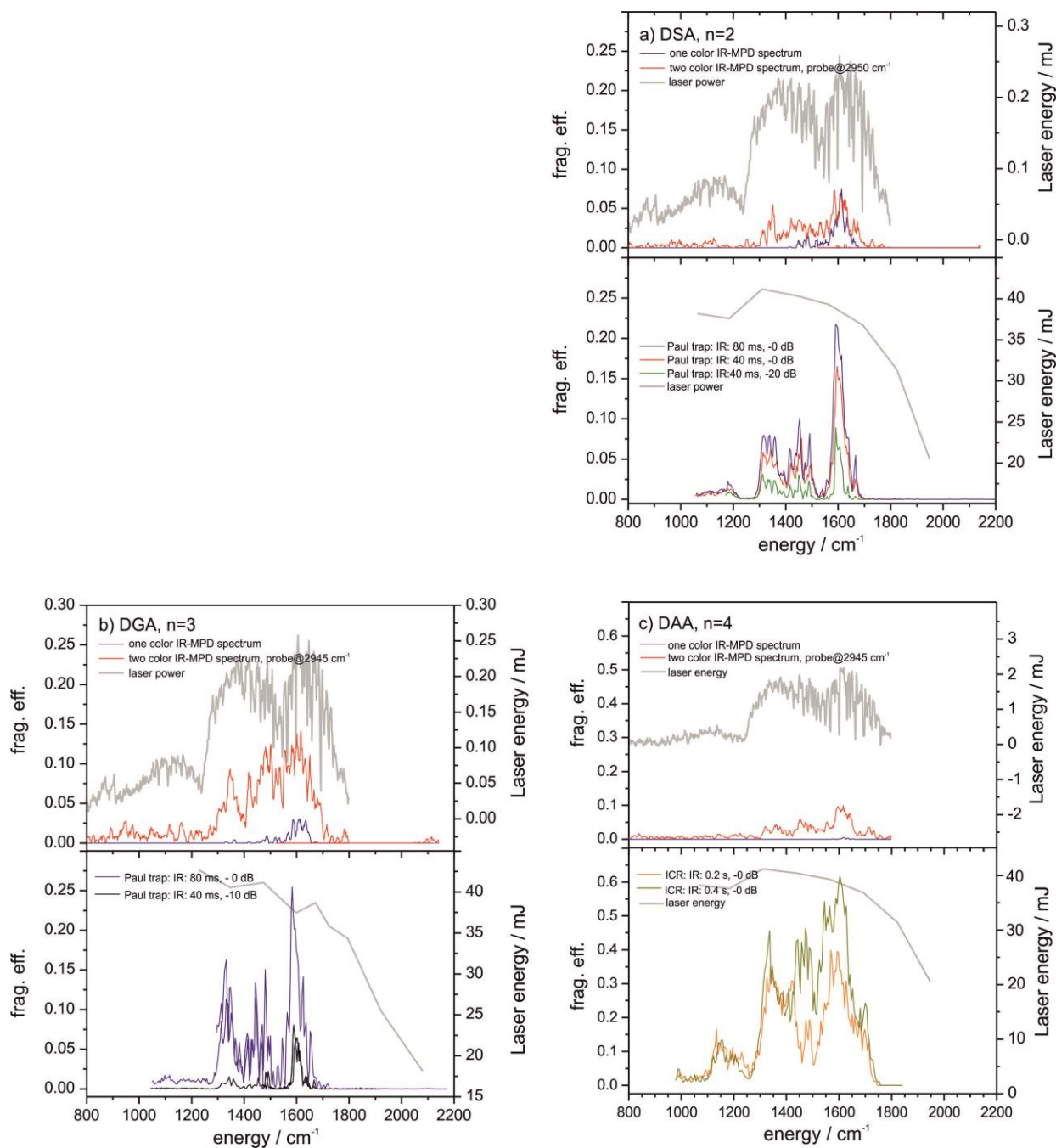


**Figure 21:** Comparison of OPO (top) and FEL (bottom) IR-MPD spectra of DDAs, a) DSA, b) DGA and c) DAA. Laser energy curves are depicted in grey.

## 2. IR-MPD spectroscopy of deprotonated and protonated dicarboxylic acids

---

### 2.11. IR-peak shift of deuterated dicarboxylic acids

We recorded IR-MPD spectra of deuterated protonated adipic acid (PAA,  $n = 4$ ). PAA has three exchangeable protons. To obtain the deuterated species with three deuterons the solid adipic acid is solved in deuterated solvents and protonated with deuterated acetic acid. In the mass spectrometer (Paul trap) the deuterated species cannot be isolated. This is not possible since in the trap helium is used as collision gas. There is still minor humidity in this gas and this is sufficient to perform proton reexchange while the deuterated species is isolated and stored (200 ms) to interact with the OPO laser beam (cf. Fig. 22).

We expect a shift of the vibrational frequency of all bands that arise from deuterated species. When all protons are exchanged this technique is able to identify the vibrational frequencies involving the bridging deuteron. The shift of the vibrational frequency is proportional to the square root of the quotient of force constant  $k$  and reduced mass  $\mu$ :

$$\tilde{\nu} = \sqrt{\frac{k}{\mu}} \quad (6)$$

This would mean a shift for the OH stretching vibration with a factor of 0.7276 when neglecting the rest of the molecule. According to the above calculation, the OH stretching vibration which arise at  $3525 \text{ cm}^{-1}$  should change deuterated to  $2565 \text{ cm}^{-1}$ . The experimentally found value is a bit higher (around  $2600 \text{ cm}^{-1}$ ). Unfortunately only the fragmentation efficiency of the OH region is high enough to make a useful analysis of the peaks. Thus the more interesting frequency shifts of bands involving the motion of the hydrogen bridge are not identified.

## 2. IR-MPD spectroscopy of deprotonated and protonated dicarboxylic acids

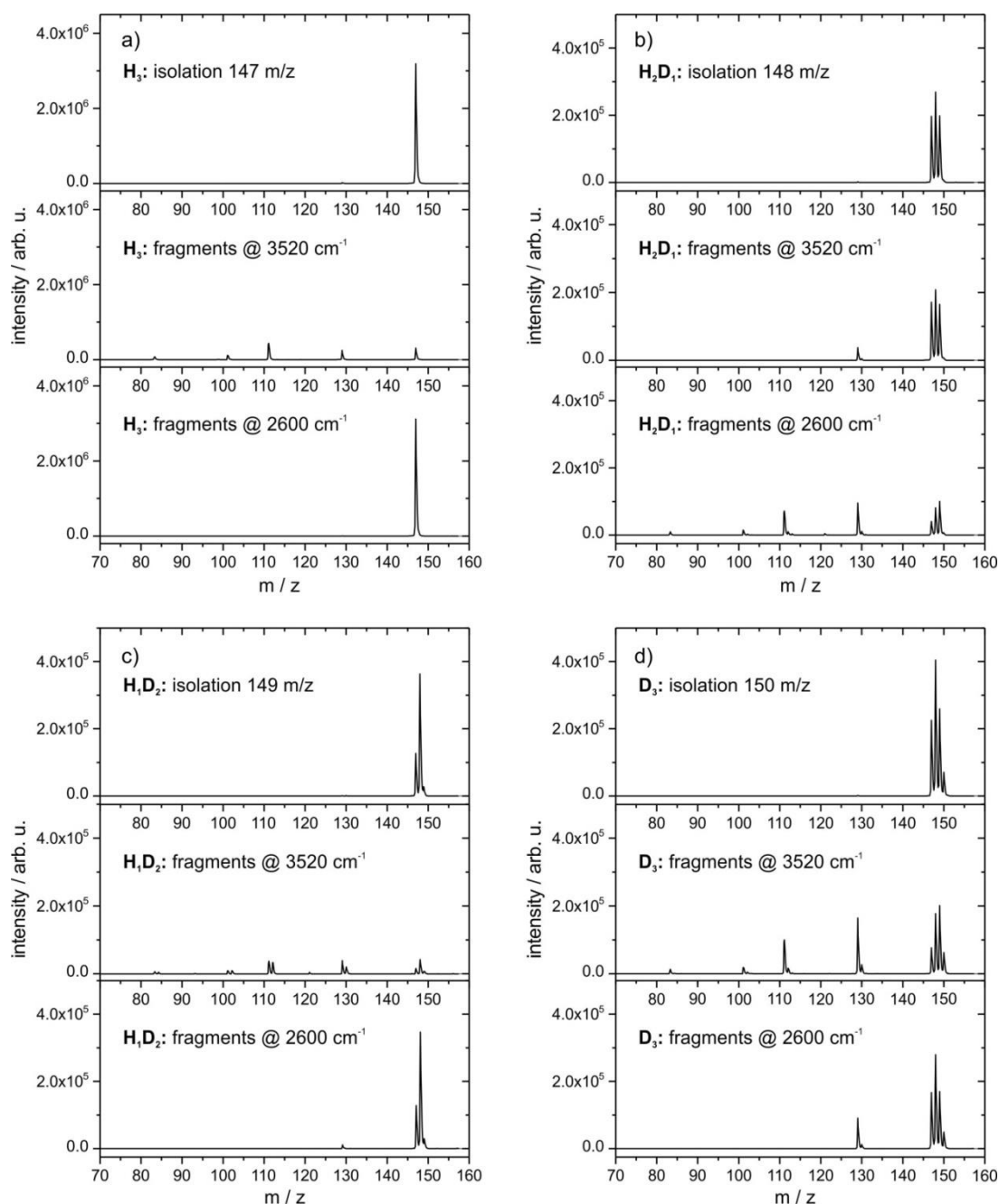


**Figure 22:** a) Isolation of  $H_3$  PAA (top), mass spectrum of the fragment peaks when the OPO laser is set to the OH stretching frequency (middle) and the mass spectrum when the OPO laser is set to the OD stretching frequency (bottom); b) Isolation of the  $H_2D_1$  PAA (top), mass spectrum of the fragment peaks when the OPO laser is set to the OH stretching frequency (middle) and the mass spectrum when the OPO laser is set to the OD stretching frequency (bottom). c) Isolation of the  $H_1D_2$  PAA (top), mass spectrum of the fragment peaks when the OPO laser is set to the OH stretching frequency (middle) and the mass spectrum when the OPO laser is set to the OD stretching frequency (bottom). d) Isolation of the  $D_3$  PAA (top), mass spectrum of the fragment peaks when the OPO laser is set to the OH stretching frequency (middle) and the mass spectrum when the OPO laser is set to the OD stretching frequency (bottom).

## 2. IR-MPD spectroscopy of deprotonated and protonated dicarboxylic acids

Further analysis of the mass spectra results in the list of all possible species (cf. Table 7). One possible fragmentation path is the loss of deuterated water (HDO and D<sub>2</sub>O). There are two possible ionic fragments. First the possible protonated anhydride, **frag-H** ( $[(\text{CH}_2)_4\text{C}_2\text{O}_3\text{H}]^+$ ). Second, a deuterium remains in the ionic fragment, **frag-D** ( $[(\text{CH}_2)_4\text{C}_2\text{O}_3\text{D}]^+$ ). The analysis of these fragments leads to the observed IR-MPD spectra.

**Table 7:** All parent and fragment ions of deuterated PAA

isolated species	fragment H	neutral fragment	fragment D	neutral fragment
<b>H<sub>3</sub></b>	<b>Frag-H</b>			
$[(\text{CH}_2)_4\text{C}_2\text{O}_4\text{H}_3]^+$	$[(\text{CH}_2)_4\text{C}_2\text{O}_3\text{H}]^+$	-H <sub>2</sub> O	—	—
147 m/z	129 m/z			
<b>H<sub>2</sub>D<sub>1</sub></b>	<b>Frag-H</b>		<b>Frag-D</b>	
$[(\text{CH}_2)_4\text{C}_2\text{O}_4\text{H}_2\text{D}_1]^+$	$[(\text{CH}_2)_4\text{C}_2\text{O}_3\text{H}]^+$	-HDO	$[(\text{CH}_2)_4\text{C}_2\text{O}_3\text{D}]^+$	-H <sub>2</sub> O
148 m/z	129 m/z		130 m/z	
<b>H<sub>1</sub>D<sub>2</sub></b>	<b>Frag-H</b>		<b>Frag-D</b>	
$[(\text{CH}_2)_4\text{C}_2\text{O}_4\text{H}_1\text{D}_2]^+$	$[(\text{CH}_2)_4\text{C}_2\text{O}_3\text{H}]^+$ ;	-D <sub>2</sub> O	$[(\text{CH}_2)_4\text{C}_2\text{O}_3\text{D}]^+$	-HDO
149 m/z	129 m/z		130 m/z	
<b>D<sub>3</sub></b>			<b>Frag-D</b>	
$[(\text{CH}_2)_4\text{C}_2\text{O}_4\text{H}_3]^+$	—	—	$[(\text{CH}_2)_4\text{C}_2\text{O}_3\text{D}]^+$	-D <sub>2</sub> O
150 m/z			130 m/z	

The isolation of the deuterated peaks does not result in a single mass peak. Due to reaction with residual water in the Paul trap all four possible deuterated species occur in the mass spectra (cf. Fig. 22). The upper graph depicts the situation with no OPO laser beam. The mass spectra in the middle comprise the situation when the OPO laser is set on the OH stretching vibration. Here we observe fragmentation due to dehydrogenation. When the

## 2. IR-MPD spectroscopy of deprotonated and protonated dicarboxylic acids

OPO laser is set on the OD stretching frequency only minor fragmentation products arise in the mass spectra. When a deuterated species is isolated more than one mass peak occurs in the mass spectra. The IR-MPD technique allows for further analysis. It is possible to calculate the contribution of a single fragment to a IR-MPD spectrum. The contribution of the **frag-H** trace (blue) is much stronger than the **frag-D** trace. The deuterated species are minor in the mass spectra thus their contribution to the IR-MPD spectra is minor as well (cf. Fig. 23).

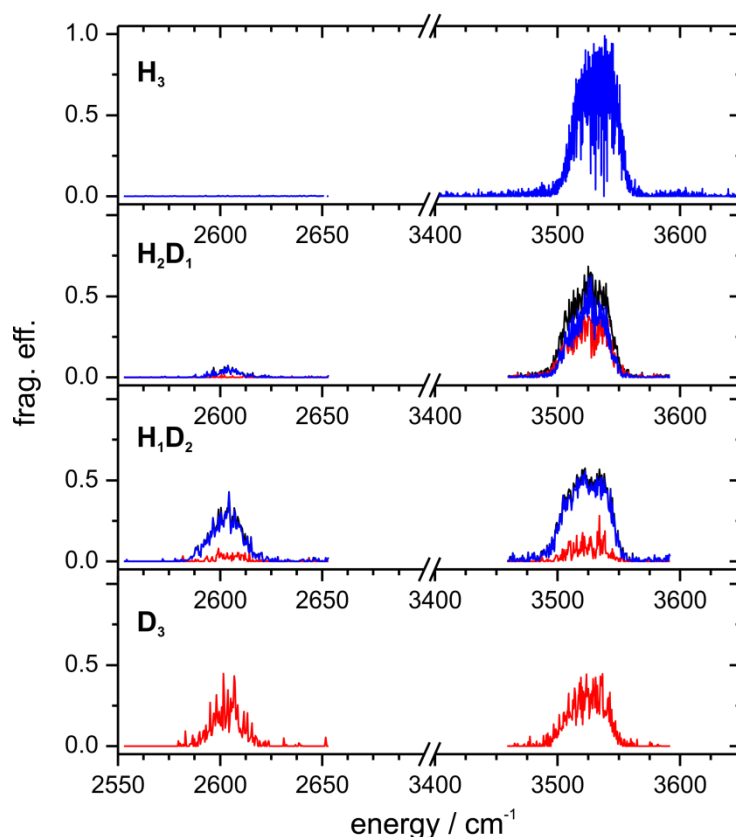


**Figure 23:** IR-MPD spectrum of PAA in different degrees of deuteration:  $\text{H}_3$  only the Frag-H trace (blue) accounts to the spectrum;  $\text{H}_1\text{D}_2$  and  $\text{H}_2\text{D}_1$  the Frag-H (blue) and Frag-D (red) trace result in a combined spectra (black);  $\text{D}_3$  fragmentation leads to ionic fragments containing a deuteron.

The free OH stretching frequency arises at  $3525\text{ cm}^{-1}$ . This band appears in all four IR-MPD spectra (cf. Fig. 23) even in the  $\text{D}_3$  complex due to the reaction with residual water. The higher the degree of deuteration the stronger arises the band at  $2600\text{ cm}^{-1}$ . In the spectra of  $\text{H}_1\text{D}_2$  the fragmentation leads to more **frag-H** than **frag-D**. The fragmentation results in more  $\text{D}_2\text{O}$  than HDO as neutral fragments due to statistical reasons. Remarkably this is not true for the  $\text{H}_2\text{D}_1$  species. Here the data shows that nearly the same amount of **frag-H** and **frag-D** gives rise to the IR-MPD spectrum. To form **frag-H** the parent ion eliminates HDO and to form **frag-D** the parent ion eliminates  $\text{H}_2\text{O}$ . The elimination of  $\text{H}_2\text{O}$  is statistically favored. To explain this phenomenon we have to consider the mass spectra (cf. Fig.

## 2. IR-MPD spectroscopy of deprotonated and protonated dicarboxylic acids

22). The isolation of the parent ion is incomplete. The isolation of  $\text{H}_1\text{D}_2$  results also in a stronger peak of  $\text{H}_2\text{D}_1$ . Both species lead to the same fragments and the observed isotope effect emerges from the incomplete isolation of the parent ion.

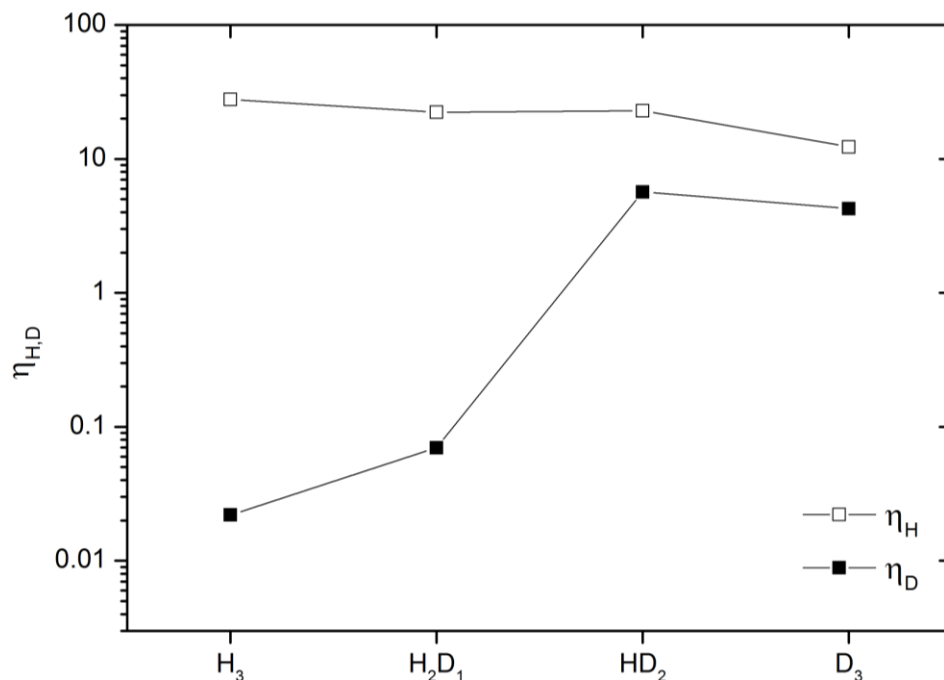


**Figure 24:** Integral values of the IR-MPD efficiency of the OH stretching vibrations (open symbols) and OD stretching vibrations (filled symbols).

The calculation of the integral values of the OH and OD stretching band does not result in any significant behavior. The IR-MPD intensity of the OH peak between  $3470 - 3590 \text{ cm}^{-1}$  shows a nearly linear decay while the IR-MPD intensity of the OD peak between  $2580 - 26030 \text{ cm}^{-1}$  rises with the degree of deuteration. The value of the  $\text{D}_3$  parent deviates due to the rehydration in the Paul trap and the following problem to isolate this species.

## 2. IR-MPD spectroscopy of deprotonated and protonated dicarboxylic acids

### 2.12. Estimation of the photon count required to fragment PAA

R-MPD spectroscopy is a multi-photon process. To fragment a molecule the absorption of many photons is required. The investigated ion absorb IR photons which are in resonance with a vibrational mode. Internal vibrational redistribution (IVR) distributes the vibrational energy and the next photon is absorbed in the same mode. This process repeats until the ion fragments<sup>3</sup>.

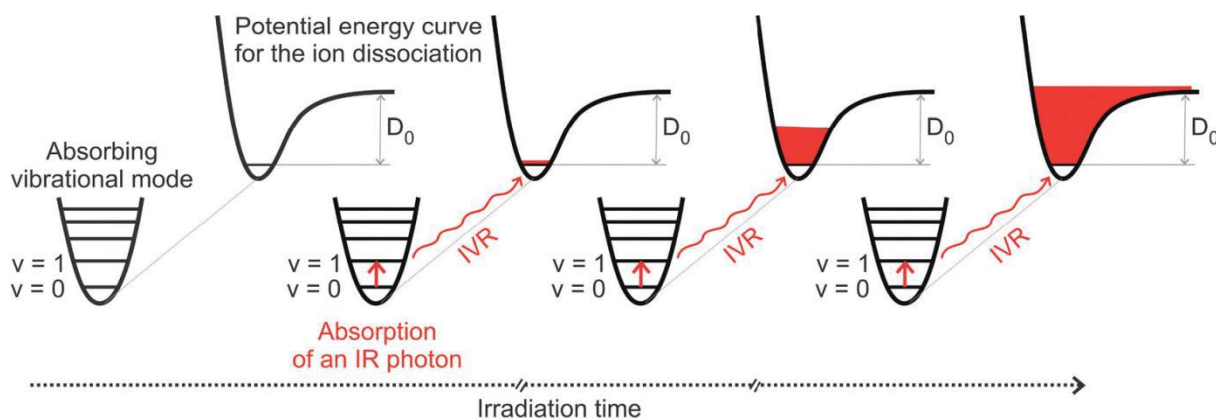


**Figure 25:** Sequential excitation and relaxation cycles during infrared multi-photon dissociation spectroscopy<sup>4</sup>.

The estimation of the photon count required for fragmentation results from the following considerations.<sup>5</sup> The fragmentation efficiency is proportional to the energy per laser pulse to the power of number of photons  $n$ .

$$\text{frag. eff.} \sim \left(\frac{\text{energy}}{\text{pulse}}\right)^n \quad (7)$$

Thus the photon count is proportional to

$$\log(\text{frag. eff.}) \sim n \cdot \log\left(\frac{\text{energy}}{\text{pulse}}\right) \quad (8)$$

Thus, plotting  $\log(\text{frag. eff.})$  in dependence of  $\log\left(\frac{\text{energy}}{\text{pulse}}\right)$  we obtain  $n$  by a linear fit (cf. Fig. 25).

The experimental data points are average values. The linear fit provides 0.5 as proportionality constant.



## 2. IR-MPD spectroscopy of deprotonated and protonated dicarboxylic acids

---

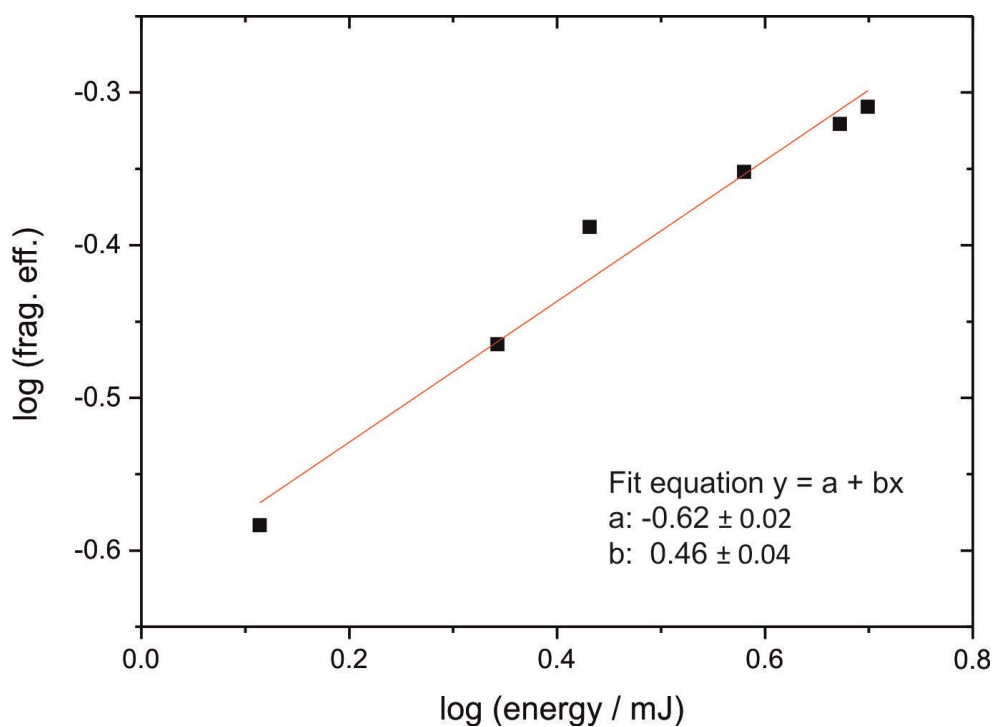


**Figure 26:** The slope of the linear fit (red line) gives an estimate of the needed number of photons for fragmentation.

Further experiments with more than one laser shot exhibit that we reach saturation with at least 4 laser shots (with laser energy of 5.0 mJ). In all experiments saturation is reached with 10 laser shots. Saturation correlates with a fragmentation efficiency of 0.9 which means that 90 % of the ion fragment. This indicates a very good overlap of the laser beam with the ion cloud.

## 2. IR-MPD spectroscopy of deprotonated and protonated dicarboxylic acids

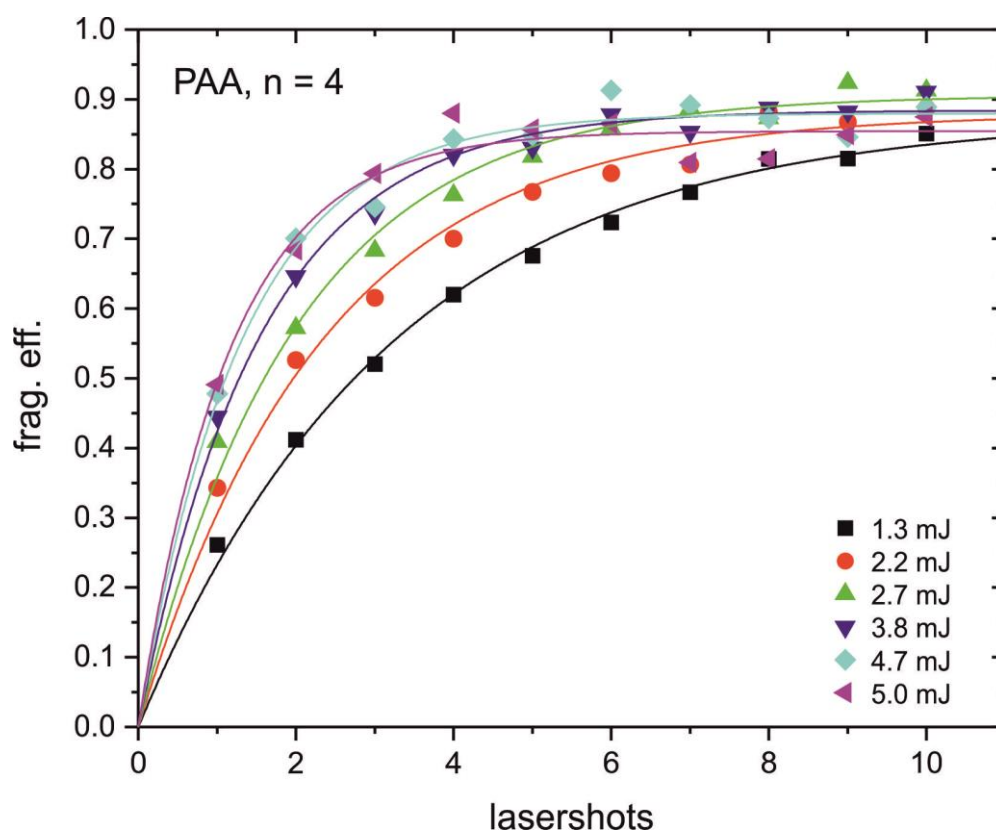


**Figure 27:** the fragmentation efficiency in dependence of laser energy and of the number of laser shots.

Three laser shots with 1.3 mJ per pulse provide 3.9 mJ and the fragmentation efficiency reaches 0.5. This energy redistributes via IVR in the molecular ion. One laser shot with 3.8 mJ leads to a slightly lower fragmentation efficiency (0.45). Thus the energy added in the system is redistributed and the thermalisation of the ions due to collisions with the buffer gas is not sufficient to cool the ions down.

## 2. IR-MPD spectroscopy of deprotonated and protonated dicarboxylic acids

### 2.13. Aromatic dicarboxylic acids

Our studies of aliphatic dicarboxylic acids provide information about the nature of intramolecular hydrogen bonding. Especially the molecular dynamic calculations show that the real situation is more complex than expected<sup>2</sup>. The flexible backbone leads to many conformers contributing to the room temperature spectra. To circumvent these problems, we investigated ionic, aromatic dicarboxylic acids. The aromatic ring is planar and rigid. Thus, the backbone is no longer flexible and less isomers contribute to the IR-MPD spectra.

DFT calculations predict that the phthalate anion features a proton bridge between two negatively charged carboxylate moieties while in terephthalate the interaction between the two carboxylic acid groups cannot occur because of the rigid phenyl ring separating them<sup>6</sup>. The IR-MPD spectra of these anions reveal that the calculation of terephthalate is in good agreement with the calculated harmonic frequencies. The phthalate spectrum shows much broader bands and there is no obvious match with the frequencies calculated for the lowest energy structure featuring an intramolecular hydrogen bond<sup>6</sup>.

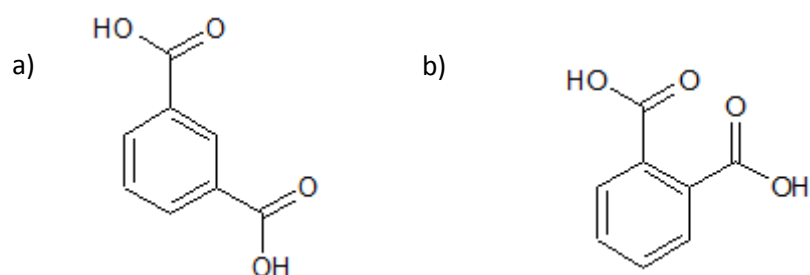


**Figure 28:** structural formular of a) phthalic acid and b) isophthalic acid

We measured the IR-MPD spectra of protonated and deprotonated phthalic and isophthalic acid. To elucidate the structures we simulated the harmonic IR spectra on MP2 level of theory with an aug-cc-pVDZ basis. The protonated and deprotonated structures of phthalic acid can form an intramolecular hydrogen bond. The formation of an intramolecular hydrogen bond is impossible in isophthalic acid. The aromatic ring is rigid and prevents that many conformers contribute to the room temperature spectra.

## 2. IR-MPD spectroscopy of deprotonated and protonated dicarboxylic acids

### 2.13.1. IR-MPD spectra of protonated aromatic dicarboxylic acids

The IR-MPD spectrum of protonated phthalic acid reveals that an intramolecular hydrogen bond exists (cf. Fig. 29). Only one free OH stretching vibration arises at  $3550\text{ cm}^{-1}$ . Very weak CH stretching modes appear at about  $3100\text{ cm}^{-1}$ . The bands in the fingerprint region are comparable to protonated succinic acid (PSA) which provides the similar number of bridging C atoms ( $n = 2$ ). Protonated phthalic acid exhibits extraordinary high fragmentation efficiency. The two color IR-MPD effect leads to a further enhancement of the fragmentation efficiency. The observed fragmentation product is the elimination of water analogue to the spectra of PDAs.

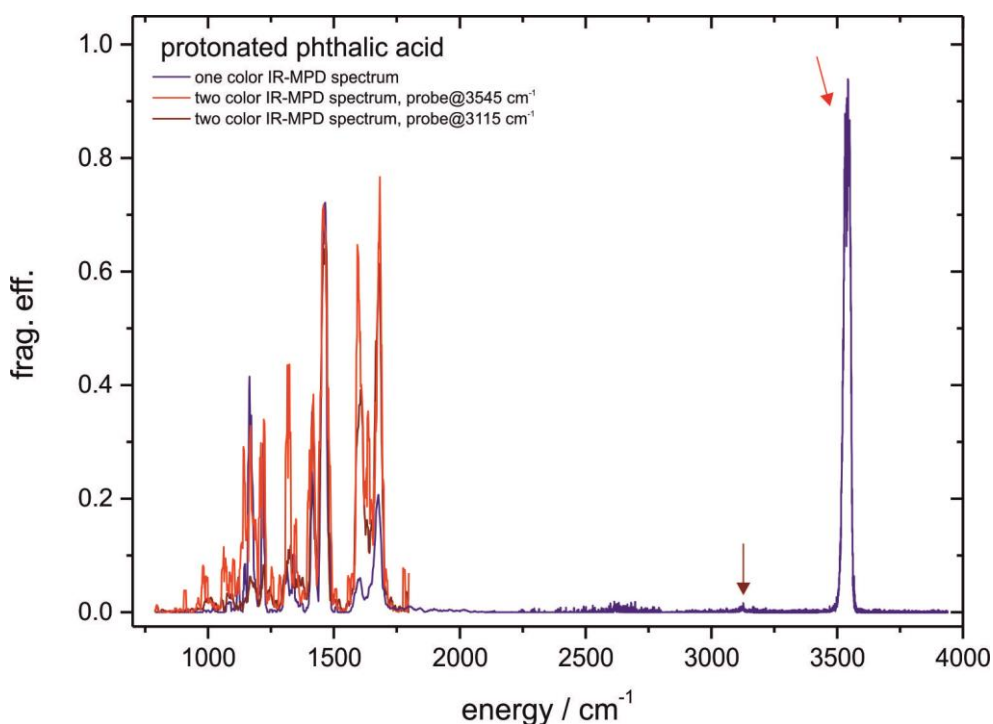


**Figure 29:** One color IR-MPD spectrum (blue) and two color IR-MPD spectrum (red) of protonated phthalic acid.

In contrast to protonated phthalic acid, protonated isophthalic acid provides a different IR-MPD spectrum. The fragmentation efficiency is much lower and all bands are broadened. Between  $3590$  and  $3500\text{ cm}^{-1}$  a broad band appears due to OH stretching vibrations. The width of the band indicates that more than one OH stretching vibration underlies this band. No CH stretching vibrations appear around  $3100\text{ cm}^{-1}$ . In the fingerprint region the fragmentation efficiency drops dramatically. Only one band at  $1550\text{ cm}^{-1}$  arises in the spectrum (cf. Fig. 30). Two color IR-MPD spectroscopy leads to fragmentation independent from the irradiated wavelength and no further bands arise. Anhydride formation is not easily feasible and requires a major change in molecular structure. In contrast to protonated phthalic acid which is easily to fragment and the IR-MPD spectrum exhibits a high

## 2. IR-MPD spectroscopy of deprotonated and protonated dicarboxylic acids

fragmentation efficiency the IR-MPD spectra of protonated isophthalic acid is weak in the fingerprint region.

The spectrum differ dramatically from the analogue aliphatic dicarboxylic acid, PGA ( $n = 3$ ). Thus, the spectrum shows that protonated isophthalic acid differs from other investigated PDAs.

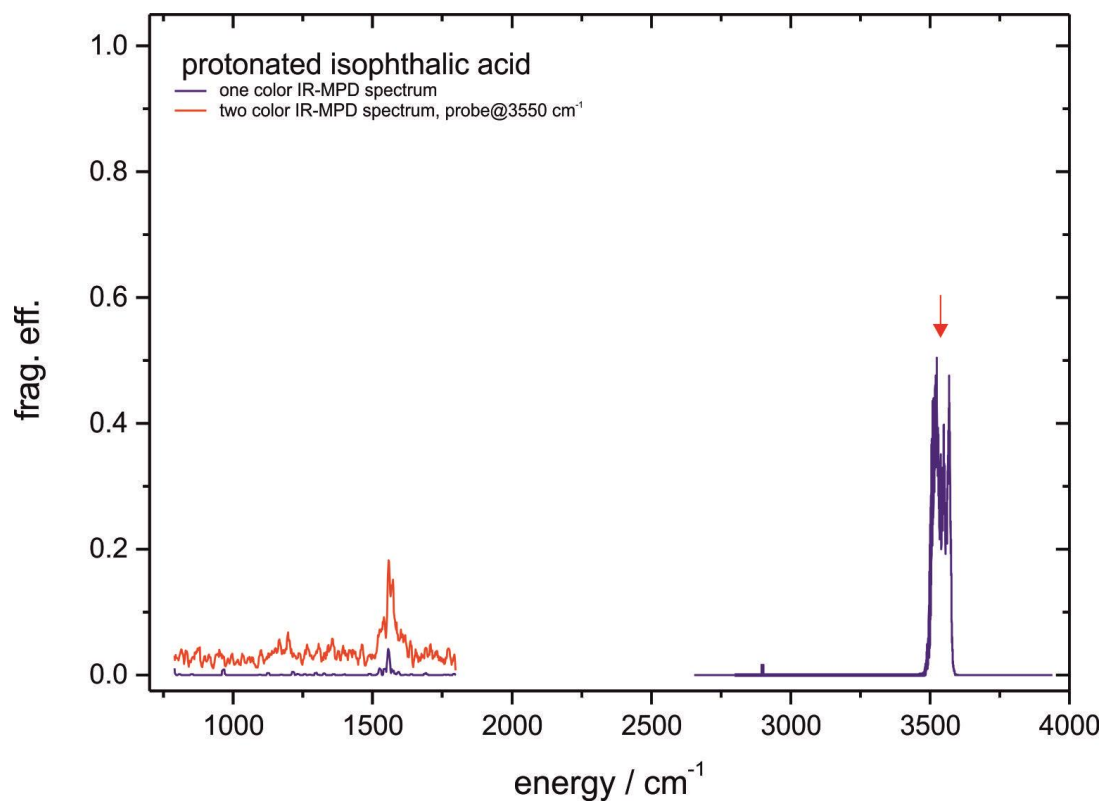


**Figure 30:** One color IR-MPD spectrum (blue) and two color IR-MPD spectrum (red) of protonated isophthalic acid.

## 2. IR-MPD spectroscopy of deprotonated and protonated dicarboxylic acids

### 2.13.2. IR-MPD spectra of deprotonated aromatic dicarboxylic acids

The investigation of deprotonated aromatic dicarboxylic acids reveals a similar picture. The main fragmentation product is carbon dioxide, respectively. The IR-MPD spectrum of phthalate shows no free OH stretching vibration (cf. Fig. 31). Thus an intramolecular hydrogen bond exists. A broad and surprisingly strong band arises at  $3050\text{ cm}^{-1}$  in the region of CH stretching vibrations. In the fingerprint region no band appears higher than  $1700\text{ cm}^{-1}$ . The observed two color effect is strong due to the direct fragmentation mechanism analogue to aliphatic dicarboxylic acids (see chapter 2.5.4). Earlier measurements of phthalate spectra with a FEL show five broad absorptions in the fingerprint region<sup>6</sup>. The resolution of the OPO spectrum is lower and the five bands interfere to three even broader bands.

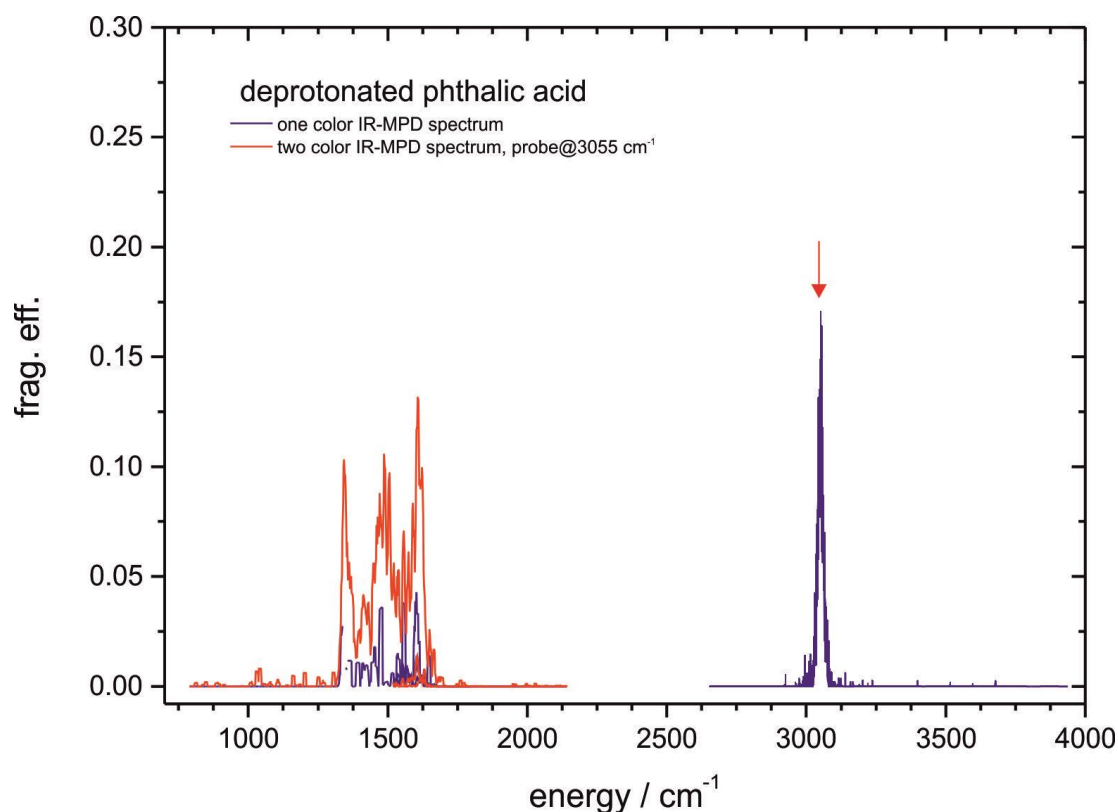


**Figure 31:** One color IR-MPD spectrum (blue) and two color IR-MPD spectrum (red) of deprotonated phthalic acid.

The IR-MPD spectrum of deprotonated isophthalic acid differs from the phthalate spectra (cf. Fig. 31). The band at  $3595\text{ cm}^{-1}$  results from a free OH stretching vibration. Thus, there is no intramolecular hydrogen bond present in isophthalate. In the CH stretching region appears a broad band. The two bands in the fingerprint region are sharp. This distinguishes the spectrum clearly from the phthalate spectrum. It is possible that the broadening of the phthalate spectrum results from the coupling of the proton transfer vibration to the other vibrational modes. The IR-MPD spectrum

## 2. IR-MPD spectroscopy of deprotonated and protonated dicarboxylic acids

differs clearly from the analogue aliphatic dicarboxylic acid (DGA,  $n = 3$ ). The observed two color effect is strong but no further bands arise in the two color IR-MPD spectra. It is possible that irradiation with resonant IR radiation does not lead to fragmentation, so called “dark modes”.

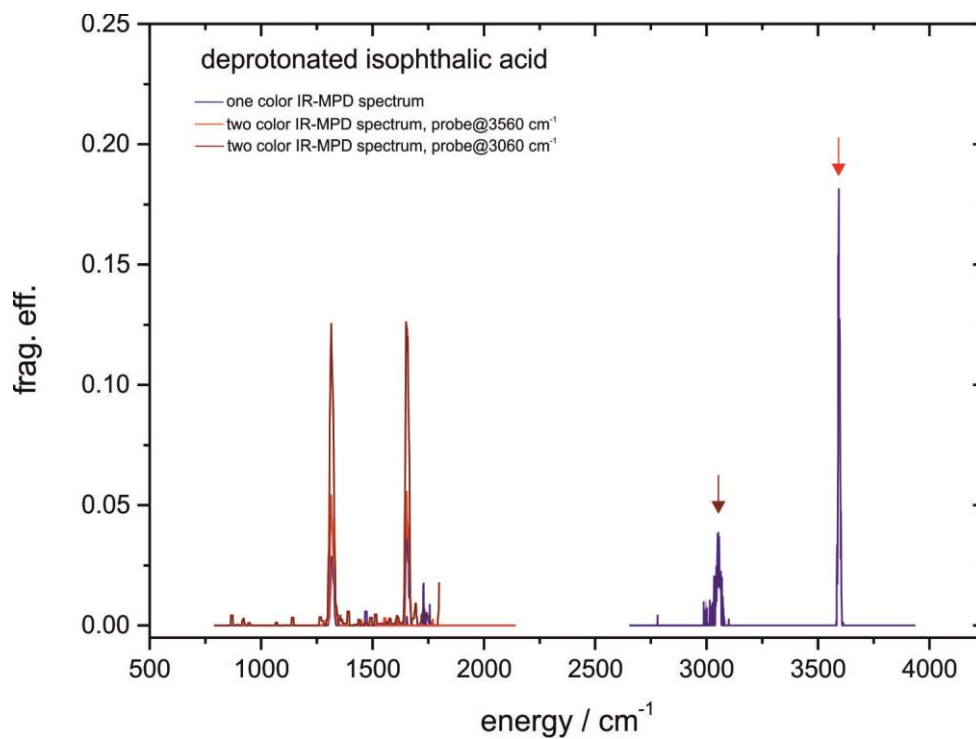


**Figure 32:** One color IR-MPD spectrum (blue) and two color IR-MPD spectrum (red) of deprotonated isophthalic acid.

## 2. IR-MPD spectroscopy of deprotonated and protonated dicarboxylic acids

### 2.13.3. Comparison of IR-MPD spectra with simulated IR spectra

The simulated spectra result from calculations on MP2 level of theory with an aug-cc-pVDZ basis. All simulated spectra are scaled with the factor 0.956.

The calculated structures of protonated phthalic acid are planar. They differ in the position of one proton. As expected it is not favorable to protonate the benzene ring.

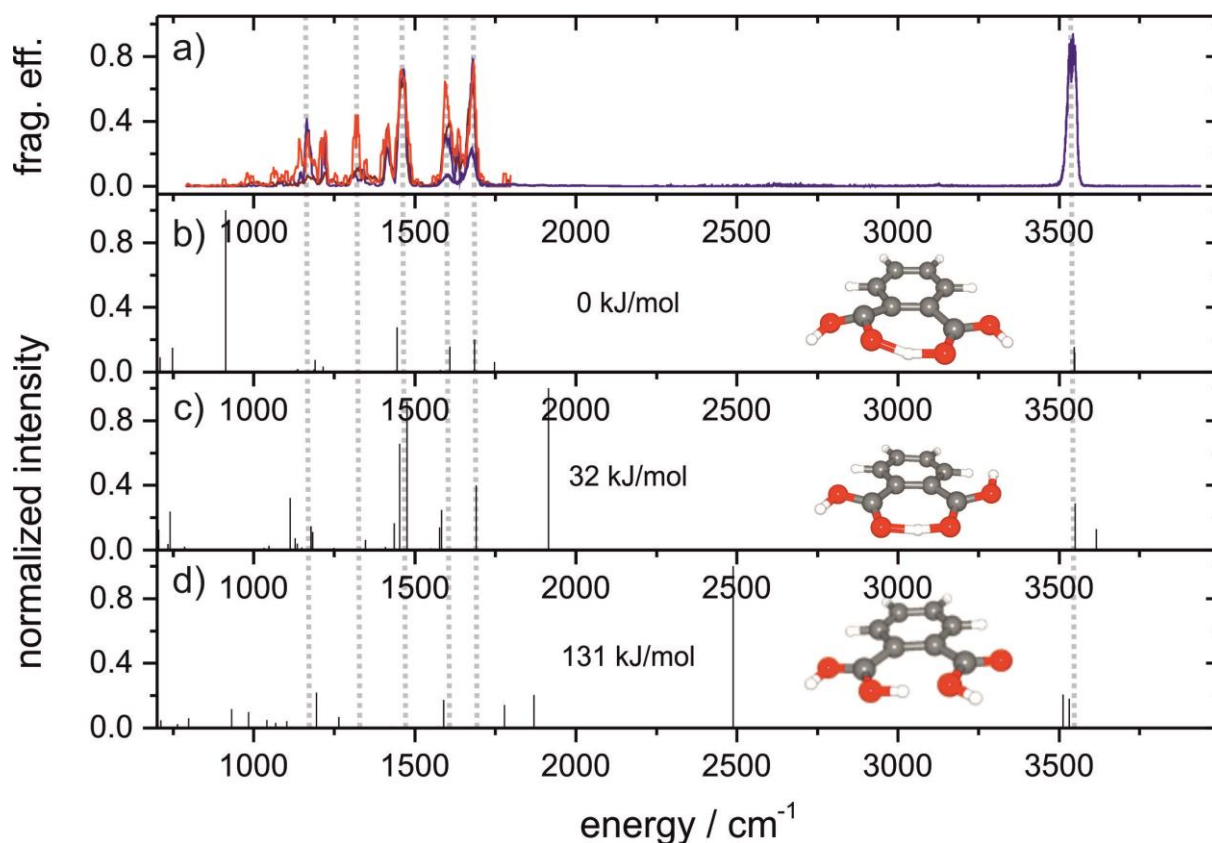


**Figure 33:** a) IR-MD spectrum of protonated phthalic acid; b) simulated IR spectrum of the calculated minimum structure (PhthalStruc1) on MP2 level of theory with a aug-cc-pVDZ basis set; c) simulated IR spectrum of a calculated structure which lies 32 kJ/mol higher in energy (PhthalStruc2); d) simulated IR spectrum of a calculated structure which lies 131 kJ/mol higher in energy (PhthalStruc3). All simulated spectra are scaled with 0.956.

The comparison of the IR-MPD spectrum of protonated phthalic acid with three simulated IR spectra reveals that the calculated minimum structure alone does not describe the experimental spectra (cf. Fig 33). Bands in the fingerprint region are missing in the simulation. Especially the band 1320 cm<sup>-1</sup> has no corresponding peak in the simulated minimum spectrum. The simulated spectra of the energetic higher structures have two OH stretching vibrations. Thus, they do not contribute to the room temperature spectra. The minimum structure possesses the strongest and symmetric intramolecular hydrogen bond. Here the hydrogen bond is clearly Zundel like<sup>7</sup>.



## 2. IR-MPD spectroscopy of deprotonated and protonated dicarboxylic acids

**Table 8:** energies, distances and angles of the calculated structures of protonated phthalic acid

	energy/ $\text{kJmol}^{-1}$	$d_1(\text{O-H})/\text{\AA}$	$d_2(\text{O}\cdots\text{H})/\text{\AA}$	$\alpha(\text{O-H}\cdots\text{O})/\text{\textcircled{C}}$
PhthalStruc 1	0	1.18	1.19	174.5
PhthalStruc 2	32	1.09	1.32	167.4
PhthalStruc 3	132	1.04	1.45	157.2

Figure 35 shows the comparison of the IR-MPD spectrum of protonated isophthalic acid with simulated spectra. In the OH stretching region three free OH stretching vibrations appear in the experimental spectra. These are in good agreement with the calculated minimum structure and the structure (IsoPhthalStruc1) which is only  $5 \text{ kJ mol}^{-1}$  higher in energy (IsoPhthalStruc2). The structure IsoPhthalStruc3 contradicts the experimental spectra. In the fingerprint region the fragmentation efficiency is very weak and only one band is visible. For a reliable assignment a better IR-MPD spectrum is needed. The only band in the fingerprint region at  $1550 \text{ cm}^{-1}$  may result from C-C stretching vibrations of the aromatic ring. Pumping the CO stretching vibration does not lead to fragmentation of the molecule. Protonated isophthalic acid fragments by the loss of water. In contrast to protonated phthalic acid the formation of an anhydride requires a major change in the structure. Thus, higher laser powers are required for fragmentation. The comparison of theory and experiment confirms that in isophthalic acid an intramolecular hydrogen bond is not present.

**Table 9:** energies, distances and angles of the calculated structures of protonated isophthalic acid

	energy/ $\text{kJmol}^{-1}$	$d_1(\text{O-H})/\text{\AA}$	$d_2(\text{O}\cdots\text{H})/\text{\AA}$	$\alpha(\text{O-H}\cdots\text{O})/\text{\textcircled{C}}$
IsoPhthalStruc 1	0	0.98	4.20	147.9
IsoPhthalStruc 2	5	0.98	4.15	147.5
IsoPhthalStruc 3	21	0.98	-	-

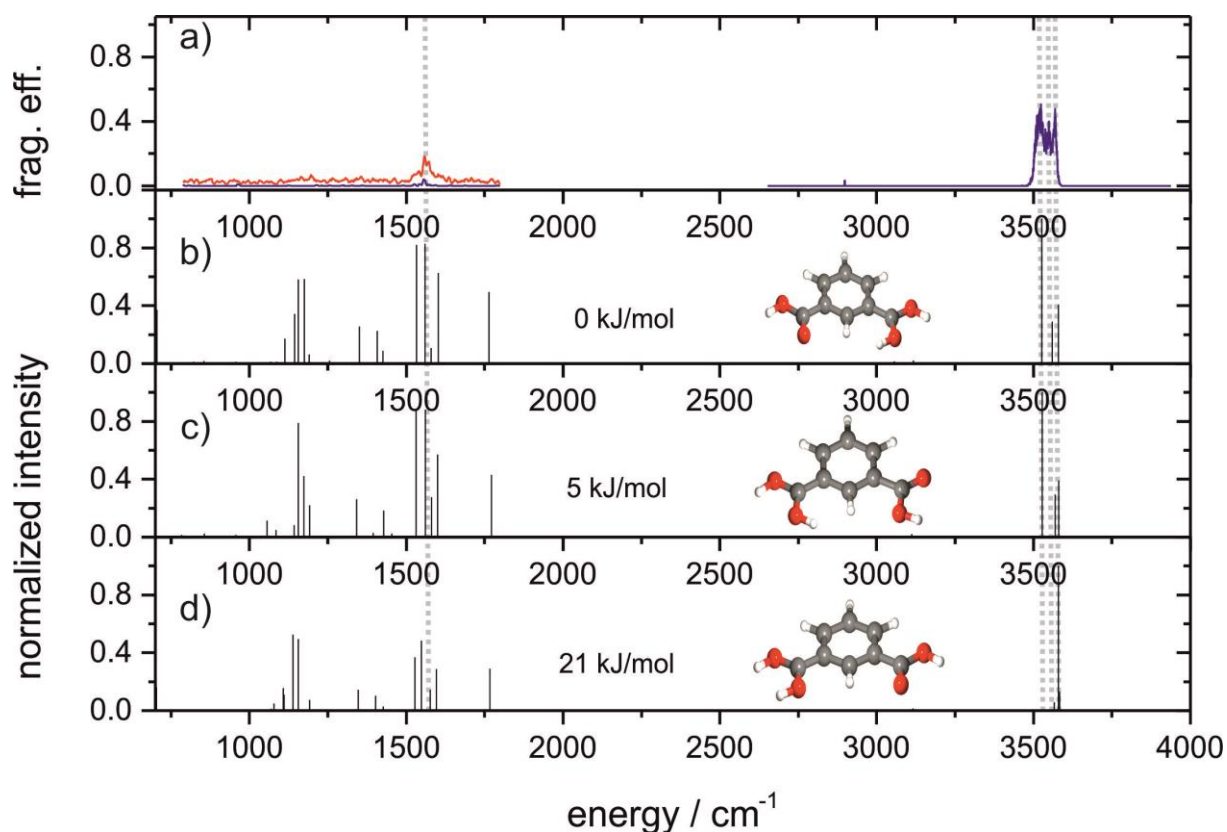


**Figure 35:** a) experimental IR-MD spectrum of protonated isophthalic acid; b) simulated IR spectrum of the calculated minimum structure (IsoPhthalStruc1) on MP2 level of theory with a aug-cc-pVDZ basis set; c) simulated IR spectrum of a calculated structure which lies 5 kJ/mol higher in energy (IsoPhthalStruc2); d) simulated IR spectrum of a calculated structure which lies 21 kJ/mol higher in energy (IsoPhthalStruc3). All simulated spectra are scaled with 0.956.

The calculated structures of protonated isophthalic acid are planar. They differ in the position of the excess proton. As expected it is not favorable to protonate the benzene ring. The proton is most likely located at a carbonyl group. In the most stable structure the proton points in the direction of the second carboxyl group. The three energetic lowest structures can possibly exist in our experiment because of the estimated temperature found in the Paul trap.

Deprotonated aromatic dicarboxylic acids fragment by the loss of carbon dioxide analogue to the aliphatic dicarboxylic acids. The IR-MPD spectrum of deprotonated phthalic shows a broad band at  $3050\text{ cm}^{-1}$  which is assigned to CH stretching vibrations. This assignment is in agreement with both shown calculated structures (cf. Fig. 36). The simulated spectra differ in the fingerprint region from each other. Both structures cannot explain the experimental spectra. The energetically higher structure (deprotphthal2) possesses a band at  $1685\text{ cm}^{-1}$  which does not appear in the experimental

## 2. IR-MPD spectroscopy of deprotonated and protonated dicarboxylic acids

spectra. Earlier DFT calculations cannot describe the experimental spectra as well. The broadening of spectral bands as well as the very poor match with computed harmonic frequencies may result from the shared proton motif probed at room temperature<sup>6</sup>.

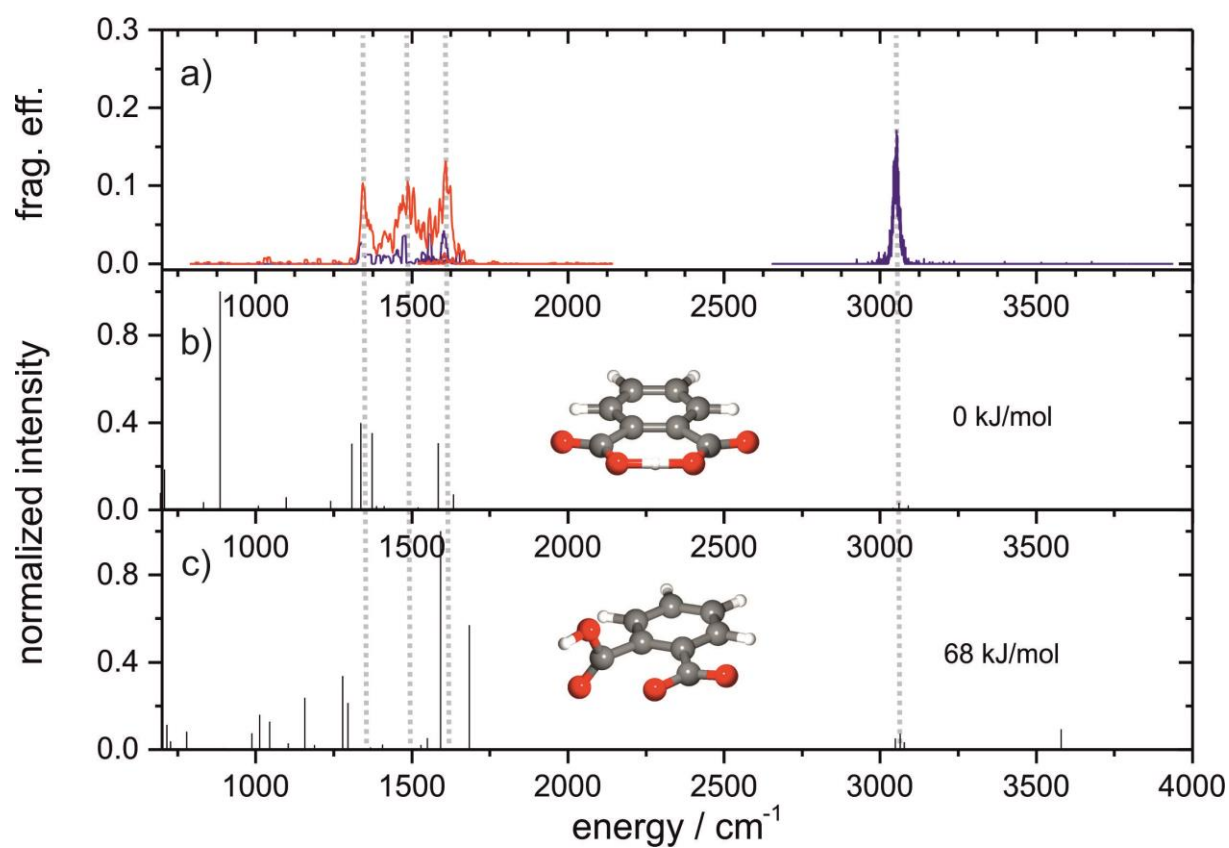


**Figure 36:** a) IR-MD spectrum of deprotonated phthalic acid; b) simulated IR spectrum of the calculated minimum structure (deprotphal1) on MP2 level of theory with aug-cc-pVDZ basis set; c) simulated IR spectrum of a calculated structure which is 68 kJ/mol higher in energy (deprotphal2). All simulated spectra are scaled with 0.956.

## 2. IR-MPD spectroscopy of deprotonated and protonated dicarboxylic acids

**Table 10:** energies, distances and angles of the calculated structures of deprotonated phthalic acid

	energy/ $\text{kJmol}^{-1}$	$d_1(\text{O-H})/\text{\AA}$	$d_2(\text{O}\cdots\text{H})/\text{\AA}$	$\alpha(\text{O-H}\cdots\text{O})/^\circ$
deprotphthal1	0	1.19	1.19	178.68
deprotphthal2	68	0.97	-	-

The IR-MPD spectrum of deprotonated isophthalic acid needs improvement. To achieve higher fragmentation efficiencies more laser power is required or the use of messenger spectroscopy may contribute to exclude “dark modes”. The appearance of a free OH stretching mode proves that no intramolecular hydrogen bond exists.

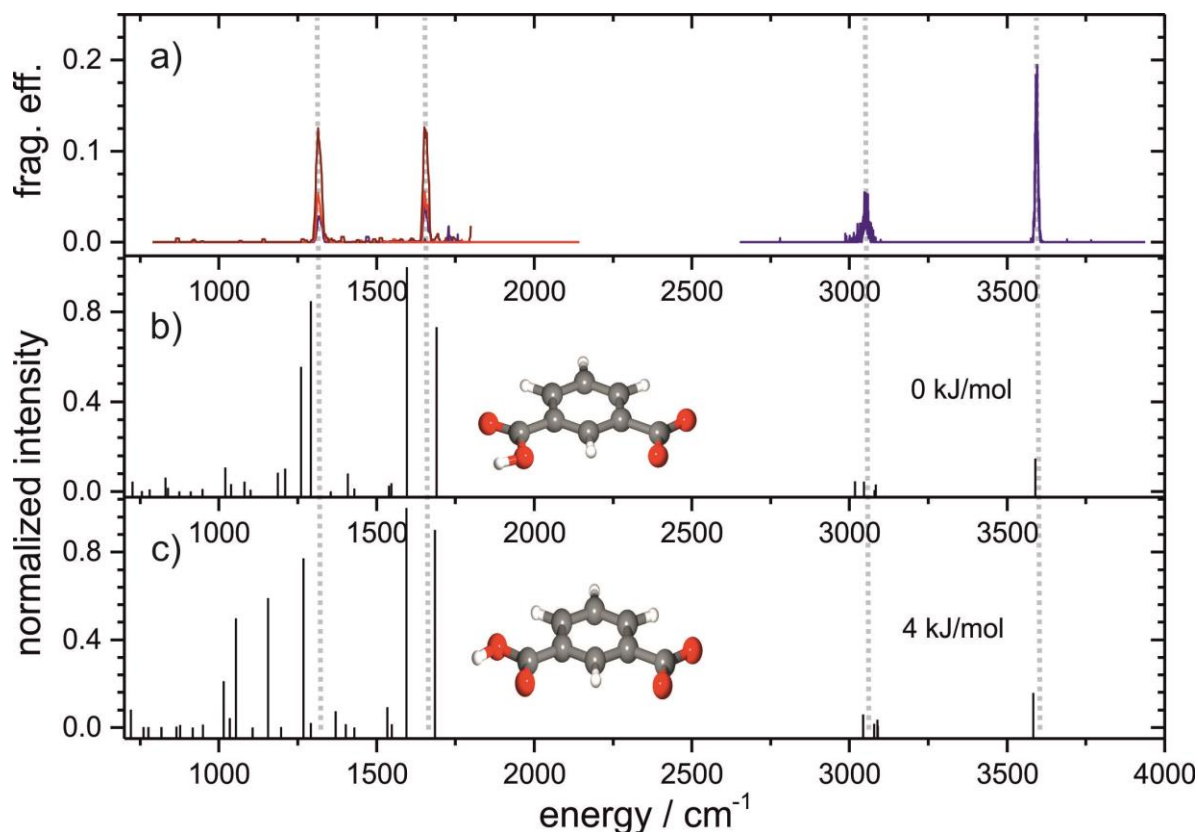


**Figure 37:** a) experimental IR-MD spectrum of deprotonated isophthalic acid; b) simulated IR spectrum of the calculated minimum structure (IsoPhthalStruc1) on MP2 level of theory with an aug-cc-pVDZ basis set; c) simulated IR spectrum of a calculated structure which is 4 kJ/mol higher in energy (IsoPhthalStruc2). All simulated spectra are scaled with 0.956.

The calculated structures of deprotonated isophthalic acid exhibit no intramolecular hydrogen bond. The simulated IR-MPD spectra resemble each other and both structures are close in energy. The calculated minimum species of deprotonated isophthalic acid cannot form an intramolecular

## 2. IR-MPD spectroscopy of deprotonated and protonated dicarboxylic acids

---

hydrogen bond as found in deprotonated phthalic acid and in the deprotonated aliphatic species. The benzene ring is rigid and planar. Thus the O-O distance is too long to stabilize an intramolecular hydrogen bond. The energy difference between the shown structures is very small. At higher temperatures (e.g. room temperature) both conformers exist simultaneously.

**Table 11:** energies, distances and angles of the calculated structures of deprotonated isophthalic acid

---

	energy/ $\text{kJmol}^{-1}$	$d_1(\text{O-H})/\text{\AA}$	$d_2(\text{O}\cdots\text{H})/\text{\AA}$	$\alpha(\text{O-H}\cdots\text{O})/\text{\textcircled{C}}$
deprotisophthal1	0	0.98	-	-
deprotisophthal2	4	0.98	-	-

---

## 2. IR-MPD spectroscopy of deprotonated and protonated dicarboxylic acids

---

### 2.14. Summary and conclusions

Experiments with the FEL and the OPO laser provide IR-MPD spectra of aliphatic dicarboxylic acids. The spectra of both methods correspond to each other. MP2 calculations of PDA and DDAs show a cyclic minimum structure with an intramolecular hydrogen bridge. Carr Parrinello simulations reveal that for PAA and DAA the direct proton transfer from one carboxyl group to the other is unfavorable. Instead proton transfer takes place by multistep chiral transformation<sup>2</sup>.

IR-MPD spectra of small PDAs and DDAs are in good agreement with the simulated spectra. Due to the flexible backbone the IR-MPD spectra of higher dicarboxylic acids are broadened. Single vibrational bands are indistinguishable. Especially in the spectra of DDAs all bands are broad. Nevertheless the bands appear in the same region as the calculated vibrational modes. It is imperative to obtain sharper IR-MPD spectra by cooling the ions. To cool the ions we developed a cold Penning trap. This experiment is in preparation in our laboratory in Kaiserslautern. Here the isolated ionic species will be cooled in a cold hexapole for precooling and after that the ions are transferred in the cooled ICR cell. This cell is cool able up to 10 K and already in use<sup>8</sup>.

Two color IR-MPD experiments reveal that the enhancement of a second IR laser is stronger in DDAs. The elimination of carbon dioxide occurs on a direct fragmentation path while the fragmentation of PDAs needs a rearrangement of the molecular structure prior to fragmentation. Thus, the spectra of DDAs are more affected by the use of a second resonant IR laser. This corresponds to our experimental findings.

The comparison of the OPO and FEL experiments reveals that both experiments are in good agreement. Minor differences arise from the different laser powers.

HD exchange experiments OH and OD stretching vibration shifts. The OH band shifts as expected. The experiment is challenging due to the residual water in the Paul trap. The deuterated species reacts with these water molecules in the radiation time and exchanges protons. Thus isolating the deuterated species is unsuccessful. Further analysis of the spectra is hindered by the fact that all parent ions leads to the same fragment peaks. The IR-MPD spectrum of deuterated species is of more interest. Here it will be possible to identify all modes which couple to the motion of the bridging proton. So far, this measurement was unsuccessful. To overcome the experimental problems IR-MPD spectroscopy in the FT-ICR is needed. In the ICR cell the background pressure is much lower than in the Paul trap.

Ionic phthalic and isophthalic acid has been investigated in the gas phase. In contrast to the aliphatic acids exhibit aromatic dicarboxylic acids a rigid backbone due to the aromatic ring. The comparison

## **2. IR-MPD spectroscopy of deprotonated and protonated dicarboxylic acids**

---

of the protonated and deprotonated phthalic acids spectra with the IR-MPD spectra of aliphatic dicarboxylic acids reveal strong similarities while the spectra of protonated and deprotonated isophthalic acid differ clearly. Intramolecular hydrogen bonds are impossible in isophthalic acid. This is documented by the measured IR-MPD spectra and by the simulated IR spectra. The fragmentation efficiency of protonated isophthalic acid is low compared to protonated phthalic acid. In both spectra the main neutral fragmentation product is water. Phthalic acid forms a stable anhydride without major changes in the molecule geometry. This is not the case in protonated isophthalic acid. To achieve a better agreement between experiment and theory the quality of the IR-MPD spectra needs to be improved. The fragmentation efficiencies are low especially in the fingerprint region. Tagging a weakly bound atom or molecule (e.g. He, N<sub>2</sub>, Ar, ...) on the molecular ion opens a favorable fragmentation channel. The differences in fragmentation efficiency and the two color effect on phthalic and isophthalic acid supports the fragmentation mechanism presented in chapter 2.5.4.).

The investigation of protonated and deprotonated dicarboxylic acids provides insights in intramolecular hydrogen bonding. Better understanding of the influence of the aliphatic and aromatic backbone and the dynamic of the proton transfer between the two acceptor sides requires further studies in experiments and theory.

### 2.15. References

1. A. Lagutschenkov, TU Kaiserslautern, 2008.
2. S. K. Min, M. Park, N. J. Singh, H. M. Lee, E. C. Lee, K. S. Kim, A. Lagutschenkov and G. Niedner-Schatteburg, *Chemistry-a European Journal*, 2010, **16**, 10373-10379.
3. D. W. Lupo and M. Quack, *Chemical Reviews*, 1987, **87**, 181-216.
4. J. Roithova and D. Schröder, *Chem. Rev.*, 2010, **110**, 1170-1211.
5. S. L. Chin, *Physical Review A*, 1971, **4**, 992-996.
6. J. Oomens, J. D. Steill and B. Redlich, *Journal of the American Chemical Society*, 2009, **131**, 4310-4319.
7. G. Zundel and H. Metzger, *Zeitschrift Fur Physikalische Chemie-Frankfurt*, 1968, **58**, 225-&.
8. S. Peredkov, A. Savci, S. Peters, M. Neeb, W. Eberhardt, H. Kampschulte, J. Meyer, M. Tombers, B. Hofferberth, F. Menges and G. Niedner-Schatteburg, *Journal of Electron Spectroscopy and Related Phenomena*, 2011, **184**, 113-118.



#### 3. H/D isotope effects in the reactions of benzene with Iron, Cobalt and Nickel cluster ions

##### 3.1. Preamble

This work has been submitted for publication in a slightly different way at *Physical Chemistry Chemical Physics* with the title: "H/D isotope effects in the reactions of benzene with Iron, Cobalt and Nickel cluster ions". The text of the publication was mainly written by me. Measurements and data evaluation were done by Jennifer Mohrbach and me / under my supervision.

##### Abstract

Reactions under single collision conditions with benzene ( $C_6H_6$ ) and with benzene- $d_6$  ( $C_6D_6$ ) of size selected cationic and anionic transition metal clusters  $Fe_n^{+/-}$ ,  $Co_n^{+/-}$  and  $Ni_n^{+/-}$  in the size range  $n = 3 - 28$  revealed that dehydrogenation by cationic clusters is sparse. Kinetic Isotope Effects (KIE) in total reaction rates are inverse and - in part - large. Dehydrogenation Isotope Effects (DIE) are normal. A previously established multistep model of adsorption and stepwise dehydrogenation from the precursor adsorbate proves suitable to rationalize the found KIEs and DIEs in principle. Particular insights into the effects of charge and of cluster size are possible but largely speculative. It is mandatory to spend further efforts in experiment, in modeling and in high level ab initio calculations in order to fully elucidate the transition metal cluster - benzene model systems.

#### 3.2. Introduction

Transition metal clusters serve as model systems to elucidate elementary processes in heterogeneous catalysis. Hydrocarbon adsorption and subsequent C-H bond activation are often the rate limiting steps in the catalytic reactions that are key to industrial processes and value creation.

Prior kinetic studies of benzene adsorption and activation focused on clusters of the transition metals niobium and rhodium<sup>1-3</sup>. While ionic niobium clusters vividly dehydrogenate benzene, apparently intact adsorption prevails on ionic rhodium clusters. Little to no observable isotope effects occurred in either cases. A most recent study documented and interpreted the prevailing H/D isotope effects in the activation of benzene by cobalt cluster cations and anions<sup>4</sup>.

Previous work on iron clusters pursued the reaction of cationic iron clusters with small molecules such as ND<sub>3</sub> and CH<sub>4</sub><sup>5,6</sup>. The bond energies of cationic iron clusters to N, ND, ND<sub>2</sub>, ND<sub>3</sub>, CD, CD<sub>2</sub> and CD<sub>3</sub> were determined. The barriers for dehydrogenation reactions exhibit an additional low energy pathway for iron  $n = 3 - 5$ <sup>5</sup>. Further studies on the reaction of iron with ammonia followed<sup>2,7</sup>. A theoretical study of the iron dimer cation with methane revealed a reaction mechanism<sup>8</sup>. Not only cations has been studied but also anionic iron clusters as well. Photoelectron spectroscopy on anionic iron benzene complexes Fe<sub>n</sub>Bz<sub>m</sub> ( $n = 1 - 7$ ,  $m = 1 - 4$ ) revealed the structures of these complexes. For larger complexes “rice-ball” like structures were found<sup>9</sup>.

Armentrout et al.<sup>10</sup> determined the bond energies of cobalt cluster cations with D, C, CD, CD<sub>2</sub>, and CD<sub>3</sub>. In addition, Armentrout et al. established the bond energies (BDE) of atomic cobalt-benzene and cobalt-dimer-benzene cations (2.65(11) and 1.73(14) eV, respectively) by analysis of thermochemical modeling of high precision flow reactor experiments. Product ions are generated via endothermic processes for the reaction of cationic cobalt clusters with nitrogen. Collision induced dissociation is the dominating process. Merely weak adsorption of nitrogen is observed for anionic clusters  $n \geq 7$ <sup>11</sup>. Another flow tube study of photoionization efficiencies of Co<sub>n</sub>(C<sub>6</sub>H<sub>6</sub>)<sub>m</sub> clusters focused onto species with multiple benzene adsorbates<sup>12,13</sup>. Photoelectron spectra of cobalt benzene anions found sandwich like structures<sup>14</sup>. Photoionization efficiency (PIE) spectra of cold cobalt clusters (Co<sub>3</sub>, Co<sub>7</sub> - Co<sub>92</sub>) revealed vertical ionization potentials (IPs) that decreased rapidly up to  $n \approx 20$ , beyond which IPs emerge more slowly and smoothly<sup>15</sup>. Knowledge of the electronic structure of cobalt clusters and of cobalt cluster benzene complexes arose from several Stern-Gerlach experiments<sup>16-19</sup>. Synchrotron ionization studies of cationic cobalt clusters revealed significant magnetization by spins and by orbital angular moments with little cluster size dependence<sup>20</sup>.

### 3. H/D isotope effects in the reactions of benzene with iron, cobalt and nickel

---

Armentrout et al. studied the reactions of nickel clusters with various small molecules such as  $D_2$ ,  $O_2$  and  $CH_4$  and determined the bond energies of  $Ni_n-D$  and  $Ni_n-CD_x$  cluster complexes<sup>21-23</sup>. The bond energies depend strongly on the cluster size for small clusters indicating changes in the electronic structure of the clusters<sup>23</sup>. Irion et al. investigated various reactions of transition metal cluster cations in an FT-ICR mass spectrometer<sup>24</sup>. Small nickel clusters merely adsorb benzene while larger clusters are able to dehydrogenate benzene. A study under single collision condition on the reaction of nickel cluster ions with benzene was performed with a tandem mass spectrometer. Three different processes were observed: the absorption of benzene with and without Ni release and the dissociation of  $C_2H_2$ . Bowen et al. performed photoelectron spectroscopy on nickel-benzene cluster anions<sup>25</sup>.

The reaction of cationic iron group clusters ( $Fe_n^+$  ( $n = 2 - 28$ ),  $Co_n^+$  ( $n = 8 - 29$ ) and  $Ni_n^+$  ( $n = 3 - 30$ )) in the reaction with ethylene revealed that dehydrogenation of ethylene prevails. The results indicate that 3d electrons play a central role in the dehydrogenation reaction<sup>26</sup>. Experiments and calculations on the adsorption of hydrogen on transition metal clusters (Sc, V, Fe, Co and Ni) reveal that the adsorption of  $H_2$  is dissociative except for the nickel clusters. Atomic and molecularly chemisorbed hydrogen is present in nickel-hydrogen complexes<sup>27</sup>.

In extension on our prior work<sup>4,28</sup>, the present study compares clusters of iron, cobalt and nickel. We chose to investigate the reaction kinetics and H/D isotope effects of size selected iron, cobalt and nickel clusters with benzene under single collision conditions by application of Fourier-Transform Ion-Cyclotron-Resonance (FT-ICR) mass spectrometry.

#### 3.3. Experimental methods

The experiments were performed with a modified Fourier-Transform Ion Cyclotron Resonance (FT-ICR) mass spectrometer (Bruker Apex IV). The ions were generated by a laser vaporization source<sup>29</sup> that utilizes the second harmonic of a Nd:YAG Laser (Spitlight 200, Innolas). Ions originate from a rotating metal disc of cobalt (purity of 99.95% , Alpha Aesar), of isotopically enriched <sup>56</sup>Fe (99.93%) and of isotopically enriched <sup>58</sup>Ni (99.61%, both Oak Ridge National Laboratories). The generated metal plasma is captured and cooled by a short transverse He pulse (40  $\mu$ s, He pressure 8-15 bar) from a homebuilt piezoelectric valve<sup>30</sup>. Further cooling is achieved by a supersonic nozzle expansion through a 20 mm long expansion channel (diameter 2mm). This set up is able to generate singly charged anions and cations without further ionisation. After having passed through a 1.4 mm skimmer the ions are accelerated and transferred via a 90° ion bender and electrostatic lenses into the high field region of a superconducting magnet (7.05 T, actively shielded). The ions were trapped for reaction and detection in a so called “infinity” ICR cell<sup>31</sup>.

In the ICR cell the ionic clusters may undergo reactions while they are trapped. Controlled admission of reaction gas via a leak valve raises the pressure from  $\leq 3 \times 10^{-10}$  mbar up to  $5 \times 10^{-9}$  mbar. This amounts to about one bimolecular reactant collision per cluster per second (single collision conditions). The nominal pressure reading stems from a commercial ultrahigh vacuum gauge (cold cathode gas discharge, calibrated for N<sub>2</sub>), which is subject of a pressure gradient towards the ICR cell. Therefore, the absolute value of pressure and reactant gas number density at the location of the stored ions is not exactly known. The reactant gases benzene and benzene-d<sub>6</sub> (Sigma Aldrich, purity >99.6 %) are degassed by several “pump and freeze” cycles ahead of their application. The kinetic curves of reactant and product ions originate from reaction delay scans and subsequent evaluation of recorded mass spectra . Fits to pseudo-first-order-kinetics occur through the “evofit” program<sup>32</sup>.

Fitting the recorded kinetics yields relative partial rate constants for association and for dehydrogenation (in the case of Fe<sub>25</sub><sup>-</sup>). The total relative rate constants  $k_{tot}^{(H,D)}(n)$  are the sum of all first step relative partial rate constants obtained by the genetic algorithm fit program. The ratio of the total rate constants with benzene  $k_{tot}^{(H)}(n)$  and with benzene-d<sub>6</sub>  $k_{tot}^{(D)}(n)$  defines the kinetic isotope effect  $KIE(n)$ :

$$KIE(n) := \frac{k_{tot}^{(H)}(n)}{k_{tot}^{(D)}(n)} \quad (1)$$

### 3. H/D isotope effects in the reactions of benzene with iron, cobalt and nickel

---

The KIE is normal if the reaction with benzene is faster than with benzene- $d_6$  (KIE>1). If the reaction with perdeutero benzene is the faster one, the KIE is inverse (KIE<1).

To reduce the amount of data we define the average degree of dehydrogenation  $\langle\chi_n\rangle$  as was done before<sup>33</sup>:

$$\langle\chi_n\rangle = \frac{1}{m} \frac{1}{k_n^{tot}} \sum_{m_i=1}^m m_i k_n(m_i) \quad (2)$$

with

$$k_n^{tot} = \sum_{m_i=1}^m k_n(m_i)$$

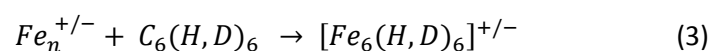
Here,  $m$  (= 6 in the present case) indicates the total amount of hydrogen or deuterium atoms available from benzene. The partial reaction rates  $k_n(m_i)$  classify according to the cluster size  $n$  and the loss of hydrogen or deuterium atoms  $m_i$  in the observed product.  $\langle\chi_n\rangle = 1$  would indicate complete dehydrogenation while  $\langle\chi_n\rangle = 0$  would indicate adsorption without any dehydrogenation.

Mass resolution in FT-ICR usually exceeds any practical needs. In the presence of reaction gas of  $\sim 1 \times 10^{-8}$  mbar, however, collisions of stored ions (at a rate of  $\sim 1 \text{ s}^{-1}$ ) accelerates the damping of the sinusoidal transients such that the fourier transformed lorentz profiles broaden considerably. In most cases, the then limited mass resolution ( $m/\Delta m \sim 10^4$ ) suffices for unambiguous assignments and analysis of product intensities. However, our present study happens to suffer from some almost coincidence of various unrelated mass peaks, which cannot be fully resolved anymore (cf. Fig. 3(a)).

## 3.4. Results and Discussion

## 3.4.1. Reactions of iron clusters

The recorded kinetics reveal that pure iron clusters react with benzene to form a single type of products. Dehydrogenation does not take place up to the limit of sensitivity of this experiment - with a single exception, the anionic iron cluster,  $Fe_{25}^-$ . Instead, benzene species remain adsorbed at the iron clusters without releasing any atomic or molecular products:



Of course, the apparently intact adsorption is not warranted. The mere mass spectra do not provide for direct structural information. The adsorbed benzene molecule is not necessarily intact and single or multiple C-H bond activation is conceivable in principle. This would lead to a hydrido-phenylic iron cluster  $Fe_n(H)C_6H_5^+$ , or to a di-hydrido-benzyne adduct  $Fe_n(H)(H)C_6H_4^+$ . The square brackets in equation (3) are meant to account for this structural ambiguity. Activation of more than one C-H bond could lead to a pairwise recombination of H atoms and desorption of molecular  $H_2$ . This is not observed in the current iron cluster experiment. We present an account of this observation in terms of tentative enthalpic considerations in chapter 3.4.4. The observed product species of eq. (3), no matter whether activated or not, thus stabilize radiatively, on the long run.

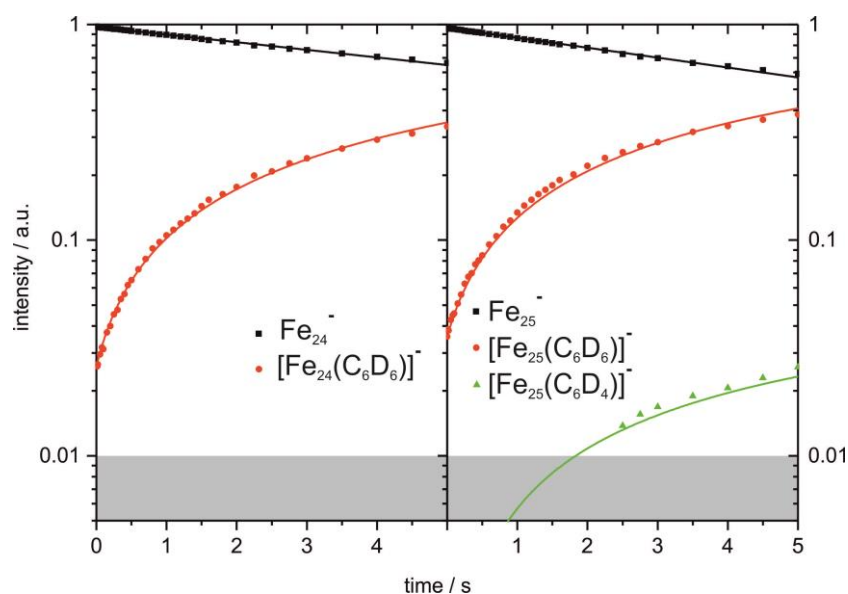


**Figure 1:** Normalized kinetics for the reaction of anionic iron clusters  $Fe_{25}^-$  (left) and  $Fe_{24}^-$  (right) with benzene under single collision conditions. The grey shaded areas mark the detection limit.

### 3. H/D isotope effects in the reactions of benzene with iron, cobalt and nickel

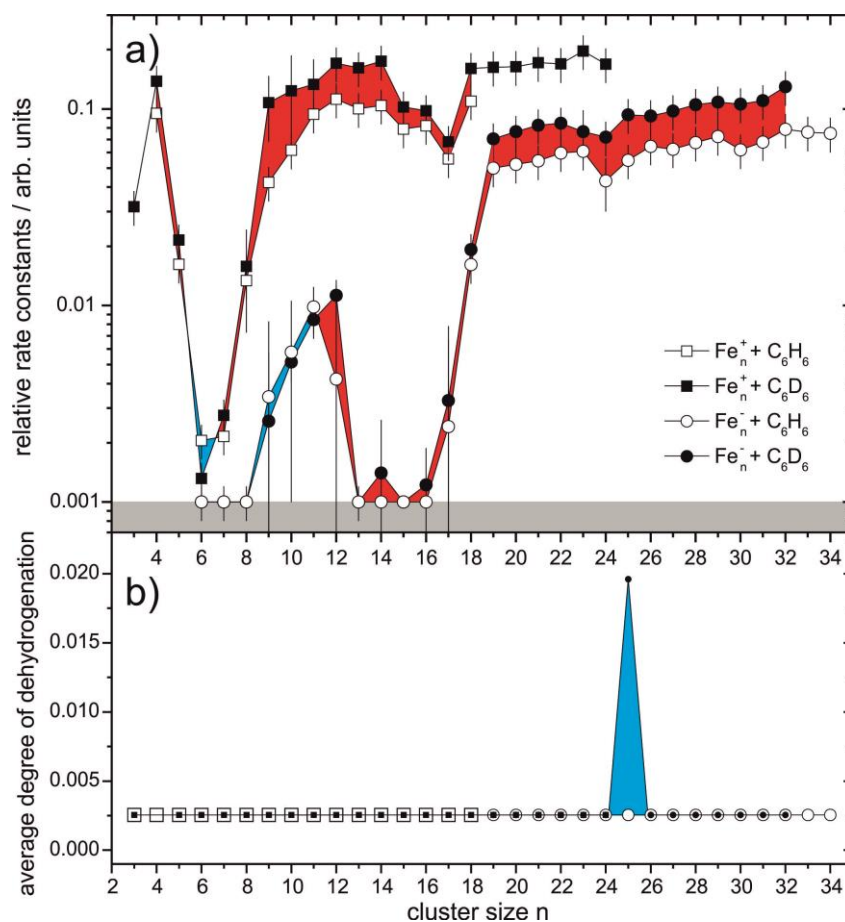


**Figure 2: (a)** Total rate constants of cationic (squares) and anionic (circles) iron clusters reacting with benzene (open symbols) and benzene-d<sub>6</sub> (filled symbols). Blue and red shading indicates the normal and inverse kinetic isotope effects KIE ( $n$ ). The grey shaded area marks the background noise level. Data values at indicated noise level refer to upper limit. **(b)** Average degree of dehydrogenation of benzene (open symbols) benzene-d<sub>6</sub> (filled symbols) when reacted by cationic (squares) and anionic (circles) iron clusters. Only  $\text{Fe}_{25}^-$  is found to dehydrogenate benzene to a minor degree. The blue shaded area emphasizes the normal dehydrogenation isotope effect (DIE). Data values at indicated noise level refer to upper limit.

Cationic iron clusters reveal strong size dependence. Small cationic iron clusters ( $n = 3, 4$ ) adsorb benzene with nearly the same efficiency as large clusters ( $n > 18$ ). There is a distinct minimum in the total relative rate constants for the cluster sizes  $n = 6 - 7$ . The rate constants rises after that again with a dip for  $n = 15, 16, 17$ . The minimum at  $n = 6$  and  $7$  corresponds to the results of previous studies on cobalt clusters which also exhibit a minimum in reactivity of cationic cobalt clusters with  $n = 6$ <sup>4</sup>. The relative rate constants of cationic iron clusters are higher for the reaction with benzene-d<sub>6</sub> than for the reaction with benzene. This leads to an inverse kinetic isotope effect (KIE).

### 3. H/D isotope effects in the reactions of benzene with iron, cobalt and nickel

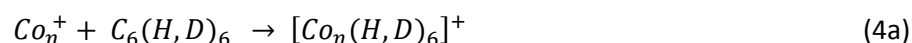
---

Anionic iron clusters have strong size dependence in the reaction with benzene, and they are less reactive than cationic iron clusters. Small anionic cluster ( $n < 9$ ) do not yield observable products in the mass spectra. Adsorption induced electron detachment is a conceivable reason. The recorded data do not provide evidence for such a “dark” reaction channel at present, however. The reactivity rises with increasing number of atoms in the cluster with a drop for the cluster sizes  $n = 13 - 16$ . This corresponds to the dip in reactivity found in cationic iron clusters. Without further studies, it is not possible to determine unambiguously the mechanistic origin of this reactivity dip. Since it appears for cationic and anionic iron clusters in the same size range it might be a structural effect. It may be speculated that at  $n=6$  octahedral coordination sets in such that an increased degree of coordinative saturation enables a reduction of reactivity. The  $n = 12 - 16$  dip in the reactivity of anionic iron clusters may originate from an all surface to surface & interior atoms transition, concomitant with a change in electronic structure. The call for suitable high level *ab initio* studies beyond the standard is obvious.

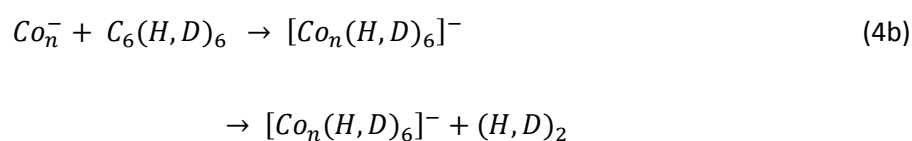
#### 3.4.2. Reactions of cobalt clusters

We have studied the size dependence of the kinetic isotope effect KIE( $n$ ) in ionic cobalt clusters before<sup>4</sup>. Our current contribution reports on a repetition of those experiments, but with a different FT-ICR mass spectrometer. In principle, we reproduce previous findings and obtain results that compare favourably. There are some deviations of the present results from the previous ones, however, to discuss in the following.

The product mass spectra from the reactions of cationic cobalt clusters with benzene and benzene- $d_6$  reveal association products only - much alike cationic cobalt cluster reactions of the previous study and much alike cationic iron cluster reactions discussed above:



Corresponding product mass spectra from the reactions of anionic cobalt clusters with benzene and benzene- $d_6$  reveal association products and dehydrogenation products:





### 3. H/D isotope effects in the reactions of benzene with iron, cobalt and nickel

A quantitative analysis of the dehydrogenation reaction is hampered by some congestion of the product mass spectra with hydroxide peaks, in conjunction with limited mass resolution in the presence of reaction gas (Fig. 3(a) and exptl. section). It can be said, however, that clusters of the same sizes as in the previous study show dehydrogenation products in the present case. The total efficiency of dehydrogenation is seemingly lower in the present study (by about 30%). Such a reduction likely relates to somewhat different storage conditions of trapped cluster ions. Residual kinetic energy of the cluster ions in the laboratory frame reduces by transformation in the center of mass frame of the collision complex. It does not vanish, however. It is well conceivable, that we conducted the present studies with somewhat less residual kinetic energy of the trapped clusters. If so, the observed reduction in dehydrogenation would point to some direct impulsive mechanism that needs to overcome an entrance channel barrier. Such a far reaching conclusion is highly speculative, however, and would need additional verification by further experiments and electronic structure calculations.

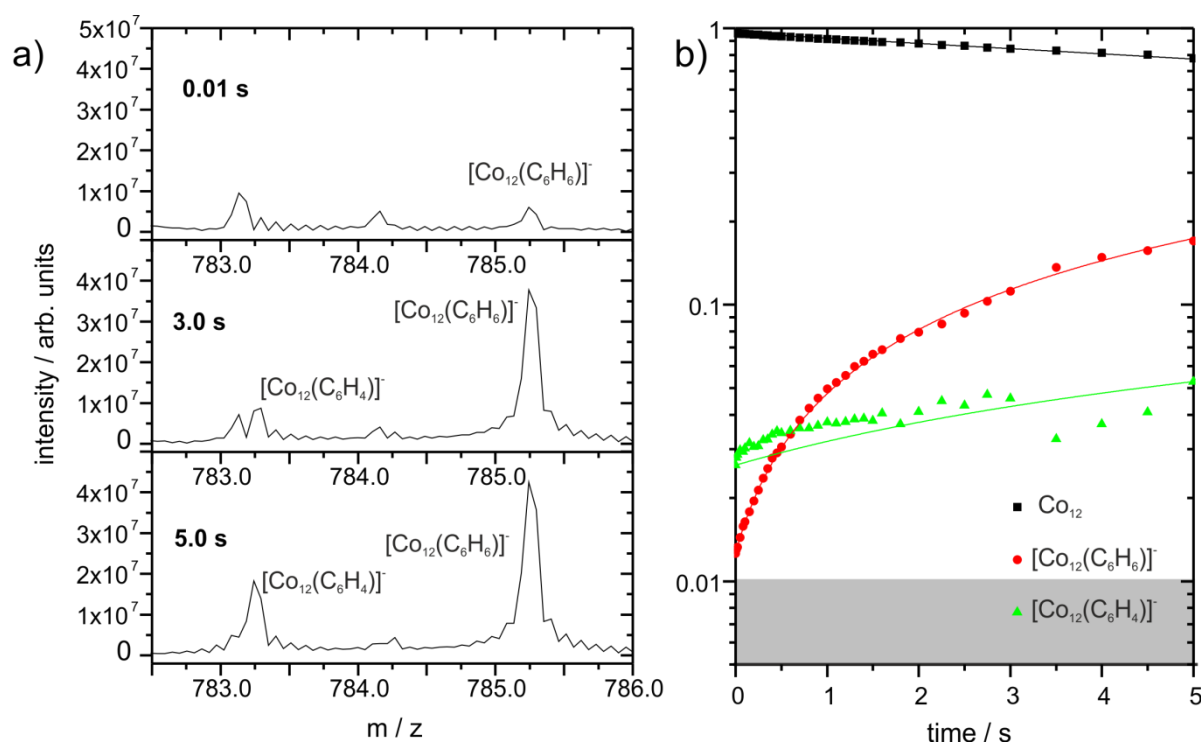


**Figure 3:** An example for the reaction kinetics of  $Co_{12}^-$  with  $C_6H_6$ . **(a)**  $Co_{12}^-$  product mass spectra at indicated reaction delays. The dehydrogenation peak  $[Co_{12}(C_6H_4)]^-$  ( $m_{\text{calc}} = 783.227$  amu) is found next to the peak of  $[Co_{13}OH]^-$   $Co_{13}OH^-$  ( $m_{\text{calc}} = 783.132$  amu) such that both partially overlap ( $\Delta m = 0.095$  amu) within the limited resolution ( $m/\Delta m \sim 10^4$ ) of the present experiments (see exptl. section for more details). **(b)** The symbols represent experimental data, solid lines represent

### 3. H/D isotope effects in the reactions of benzene with iron, cobalt and nickel

---

numerical fits by a generic algorithm to first order kinetics. Association (red, circles) behaves the expected way. Dehydrogenation (green, triangles) fits not with the experimental data. The data points at early reaction times seem to overestimate the reality, which might be due to an extra oxide peak obscuring.

Of course, the square bracket notation in eq. (4a) is a formal one, very much as discussed in conjunction with eq. (3) in the case of iron. It is well possible that single or double C-H bond activation of benzene takes place, yielding  $Co_n(H)C_6H_5^+$  or  $Co_n(H)(H)C_6H_4^+$  products as well.

Fitting the recorded kinetics yields relative total rate constants for association (Fig. 4). Note that issues on the intensities of dehydrogenation products do not enter. Instead we evaluate the parent cluster ions decline. The total rates of reactions reveal a pronounced cluster size dependence in magnitude, and a large inverse kinetic isotope effect  $KIE(n)$ , which is on the order of two, much in parallel to what was observed in the case of iron clusters. The reduced total rate constant of  $Co_6^+$  is consistent with the findings of our previous study<sup>4</sup> - corresponding to the newly observed minimum in the total reactivity of  $Fe_6^+$  and  $Fe_7^+$  (cf. Fig. 2(a)). This similarity is in support of the speculation on an octahedral coordination motif at  $n = 6$  in both cases.

It is elucidating to compare transition metal cluster – benzene reaction rates of the  $3d^7$  element cobalt to those of the isoelectronic  $4d^7$  element rhodium as obtained before<sup>34</sup>. Clusters up to  $Rh_{13}^+$  preferentially yield dehydrogenated products  $Rh_nC_6H_4^+$  with the sole exception of  $Rh_6^+$  which preferentially attaches benzene without dehydrogenation. Here as well, the reactivity reduces at cluster size  $n = 6$ , although in a different way. We will try to put all of these findings together when discussing the common features in the present experiments in chapter 3.4.4.

### 3. H/D isotope effects in the reactions of benzene with iron, cobalt and nickel

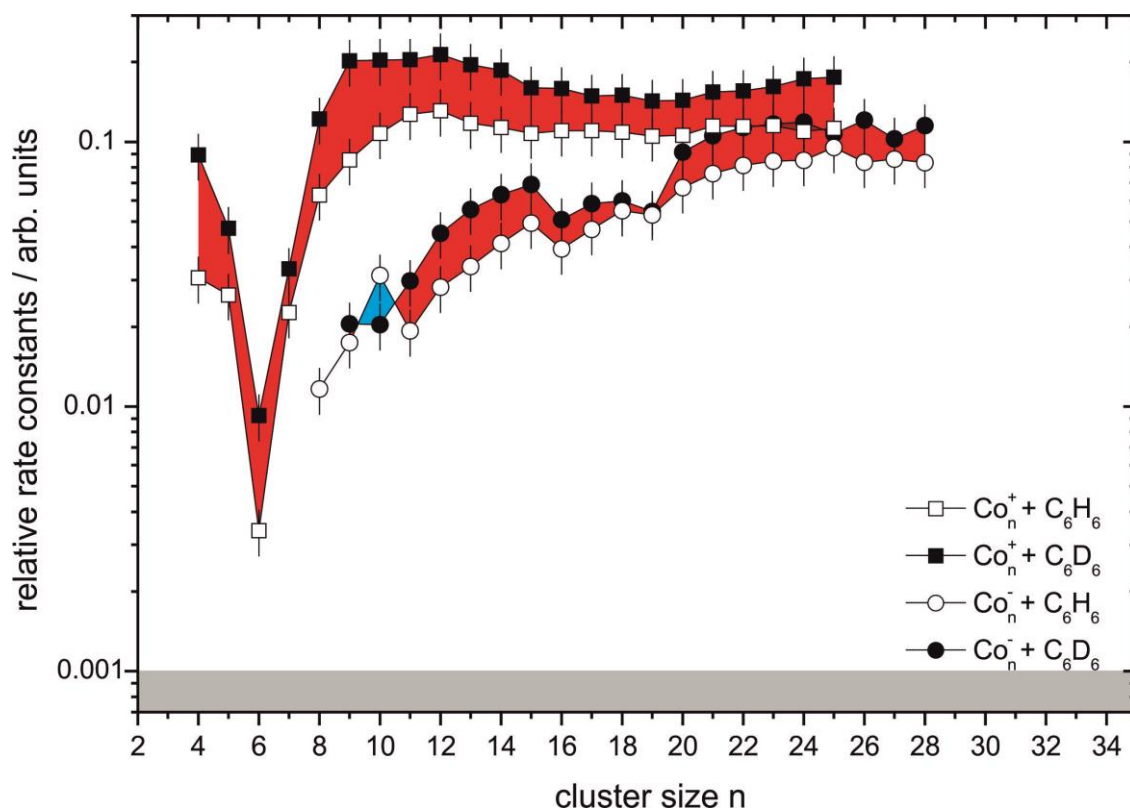
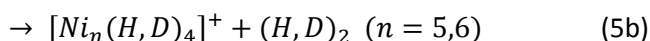
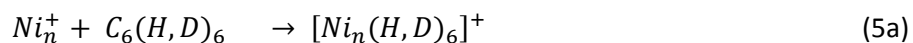


**Figure 4:** Total rate constants of cationic (squares) and anionic (circles) cobalt clusters reacting with benzene (open symbols) and benzene-d<sub>6</sub> (filled symbols). Blue and red shading indicates the normal and inverse kinetic isotope effects KIE (n). The noise equivalent level of the present experiments is indicated by grey shading.

Anionic cobalt cluster reactions provide for less strong size dependence than anionic iron clusters. All  $Co_n^-$  clusters ( $n = 8 - 28$ ) do yield observable products. Adsorption induced electron detachment seems less conceivable than in the case of iron. There is no evidence for a concomitant “dark” reaction channel. The reactivity of anionic cobalt clusters rises steadily with cluster size, little to no cluster size specific modulation prevailing. There is slight dip in the rate constants at cluster sizes  $n = 16 - 19$ . These sizes correspond to the pronounced dips in the rate constants of cationic ( $n = 15 - 17$ ) and anionic iron clusters ( $n = 13 - 16$ ). This common effect hints to a structural feature, which is to elucidate further.

#### 3.4.3. Reactions of nickel clusters

Cationic nickel cluster react with benzene and benzene- $d_6$  towards a single reaction product. Only apparently intact adsorption products appear with mere two exceptions found: Small cationic nickel cluster ( $n=5,6$ ) manage to dehydrogenate benzene.



The total relative rate constants of cationic nickel clusters (Fig. 5(a)) reveals largely constant values irrespective of size – except for  $Ni_3^+$  and  $Ni_5^+$  being less reactive. The largest clusters ( $n = 20$  and beyond) seemingly attach benzene with collision rate. Small cationic nickel cluster ( $n = 5, 6$ ) are the only cationic clusters which are able to dehydrogenate benzene. Such exceptions inevitably point towards local (means: cluster size dependent) variations in electronic and/or geometric structure of these exceptional clusters. Throughout all of the studied size range benzene- $d_6$  attaches more efficient than benzene does. This yields an inverse KIE (coded red in Fig. 5(a)).

### 3. H/D isotope effects in the reactions of benzene with iron, cobalt and nickel

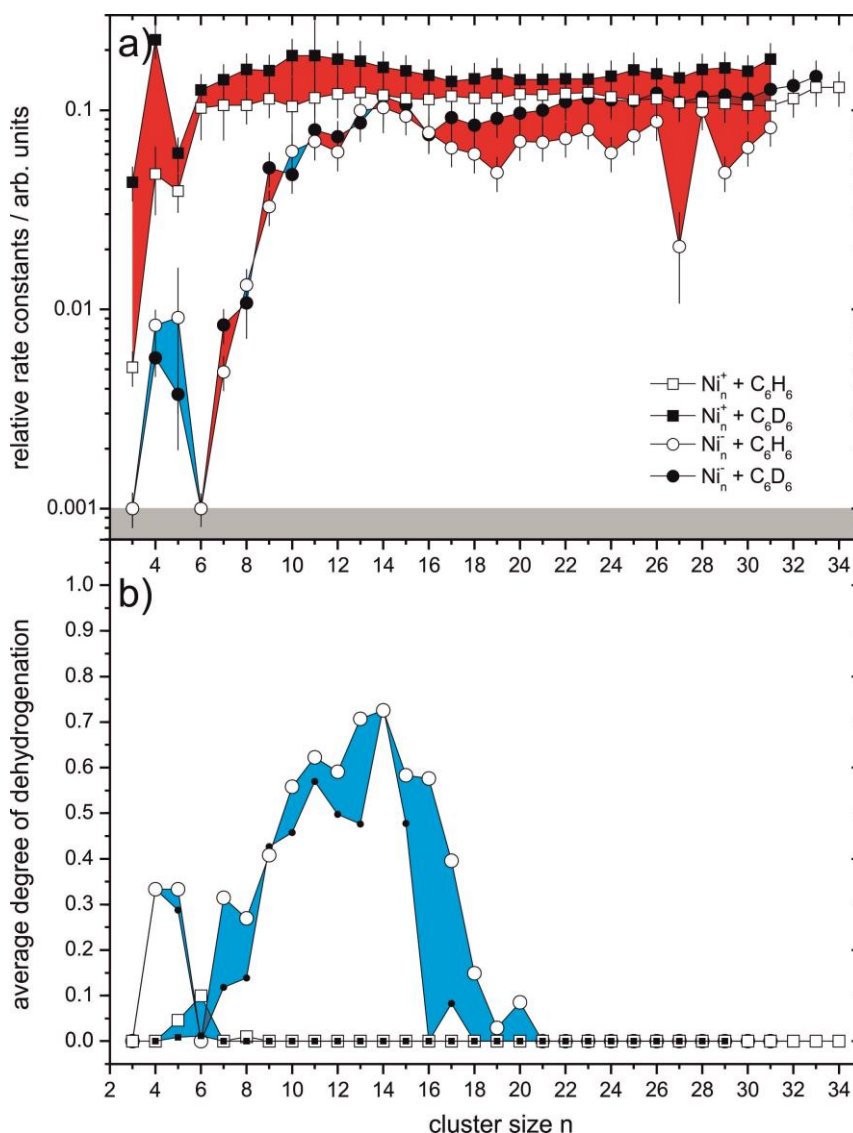
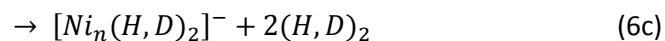
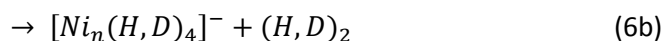
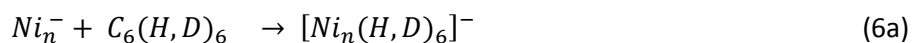


**Figure 5: (a)** Total rate constants of cationic (squares) and anionic (circles) nickel clusters reacting with benzene (open symbols) and benzene- $\text{d}_6$  (filled symbols). Red shading indicates inverse kinetic isotope effect KIE ( $n$ ) which is the only found KIE ( $n$ ) in cationic nickel clusters. Small anionic nickel clusters exhibit also a normal KIE ( $n$ ). Grey shading indicates the noise equivalent level of the present experiments. **(b)** Average degree of dehydrogenation  $\langle \chi_n \rangle$  of benzene (open symbols) benzene- $\text{d}_6$  (filled symbols) when reacted by cationic (squares) and anionic (circles) nickel clusters. The blue shaded areas indicate a normal dehydrogenation isotope effect (DIE > 1).

Anionic nickel clusters of a wide size range ( $n = 4 - 20$ ) react vividly into multiple observable product channels in parallel. This observation is in remarkable contrast to the lack of dehydrogenation by anionic iron clusters. The reduced reactivity of anionic cobalt clusters falls in between of both cases.

### 3. H/D isotope effects in the reactions of benzene with iron, cobalt and nickel

---



We label these reaction processes as adsorption (eq. 6a), dehydrogenation (eq. 6b), twofold dehydrogenation (eq. 6c) and total dehydrogenation (eq. 6d). The observation of strong dehydrogenation points to likely C-H bond activation in general, maybe even in cases of seemingly simple adsorption (eq. 6a). There is a minimum in reactivity for anionic clusters with  $n = 6$ . Remarkably, this minimum is consistent with the findings for iron and cobalt clusters (both anionic and cationic). Hence, it is possible that a special structural feature hampers the adsorption of benzene to the cluster surface. An octahedral structure may be conceivable. The rate constants rises with increasing cluster size. C-H bond activation takes place in the range of  $7 < n < 21$ . Larger clusters adsorb benzene apparently intact. While C-H bond activation domains the rate constants the KIE remains in the range of the experimental uncertainty. For clusters with  $n > 17$  the reaction with benzene- $d_6$  becomes considerably faster which leads to an inverse KIE. The average degree of dehydrogenation is higher for the reaction of benzene than for those of benzene- $d_6$ . The resulting normal DIE codes blue in Fig. 5(b).

#### 3.4.4. Interpretation of features that are common to iron, cobalt, and nickel cluster cations and anions

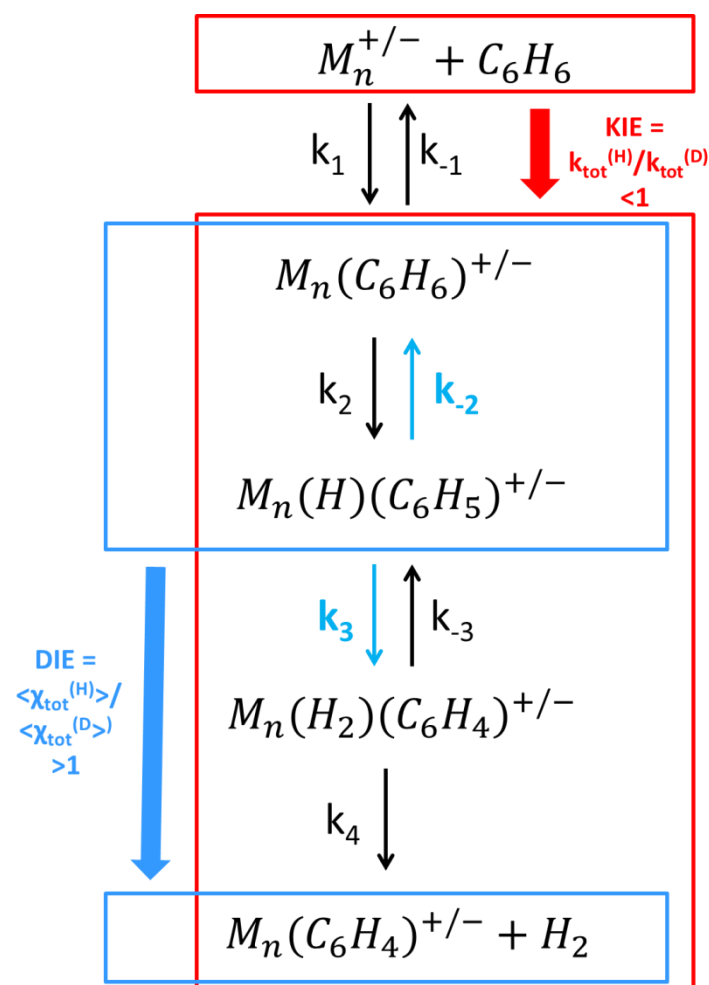
We have found dependencies of rates, of KIEs and of DIEs on cluster sizes, on cluster composition, on cluster charge and on benzene deuteration. It is hardly possible to interpret these particular size dependent features on their own. Such a task would take dedicated large scale *ab initio* studies on top - at risk to reach computational and methodological limits. For the time being, such limitations exist.

The more it is intriguing to see that certain features prevail - or at least dominate - in all of the investigated reactions. These are in particular:

- (1) The kinetic isotope effect is inverse,  $KIE < 1$ . This most notably holds for cationic and anionic clusters of all sizes - only few, single cluster sizes being exempt with a normal  $KIE > 1$ .
- (2) The dehydrogenation isotope effect is normal,  $DIE > 1$ , wherever observed. This holds equally for the sole iron cluster dehydrogenating ( $Fe_{25}^-$ ), for the qualitative data on the anionic cobalt clusters, and for the recorded DIE values of anionic nickel clusters  $Ni_6^- - Ni_{20}^-$ , that were found to lead to high degrees of benzene dehydrogenation.
- (3) Cationic clusters of iron, nickel and cobalt do not lead to recordable dehydrogenation products of benzene. It takes anionic clusters to do so – no exemptions found throughout the range of cluster sizes studied.
- (4) The total reaction rate asymptotically reaches maximum values towards larger cluster sizes. It seems to become close to collision rate, which implies unit adsorption efficiency. This is unit sticking coefficient in terms of the language of surface science.

We have established before a multistep reaction motif/model that managed to explain the findings (1) and (2), namely inverse KIE and normal DIE<sup>4</sup>.

### 3. H/D isotope effects in the reactions of benzene with iron, cobalt and nickel



**Scheme 1:** Kinetic model

This scheme of consecutive elementary processes is able to explain the prevailing inverse kinetic isotope effect. Scheme 1 equally holds for reactions with benzene- $d_6$ . In short, the adsorption and desorption ( $k_1$  and  $k_{-1}$ ) is followed by endoergic C-H bond activation and reverse recombination ( $k_2$  and  $k_{-2}$ ). A second C-H bond activation step ( $k_3$ ) precedes desorption of molecular hydrogen ( $k_4$ ). The C-H bond recombination ( $k_{-2}$ ) and the second C-H bond activation ( $k_3$ ) start from a cold hydrido-phenyl cluster structure. A considerable normal kinetic isotope effect ( $\text{KIE} \gg 1$ ) in  $k_{-2}$  and  $k_3$  results from the combination of H/D isotope effects in the zero point energy of the metal hydride bond with mass dependent H/D tunneling across the likely prevailing activation barriers. In remarkable contrast, the other elementary steps account for little to no KIE. An in detail account of this proposed model may be found elsewhere<sup>4</sup>. The overall combination of these seven elementary processes give rise to an observable inverse KIE for association and a normal DIE for dehydrogenation. This was observed in the reaction of cobalt clusters<sup>4</sup>, and it is reconfirmed in the newly recorded reactions of iron and nickel cluster cations and anions with benzene and benzene- $d_6$ .



### 3. H/D isotope effects in the reactions of benzene with iron, cobalt and nickel

---

The finding (3) - dehydrogenation by anionic clusters only - is explained by nucleophilic attack of the anionic clusters (in particular  $Ni_n^-$ ,  $n < 20$ ) directly to an aromatic C-H bond of benzene upon collision encounter. This may occur through  $\eta_1$  coordination at an individual H-C bond. Cationic clusters likely prefer electrophilic  $\eta_6$  coordination to the aromatic ring. Higher activation barriers towards C-H bond activation are likely, and in the present cases seemingly hamper activation in total.

The finding (4) - charge does not matter in the asymptotic limit of large clusters ( $n > 20$ ) - is to be expected. Localized charge differences vanish the smaller the partial charge per metal cluster atom becomes by enlarging the cluster size  $n$ . We have assumed that  $\eta_1$  coordination to individual H-C bonds is necessary for effective subsequent dehydrogenation. The decrease in localized partial charges upon enlarging anionic cluster sizes hampers this mechanism. In line with this effect, the dehydrogenation of benzene by anionic cobalt clusters dies out beyond  $n = 20$ . Instead,  $\eta_6$  coordination to the aromatic ring takes over – even in the case of anionic clusters  $n > 20$ . In addition the larger clusters act as increasing heat bath which effectively sink the released heat of benzene absorption. Prevailing activation barriers may not be overcome anymore thus rendering any kind of bond activation unlikely.

#### 3.4.5. Interpretation of the differences in reactions of iron, cobalt, and nickel cluster cations and anions with benzene and benzene-d6

Beyond the above outlined common features there are subtle differences in the observed reactions to discuss:

- (5) The studied cluster anions react in general less efficient than cations with differences diminishing as clusters sizes reach 20 atoms and beyond. Small cluster cations act as effective electrophiles and manage to activate C-H bonds efficiently. This mechanism seems to operate once localized net anionic charge comes in its way. Delocalized anionic charge, however, does not hamper the electron withdrawal from C-H bonds.
- (6) There is a dip in the reactivity of  $Fe_n^+ / Co_n^+$   $n = 6$  as opposed to  $n = 5$  for  $Ni_n^+$ . This seemingly relates to particular structural effect. One may speculate about a possible octahedral coordination in the case of Fe and Co. Prior studies on the attachment of molecular hydrogen to neutral cobalt clusters found  $Co_6^0$  to attach hydrogen less efficient than other cluster sizes as well<sup>35</sup>. Neutral iron cluster of that size were not studied,  $n = 8$  proving

### 3. H/D isotope effects in the reactions of benzene with iron, cobalt and nickel

---

inefficient to attach H<sub>2</sub> though. Neutral nickel clusters were found to lack efficient hydrogen attachment at n = 9. It thus looks as if charge state (cationic or neutral or anionic) makes little or no difference to iron or cobalt clusters. In contrast, cationic, neutral and anionic cobalt clusters reveal size specific lack of attachment or reactivity at different cluster sizes. In short: iron and cobalt are much alike, nickel is different.

- (7) Another finding of differences in the behaviour of iron, cobalt and nickel relates to the average degree of dehydrogenation  $\chi_n$  by anionic clusters:  $\chi_n(Fe_n^-) \ll \chi_n(Co_n^-) < \chi_n(Ni_n^-)$ . Without further insight on the energetics and structures of the investigated clusters at hand, it is hardly possible to interpret these differences in detail. It is noteworthy to contrast the high reactivity of anionic nickel clusters with benzene to the lack of molecular hydrogen activation by cationic nickel clusters as observed before<sup>27</sup>. The possibility of a charge induced structural transition comes into mind. Therefore, it is in particular worthwhile to consider a large scale computational study of these two systems in comparison.

#### 3.5. Summary

In extension of our prior work<sup>4, 28</sup> we investigated the reaction with benzene and benzene-d<sub>6</sub> of size selected cationic and anionic transition metal clusters  $Fe_n^{+/-}$ ,  $Co_n^{+/-}$  and  $Ni_n^{+/-}$  in the size range  $n = 3 - 28$ . Dehydrogenation by cationic clusters is sparse, it occurs in reactions by anionic clusters of cobalt and nickel. Kinetic isotope effects KIE(n) in total reaction rates are inverse and - in part - large, dehydrogenation isotope effects DIE(n) are normal. A previously established multistep model of adsorption and stepwise dehydrogenation from the precursor adsorbate proves suitable to rationalize the found KIEs and DIEs in principle. Particular insights into the effects of charge and of cluster size are speculative. It is mandatory to spend further efforts in experiment, in modeling and in high level ab initio calculations in order to fully elucidate the transition metal cluster - benzene model systems.

#### Acknowledgement

This work was supported by the German research foundation DFG within the transregional collaborative research center SFB/TRR 88 "Cooperative effects in homo and heterometallic complexes" (3MET) and by the state research center OPTIMAS. We benefitted from inspiring discussions with Marc Prosenc and Frederic Patureau.

#### 3.6. References

1. C. Berg, M. Beyer, U. Achatz, S. Joos, G. Niedner-Schatteburg and V. E. Bondybey, *Journal of Chemical Physics*, 1998, **108**, 5398-5403.
2. K. O. Fossan and E. Uggerud, *Dalton Transactions*, 2004, 892-897.
3. B. Pfeffer, S. Jaberg and G. Niedner-Schatteburg, *Journal of Chemical Physics*, 2009, **131**.
4. M. Tombers, L. Barzen and G. Niedner-Schatteburg, *The Journal of Physical Chemistry A*, 2012, **117**, 1197-1203.
5. R. Liyanage, J. B. Griffin and P. B. Armentrout, *J. Chem. Phys.*, 2003, **119**, 8979-8995.
6. R. Liyanage, X. G. Zhang and P. B. Armentrout, *J. Chem. Phys.*, 2001, **115**, 9747-9763.
7. M. P. Irion and P. Schnabel, *J. Phys. Chem.*, 1991, **95**, 10596-10599.
8. S. Chiodo, I. Rivalta, M. D. Michellini, N. Russo, E. Sicilia and J. M. Ugalde, *Journal of Physical Chemistry A*, 2006, **110**, 12501-12511.
9. W. J. Zheng, S. N. Eustis, X. Li, J. M. Nilles, O. C. Thomas, K. H. Bowen and A. K. Kandalam, *Chem. Phys. Lett.*, 2008, **462**, 35-39.
10. M. Citir, F. Liu and P. B. Armentrout, *Journal of Chemical Physics*, 2009, **130**, 16.
11. E. Kapiloff and K. M. Ervin, *Journal of Physical Chemistry A*, 1997, **101**, 8460-8469.
12. T. Kurikawa, M. Hirano, H. Takeda, K. Yagi, K. Hoshino, A. Nakajima and K. Kaya, *J. Phys. Chem.*, 1995, **99**, 16248-16252.
13. Z. Xiuyun and W. Jinlan, *Journal of Physical Chemistry A*, 2008, **112**, 296-304304.
14. M. Gerhards, O. C. Thomas, J. M. Nilles, W. J. Zheng and K. H. Bowen, *Journal of Chemical Physics*, 2002, **116**, 10247-10252.
15. S. Yang and M. B. Knickelbein, *Journal of Chemical Physics*, 1990, **93**, 1533-1539.
16. I. M. L. Billas, A. Chatelain and W. A. Deheer, *Science*, 1994, **265**, 1682-1684.
17. X. S. Xu, S. Y. Yin, R. Moro and W. A. de Heer, *Phys. Rev. Lett.*, 2005, **95**, 4.
18. F. W. Payne, W. Jiang, J. W. Emmert, J. Deng and L. A. Bloomfield, *Physical Review B*, 2007, **75**, 10.
19. M. B. Knickelbein, *Journal of Chemical Physics*, 2006, **125**.
20. S. Peredkov, M. Neeb, W. Eberhardt, J. Meyer, M. Tombers, H. Kampschulte and G. Niedner-Schatteburg, *Phys. Rev. Lett.*, 2011, **107**, 5.
21. F. Liu, R. Liyanage and P. B. Armentrout, *The Journal of Chemical Physics*, 2002, **117**, 132-141.
22. D. Vardhan, R. Liyanage and P. B. Armentrout, *Journal of Chemical Physics*, 2003, **119**, 4166-4178.
23. F. Liu, X.-G. Zhang, R. Liyanage and P. B. Armentrout, *The Journal of Chemical Physics*, 2004, **121**, 10976-10990.
24. M. P. Irion, *Int. J. Mass Spectrom. Ion Process.*, 1992, **121**, 1-47.
25. W. J. Zheng, J. M. Nilles, O. C. Thomas and K. H. Bowen, *Journal of Chemical Physics*, 2005, **122**.
26. M. Ichihashi, T. Hanmura and T. Kondow, *Journal of Chemical Physics*, 2006, **125**.
27. I. Swart, F. M. F. de Groot, B. M. Weckhuysen, P. Gruene, G. Meijer and A. Fielicke, *Journal of Physical Chemistry A*, 2008, **112**, 1139-1149.
28. L. Barzen, M. Tombers, C. Merkert, J. Hewer and G. Niedner-Schatteburg, *International Journal of Mass Spectrometry*, 2012, **330-332**, 271-276.
29. C. Berg, T. Schindler, G. Niedner-Schatteburg and V. E. Bondybey, *J. Chem. Phys.*, 1995, **102**, 4870-4884.
30. D. Proch and T. Trickl, *Rev. Sci. Instrum.*, 1989, **60**, 713-716.
31. P. Caravatti and M. Allemann, *Org. Mass Spectrom.*, 1991, **26**, 514-518.
32. M. Graf, 2006.
33. G. Niedner-Schatteburg, Habilitation Thesis, TU München, 1996.

### 3. H/D isotope effects in the reactions of benzene with iron, cobalt and nickel

---

34. C. Berg, M. Beyer, T. Schindler, G. Niedner-Schatteburg and V. E. Bondybey, *Journal of Chemical Physics*, 1996, **104**, 7940-7946.
35. J. Conceicao, R. T. Laaksonen, L. S. Wang, T. Guo, P. Nordlander and R. E. Smalley, *Physical Review B*, 1995, **51**, 4668-4671.

## 3.7. Supplementary Material

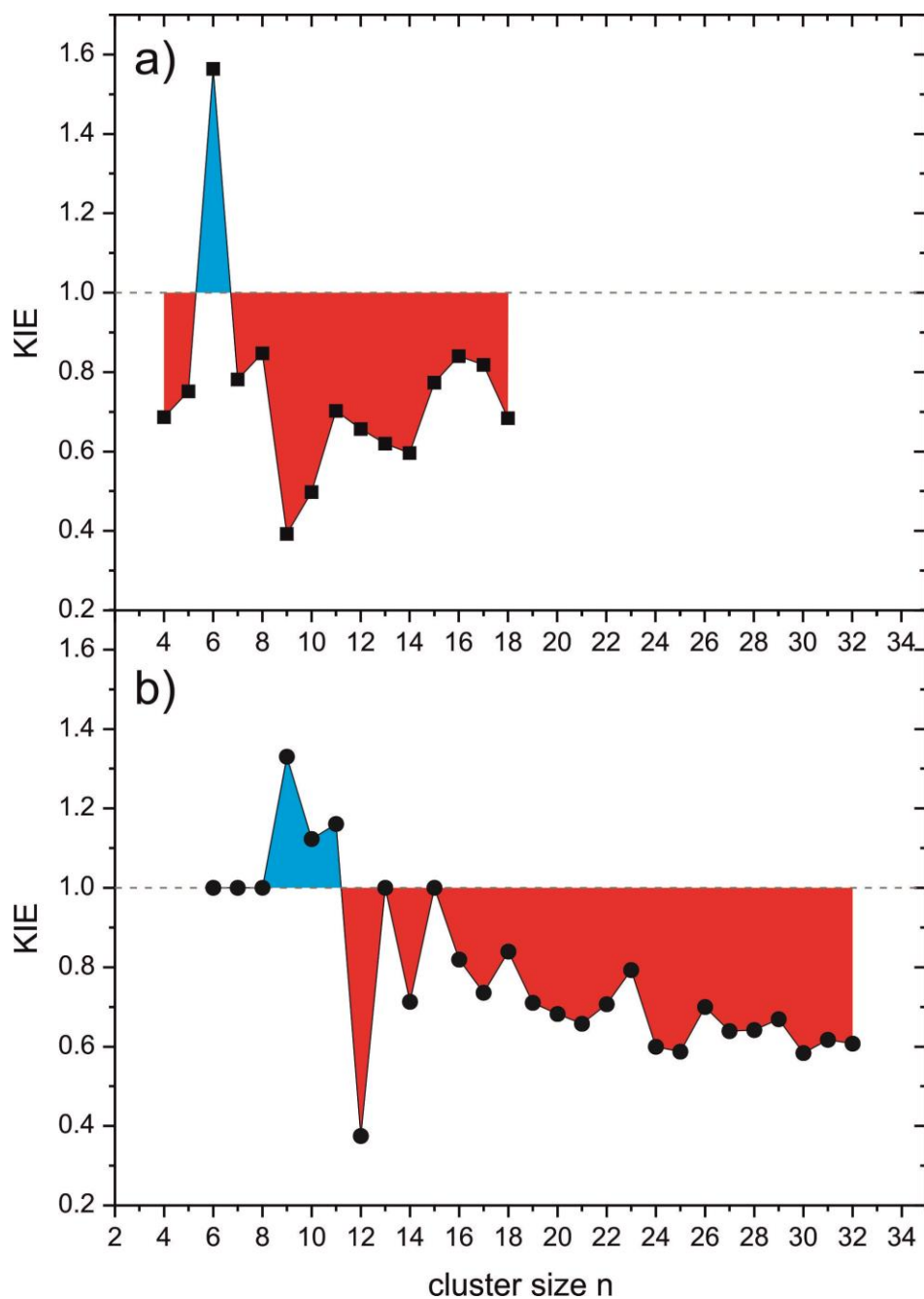


**Figure S1:** KIE( $n$ ) of (a) cationic iron clusters (squares) and of (b) anionic iron clusters (circles). The dotted lines indicate KIE = 1. Blue shaded area indicates a normal KIE while red areas register an inverse isotope effect.

### 3. H/D isotope effects in the reactions of benzene with iron, cobalt and nickel

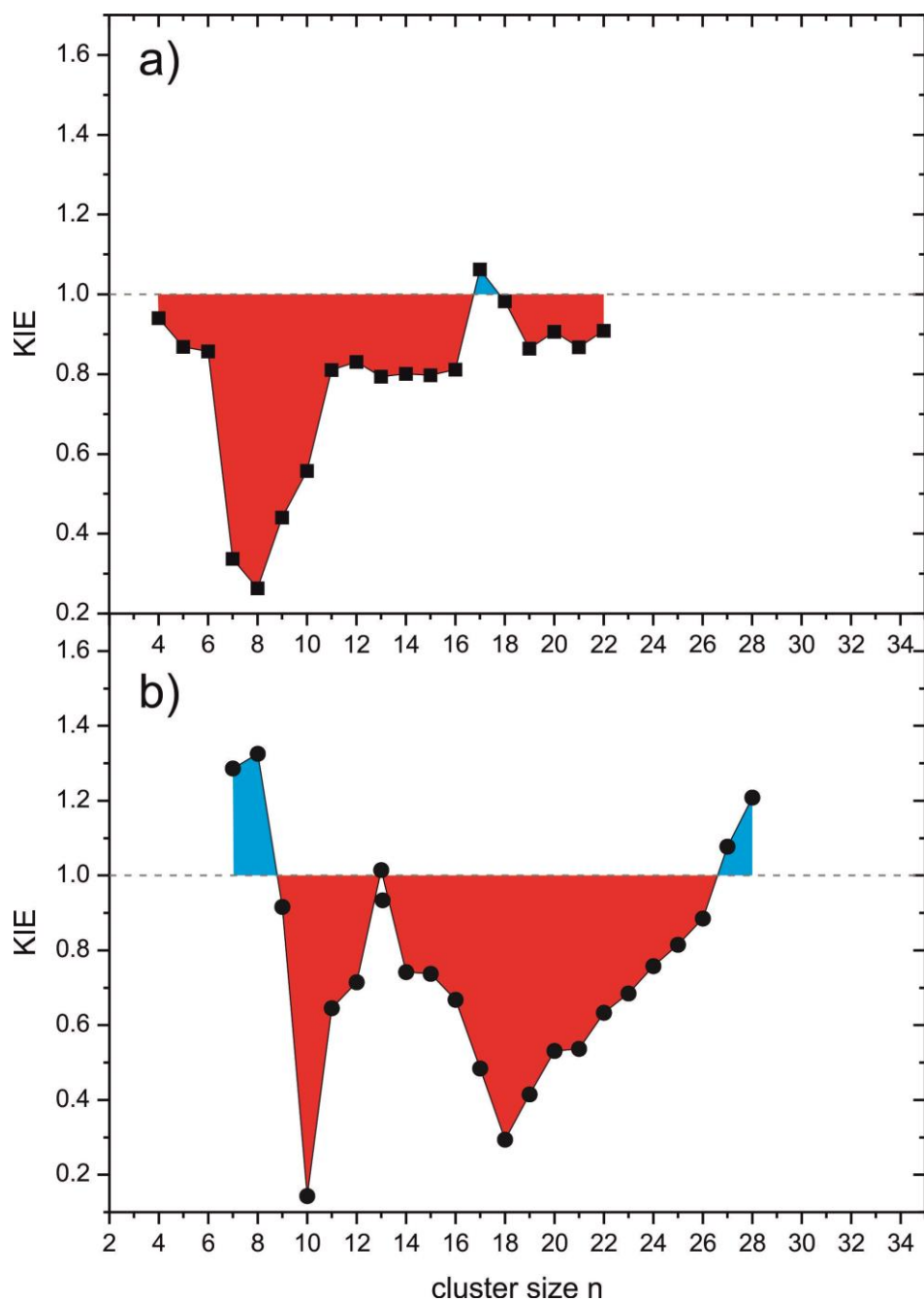


**Figure S2:** KIE( $n$ ) of **(a)** cationic cobalt clusters (squares) and of **(b)** anionic cobalt clusters (circles). The dotted lines indicate KIE = 1. Blue shaded area indicates a normal KIE while red areas register an inverse isotope effect.

### 3. H/D isotope effects in the reactions of benzene with iron, cobalt and nickel

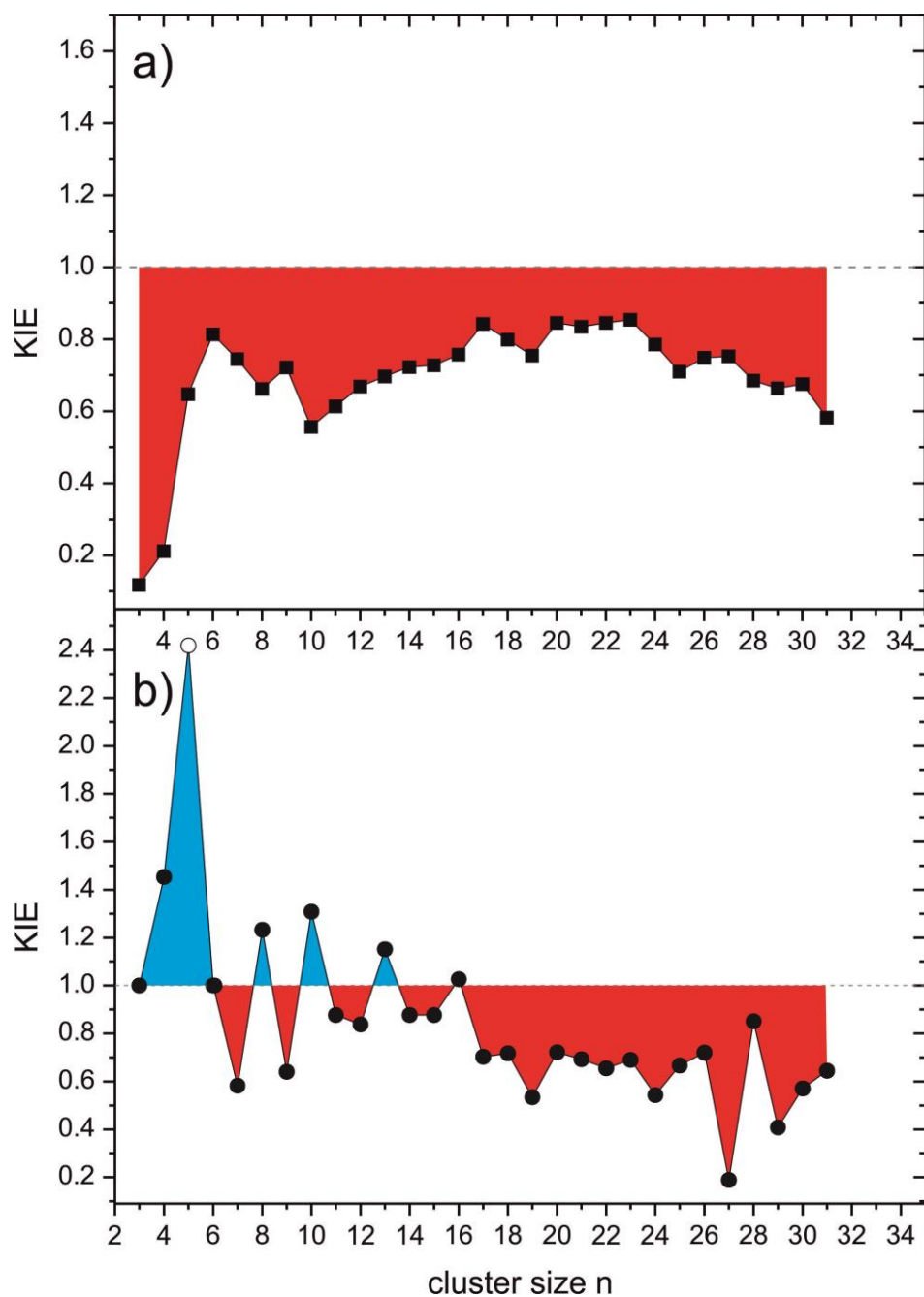


**Figure S3:** KIE of (a) cationic nickel clusters (squares) and (b) of anionic nickel clusters (circles). The dotted lines indicate KIE = 1. Blue shaded area indicates a normal KIE while red areas register an inverse isotope effect.



### 3. H/D isotope effects in the reactions of benzene with iron, cobalt and nickel

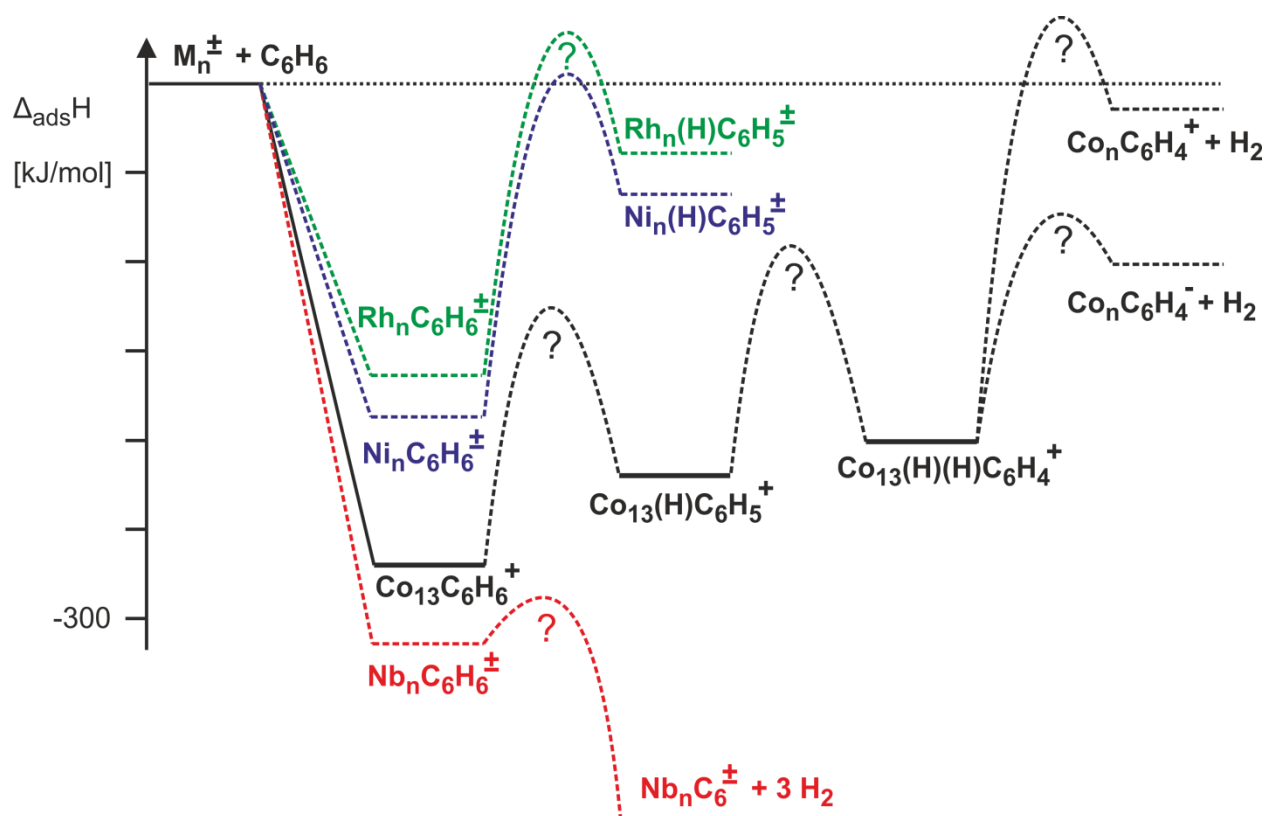


**Figure S4:** Qualitative scheme of the energetics along the reaction coordinate of C-H bond activations in  $Co_{13}^{+/-} + C_6H_6$  (black line) as compared to  $Nb_n^{+/-} + C_6H_6$  (dashed red line) and  $Rh_n^{+/-} + C_6H_6$  (dashed green line). Niobium readily activates benzene while rhodium adsorbs without activation. Neither of both reveals considerable KIEs - irrespective of charge or cluster size. Benzene activation by cobalt clusters is in between and gives rise to KIEs – largely independent of charge and across an intermediate range of cluster sizes. Calculated enthalpies of intermediates along the reaction coordinate of dehydrogenation in  $[Co_{13}C_6H_6]^+$  are indicated in bold – no corresponding values known in the cases of rhodium or niobium. Other charge states and other cluster sizes of  $Co_{13}^{+/-}$  may possess shift values of these enthalpies. The cobalt related part of the diagram closely resembles Scheme (9) within the text body of the publication. The level of theory in the cobalt cluster DFT calculations was PBE/PBE0/cc-pVDZ(C,H),Stuttgart ECP(Co).

#### 3.8. Temperature dependent kinetic studies on the reaction of cationic iron clusters with benzene

Kinetic data are related to thermodynamic data. Obtaining thermodynamic data requires temperature dependent reactivity studies which have a long tradition. Investigations on protonated water clusters  $H^+(H_2O)_n$  ( $n = 5, \dots, 65$ ) were investigated under collision free conditions in an ICR ion trap<sup>1</sup>. Due to absorption of the black body background irradiation the clusters evaporate water molecules. The rates of evaporation exhibit an lifetime proportional to  $1/n$ . Some clusters (e.g.  $n = 21$  or 55) deviate from the overall trend. These deviations are attributed to higher stabilities. Other FT-ICR studies of ionic water clusters containing small organic molecules reveal that the loss of a ligand molecule occurs spontaneously and is pressure independent. The ions gain the energy required for the fragmentation by absorption of blackbody radiation<sup>2</sup>. The BIRD method has no mass limit and is selective for low-energy fragmentation. The temperature dependence of the dissociation rate constants generate Arrhenius activation energies<sup>3</sup>. Gas phase studies of unimolecular decay kinetics of an anionic fullerene derivate encapsulating one water molecule is studied in a temperature programmable FT-ICR cell<sup>4</sup>. The rate constants for the loss of water as a function of temperature are evaluated by the use of the Arrhenius equation to yield an activation energy.

The modified FT-ICR mass spectrometer allows the admission of thermalized reaction gas into the ICR cell. Therefore the reaction gas is added over a long copper tube spiraling around a cooled copper block (see chapter bla for a detailed picture). For XMCD measurements cooled helium is pulsed into the ICR cell<sup>5, 6</sup>. The pulsed admission allows for higher gas density in the ICR cell. The ions are effectively cooled. In the case of continuous admission, as required for reactivity studies, the ions are not effectively cooled. To achieve thermalisation of the cluster ion cloud a different approach is required. Nevertheless, we performed measurements with thermalized reaction gas (benzene). The reaction gas is admitted into the ICR cell via a leak valve. A thermostat (*Hake K41* with a *Hake DC50* controller) allows for thermalisation of the reaction gas.

Room temperature studies on cationic iron clusters reveal strong size dependence (see chapter 3.4.1.). Most remarkably is a minimum in the total relative rate constants for the cluster sizes  $n = 6 - 7$  and a dip for  $n = 15, 16, 17$ . Temperature dependent studies reveal the same trends as the room temperature measurements (cf. Fig. 5). The influence of the variation in temperature is small. For the most cluster sizes the total relative rate constants at room temperature and higher (red and orange, CF. Fig. 5) are higher as the rate constants obtained at lower temperatures. This is not the case for all cluster sizes.

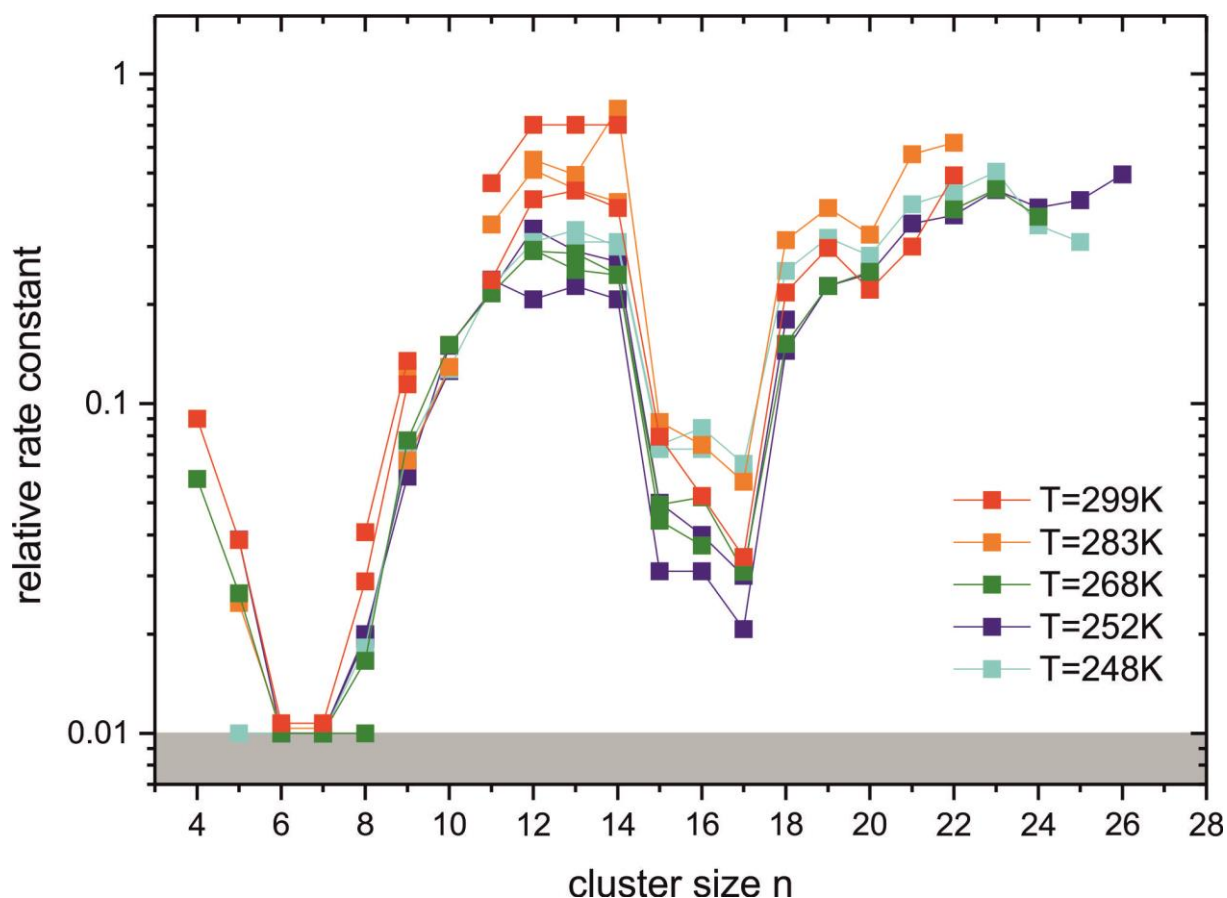


**Figure 5:** temperature dependent kinetic measurements of the reaction of cationic iron clusters with benzene. the neutral benzene is added over a leak valve and thermalized by a the modified cooling block of the FT-ICR mass spectrometer.

The deviations from the ideal behavior, faster reactions at higher temperatures, can be explained by the temperature of the cluster ions. Controlling the temperature of the reaction gas is not sufficient to cool the cluster ions. The temperature of the cluster cations is not effected by the temperature of the reaction gas. The studies has been performed by a pressure of  $3 \cdot 10^{-9}$  mbar. In these pressure region collision with the reaction gas are rare (single collision conditions) and thermalisation of the cluster temperature is impossible.

This is a first attempt of temperature dependent kinetic studies. The thermalisation of the reaction gas is insufficient to obtain a distinct temperature dependence of the relative rate constants. The estimation of the activation energy is out of reach so far. The thermalisation of the cluster ions requires the addition of a second neutral gas (e.g. helium). This neutral gas is pulsed in the ICR cell to reach higher pressures and to cool or heat the cluster temperature effectively. This experiments are

### **3. H/D isotope effects in the reactions of benzene with Iron, Cobalt and Nickel**

---

planned and with small modifications on the experimental set up possible in near future. The estimation of activation energies will provide deeper insights and better understanding of reactions with cluster ions.

#### 3.9. References

1. T. Schindler, C. Berg, G. Niedner-Schatteburg and V. E. Bondybey, *Chem. Phys. Lett.*, 1996, **250**, 301-308.
2. D. Thoelmann, D. S. Tonner and T. B. McMahon, *The Journal of Physical Chemistry*, 1994, **98**, 2002-2004.
3. W. D. Price, P. D. Schnier and E. R. Williams, *Anal. Chem.*, 1996, **68**, 859-866.
4. O. Hampe, T. Karpuschkin, M. Vonderach, P. Weis, Y. M. Yu, L. B. Gan, W. Klopper and M. M. Kappes, *Phys. Chem. Chem. Phys.*, 2011, **13**, 9818-9823.
5. S. Peredkov, M. Neeb, W. Eberhardt, J. Meyer, M. Tombers, H. Kampschulte and G. Niedner-Schatteburg, *Phys. Rev. Lett.*, 2011, **107**, 233401.
6. S. Peredkov, A. Savci, S. Peters, M. Neeb, W. Eberhardt, H. Kampschulte, J. Meyer, M. Tombers, B. Hofferberth, F. Menges and G. Niedner-Schatteburg, *Journal of Electron Spectroscopy and Related Phenomena*, 2011, **184**, 113-118.



#### 4. H/D isotope effects in the reaction of benzene with Cobalt Gold and Cobalt Rhodium bimetallic cluster ions

---

#### 4. H/D isotope effects in the reactions of benzene with Cobalt Gold and Cobalt Rhodium bimetallic cluster ions

##### 4.1. Preamble

This work is dedicated for publication in a slightly different way at *Journal of Chemical Physics* with the title: "H/D isotope effects in the reaction of benzene with Cobalt Gold and Cobalt Rhodium bimetallic cluster ions". The text of the publication was mainly written by me. Measurements and data evaluation were done by Jennifer Mohrbach and me.

##### Abstract

In continuation to our prior work on ionic bimetallic cobalt platinum clusters we investigated further bimetallic cobalt clusters. Kinetic Isotope Effects (KIE) in total reaction rates are inverse and – in part – large. Dehydrogenation Isotope Effects (DIE) are normal. A previously established multistep model of adsorption and stepwise dehydrogenation from the precursor adsorbate proves suitable to rationalize the found KIEs and DIEs in principle. Particular insights into the effects of charge and of cluster size are possible but largely speculative. Accordingly, the elucidation of the transition metal cluster – benzene system requires further efforts in experiment, in modeling and in high level ab initio calculations.

##### 4.2. Introduction

The elucidation of elementary processes in heterogeneous catalysis is necessary to gain knowledge on catalysis. Transition metal clusters may serve as model systems to illuminate heterogeneous catalytic processes. Hydrocarbon adsorption and subsequent C-H bond activation steps are often rate limiting in many catalyzed reactions. A catalytically active transition metal is cobalt with numerous applications as heterogeneous catalyst, in particular as an important metal component in the benzene hydrogenation at low temperatures<sup>1</sup>. Its redox properties allow for ease of electron transfer via unstable intermediates<sup>2</sup>. Gas phase studies on cobalt clusters investigated the unique catalytic properties of this transition metal. Armentrout *et al.*<sup>3</sup> determined the bond energies to D, C, CD, CD<sub>2</sub> and CD<sub>3</sub> on cobalt cluster cations through methane activation. Furthermore, Armentrout *et al.* determined the bond energies (BDE) of cobalt-benzene and cobalt-dimer-benzene cations (2.65(11) and 1.73(14) eV, respectively)<sup>4</sup>. The structure of cobalt benzene adducts has been investigated by different research groups<sup>5-7</sup>. The benzene activation by cationic and anionic cobalt clusters revealed that dehydrogenation by cationic clusters is sparse, while it is ubiquitous in reactions by anionic clusters and the H/D exchange revealed a large inverse kinetic isotope effect KIE<sup>8</sup>. Prior gas phase studies of benzene adsorption and activation focused on niobium and rhodium clusters<sup>9-11</sup>. Apparently intact adsorption prevails on ionic rhodium clusters while ionic niobium clusters vividly dehydrogenate benzene. Little to no observable isotope effects occurred in either cases.

One possible approach to enhance the catalytic properties of cobalt is the combination with other transition metals. Bimetallic PtCo catalysts exhibit a higher activity in benzene hydrogenation than monometallic Co and Pt catalysts<sup>1</sup>. A flow and batch reactor study on the hydrogenation of benzene over silica-supported PtCo, PdCo, RuCo bimetallic and the corresponding monometallic catalysts reveals the trend: PtCo >> PdCo > RuCo ~ Pt ~ Co ~ Ru ~ Pd<sup>12</sup>. The gas phase study on mixed ionic  $Co_nPt_m^{+/-}$  clusters in the size range  $n + m \leq 8$  reveals that dehydrogenation by cationic cobalt clusters  $Co_n^+$  is sparse but it is effective in small bimetallic clusters,  $n + m \leq 3$ . Kinetic Isotope Effects KIE(n) in total reaction rates are inverse and – in part – large<sup>13</sup>.

The investigation of kinetic isotope effect (KIE) may contribute to elucidate the elemental processes on the cluster surface. The investigation of C-H bond reductive elimination of benzene from phenyl metal hydrides revealed a normal kinetic isotope effect in the case of molybdenocene and an inverse KIE in the case of tungstenocene<sup>14</sup>. Relative barrier heights may determine the kinetics and suffice to switch observable KIEs. The study of temperature dependent alkane reductive elimination from alkyl metal hydrides leads to similar interpretations<sup>15-18</sup>. the absence of a KIE in the reaction of neutral



#### 4. H/D isotope effects in the reaction of benzene with Cobalt Gold and Cobalt Rhodium bimetallic cluster ions

---

zirconium with ethylene and propylene is interpreted in terms of a stepwise association – activation mechanism<sup>19</sup>.

In this work we combine cobalt with other catalytically active transition metals, namely gold and rhodium. Gold is a highly catalytic active transition metal which has the ability to accept hydrogen atoms from a chemisorbed molecule and therefore catalyzes dehydrogenation reactions<sup>20</sup>. The second investigated metal is rhodium which exhibit a high reactivity towards hydrogen and is an effective hydrogenation catalyst<sup>21-24</sup>. Now, we present our results on  $Co_nAu_m^{+/-}$  and  $Co_nRh_m^{+/-}$  clusters and compare them with the results on  $Co_nPt_m^{+/-}$  clusters.

## 4. H/D isotope effects in the reaction of benzene with Cobalt Gold and Cobalt Rhodium bimetallic cluster ions

---

### 4.3. Materials and Methods

All experiments are realized with a modified Fourier-Transform Ion Cyclotron Resonance (FT-ICR) mass spectrometer (Bruker Apex IV). Ion generation took place by a laser vaporization source<sup>25</sup>. Ions originate from a rotating alloy disc (CoAu alloy: 90 at% Co and 10 at.% Au; CoRh alloy: 90 at% Co, 10 at.% Rh). The second harmonic of a Nd:YAG Laser (Spitlight 200, Innolas) generates a metal plasma which is captured and cooled by a short transverse He pulse (40  $\mu$ s, He pressure 8-15 bar) from a homebuilt piezoelectric valve<sup>26</sup>. A supersonic nozzle expansion through a 20 mm long expansion channel (diameter 2mm) provides further cooling. This set up generates singly charged anions and cations without further ionisation step. After having passed through a 1.4 mm skimmer the ions are accelerated and transferred via a 90° ion beam bender and electrostatic lenses into the high field region of a superconducting magnet (7.05 T, actively shielded). The ions are trapped for reaction and detection in a so called “infinity” ICR cell<sup>27</sup>.

In the ICR cell the ions are trapped and may undergo reactions. A leak valve allows for controlled admission of reaction gas and raises the pressure from  $\leq 3 \times 10^{-10}$  mbar up to  $3 \times 10^{-9}$  mbar in the ICR cell. This results in about one bimolecular reactant collision per cluster per second (single collision conditions). The nominal pressure reading derives from a commercial ultrahigh vacuum gauge, which is subject of a pressure gradient towards the ICR cell. Therefore, the absolute value of pressure and reactant gas number density at the location of the stored ions is not known exactly. The reactant gases benzene and benzene- $d_6$  (Sigma Aldrich, purity >99.6 %) are degassed by several “pump and freeze” cycles previous to their application. The kinetic curves of reactant and product ions arise from reaction delay scans and subsequent evaluation of recorded mass spectra. Fits to pseudo-first-order-kinetics are conducted by the “evofit” program<sup>28</sup>, a genetic algorithm fit program.

Fitting the recorded kinetics yields relative partial rate constants for association and for dehydrogenation. The total relative rate constants  $k_{tot}^{(H,D)}(n)$  are the sum of all first step relative partial rate constants obtained by the genetic algorithm fit program. The ratio of the total rate constants with benzene  $k_{tot}^{(H)}(n)$  and with benzene- $d_6$   $k_{tot}^{(D)}(n)$  defines the kinetic isotope effect  $KIE(n)$ :

$$KIE(n) := \frac{k_{tot}^{(H)}(n)}{k_{tot}^{(D)}(n)} \quad (1)$$

#### 4. H/D isotope effects in the reaction of benzene with Cobalt Gold and Cobalt Rhodium bimetallic cluster ions

---

A normal KIE means that the reaction with benzene is faster than with benzene- $d_6$  (KIE > 1). If the reaction with perdeutero benzene is the faster one, the KIE is inverse (KIE < 1).

To reduce the amount of data we define the average degree of dehydrogenation  $\langle \chi_n \rangle$  as was done before<sup>29</sup>:

$$\langle \chi_n \rangle = \frac{1}{m} \frac{1}{k_n^{tot}} \sum_{m_i=1}^m m_i k_n(m_i) \quad (2)$$

with

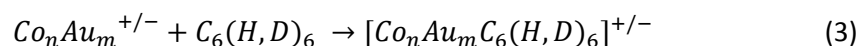
$$k_n^{tot} = \sum_{m_i=1}^m k_n(m_i)$$

Here,  $m$  (= 6 in the present case) indicates the total amount of hydrogen or deuterium atoms available from benzene. The partial reaction rates  $k_n(m_i)$  classify according to the cluster size  $n$  and the loss of hydrogen or deuterium atoms  $m_i$  in the observed product.  $\langle \chi_n \rangle = 1$  would indicate complete dehydrogenation while  $\langle \chi_n \rangle = 0$  would indicate adsorption without any dehydrogenation.

### 4.4. Results and discussions

#### 4.4.1. Reactions of cobalt gold cluster

We recorded the reaction kinetics of  $Co_nAu_m^{+/-}$  cluster. The investigated cluster sizes react with benzene and benzene- $d_6$  to form a single type of products:



This prevails for anionic as well as cationic clusters and for the reaction with both benzene and perdeutero benzene. The sum formula is well defined through the high resolution mass spectrometry while the structure is not. The square parenthesis indicates this ambiguity in its molecular structure. It is reasonable, that benzene does react beyond mere attachment to the cluster ions. The formation of a hydrido-phenylic complex ( $[Co_nAu_mC_6(H,D)_5(H,D)]^{+/-}$ ) is possible. Activation of multiple C-H bonds would lead to a subsequent pair wise recombination of the hydridic H-atoms and desorption of molecular hydrogen which is not observed. Anionic clusters may stabilize by electron detachment. By the time, we found no evidence for such neutralization processes.

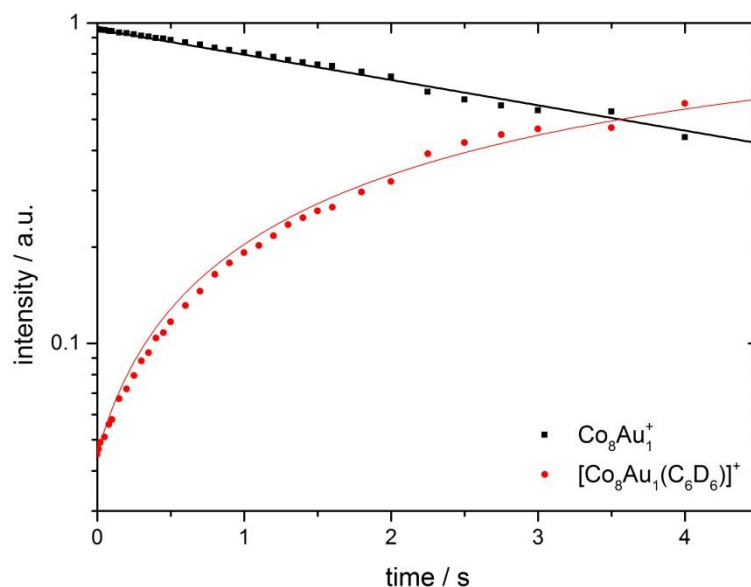


**Figure 1:** An example for the reaction kinetics of  $Co_8Au_1^+$  (black, squares) with  $C_6D_6$ . Symbols represent experimental data, solid lines represent numerical fits by a genetic algorithm to pseudo-first-order-kinetics.

Fitting the recorded kinetics yields relative total rate constants for association (cf. Figure 2 and Figure 3). Cationic clusters reveal a pronounced cluster size dependence. Pure cobalt clusters show a

#### 4. H/D isotope effects in the reaction of benzene with Cobalt Gold and Cobalt Rhodium bimetallic cluster ions

distinct minimum in the reaction rate for the cluster with six atoms. This reproduces our previous findings well<sup>13</sup> and corresponds also to the observed minimum in the total reactivity of  $Fe_6^+$  and  $Fe_7^+$  (cf. chapter 4). This similarity is in support of the speculation on an octahedral coordination motif at  $n = 6$  in both cases.

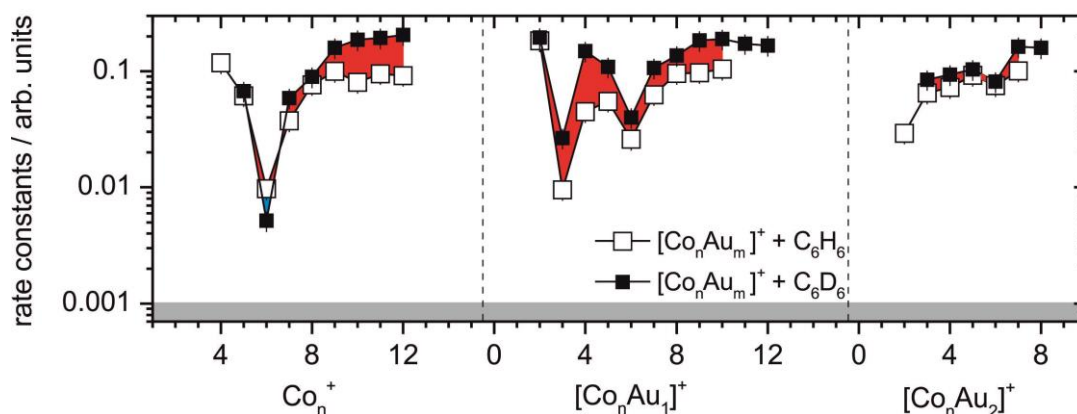


**Figure 2:** Total rate constants for the reaction of  $Co_nAu_m^+$  with benzene (open symbols) and perdeutero benzene (solid symbols). The observed inverse Kinetic Isotope Effect (KIE) is emphasized by red shading of the areas in between of the corresponding rate constants. The noise equivalent level of the present experiments is indicated in grey.

The addition of a gold atom to the cobalt clusters changes the situation dramatically. Two drops in the relative rate constants appear (cf. Figure 2). The first drop in reactivity arises in the cluster size  $Co_3Au_1^+$ . This cluster size constitutes of four atoms. Several structures are possible, e.g. trigonal planar structure with a gold atom on top. Obviously the high resolution mass spectrometer does not provide such information. To gain structural information IR-MPD studies on cluster adsorbate complexes are recommended and planned. The second drop in the relative rate constants provides the cluster size  $Co_5Au_1^+$ . Remarkably, the cluster of six atoms provides also a minimum in the rate constants. The additional gold atom seems to reduce the drop in reactivity compared to pure cobalt clusters. Possibly, the different atom sizes may disturb the possible octahedral structure.

The relative rate constants rise with the cluster size for clusters containing two gold atoms. A small drop of reactivity arises at the cluster size  $Co_7Au_2^+$ . This minimum is not distinct.

In all observed cluster sizes the reaction with perdeutero benzene is faster than the reaction with benzene. This equals an inverse isotope effect. Eventually, gold atoms in the mixed clusters enhance

#### 4. H/D isotope effects in the reaction of benzene with Cobalt Gold and Cobalt Rhodium bimetallic cluster ions

the rate constants in comparison of pure cobalt clusters. Small cationic mixed clusters exhibit higher reactivity. The inverse isotope effect decreases with the addition of gold atoms.

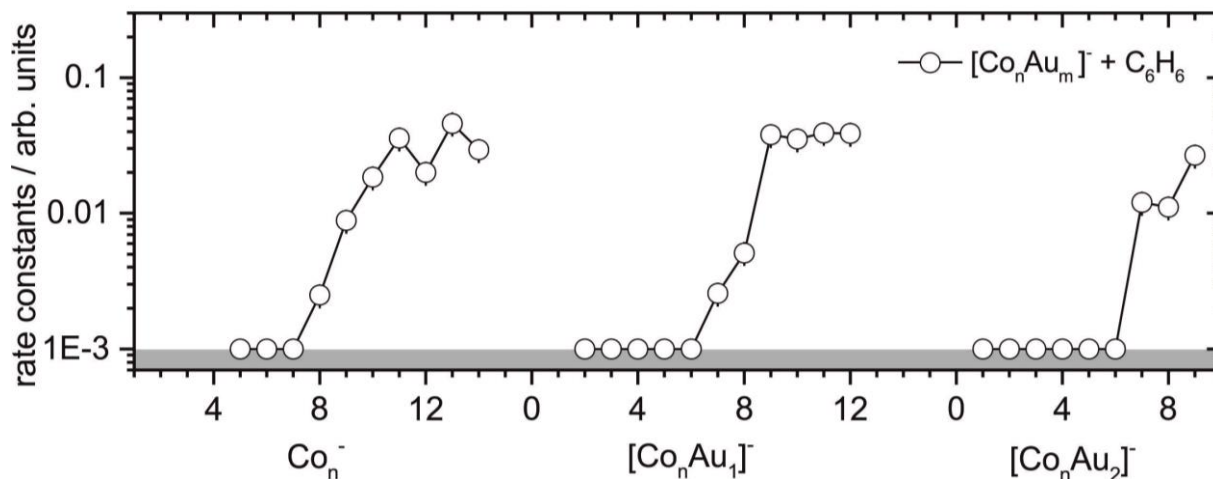


**Figure 3:** Total rate constants for the reaction of  $Co_nAu_m^-$  with benzene. The noise equivalent level of the present experiments is indicated by grey shading.

Only the reaction of anionic cobalt gold clusters with benzene provides for relative rate constants. The reaction with perdeutero benzene is missing and needs recapitulation of both reactions to ensure comparable reaction conditions. The relative rate constants of anion clusters are one magnitude minor to the rate constants of cationic clusters. Small pure cobalt clusters show no reaction with benzene due to charge interaction. The negative charge and the high electron density repel each other. The negative charge is more distributed in larger clusters. Thus a reaction can take place. In pure cobalt clusters a reaction occurs in clusters containing more than seven atoms ( $n > 7$ ). The rise of the total rate constants in mixed clusters starts with the cluster sizes  $Co_6Au_1^-$  and  $Co_6Au_2^-$ . Once the critical atom number in the cluster is reached the relative rate constants rises nearly linearly. No distinct rises or drops occur in the rate constants.

#### 4.4.2. Reaction of cobalt rhodium cluster

The recorded kinetics of mixed ionic cobalt rhodium clusters reveal that only two processes take place. In a first step the clusters absorb benzene and perdeutero benzene seemingly intact (cf. (3a)). In a proceeding step we observe the desorption of one molecular hydrogen (cf. (3b)). Desorption of more than one hydrogen molecule or an odd number of hydrogen atoms does not occur.

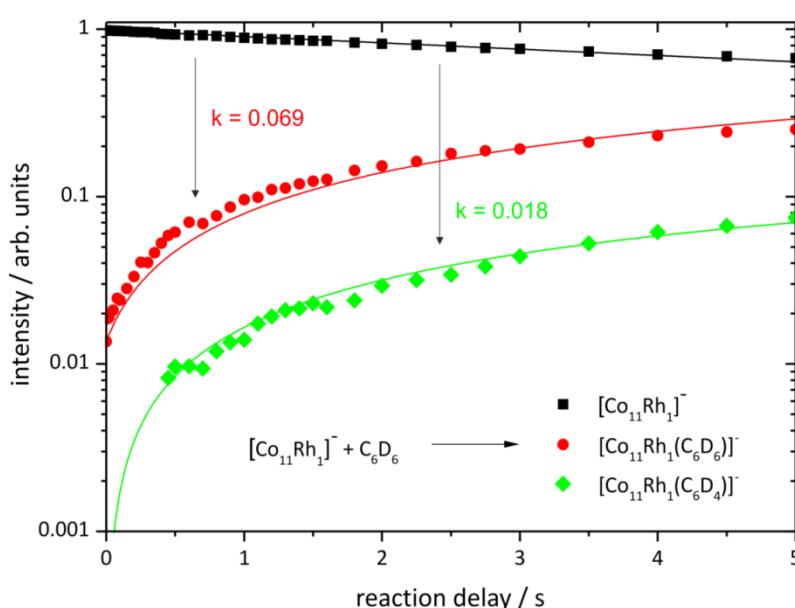
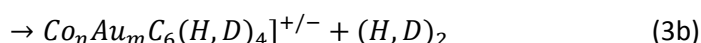
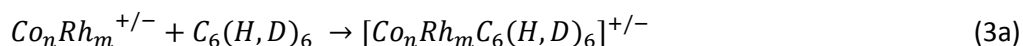


**Figure 4:** An example for the reaction kinetics of  $\text{Co}_{11}\text{Rh}_1^-$  with benzene- $d_6$ . The symbols represent experimental data, solid lines represent numerical fits by a generic algorithm to pseudo-first-order-kinetics. Association products (red, circles) and dehydrogenation (green, diamonds) behave the expected way.

Fitting the recorded kinetics yields relative total rate constants for association (cf. Figure 5). Cationic clusters reveal a pronounced cluster size dependence. In this reaction kinetic the pure cobalt cluster containing six atoms reveals a minimum in the rate constants as expected<sup>13</sup> and corresponds to the observed minimum in the total reactivity of  $\text{Fe}_6^+$  and  $\text{Fe}_7^+$  and  $\text{Ni}_6^-$  (cf. chapter 4). This similarity is in support of the speculation on an octahedral coordination motif at  $n = 6$ .

The addition of one rhodium atom changes the situation dramatically. The relative rate constants rise with increasing cluster size. A shallow minimum in rate constant arises for the cluster consisting of

#### 4. H/D isotope effects in the reaction of benzene with Cobalt Gold and Cobalt Rhodium bimetallic cluster ions

seven atoms. This finding deviates from the cobalt behavior. For higher cluster sizes the rate constants rises until the maximum reaction rate is reached.

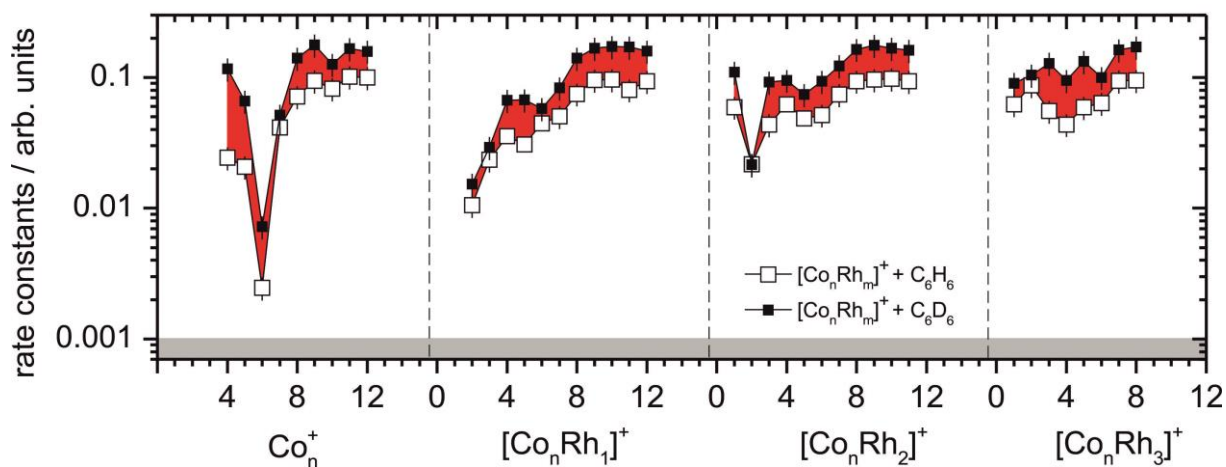


**Figure 5:** Total rate constants for the reaction of  $Co_nRh_m^+$  with benzene (open symbols) and benzene- $d_6$ . The observed inverse Kinetic Isotope Effect (KIE) is emphasized by red shading of the areas in between of the corresponding rate constants. The noise equivalent level of the present experiments is indicated in grey.

Two rhodium atoms in mixed cobalt clusters increase the rate constants compared to small cobalt clusters. Here, we observe a drop in reactivity for the cluster size  $Co_2Rh_2^+$ . It may be due to structural or electronic effects. A possible structure is a tetrahedron and a quadratic planar structure. To decide which structure is likely further studies are needed. Clusters containing three rhodium atoms exhibit no distinct drops and rises in their relative rate constants. The relative rate constants rise with increasing cluster size until the maximal observed reaction rate is reached. This experimental maximal rate constant may equal the collision rate which means that every collision leads to an adsorption of benzene to the cluster surface.

Pure cationic rhodium clusters react with benzene under total or partial dehydrogenation in competition with nondissociative adsorption<sup>30</sup>. The reaction with perdeutero benzene has little effect upon the observed reactions. The KIE values vary between 0.5 and 0.8.



#### 4. H/D isotope effects in the reaction of benzene with Cobalt Gold and Cobalt Rhodium bimetallic cluster ions

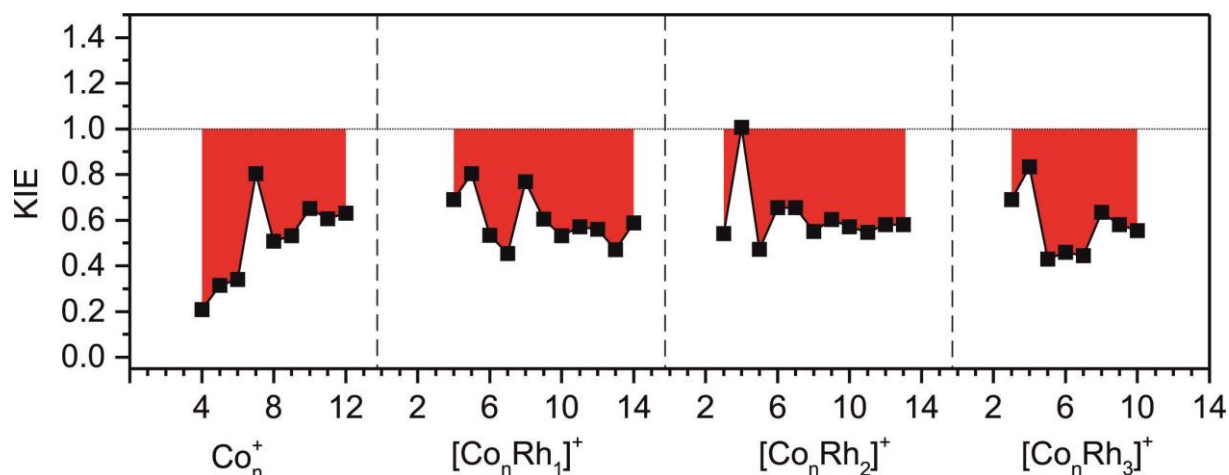


**Figure 6:** the ratio of  $k(\text{H})/k(\text{D})$  equation (1). Red shaded areas symbolize inverse KIE which prevails and blue shaded areas indicates a normal KIE

The relative rate constants of anionic cobalt rhodium clusters (cf. Figure 7) are less reactive compared to the cationic clusters. Pure cobalt clusters show the same behavior reported in chapter 4, reaction products appear in the mass spectrum for pure cobalt clusters containing more than six atoms in the reaction with benzene and more than seven atoms in the reaction with benzene- $d_6$ . The relative rate constants rise with increasing cluster size. A drop in reactivity appears for the cluster size  $n = 10$ .

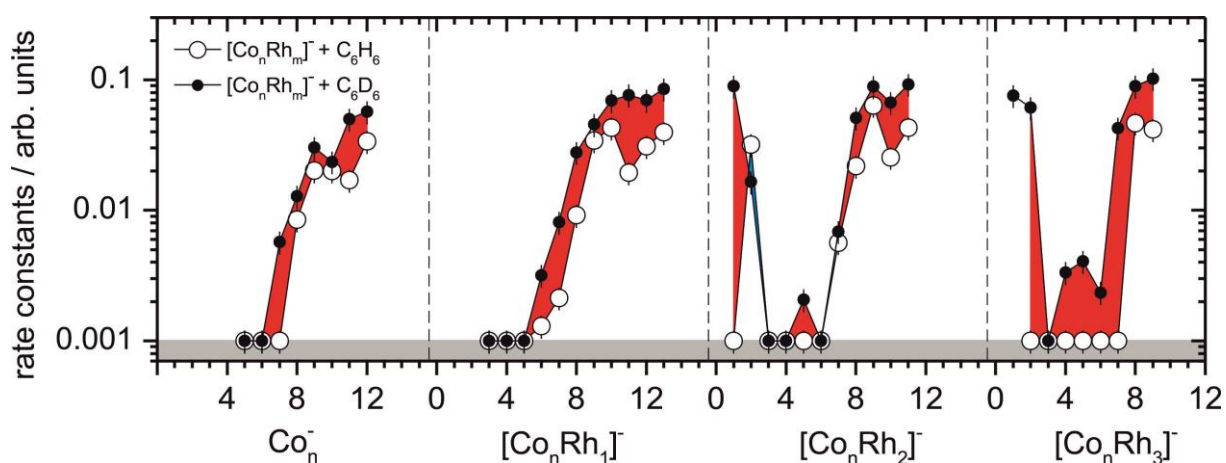


**Figure 7:** Total rate constants for the reaction of  $\text{Co}_n\text{Rh}_m^-$  with benzene (open symbols) and benzene- $d_6$  (solid symbols). The observed inverse Kinetic Isotope Effect (KIE) is emphasized by red shading of the areas in between of the corresponding rate constants. The noise equivalent level of the present experiments is indicated by grey shading.

cobalt clusters with one additional rhodium atom show the same behavior. The rate constants rise with increasing cluster size until the upper limit is reached. This upper limit may represent the collision rate.

#### 4. H/D isotope effects in the reaction of benzene with Cobalt Gold and Cobalt Rhodium bimetallic cluster ions

The addition of more than one rhodium atom leads to a pronounced size dependence of the relative rate constants. The relative rate constants decrease for  $3 < n < 7$  for two rhodium atoms and  $3 < n < 8$  for clusters containing three rhodium atoms. The observed isotope effect is inverse with one exception  $Co_3Rh_2^-$ . The values of the inverse KIE range from 0.01 to 1.9.

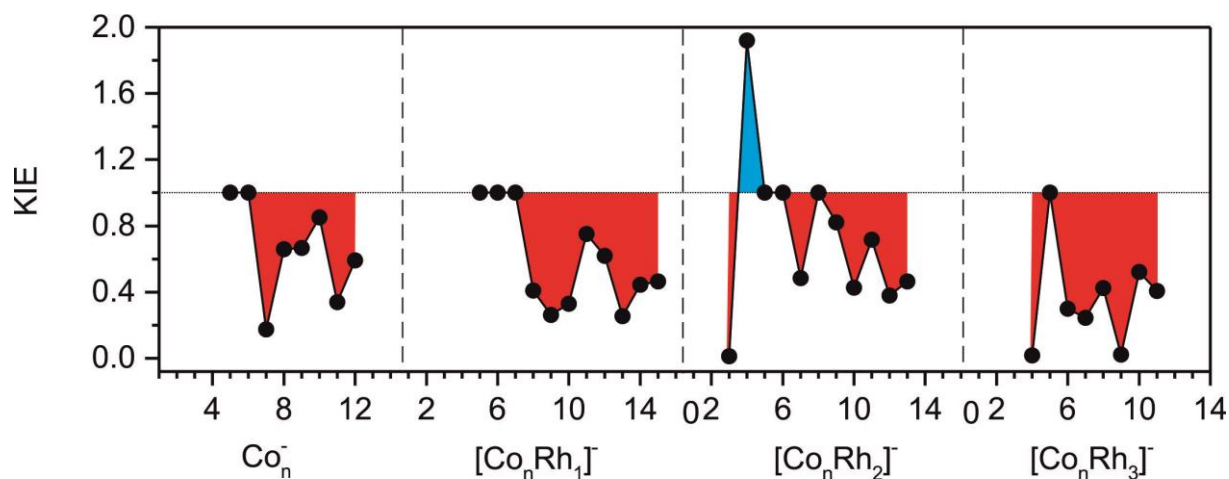


**Figure 8:** The ratio of  $k(H)/k(D)$  see equation (1). Red shaded areas symbolize inverse KIE which prevails and blue shaded areas indicates a normal KIE.

Pure anionic rhodium clusters react with benzene under partial dehydrogenation<sup>9</sup>. Since cationic and anionic rhodium clusters are able to dehydrogenate benzene, we observe dehydrogenation products in mixed rhodium clusters as well<sup>9,30</sup>.

#### 4. H/D isotope effects in the reaction of benzene with Cobalt Gold and Cobalt Rhodium bimetallic cluster ions

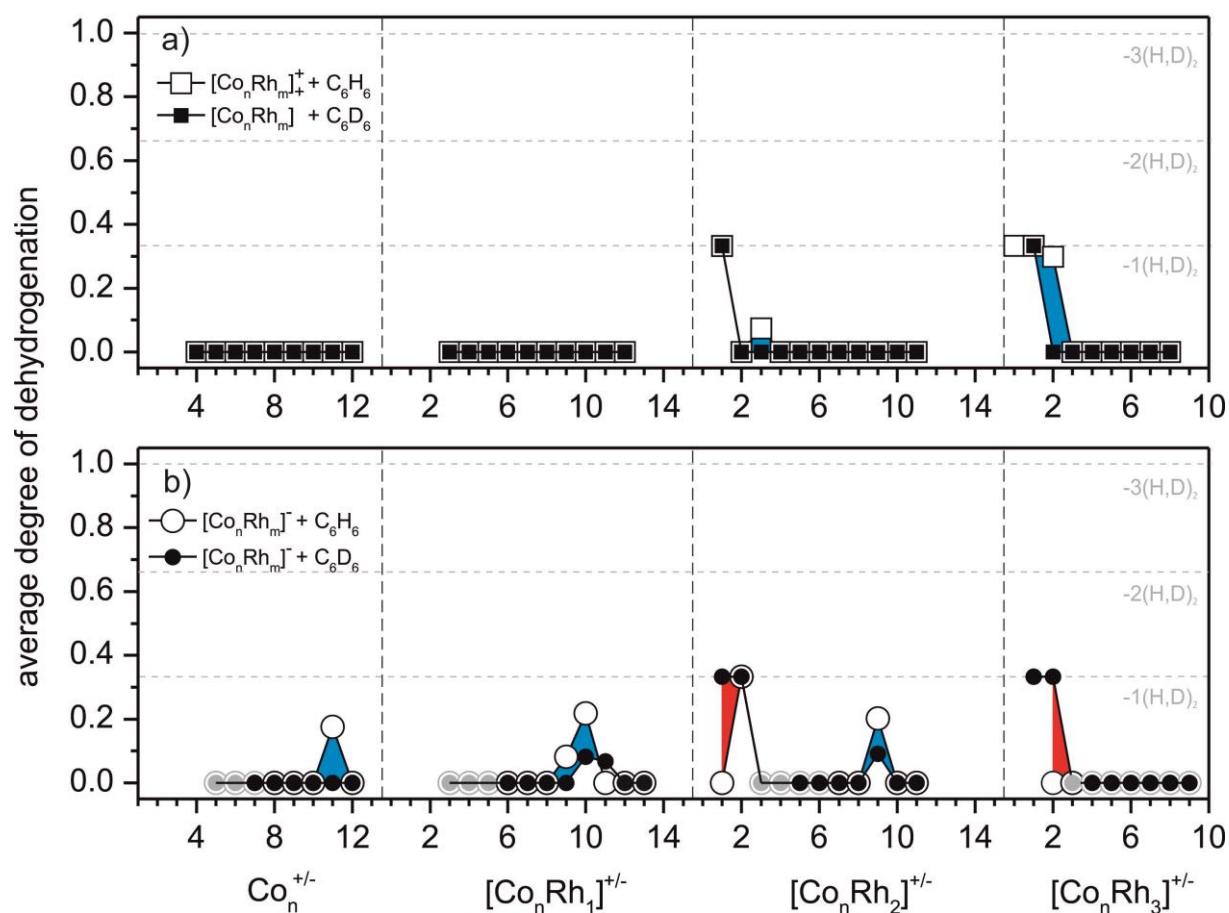


**Figure 9:** Average degree of dehydrogenation  $\langle \chi_n \rangle$  (a) by pure and mixed cationic clusters and (b) by pure and mixed anionic clusters. Blue areas indicate a normal Dehydrogenation Isotope Effect (DIE > 1). Those values that are indicated in grey arise from vanishing total reaction rates. Solid symbols represent reaction with benzene- $d_6$ , open symbols with benzene. Uncertainties are within the size of the symbols.

No dehydrogenation products occur in the mass spectra of pure cationic cobalt clusters and clusters containing one rhodium atom. The characteristics of rhodium dominate in small clusters containing two or three rhodium atoms. These clusters show products of a single dehydrogenation step. Dehydrogenation becomes a common feature in the reactions of anionic cluster. Only  $Co_{11}^-$  forms dehydrogenation products. The addition of one rhodium atom expands this effect to the range of  $9 > n > 11$ . Two rhodium clusters shift this reactive range to the cluster size  $n = 9$ . Here also small  $Co_nRh_2^-$  clusters ( $n = 1, 2$ ) show dehydrogenation products. The characteristics of rhodium predominate in the reaction with benzene. Surprisingly for these small clusters an inverse isotope effect prevails while for the other cluster sizes a normal dehydrogenation isotope effect occurs.

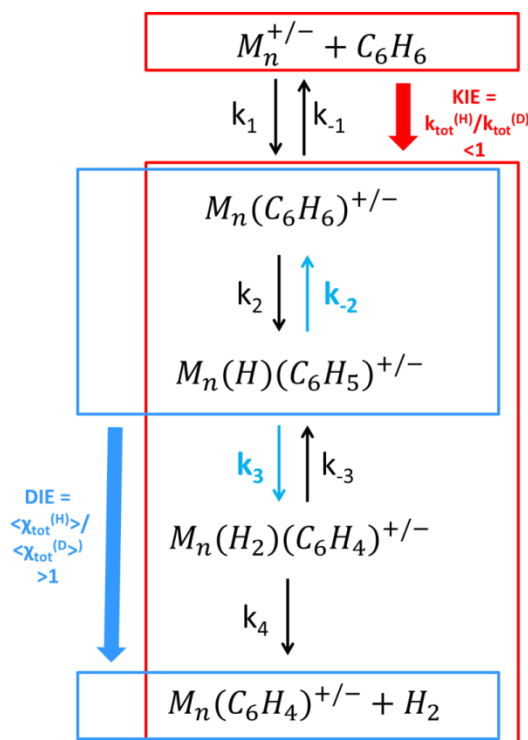
#### 4. H/D isotope effects in the reaction of benzene with Cobalt Gold and Cobalt Rhodium bimetallic cluster ions

##### 4.4.3. Comparison of the studies on mixed clusters

In this paper we investigate the reaction of cobalt gold and cobalt rhodium clusters with benzene and benzene- $d_6$ . Strikingly, the investigated cluster sizes have common features.

- (1) We find an inverse KIE  $< 1$  that prevails in all investigated ionic clusters – only few, single cluster sizes exhibit a normal KIE  $> 1$ .
- (2) The normal dehydrogenation isotope effect, DIE  $> 1$  predominates with only few single exceptions.
- (3) The relative reaction rates asymptotically reaches maximum values towards larger cluster sizes. It possibly becomes close to collision rate which means that every bimolecular collision leads to adsorption.

We have established a multistep reaction model that accomplished to explain the inverse KIE (1) and the normal DIE (2)<sup>8</sup>.



**Scheme 1:** Kinetic model

Scheme 1 equally holds for reactions with benzene- $d_6$ . In the first step of elementary processes, the adsorption and desorption ( $k_1$  and  $k_{-1}$ ) is followed by endoergic C-H bond activation and reverse recombination ( $k_2$  and  $k_{-2}$ ). After the first C-H activation step a second activation steps succeeds ( $k_3$ ).

#### 4. H/D isotope effects in the reaction of benzene with Cobalt Gold and Cobalt Rhodium bimetallic cluster ions

---

This elementary step is followed by the desorption of molecular hydrogen ( $k_4$ ). A cold hydrido-phenyl cluster structure is origin of the C-H bond recombination ( $k_2$ ) and the second C-H bond activation ( $k_3$ ). Both elementary processes exhibit a considerable normal kinetic isotope effect ( $KIE \gg 1$ ) resulting from the combination of H/D isotope effects in the zero point energy of the metal hydride bond with mass dependent H/D tunneling across the likely prevailing activation barriers. All other elementary steps account for little to no KIE. An in detail account of this proposed model may be found elsewhere<sup>8</sup>. The combination of these elementary processes gives rise to the observed inverse KIE and the normal DIE. This seems to be a common motif in cobalt complexes<sup>8,13</sup> and is observed in iron and nickel clusters as well (see chapter 4).

To compare the different mixed clusters we depicted the red shaded area of the inverse isotope effect to symbolize the selected mixed clusters (cf. Figure 10). Throughout the experiments the pressure of the reaction gas maintains the constant value of  $3 \cdot 10^{-9}$  mbar. Thus the experimental conditions are comparable. Some overall trends arise:

- (1) Pure cobalt clusters exhibit a drop in reactivity for the cluster size  $n = 6$ . We assume a special structural motif (e.g. octahedral structure) since the drop occurs in cationic and anionic clusters as well.
- (2) With one additional transition metal atom this minimum is no longer distinct and may shift to a different cluster size. The assumed octahedral structure may be disturbed. Two or more additional transition metal atoms to the cobalt clusters changes the minima as well.
- (3) The inverse KIE is more pronounced in  $Co_nPt_m^{+/-}$  clusters as in  $Co_nAu_m^{+/-}$  and in  $Co_nRh_m^{+/-}$ .

It is hardly possible to interpret these features without large scale *ab initio* studies on top – at risk to reach computational and methodological limits.

#### 4. H/D isotope effects in the reaction of benzene with Cobalt Gold and Cobalt Rhodium bimetallic cluster ions

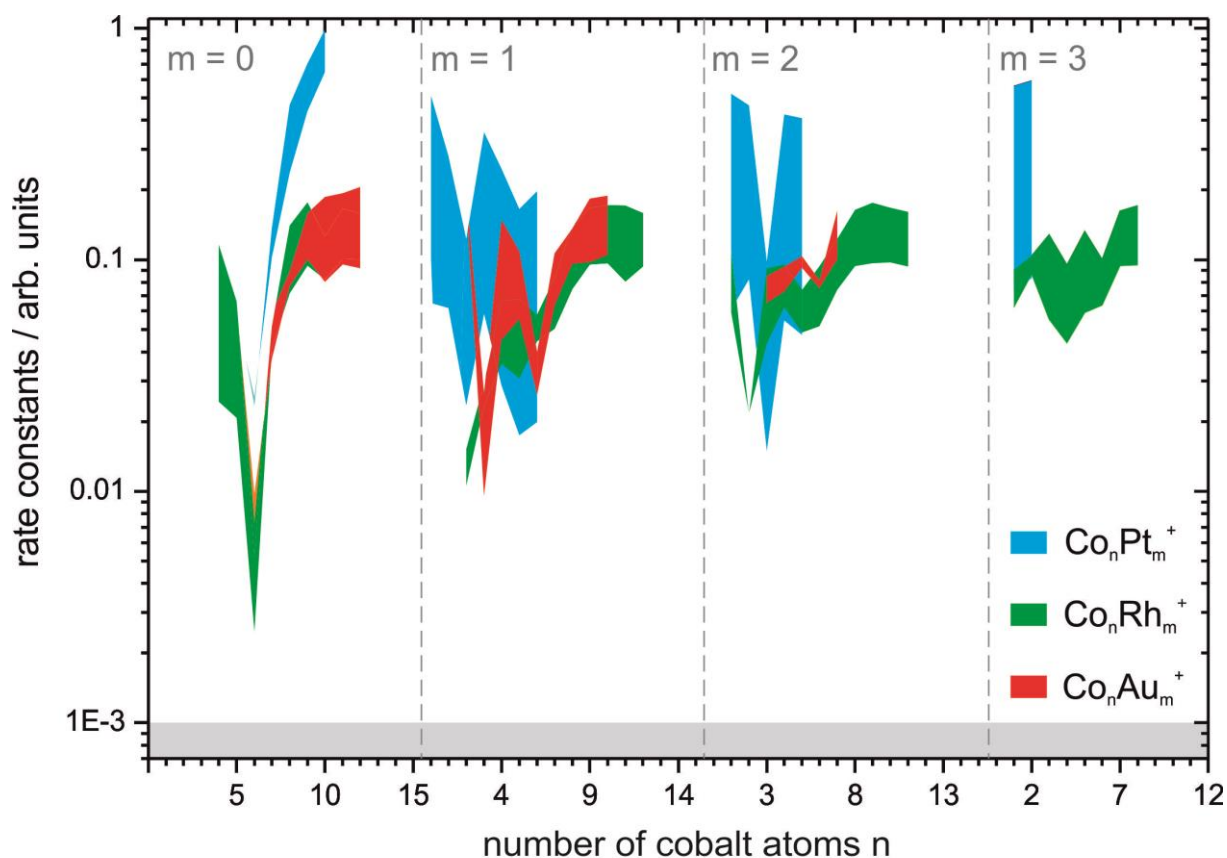


**Figure 10:** Comparison of the relative rate constants of cationic  $Co_nAu_m^+$  clusters (red areas),  $Co_nRh_m^+$  clusters (green areas) and  $Co_nPt_m^+$  clusters (blue areas) in reaction with benzene and benzene- $d_6$ .

The rate constants of mixed anionic clusters are about one magnitude minor compared to cationic clusters (cf. Figure 10 and Figure 11). This is true for all investigated mixed clusters. Small cluster cations manage to activate C-H bonds efficiently while acting as electrophil. This mechanism seizes to operate in anionic clusters. The localized net anionic charge comes in its way. In larger clusters the anionic charge is delocalized and does not hamper the electron withdrawal from C-H bonds. The measurement of small anionic pure cobalt clusters are in good agreement. Differences may arise due to different residual kinetic energy of the stored cluster ions due to different trapping conditions. The addition of transition metal atoms to the pure anionic cobalt cluster leads to dramatic alteration of the size dependency of the cobalt clusters. the comparison of Pt and Rh is hampered by the insufficient overlap of the two size ranges.

In contrast to the cationic clusters the inverse KIE is not enhanced in the  $Co_nPt_m^-$  clusters. The addition of rhodium atoms to anionic cobalt clusters leads to a decrease in reactivity for certain cluster size range.  $Co_nPt_m^-$  clusters containing three atoms are the most reactive due which may result from cooperative effects.

#### 4. H/D isotope effects in the reaction of benzene with Cobalt Gold and Cobalt Rhodium bimetallic cluster ions

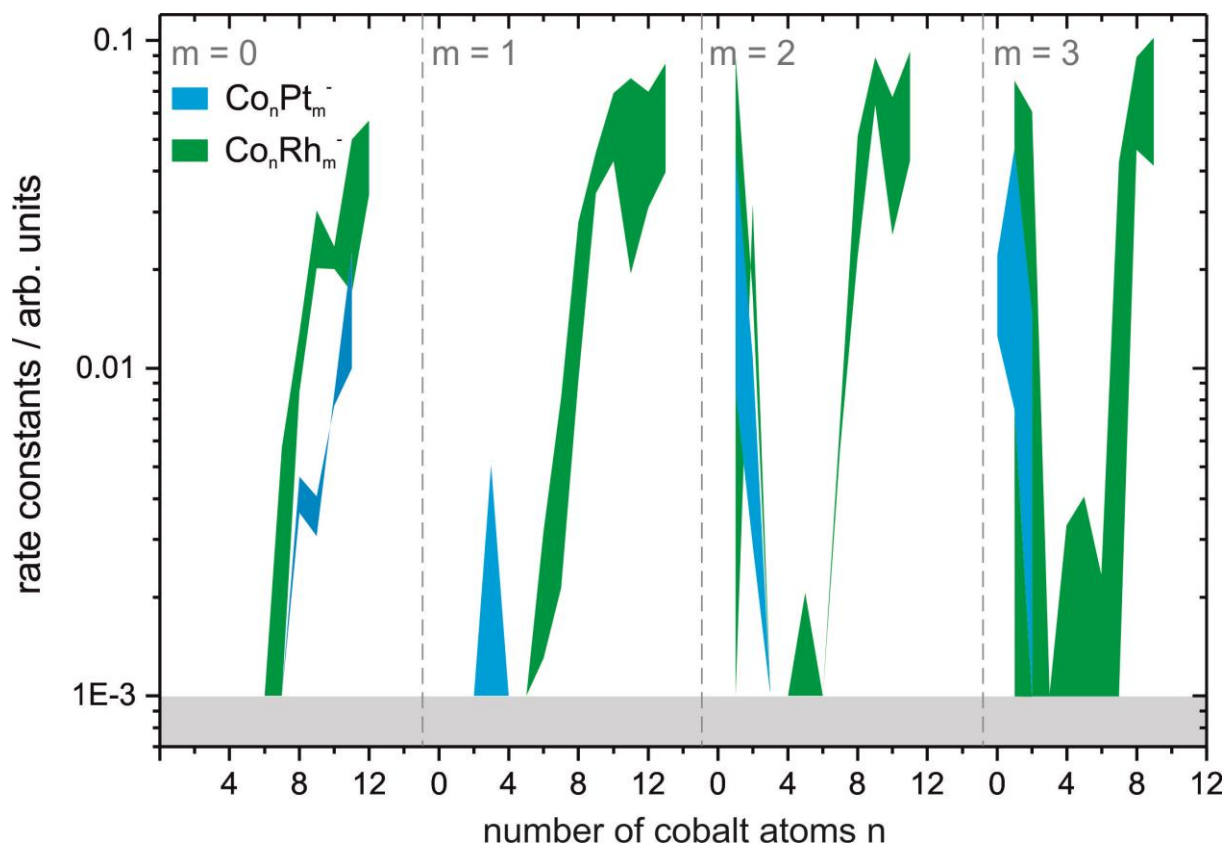


**Figure 11:** Comparison of the relative rate constants of anionic  $Co_nRh_m^-$  clusters (green areas) and  $Co_nPt_m^-$  clusters (blue areas) in reaction with benzene and benzene- $d_6$ .

##### 4.5. Summary and conclusions

The addition of transition metal atoms to ionic cobalt clusters modifies the catalytic activity of these clusters. We studied in this paper two different transition metals, gold and rhodium. Both metals affect the relative rate constants of the reaction with benzene and perdeutero benzene in a different way. In the case of mixed cobalt gold clusters no dehydrogenation products occur in the mass spectra and seemingly intact adsorption to the clusters prevails. In mixed cobalt rhodium clusters two processes occur, first the seemingly intact adsorption of benzene and second the dehydrogenation of a single hydrogen molecule. In both investigated species we observe an inverse kinetic isotope effect ( $KIE < 1$ ). In the case of cobalt rhodium clusters dehydrogenation takes place and a normal dehydrogenation isotope effect ( $DIE > 1$ ) is dominant to the inverse DIE. This experimental findings are in line with our previous measurements of mixed ionic cobalt platinum clusters<sup>13</sup>. A multistep reaction model is able to explain the inverse KIE and the normal DIE<sup>8</sup>.

##### Acknowledgment

This work was supported by the German research foundation DFG within the transregional collaborative research center SFB/TRR 88 "Cooperative effects in homo and heterometallic complexes" (3MET) and by the state research center OPTIMAS. We benefitted from inspiring discussions with Marc Prosenc and Frederic Patureau.



##### 4.6. References

1. S. L. Lu, W. W. Lonergan, J. P. Bosco, S. R. Wang, Y. X. Zhu, Y. C. Xie and J. G. Chen, *Journal of Catalysis*, 2008, **259**, 260-268.
2. W. H. B. Cornils, R. Schlögl, C.H. Wong, *Catalysis from A to Z*, Wiley-VCH.
3. M. Citir, F. Liu and P. B. Armentrout, *Journal of Chemical Physics*, 2009, **130**, 16.
4. F. Meyer, F. A. Khan and P. B. Armentrout, *Journal of the American Chemical Society*, 1995, **117**, 9740-9748.
5. Z. Xiuyun and W. Jinlan, *Journal of Physical Chemistry A*, 2008, **112**, 296-304304.
6. M. Gerhards, O. C. Thomas, J. M. Nilles, W. J. Zheng and K. H. Bowen, *Journal of Chemical Physics*, 2002, **116**, 10247-10252.
7. S. Yang and M. B. Knickelbein, *Journal of Chemical Physics*, 1990, **93**, 1533-1539.
8. M. Tombers, L. Barzen and G. Niedner-Schatteburg, *The Journal of Physical Chemistry A*, 2012, **117**, 1197-1203.
9. C. Berg, M. Beyer, U. Achatz, S. Joos, G. Niedner-Schatteburg and V. E. Bondybey, *Journal of Chemical Physics*, 1998, **108**, 5398-5403.
10. K. O. Fossan and E. Uggerud, *Dalton Transactions*, 2004, 892-897.
11. B. Pfeffer, S. Jaberg and G. Niedner-Schatteburg, *Journal of Chemical Physics*, 2009, **131**.
12. S. L. Lu, C. A. Menning, Y. X. Zhu and J. G. Chen, *Chemphyschem*, 2009, **10**, 1763-1765.
13. L. Barzen, M. Tombers, C. Merkert, J. Hewer and G. Niedner-Schatteburg, *International Journal of Mass Spectrometry*, 2012, **330**, 271-276.
14. D. G. Churchill, K. E. Janak, J. S. Wittenberg and G. Parkin, *Journal of the American Chemical Society*, 2003, **125**, 1403-1420.
15. T. O. Northcutt, D. D. Wick, A. J. Vetter and W. D. Jones, *Journal of the American Chemical Society*, 2001, **123**, 7257-7270.
16. W. D. Jones, *Accounts of Chemical Research*, 2003, **36**, 140-146.
17. K. E. Janak and G. Parkin, *Journal of the American Chemical Society*, 2003, **125**, 6889-6891.
18. E. Janak Kevin, G. Churchill David and G. Parkin, in *Activation and Functionalization of C?H Bonds*, American Chemical Society, 2004, vol. 885, ch. 5, pp. 86-104.
19. M. Porembski and J. C. Weisshaar, *J. Phys. Chem. A*, 2000, **104**, 1524-1531.
20. G. C. Bond and D. T. Thompson, *Catalysis Reviews-Science and Engineering*, 1999, **41**, 319-388.
21. M. R. Zakin, D. M. Cox and A. Kaldor, *J. Chem. Phys.*, 1988, **89**, 1201-1202.
22. D. M. Cox, P. Fayet, R. Brickman, M. Y. Hahn and A. Kaldor, *Catalysis Letters*, 1990, **4**, 271-278.
23. W. F. Graydon and M. D. Langan, *Journal of Catalysis*, 1981, **69**, 180-192.
24. M. L. Mandich, L. F. Halle and J. L. Beauchamp, *Journal of the American Chemical Society*, 1984, **106**, 4403-4411.
25. C. Berg, T. Schindler, G. Niedner-Schatteburg and V. E. Bondybey, *J. Chem. Phys.*, 1995, **102**, 4870-4884.
26. D. Proch and T. Trickl, *Review of Scientific Instruments*, 1989, **60**, 713-716.
27. P. Caravatti and M. Allemann, *Org. Mass Spectrom.*, 1991, **26**, 514-518.
28. M. Graf, 2006.
29. G. Niedner-Schatteburg, Habilitation Thesis, TU München, 1996.
30. C. Berg, M. Beyer, T. Schindler, G. Niedner-Schatteburg and V. E. Bondybey, *Journal of Chemical Physics*, 1996, **104**, 7940-7946.

#### 4. H/D isotope effects in the reaction of benzene with Cobalt Gold and Cobalt Rhodium bimetallic cluster ions

---

## 5. Benzene activation and H/D isotope effects in reactions of mixed cobalt platinum clusters: the influence of charge and of composition

---

### 5. Benzene activation and H/D isotope effects in reactions of mixed cobalt platinum clusters: the influence of charge and of composition

#### 5.1. Preamble

This work is published in *The International Journal of Mass Spectrometry* with the title: "Benzene activation and H/D isotope effects in reactions of mixed cobalt platinum clusters: The influence of charge and of composition" within the special issue dedicated to Peter B. Armentrout on the occasion of his 60<sup>th</sup> birthday. The text of the publication was mainly written by Lars Barzen. Measurements and data evaluation were done by Lars Barzen, Matthias Tombers, Joachim Hewer and me. Structural and energetic calculations were made by Gereon Niedner-Schatteburg.

Full reference to the publication:

L. Barzen, M. Tombers, C. Merkert, J. Hewer, G. Niedner-Schatteburg, Benzene activation and H/D isotope effects in reactions of mixed cobalt platinum clusters: The influence of charge and of composition, *International Journal of Mass Spectrometry*, 330 (2012) 271-276.

#### Abstract

A dedicated ion trap served to investigate the reaction with benzene and benzene-d<sub>6</sub> under single collision conditions of size selected bimetallic cobalt platinum clusters  $Co_nPt_m^\pm$  in the size range  $n + m \leq 8$ . Dehydrogenation by cationic cobalt clusters  $Co_n^+$  is sparse, it is effective in small bimetallic clusters  $Co_nPt_m^+$ ,  $n + m \leq 3$ . Single platinum atoms promote benzene dehydrogenation while further cobalt atoms quench it. Mixed triatomic clusters  $Co_2Pt_1^-$  and  $Co_1Pt_2^-$  are special in causing effective reactions in a cooperative way. Kinetic Isotope Effects KIE(n) in total reaction rates are inverse and – in part – large, Dehydrogenation Isotope Effects DIE(n) are normal. A multistep model of adsorption and stepwise dehydrogenation from the precursor adsorbate proves suitable to rationalize the found KIEs and DIEs in principle. The pronounced influence of cluster charge and of cluster composition demands for further investigation.

## 5. Benzene activation and H/D isotope effects in reactions of mixed cobalt platinum clusters: the influence of charge and of composition

---

### 5.2. Introduction

Bimetallic transition metal clusters may serve as model systems for the elucidation of elementary processes in heterogeneous catalysis. Hydrocarbon adsorption and subsequent C-H bond activation are amongst the most important steps in many catalyzed reactions, and either is often rate limiting. Cobalt has numerous applications as heterogeneous catalyst based on its redox properties that allow for ease of electron transfer via unstable intermediates [1]. Platinum is well known for its capability to cause catalytic hydrogenation and/or dehydrogenation of many functional groups at low temperature [1]. In batch and flow reactor studies bimetallic PtCo catalysts are more active in benzene hydrogenation than monometallic Co and Pt catalysts [2]. The activity showed to follow the trend: PtCo >> PdCo > RuCo ~ Pt ~ Co ~ Ru ~ Pd [3]. Cobalt monolayers on bulk platinum exhibited low temperature hydrogenation properties e.g. on cyclohexene [4]. Transition metal cluster alloys have found application as oxygen-reduction catalyst in the polymer electrolyte membrane of fuel-cells to improve and reduce platinum loading [5-7]. Magnetic cobalt platinum nanoparticles are considered suitable media for ultra-high density magnetic recording [8]. An introductory overview over recent work on cobalt platinum nano particles can be found elsewhere [9].

Prior gas phase studies of benzene adsorption and activation focused on niobium and rhodium clusters [10-12]. Vivid dehydrogenation through niobium cluster cations and anions alike contrast to mere adsorption by  $Rh_n^\pm$ . Little to no observable isotope effects prevailed in either cases. Prior ion trap investigations revealed catalytic dehydrogenation of saturated and aromatic cyclic hydrocarbons by small platinum clusters  $Pt_n^+$ ,  $n \leq 4$  [13]. Methane activation through platinum clusters proved sensitive to their charge states and/or structures with  $n = 4$  behaving special [14], and a normal H/D isotope effect in dehydrogenation was found subsequently [15].

The relative scale of binding strength in complexes of atomic transition metal is established well. Armentrout et al. have conducted multiple guided ion beam studies and found the following trends in binding energies:  $[Pt-CH_3]^+ > [Co-CH_3]^+ > [Rh-CH_3]^+$  and  $[Pt-H]^+ > [Co-H]^+ > [Rh-H]^+$  [16-22]. In a recent study with complexed platinum cations they found the thermal C-H bond activation of benzene reversible [23]. By guided beam studies of cobalt cluster cations Armentrout et al. obtained cluster binding energies [24], deuteride - cluster binding energies [25] and methyl - cluster binding energies [26].

Density functional theory showed capable to allow for structural predictions on small neutral and anionic cobalt clusters  $Co_n^{0,-}$ ,  $n \leq 6$  [27] and of neutral cobalt-platinum "nanoalloy" clusters  $Co_nPt_m$ ,  $n + m \leq 5$  [9]. Triangular, rhombic and trapezoidal structures prevailed.

## 5. Benzene activation and H/D isotope effects in reactions of mixed cobalt platinum clusters: the influence of charge and of composition

---

Our present study serves to investigate the reactions of benzene  $C_6H_6$  and perdeutero benzene  $C_6D_6$  under single collision conditions with isolated bimetallic cobalt platinum clusters  $Co_nPt_m^\pm$ ,  $n + m \leq 8$ , by application of Fourier-Transform Ion-Cyclotron-Resonance (FT-ICR) mass spectrometry.

## 5. Benzene activation and H/D isotope effects in reactions of mixed cobalt platinum clusters: the influence of charge and of composition

---

### 5.3. Material and methods

The experiments were performed with a modified Fourier-Transform Ion-Cyclotron-Resonance (FT-ICR) mass spectrometer (Bruker Apex III). We generated the mixed cobalt platinum clusters with a homebuilt laser vaporization source (LVAP) as described before [12, 28]. The second harmonic of a pulsed Continuum Nd-YAG laser is used to evaporate off atoms from a 0.4 – 1.0 mm thick rotating Cobalt Platinum alloy target (HMW Hauner, Co:Pt molar ratio of 2:1). The emerging metal plasma is cooled and made to yield clusters by a short transverse pulse (40  $\mu$ s, Helium, 8-15 bar) from a homebuilt piezoelectric valve [29]. Further cooling arises from the subsequent supersonic nozzle expansion through a 20 mm long channel (diameter of 2 mm) into vacuum ( $10^{-6}$  mbar). There is no further ionization step in addition. All investigated ions are generated within the laser induced plasma. Unfortunately, the current ion source yielded neither  $\text{Pt}_2^+$  nor  $\text{Pt}_3^+$  clusters while utilizing the present mixed metal target. Future experiments with a pure platinum target will help this.

Past a 1.4 mm diameter skimmer the cold cluster ions are accelerated, fed into a cw quadrupole ion bender ( $90^\circ$ ) and steered by electrostatic lenses into the high field region of a superconducting magnet (7.05 Tesla, actively shielded) while appropriately decelerated. Eventually, the cluster ions are trapped for reaction and/or detection within the FT-ICR cell of so called “infinity” type [30].

Internal degrees of freedom of the cluster ions are relaxed to sub thermal energies through the supersonic expansion in the cluster source. Kinetic energies of the heavy cluster ions is limited by the storage in the ion trap to  $E_{\text{kin,lab}} < 0.5$  eV (laboratory frame value). In collisions with light neutral gases the collision energies in the center of mass frame amount to quasi thermal values  $E_{\text{kin,cm}} \sim 0.1$  eV and below.

In order to pursue the reactivity studies with benzene ( $\text{C}_6\text{H}_6$ ) / benzene- $d_6$  ( $\text{C}_6\text{D}_6$ ) we permitted the controlled admission of a reaction gas in order to raise the pressure in the ultrahigh vacuum chamber of the FT-ICR mass spectrometer, where the ICR trapping cell is located, from  $\sim 3 \times 10^{-10}$  to typically  $1-5 \times 10^{-9}$  mbar such that a single bimolecular reactant collision per cluster per second takes place (single collision conditions). A commercial ultrahigh vacuum gauge (cold cathode gas discharge, calibrated for  $\text{N}_2$ ) provides for a nominal pressure reading. Commercially available benzene/benzene- $d_6$  (Sigma-Aldrich, purity  $\geq 99.6$  %) was applied after degassing by multiple “pump and freeze” cycles. Kinetic curves of reactant and product ions extract from mass spectra of trapped cluster ions while exposed to the cw admitted reactant gases and under variation of reaction delays between cluster ion admission and detection. Fits to pseudo-first-order-kinetics arise through a genetic algorithm (“evofit” program [31]).

## 5. Benzene activation and H/D isotope effects in reactions of mixed cobalt platinum clusters: the influence of charge and of composition

---

An exact absolute calibration of the reactant gas pressure at the location of the ICR cell is at present not possible. There is a pressure gradient between gauge and ICR cell of about a factor of 4, the exact value not being known, and most likely depending on the chemical nature of the prevailing neutral gas. Gauging against known reactions is conceivable, in principle, and tedious, in practice. There are few absolute rate constants of bimolecular reactions of small molecular ions with neutral benzene published. None of these ions is accessible with the current ICR setup for technical reasons, however. Reactions of benzene cations with benzene and other hydrocarbon molecules were shown to vary largely depending on the ion precursor [32]. Future attempts in gauging the absolute reactant gas density of the present ICR setup are pending. For the time being we rely on the evaluation of relative rate constants that compare against each other. From studies of large cobalt clusters up to  $\text{Co}_{28}^+$  with benzene it may be concluded that the fastest observed reaction rates come close to collision rate. This would relate to a benzene to cobalt surface sticking coefficient of unity, and we have normalized the recorded relative rate constants accordingly. The noise equivalent detection limit of the relative rate constants amounts to  $k \approx 0.0025$ .

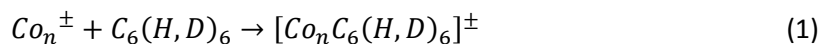
We pursued accompanying *ab initio* modeling of clusters and products by density functional theory (DFT). We utilize a level of theory that is similar to our study on pure cobalt clusters. A combination of the Stuttgart relativistic effective core potentials for Co and Pt with cc-pVDZ basis sets for carbon and hydrogen [33-35] proved appropriate in conjunction with the PBE0 hybrid exchange correlation functional [36] as implemented in the Gaussian 09 program suite [37]. No effort was made to cover all cluster sizes. Instead we focused onto stationary points of the  $^M[\text{Co}_n\text{Pt}_m, \text{C}_6\text{H}_6]^+$  potential hypersurfaces with  $n + m = 3$  and variation of the spin state multiplicity  $M$ . Full coverage of these investigations remains to a future publication[38] while some preliminary results will be discussed here as needed.

## 5. Benzene activation and H/D isotope effects in reactions of mixed cobalt platinum clusters: the influence of charge and of composition

---

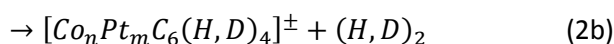
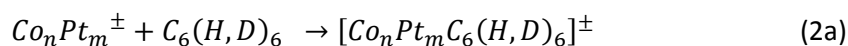
### 5.4. Results and discussion

The recorded kinetics reveal that pure cobalt clusters  $Co_nPt_m^\pm$ ,  $m = 0$ , react with benzene to form a single type of products:



This holds both for cationic clusters as well as for anionic clusters, and for reactions with benzene  $C_6H_6$  and perdeutero benzene  $C_6D_6$  alike. Dehydrogenation does not take place up to the limit of sensitivity of this experiment in the range of  $n = 3 - 10$  – with the  $Co_{9,10}^- + C_6H_6$  cases exempt, where some additional products form ( $[Co_{9,10}C_6H_4]^-$ , see eq. 2b below). Indication of the product species in (4.1) in square parenthesis shall indicate the ambiguity in its molecular structure. While the sum formula is well determined through the high resolution mass detection its structure, of course, is not. It is well conceivable, that benzene does react beyond mere attachment to the cobalt cluster. It may well have experienced activation of some C-H bond thereby forming a hydrido phenylic complex of the form  $Co_n(H)C_6H_5^\pm$ . Activation of multiple C-H bonds would induce a subsequent pair wise recombination of the hydridic H-atoms and desorption of molecular  $H_2$ . While this is not observed either the benzene adsorbate cluster complex or the hydrido phenylic complex stabilize radiatively on the long run. Anionic cobalt cluster cations may stabilize by electron detachment, in addition. As of now, we do not have evidence for such processes in the current case.

Mixed cationic and anionic clusters  $Co_nPt_m^\pm$ ,  $n, m \geq 1$ , react with benzene  $C_6H_6$  and with perdeutero benzene  $C_6D_6$  either through association (2a) or through dehydrogenation (2b):



The ratio of both varies with cluster size, with cluster charge and somewhat with the reactant. No products of reactions were observed that would proceed beyond single dehydrogenation (4.2b). In particular, there was no evidence for loss of odd numbers of H-atoms or for loss of more than a single molecule of  $H_2$ . It is therefore most likely that a single molecular hydrogen evolves per encounter of cluster and reactant. Seemingly, C-H and C-D bond activation ceases after two instances per benzene molecule at most.



## 5. Benzene activation and H/D isotope effects in reactions of mixed cobalt platinum clusters: the influence of charge and of composition

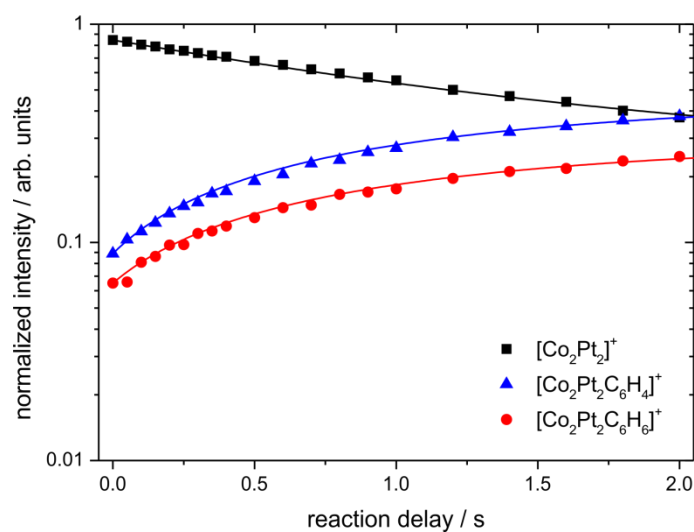


**Fig. 1:** An example for the reaction kinetics of  $Co_2Pt_2^+$  (black, squares) with  $C_6H_6$ . Symbols represent experimental data, solid lines represent numerical fits by a genetic algorithm to pseudo first order kinetics. Association (red, circles) and dehydrogenation (blue, triangles) take place in parallel.

Fitting the recorded kinetics (cf. e.g. in the case of  $Co_2Pt_2^+ + C_6H_6$  at Fig. 1) yields relative partial rate constants for association and for dehydrogenation, and the relative total rate constants.

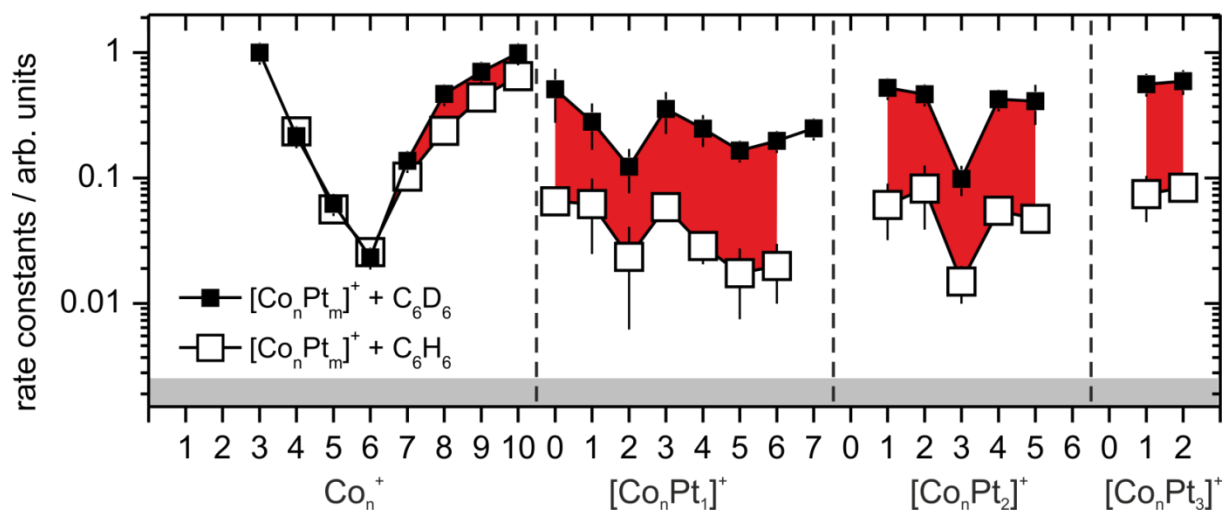


**Fig. 2:** Total rate constants for the reaction of  $Co_nPt_m^+$  with benzene (open symbols) and perdeutero benzene (solid symbols). The observed inverse Kinetic Isotope Effect (KIE) is emphasized by red shading of the areas in between of the corresponding rate constants. The noise equivalent level of the present experiments is indicated by grey shading.

## 5. Benzene activation and H/D isotope effects in reactions of mixed cobalt platinum clusters: the influence of charge and of composition

---

Total reaction rates with benzene and with perdeutero benzene of pure cationic cobalt clusters  $\text{Co}_n^+$  reveal a pronounced size dependence. The rates of  $\text{Co}_6^+$  diminish by a factor of 40 with respect to larger and smaller clusters. The very cause is unknown while numerous speculations arise. A drop with cluster size in the total association rate of alkanes on small niobium cluster cations was attributed before to an increase of coordinative saturation and a concomittant drop of reactivity [10]. In principle such an argument might hold for the case of cobalt as well. In reactions with benzene the same study found a rise in total reaction rate upon increase of the size of these clusters, possibly due to the rise in heat capacity that helps to dissipate the released heat of adsorption. A combination of both counteracting effects, however, was not observed up to now in the reactions of transition metal clusters.

Notably there is little difference whether reacting benzene  $\text{C}_6\text{H}_6$  or perdeutero benzene  $\text{C}_6\text{D}_6$ . It is common practice to discuss such differences in terms of a Kinetic Isotope Effect (KIE) defined as the ratio of hydrogenic rate constant  $k_{tot}^{(H)}(n)$  and perdeutero rate constant  $k_{tot}^{(D)}(n)$ :

$$KIE(n) = \frac{k_{tot}^{(H)}(n)}{k_{tot}^{(D)}(n)} \quad (3)$$

Normal KIE  $> 1$  or inverse KIE  $< 1$  elucidate indirectly the underlying micro kinetics. (Throughout all of this paper blue and red colors code for normal and inverse KIEs). In the present case of  $\text{Co}_n^+ + \text{C}_6\text{H}_6/\text{C}_6\text{D}_6$  reactions, the KIE is small ( $< 0.5$ ) and inverse.

## 5. Benzene activation and H/D isotope effects in reactions of mixed cobalt platinum clusters: the influence of charge and of composition

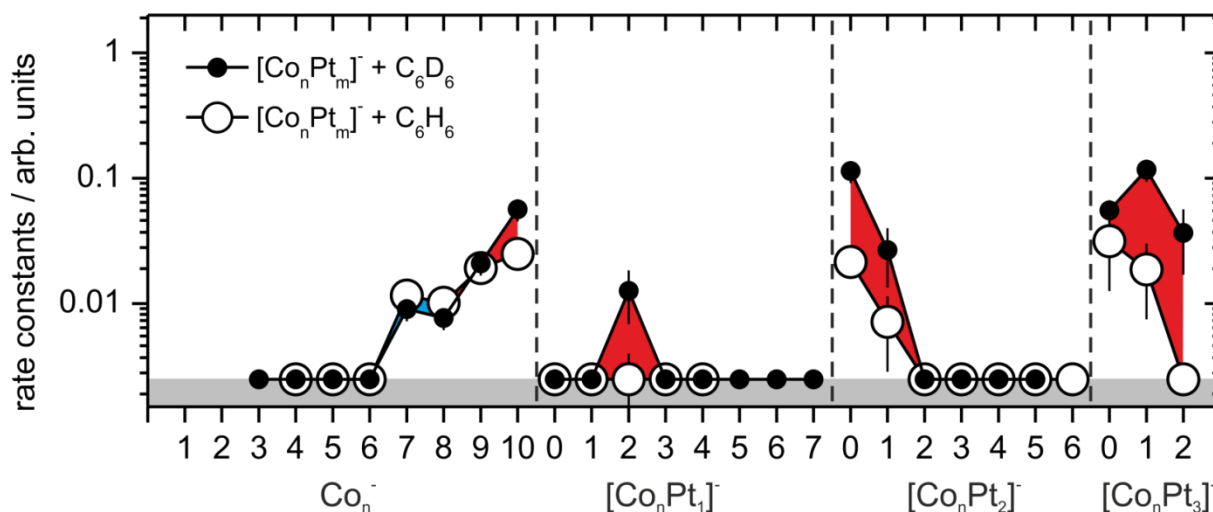


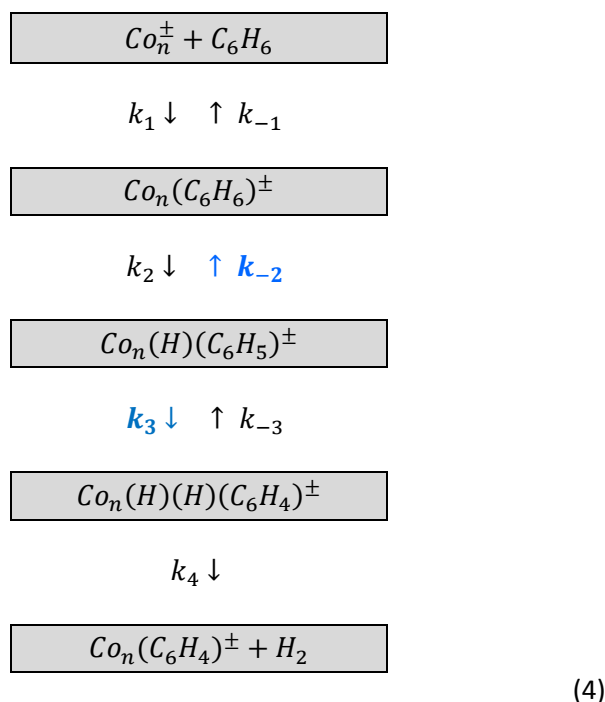
**Fig. 3:** Total rate constants for the reaction of  $Co_nPt_m^-$  with benzene (open symbols) and perdeutero benzene (solid symbols). The observed inverse Kinetic Isotope Effect (KIE) is emphasized by red shading of the areas in between of the corresponding rate constants. Some normal KIE is signified by blue shading. The noise equivalent level of the present experiments is indicated by grey shading.

Anionic cobalt clusters  $Co_n^-$  with  $n \leq 6$  do not yield observable products while collisions with benzene inevitably take place at collision rates that are high enough to allow for detection of products down to 1% collision efficiency. Adsorption induced electron detachment is a conceivable reason, while our recorded data do not provide evidence for such a “dark” reaction channel. Further insight could arise from the inspection of size dependencies in heats of adsorption  $\Delta_{ads}H(Co_n^- - C_6H_6)$  and in electron detachment enthalpies  $\Delta_{detach}H([Co_nC_6H_6]^-)$  of all conceivable isomers, none of which is known as of now. Instead, basic thermodynamics regards the cluster as a finite heat bath that serves to dissipate the heat of adsorption. The more effective the dissipation the less probable becomes the benzene eventually evaporating off the cluster. With increasing cluster size the total adsorption efficiency improves. The rises in adsorption efficiency are apparent in the rate constants of anionic clusters  $Co_n^-$ ,  $n \geq 7$ . The according reactions of  $Co_n^-$  with  $C_6D_6$  reveal a small inverse KIE ( $< 0.5$ ) with  $n = 7, 8$  exempt (normal KIE).

We have most recently undertaken a systematic evaluation of KIEs in cobalt cluster reactions with benzene and worked out a multi step reaction model (4) that managed to explain this somewhat surprising finding [39]. The argumentation runs – in short – as follows:

## 5. Benzene activation and H/D isotope effects in reactions of mixed cobalt platinum clusters: the influence of charge and of composition

---



Scheme (4) equally holds for reactions with  $C_6D_6$ . The observable reactions of association and of dehydrogenation comprise the consecutive elementary processes: adsorption and desorption ( $k_1$  and  $k_{-1}$ ), C-H bond activation and its recombination ( $k_2$  and  $k_{-2}$ ), second C-H bond activation and its recombination ( $k_3$  and  $k_{-3}$ ), and molecular desorption of  $H_2$  ( $k_4$ ). Most of these processes provide for little to no KIE (for more detail see [39]). Merely the C-H recombination ( $k_{-2}$ ) and the second C-H activation ( $k_3$ ) provide for a normal KIE, in part due to zero point effects and mostly due to strong mass effects in H/D tunneling. Altogether the combination of KIEs from these seven elementary processes results in an observable inverse KIE for association and in a normal KIE for dehydrogenation – as indeed observed in the experiments with pure cobalt clusters up to  $n = 27$  [39].

When doping cobalt clusters with a single platinum atom or with a few platinum atoms one obtains mixed clusters  $Co_nPt_m^\pm$ , at present with  $n \leq 7$  and  $m \leq 3$ . These mixed clusters undergo – in principle – the same reactions (2a,b) as pure cobalt clusters.

Once more, there is no reaction observed that would go beyond single dehydrogenation (2b). Differences with respect to the pure clusters arise as follows: The remarkable size dependence of cationic rates diminishes in the reactions of mixed clusters. The inverse KIE persists in the mixed clusters, and it increases significantly as compared to the inverse KIE of pure cobalt clusters. Anionic mixed clusters are less reactive by more than an order of magnitude (cf. Figs 2 and 3). While pure anionic cobalt clusters set in to react at  $n = 7$  and beyond, only small mixed clusters of five atoms at most react at all. These are namely  $Co_2Pt_1^-$ ,  $Co_1Pt_2^-$ ,  $Co_1Pt_3^-$ ,  $Co_2Pt_3^-$ , and the pure platinum

## 5. Benzene activation and H/D isotope effects in reactions of mixed cobalt platinum clusters: the influence of charge and of composition

---

clusters  $Pt_2^-$  and  $Pt_3^-$ . Inverse KIEs prevail throughout, and they are larger in anionic mixed clusters than in pure cobalt clusters.

It is worthwhile to deliberate on the likely origin of the enhanced inverse KIEs in heterogeneous clusters. As a starting point one may assume the previous micro kinetic model of scheme (4) valid for heterogeneous clusters as well. If so then it is once more the recombination of the hydridic hydrogen atom with the phenyl ligand (microscopic rate constant  $k_{-2}$  in scheme (4) which is subject to a normal KIE (in backwards direction). The platinum heteroatom would enhance this KIE which implies that platinum would drive hydrogenation more efficiently than cobalt – as is anticipated by prior studies (cf. introduction). Moreover the experiments with pure anionic platinum clusters show efficient dehydrogenation of benzene (2b). Namely  $Pt_2^-$  reacts efficiently with either benzene or perdeutero benzene as compared to  $CoPt^-$  which does not provide for any reaction rate within our experimental uncertainties. Similarly,  $Pt_3^-$  readily reacts effectively with either benzene or perdeutero benzene while  $CoPt_2^-$  does so slowly if at all. The thus emerging picture of a more efficient hydrogen release from heterogeneous clusters – in conjunction with the inverse KIE in the total overall reaction rates – furthermore implies large tunneling contributions to  $k_{-2}$ . This is the major cause of the normal KIE  $> 7$  in  $k_{-2}$  which in turn explains the inverse KIE in the overall reaction.  $Co_nPt_2^-$  only reacts as long as  $n \leq 1$ . This particular cooperativity of small heterogeneous metal clusters of at most three atoms is noteworthy.

Association (2a) and dehydrogenation (2b) are competing parallel reactions. The branching ratio amongst both varies with size, charge and composition of clusters, and with the deuteration of benzene. In order to discuss the degree of activation and to provide for some data reduction, we define a so called “average degree of dehydrogenation”  $\langle \chi_n \rangle$  as before [40]:

$$\langle \chi_n \rangle = \frac{1}{m} \frac{1}{k_n^{tot}} \sum_{m_i=1}^m m_i k_n(m_i) \quad (5)$$

with

$$k_n^{tot} = \sum_i k_n(m_i) \quad (6)$$

Here,  $m$  ( $= 6$  in the present case) indicates the total amount of hydrogen or deuterium atoms as available from  $C_6H_6/C_6D_6$ . The partial reaction rate  $k_n(m_i)$  classifies according to the cluster size  $n$  and the loss of hydrogen or deuterium atoms  $m_i$  in the observed product.  $\langle \chi_n \rangle = 1$  would indicate complete dehydrogenation,  $\langle \chi_n \rangle = 0$  would indicate adsorption without any dehydrogenation.

## 5. Benzene activation and H/D isotope effects in reactions of mixed cobalt platinum clusters: the influence of charge and of composition

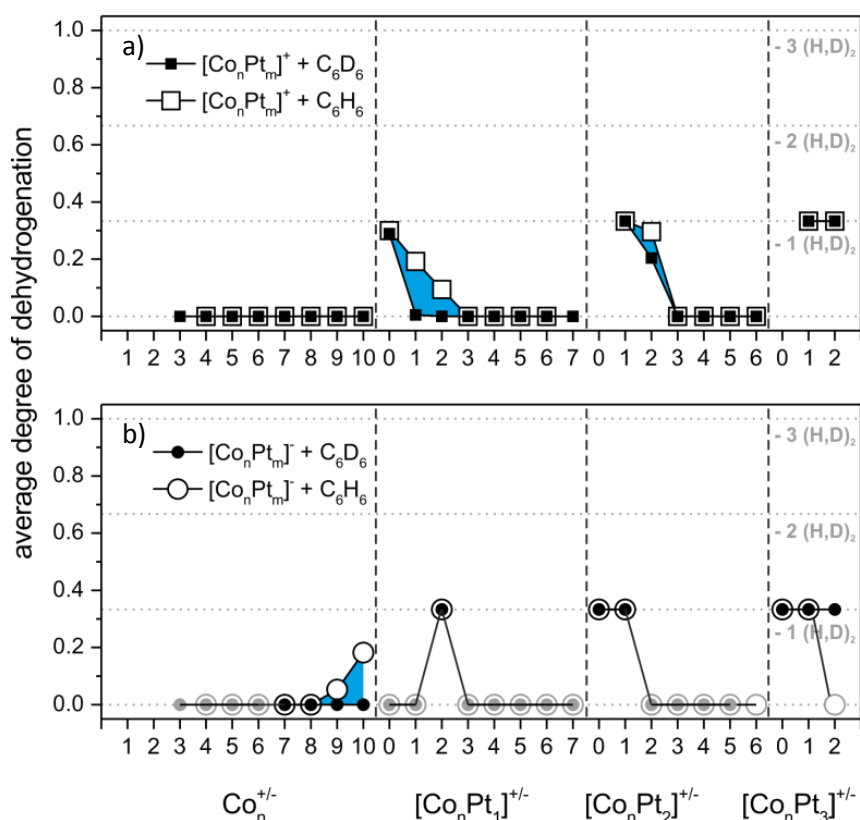


**Fig. 4:** Average degree of dehydrogenation  $\langle \chi_n \rangle$  **(a)** by pure and mixed cationic clusters and **(b)** by pure and mixed anionic clusters. Blue areas indicate a normal Dehydrogenation Isotope Effect ( $DIE > 1$ ). Those  $\langle \chi_n \rangle = 0$  values that are indicated in grey arise from vanishing total reaction rates  $k_{tot}(n) = 0$ . Solid symbols represent reaction with  $C_6D_6$ , open symbols with  $C_6H_6$ . Uncertainties are within the size of the symbols.

The thus obtained values of  $\langle \chi_n \rangle$  range between 0 and 1/3. The latter signifies a branching ratio of (2a) : (2b) of 0 : 1, in other words: single dehydrogenation only. The observable influence of deuteration is small. We label the kinetic isotope effect on  $\langle \chi_n \rangle$  as a Dehydrogenation Isotope Effect (DIE):

$$DIE(n) = \frac{\langle \chi_n^{(H)} \rangle}{\langle \chi_n^{(D)} \rangle} \quad (7)$$

The (few) cases where  $DIE(n) \neq 1$  are:  $Co_1Pt_2^+$ ,  $Co_2Pt_1^+$ ,  $Co_2Pt_2^+$ ,  $Co_9^-$ , and  $Co_{10}^-$ . All of these reveal a normal  $DIE$ . From our micro kinetic model of consecutive elementary steps (scheme (4)) we recall likely tunneling contributions in hydrogen migration steps  $k_2$  (C-H recombination) and  $k_3$

## 5. Benzene activation and H/D isotope effects in reactions of mixed cobalt platinum clusters: the influence of charge and of composition

---

(second C-H activation). The former served to rationalize the inverse KIE in the observed total rates, the latter explains the observation of a normal *DIE*.

The observed isotope effects, both KIEs and DIEs, are thereby well interpreted - the observed effects of cluster size and of composition remain to discuss. The most pronounced size effects are: (1) the quenching of the total reactivity in anionic cobalt clusters through addition of a single or a few platinum atoms (cf. Fig. 3); (2) the quenching of the average degree of dehydrogenation in small mixed cationic clusters  $Co_{1,2}Pt_{1,2}^+$  through addition for single further cobalt atoms (cf. Fig. 4a) ; and (3) the almost “magic” size dependence of the average degree of dehydrogenation in mixed anionic clusters with e.g.  $Co_2Pt_1^-$  and  $Co_1Pt_2^-$  sticking out as compared to others (cf. Fig. 4b). None of these three effects is accessible to an unambiguous interpretation. They challenge further investigations.

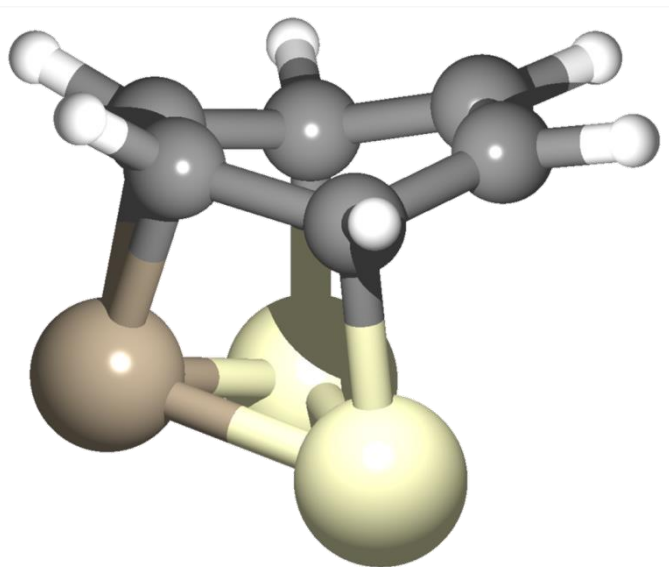


**Fig. 5:** A calculated (PBE0/Stuttgart ECP; cc-pVDZ) association complex by example:  $Co_1Pt_2(C_6H_6)^-$  in singlet spin state. The cobalt atoms favor  $\eta_2$  coordination (“on bridge”) towards two carbon atoms within the benzene ring. The two platinum atoms favor  $\eta_1$  coordination (“on top”) to single carbon atoms. Some aromaticity is lost by forcing the ring into a non planar geometry (further discussion see text).

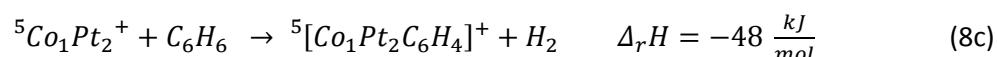
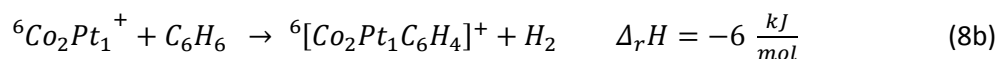
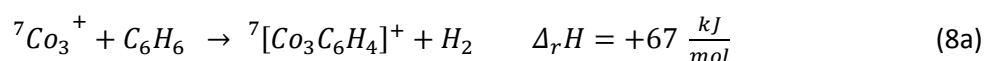
We have started a systematic *ab initio* approach on structures and energetic of the seemingly “magic”  $Co_nPt_m^+$ ,  $n + m = 3$  case [33-37]. This investigation is still in progress. Some preliminary – yet robust – findings help to elucidate the interaction of these clusters with benzene at this stage: All

## 5. Benzene activation and H/D isotope effects in reactions of mixed cobalt platinum clusters: the influence of charge and of composition

---

clusters with cobalt favor high spin states. Cobalt atoms favor  $\eta_2$  coordination (“on bridge”) towards  $C_2$  units in benzene. The coordination and hybridization at the carbon center remains constant before and after coordination, i.e., the C-C  $\pi$  bond is replaced by a metallacycle. Platinum atoms favor  $\eta_1$  coordination (“on top”) to single carbon atoms in benzene. The coordinating C becomes  $sp^3$  hybridized instead of  $sp^2$ , which results in the puckering of the ring. This clearly weakens the  $\pi$  bond, creating a radical center at the adjacent carbon atom. The ability to activate a C-H bond in proximity follows. In all cases investigated thus far the side on coordination of a triangular metal cluster with maximum hapticity towards benzene proved most stable (cf. Fig. 5). Single or twofold C-H bond activation with migration of the activated hydrogen onto the metal cluster leads to a tilt of the benzene plane with respect to the metal triangle. It is open as of now whether benzene adsorption induces structural changes of the mixed clusters.

Further support of the experimental findings arise from computed (yet preliminary) enthalpies, confirmation pending. - Benzene dehydrogenation by homogeneous Cobalt cluster cations  $Co_3^+$  seems endoergic, and it is predicted exoergic for mixed cluster cations  $Co_2Pt_1^+$  and  $Co_1Pt_2^+$ :



The same high spin multiplicities prevail in reactants and products while other spin states may get involved in the course of the reaction. The influence of spin orbit coupling may be significant in the mixed clusters as induced by the high nuclear charge of platinum. The present level of DFT does not cover this, however. The experimentally observed rise in dehydrogenation efficiency upon replacement of cobalt for platinum is well in agreement with the calculated ergicities at the present – albeit limited – level of theory. A complete documentation and discussion of the ongoing computations remains to a future publication in due time [38].



## 5. Benzene activation and H/D isotope effects in reactions of mixed cobalt platinum clusters: the influence of charge and of composition

---

### 5.5. Summary and conclusions

We investigated the reaction with benzene and benzene-d<sub>6</sub> of size selected bimetallic cobalt platinum clusters  $Co_nPt_m^\pm$  in the size range  $n + m \leq 8$  in extension of prior work on reaction of transition metal clusters with benzene [14, 15]. Dehydrogenation by cationic cobalt clusters  $Co_n^+$  is sparse, it is effective in small bimetallic clusters  $Co_nPt_m^+$ ,  $n + m \leq 3$ . Thus single platinum atoms promote benzene dehydrogenation while further cobalt atoms quench it. Mixed triatomic clusters  $Co_2Pt_1^-$  and  $Co_1Pt_2^-$  are special in causing effective reactions and single dehydrogenation through some kind of cooperativity while  $Co_nPt_{1,2}^-$ ,  $n \geq 3$  do not react at all.

Kinetic Isotope Effects KIE(n) in total reaction rates are inverse and – in part - large, Dehydrogenation Isotope Effects DIE(n) are normal. A multistep model of adsorption and stepwise dehydrogenation from the precursor adsorbate proves suitable to rationalize the found KIEs and DIEs in principle. Particular insights into the cause of the found effects of charge, size and composition of mixed clusters shall arise from ongoing ab initio modeling of especially the  $n + m = 3$  case. Further experiments are under way as well.

### Acknowledgment

This work was supported by the German research foundation DFG within the transregional collaborative research center SFB/TRR 88 “Cooperative effects in homo and heterometallic complexes (3MET)” and by the state research center OPTIMAS. Markus Becherer participated in part of the experiments. We benefitted from inspiring discussions with Marc Prosenc and Frederic Patureau. We thank the referees for valuable comments.

## 5. Benzene activation and H/D isotope effects in reactions of mixed cobalt platinum clusters: the influence of charge and of composition

---

### 5.6. References

- [1] B. Cornils, W.A. Hermann, R. Schlögl, C.-H. Wong, *Catalysis from A to Z*, Wiley-VCH, Weinheim, 2000.
- [2] S. Lu, W.W. Lonergan, J.P. Bosco, S. Wang, Y. Zhu, Y. Xie, J.G. Chen, Low temperature hydrogenation of benzene and cyclohexene: A comparative study between  $\gamma$ -Al<sub>2</sub>O<sub>3</sub> supported PtCo and PtNi bimetallic catalysts, *Journal of Catalysis*, 259 (2008) 260-268.
- [3] S. Lu, C.A. Menning, Y. Zhu, J.G. Chen, Correlating Benzene Hydrogenation Activity with Binding Energies of Hydrogen and Benzene on Co-Based Bimetallic Catalysts, *Chemphyschem*, 10 (2009) 1763-1765.
- [4] N.A. Khan, L.E. Murillo, J.G. Chen, Observation of novel low-temperature hydrogenation activity on Co/Pt(III) surfaces, *Journal of Physical Chemistry B*, 108 (2004) 15748-15754.
- [5] V.R. Stamenkovic, B.S. Mun, M. Arenz, K.J.J. Mayrhofer, C.A. Lucas, G. Wang, P.N. Ross, N.M. Markovic, Trends in electrocatalysis on extended and nanoscale Pt-bimetallic alloy surfaces, *Nat Mater*, 6 (2007) 241-247.
- [6] Y. Bing, H. Liu, L. Zhang, D. Ghosh, J. Zhang, Nanostructured Pt-alloy electrocatalysts for PEM fuel cell oxygen reduction reaction, *Chemical Society Reviews*, 39 (2010) 2184-2202.
- [7] S. Mukerjee, S. Srinivasan, Enhanced electrocatalysis of oxygen reduction on platinum alloys in proton-exchange membrane fuel-cells, *Journal of Electroanalytical Chemistry*, 357 (1993) 201-224.
- [8] M.N. Dave, M.L. Wears, J. Michael, C. Desmond, Fabrication and characterization of nano-particulate PtCo media for ultra-high density perpendicular magnetic recording, *Nanotechnology*, 18 (2007) 205301.
- [9] A. Sebetci, Density functional study of small cobalt-platinum nanoalloy clusters, *Journal of Magnetism and Magnetic Materials*, 324 (2012) 588-594.
- [10] C. Berg, M. Beyer, U. Achatz, S. Joos, G. Niedner-Schatteburg, V.E. Bondybey, Effect of charge upon metal cluster chemistry: Reactions of Nb-n and Rh-n anions and cations with benzene, *Journal of Chemical Physics*, 108 (1998) 5398-5403.
- [11] B. Pfeffer, S. Jaberg, G. Niedner-Schatteburg, Reactions of simple aromatic heterocycles with niobium cluster ions (n < 30), *Journal of Chemical Physics*, 131 (2009).
- [12] C. Berg, T. Schindler, G. Niednerschatteburg, V.E. Bondybey, Reactions of simple Hydrocarbons with Nb<sub>n</sub><sup>+</sup> - Chemisorption and Physisorption on Ionized Niobium Clusters, *Journal of Chemical Physics*, 102 (1995) 4870-4884.
- [13] G.S. Jackson, F.M. White, C.L. Hammill, R.J. Clark, A.G. Marshall, Gas-phase dehydrogenation of saturated and aromatic cyclic hydrocarbons by Pt-n(+) (n=1-4), *Journal of the American Chemical Society*, 119 (1997) 7567-7572.

## 5. Benzene activation and H/D isotope effects in reactions of mixed cobalt platinum clusters: the influence of charge and of composition

---

- [14] U. Achatz, C. Berg, S. Joos, B.S. Fox, M.K. Beyer, G. Niedner-Schatteburg, V.E. Bondybey, Methane activation by platinum cluster ions in the gas phase: effects of cluster charge on the Pt-4 tetramer, *Chemical Physics Letters*, 320 (2000) 53-58.
- [15] M.K. Beyer, G. Kummerlowe, I. Balteanu, S. Zheng, O.P. Balaj, V.E. Bondybey, Activation of methane and methane-d 4 by ionic platinum clusters, *International Journal of Mass Spectrometry*, 254 (2006).
- [16] Y.M. Chen, P.B. Armentrout, Activation of C<sub>2</sub>H<sub>6</sub>, C<sub>3</sub>H<sub>8</sub>, and C-C<sub>3</sub>H<sub>6</sub> by gas-phase Rh<sup>+</sup> and the thermochemistry of Rh-ligand complexes, *Journal of the American Chemical Society*, 117 (1995) 9291-9304.
- [17] Y.M. Chen, J.L. Elkind, P.B. Armentrout, Reactions of Ru<sup>+</sup>, Rh<sup>+</sup>, Pd<sup>+</sup>, and Ag<sup>+</sup> with H-2, HD, and D-2, *Journal of Physical Chemistry*, 99 (1995) 10438-10445.
- [18] R. Georgiadis, E.R. Fisher, P.B. Armentrout, Neutral and ionic metal hydrogen and metal-carbon bond-energies - reactions of Co<sup>+</sup>, Ni<sup>+</sup>, and Cu<sup>+</sup> with ethane, propane, methylpropane, and dimethylpropane, *Journal of the American Chemical Society*, 111 (1989) 4251-4262.
- [19] E.R. Fisher, L.S. Sunderlin, P.B. Armentrout, Guided ion-beam studies of the reactions of Co<sup>+</sup> and Ni<sup>+</sup> with CH<sub>3</sub>Cl, CH<sub>3</sub>Br, CH<sub>3</sub>I - implications for the metal-methyl ion bond-energies, *Journal of Physical Chemistry*, 93 (1989) 7375-7382.
- [20] Y.M. Chen, D.E. Clemmer, P.B. Armentrout, Conversion of CH<sub>4</sub> to CH<sub>3</sub>OH - reactions of CoO<sup>+</sup> WITH CH<sub>4</sub> and D-2, Co<sup>+</sup> with CH<sub>3</sub>OD and D<sub>2</sub>O, and Co<sup>+</sup>(CH<sub>3</sub>OD) with Xe, *Journal of the American Chemical Society*, 116 (1994) 7815-7826.
- [21] X.G. Zhang, R. Liyanage, P.B. Armentrout, Potential energy surface for activation of methane by Pt<sup>+</sup>: A combined guided ion beam and DFT study, *Journal of the American Chemical Society*, 123 (2001) 5563-5575.
- [22] J.L. Elkind, P.B. Armentrout, Effect of kinetic and electronic-energy on the reactions of Co<sup>+</sup>, Ni<sup>+</sup>, and Cu<sup>+</sup> with H-2, HD, and D<sub>2</sub>, *Journal of Physical Chemistry*, 90 (1986) 6576-6586.
- [23] B. Butschke, D. Schroeder, H. Schwarz, Thermal C-H Bond Activation of Benzene with Cationic Pt(CX<sub>3</sub>(L) (+) Complexes in the Gas Phase: A Combined Experimental/Theoretical Study (X = H, D; L=1,10-Phenanthroline, 2,2'-Bipyrimidine, 2,2'-Bipyridine, and (o,o'-Cl<sub>2</sub>C<sub>6</sub>H<sub>3</sub>)N=C(CH<sub>3</sub>)-C(CH<sub>3</sub>)=N(o,o'-Cl<sub>2</sub>C<sub>6</sub>H<sub>3</sub>)), *Organometallics*, 28 (2009) 4340-4349.
- [24] S. Goebel, C.L. Haynes, F.A. Khan, P.B. Armentrout, Collision-induced dissociation studies of Co(CO)(X)(+), X=1-5 - sequential bond-energies and the heat of formation of Co(CO)(<sub>4</sub>), *Journal of the American Chemical Society*, 117 (1995) 6994-7002.
- [25] F.Y. Liu, P.B. Armentrout, Guided ion-beam studies of the kinetic-energy-dependent reactions of Co-n(+) (n=2-16) with D-2: Cobalt cluster-deuteride bond energies, *Journal of Chemical Physics*, 122 (2005).

## 5. Benzene activation and H/D isotope effects in reactions of mixed cobalt platinum clusters: the influence of charge and of composition

---

- [26] M. Citir, F. Liu, P.B. Armentrout, Methane activation by cobalt cluster cations, Co-n(+) (n=2-16): Reaction mechanisms and thermochemistry of cluster-CH<sub>x</sub> (x=0-3) complexes, *Journal of Chemical Physics*, 130 (2009).
- [27] A. Sebetci, Cobalt clusters (Co(n), n ≤ 6) and their anions, *Chemical Physics*, 354 (2008) 196-201.
- [28] S. Maruyama, L.R. Anderson, R.E. Smalley, Direct injection supersonic cluster beam source for FT-ICR studies of clusters, *Review of Scientific Instruments*, 61 (1990) 3686-3693.
- [29] D. Proch, T. Trickl, A high-intensity multi-purpose piezoelectric pulsed molecular-beam source, *Review of Scientific Instruments*, 60 (1989) 713-716.
- [30] P. Caravatti, M. Allemann, The infinity cell - a new trapped-ion cell with radiofrequency covered trapping electrodes for Fourier-Transform Ion-Cyclotron Resonance mass-spectrometry, *Organic Mass Spectrometry*, 26 (1991) 514-518.
- [31] M. Graf, Habilitation Thesis, TU Kaiserslautern, Kaiserslautern, 2006
- [32] M.L. Gross, D.H. Russell, R.J. Aerni, S.A. Bronczyk, Ion-molecule reaction chemistry of various gas-phase C<sub>6</sub>H<sub>6</sub> radical cations, *Journal of the American Chemical Society*, 99 (1977) 3603-3609.
- [33] M. Kaupp, P.V. Schleyer, H. Stoll, H. Preuss, Pseudopotential approaches to Ca, Sr, and Ba hydrides - why are some alkaline-earth MX<sub>2</sub> compounds bent, *Journal of Chemical Physics*, 94 (1991) 1360-1366.
- [34] A. Bergner, M. Dolg, W. Kuchle, H. Stoll, H. Preuss, Ab-initio energy-adjusted pseudopotentials for elements of groups 13-17, *Molecular Physics*, 80 (1993) 1431-1441.
- [35] M. Dolg, H. Stoll, H. Preuss, R.M. Pitzer, Relativistic and correlation-effects for element 105 (Hahnium, Ha) - a comparative-study of M and MO (M=Nb, Ta, Ha) using energy-adjusted abinitio pseudopotentials, *Journal of Physical Chemistry*, 97 (1993) 5852-5859.
- [36] C. Adamo, V. Barone, Toward reliable density functional methods without adjustable parameters: The PBE0 model, *Journal of Chemical Physics*, 110 (1999) 6158-6170.
- [37] M.J. Frisch, G.W. Trucks, H.B. Schlegel, Gaussian 09, in, Gaussian, Inc., Wallingford CT, 2009.
- [38] G. Niedner-Schatteburg, unpublished results and work in progress
- [39] M. Tombers, L. Barzen, G. Niedner-Schatteburg, Inverse H/D isotope effects in benzene activation by cationic and anionic cobalt clusters, submitted to *Journal of Physical Chemistry*.
- [40] G. Niedner-Schatteburg, Habilitation Thesis, TU München, Garching, 1996

### 6. Summary / Zusammenfassung

#### 6.1. Summary

This thesis combines mass spectrometric studies on ionic dicarboxylic acids and transition metal cluster adsorbate complexes. IR-MPD spectra of protonated and deprotonated aliphatic and aromatic dicarboxylic acids provide insights in the nature of intramolecular hydrogen bonding. Investigations of their fragmentation behavior are supported by MP2 calculations. Prior work on cobalt transition metal clusters is extended to iron and nickel and three cobalt alloys have been studied.

IR-MPD spectra of protonated and deprotonated dicarboxylic acids (PDAs and DDAs,  $\text{HOOC}-(\text{CH}_2)_n-\text{COOH}$ , ( $n = 1 - 5$ )) has been recorded in the CO stretching region and in the OH stretching region. The longer the alkyl chain, the more flexible is the backbone, the more structures contribute to the spectra. This leads to a broadening in the recorded room temperature spectra. Quantum chemical calculations on MP2 level of theory with a double  $\zeta$  basis show that ionic dicarboxylic acids form cyclic structures with an intramolecular hydrogen bond in the gas phase. While protonated dicarboxylic acids fragment easily by the elimination of water, the fragmentation efficiency of deprotonated acids drops. Main fragment of deprotonated dicarboxylic acids is carbon dioxide. This different fragmentation behavior corresponds to the calculated fragmentation paths. PDAs with  $n \geq 2$  can form protonated anhydride structures with coordinated water. This reorganization facilitates the elimination of water. DDAs can fragment directly but higher fragmentation energy is needed. Two color IR-MPD experiments support this theory. In addition enhancement of a second IR laser is stronger in DDAs due to the direct fragmentation path. Thus, the spectra of DDAs are more affected by the use of a second resonant IR laser. The comparison of the OPO and FEL experiments reveals that both experiments are in good agreement. Minor differences arise from the different laser powers.

HD exchange experiments with PAA reveal strong OH and OD stretching vibration. The OH band shifts to lower frequencies as expected. The IR-MPD spectrum of deuterated species is of interest. Here it will be possible to identify all modes which couple to the motion of the bridging proton. So far, this measurement was unsuccessful. To overcome the experimental problems IR-MPD spectroscopy in the FT-ICR is needed.

Ionic phthalic and isophthalic acid have been investigated in the gas phase. In contrast to the aliphatic acids aromatic dicarboxylic acids exhibit a rigid backbone due to the aromatic ring. The comparison of the protonated and deprotonated phthalic acids spectra with the IR-MPD spectra of aliphatic dicarboxylic acids reveals strong similarities while the spectra of protonated and

deprotonated isophthalic acid differ clearly. Isophthalic acid is not able to form intramolecular hydrogen bonds. This is documented by the measured IR-MPD spectra and by the simulated IR spectra. The fragmentation efficiency of protonated isophthalic acid is low compared to protonated phthalic acid. In both spectra the main neutral fragmentation product is water. In contrast to isophthalic acid, phthalic acid forms a stable anhydride without major changes in the molecule geometry. The differences in fragmentation efficiency and the two color effect on phthalic and isophthalic acid supports the fragmentation mechanism presented in chapter 2.5.4.

The investigation of protonated and deprotonated dicarboxylic acids provides insights in intramolecular hydrogen bonding. Better understanding of the steric influence and the dynamic of the backbone requires further experiments and theory. It is imperative to obtain sharper IR-MPD spectra by cooling the ions. The modifications of the FT-ICR setup shall shortly allow for the investigation of cold ions ( $T < 20$  K). Here the isolated ionic species will be cooled in a cold hexapole for precooling and after that the ions are transferred into the cooled ICR cell.

In extension of our prior work we investigated the reaction with benzene and benzene- $d_6$  of size selected cationic and anionic transition metal clusters  $Fe_n^{+/-}$ ,  $Co_n^{+/-}$  and  $Ni_n^{+/-}$  in the size range  $n = 3 - 28$ . Dehydrogenation by cationic clusters is sparse, it occurs in reactions by anionic clusters of cobalt and nickel. Kinetic isotope effects KIE(n) in total reaction rates are inverse and - in part - large, dehydrogenation isotope effects DIE(n) are normal. A previously established multistep model of adsorption and stepwise dehydrogenation from the precursor adsorbate proves suitable to rationalize the found KIEs and DIEs in principle. Particular insights into the effects of charge and of cluster size are speculative. It is mandatory to spend further efforts in experiment, in modeling and in high level ab initio calculations in order to fully elucidate the transition metal cluster - benzene model systems. Temperature dependent kinetic studies have been performed. For the estimation of activation energies thermalization of the reaction gas does not suffice. Thermalization of the clusters requires the pulsed addition of thermalized helium.

The addition of transition metal atoms to ionic cobalt clusters modifies the catalytic activity of these clusters. In this thesis we studied three different transition metals, platinum, gold and rhodium. All metals affect the relative rate constants of the reaction with benzene and perdeutero benzene in a different way. In the case of mixed cobalt gold clusters no dehydrogenation products occur in the mass spectra and seemingly intact adsorption to the clusters prevails. In mixed cobalt rhodium clusters two processes occur, first the seemingly intact adsorption of benzene and second the dehydrogenation of a single hydrogen molecule. Dehydrogenation is effective in small bimetallic clusters  $Co_nPt_m^+$ ,  $n + m \leq 3$ . Thus single platinum atoms promote benzene dehydrogenation while

## 6. Summary / Zusammenfassung

---

further cobalt atoms quench it. Mixed triatomic clusters  $Co_2Pt_1^-$  and  $Co_1Pt_2^-$  are special in causing effective reactions and single dehydrogenation through some kind of cooperativity while  $Co_nPt_{1,2}^-$ ,  $n \geq 3$  do not react at all. In all investigated species we observe an inverse kinetic isotope effect (KIE < 1). In the case of cobalt rhodium clusters dehydrogenation takes place and a normal dehydrogenation isotope effect (DIE > 1) is dominant. A multistep reaction model is able to explain the inverse KIE and the normal DIE. A new mass spectrometer concept of an additional multipole collision cell for metal cluster adsorbate formation is currently under construction. Subsequent cooling shall achieve high resolution IR-MPD spectra of transition metal cluster adsorbate complexes.

### 6.2. Zusammenfassung

In der vorliegenden Arbeit werden die Ergebnisse aus massenspektrometrischen Untersuchungen an ionischen Dicarbonsäuren und Übergangsmetallcluster-Adsorbatkomplexen gezeigt. Erkenntnisse über die Natur von intramolekularen Wasserstoffbrückenbindungen werden durch IR-MPD-Spektren von protonierten und deprotonierten Dicarbonsäuren erlangt. Untersuchungen ihres Fragmentationsverhalten werden unterstützt durch *ab initio* Rechnungen auf MP2 Niveau. Frühere Arbeiten an Cobaltclustern werden erweitert auf Eisen und Nickelcluster. Zusätzlich werden auch drei Cobaltlegierungen untersucht.

IR-MPD Spektren von protonierten und deprotonierten Dicarbonsäuren werde im CO-Streckschwingungsbereich und im OH Streckschwingungsbereich aufgenommen. Je länger die Alkylketten, desto flexibler ist das Rückgrat, desto mehr Strukturen tragen zum Spektrum bei. Dies führt zu einer Verbreiterung der bei Raumtemperatur aufgenommen Spektren. Quantenchemische Rechnungen auf MP2 Niveau mit einer *double*  $\zeta$  Basis zeigen, dass ionische Dicarbonsäuren in der Gasphase cyclische Strukturen mit einer intramolekularen Wasserstoffbrückenbindung ausbilden. Während protonierte Dicarbonsäuren leicht fragmentieren und dabei Wasser eliminieren, sinkt die Fragmentationseffizienz für deprotonierte Dicarbonsäuren. Das Hauptfragment von deprotonierten Dicarbonsäuren ist Kohlendioxid. Das unterschiedliche Fragmentationsverhalten korrespondiert mit den berechneten Fragmentationswegen. Protonierte Dicarbonsäuren mit zwei oder mehr  $\text{CH}_2$ -Gruppen in der Alkylkette können ein Anhydrid mit einem koordinierten Wassermolekül bilden. Diese Reorganisation der molekularen Struktur erleichtert die Abspaltung von Wasser. Deprotonierte Dicarbonsäuren besitzen einen direkten Fragmentationsweg, der mehr Energie benötigt. Die Berechnungen zum Fragmentationsverhalten werden ebenfalls durch Zwei-Farben-IR-MPD-Experimente unterstützt. Die Verstärkung der Fragmentationseffizienz durch den zweiten IR Laser ist größer in den Spektren der deprotonierten Säuren. Der Vergleich zwischen OPO und FEL basierten IR-MPD Spektren zeigt eine gute Übereinstimmung und die kleinen Unterschiede können durch die verschiedenen Laserleistungen erklärt werden.

Deuteriumaustausch Experimente an protonierter Adipinsäure zeigen, dass die OH-Streckschwingung durch Substitution mit dem schwereren Isotop zu kleineren Frequenzen verschiebt. Das gesamte IR-MPD Spektrum der deuterierten Adipinsäure ist von großem Interesse. Alle Banden die zu kleineren Frequenzen verschieben, sind mit der Bewegung eines Deuterons verknüpft. Bisher war die Messung des IR-MPD Spektrums der vollständig deuterierten Spezies noch nicht erfolgreich. Die experimentellen Probleme können mit einem FT-ICR Massenspektrometer überwunden werden.



## 6. Summary / Zusammenfassung

---

Ionische Phthal- und Isophthalsäure wurden in der Gasphase untersucht. Im Gegensatz zu aliphatischen Dicarbonsäuren ist das Rückgrat der aromatischen Säuren durch den starren Benzolring fixiert. Der Vergleich von protonierten und deprotonierten Spektren der Phthalsäure mit Spektren von aliphatischen Dicarbonsäuren zeigt große Ähnlichkeiten während die Spektren der Isophthalsäure davon abweichen. Isophthalsäure kann keine intramolekularen Wasserstoffbrückenbindungen ausbilden. Dies wird sowohl durch die gemessenen IR-MPD - Spektren als auch durch die simulierten IR-Spektren belegt. Die Fragmentationseffizienz der protonierten Isophthalsäure ist gering verglichen mit der von Phthalsäure. In beiden Spektren ist das Hauptfragment Wasser. Im Gegensatz zur Phthalsäure kann Isophthalsäure keine stabile Anhydridstruktur ausbilden, die die Abspaltung von Wasser erleichtert.

Untersuchungen von protonierten und deprotonierten Dicarbonsäuren dokumentieren den sterischen Einfluss auf intramolekulare Wasserstoffbrückenbindungen. Für ein besseres Verständnis dieser Einschränkungen werden weitere Experimente von kalten Ionen und weitere *ab initio* Rechnungen benötigt. Änderungen am Aufbau des FT - ICR - Massenspektrometers werden in Kürze die Untersuchung von kalten Ionen ermöglichen. Die isolierten Ionen werden dazu zunächst in einem Hexapol vorgekühlt und erst danach in die kalte ICR - Zelle überführt.

Zur Erweiterung unserer bisherigen Arbeit im Bereich der Übergangsmetallcluster, untersuchten wir die Reaktion von  $Fe_n^{+/-}$ ,  $Co_n^{+/-}$  und  $Ni_n^{+/-}$  ( $n = 3 - 28$ ) mit Benzol und Perdeutero - Benzol. Kationische Cluster liefern nur wenig Dehydrierungsprodukte während anionische Cluster viel reaktiver sind. Der kinetische Isotopeneffekt (KIE) der totalen Geschwindigkeitskonstanten ist invers und teilweise sehr groß. Ein kinetisches Modell, das mehrere Adsorptions- und Dehydrierungsschritte beinhaltet, ist geeignet, um sowohl den gefundenen inversen KIE als auch den normalen Isotopeneffekt zu erklären. Genauere Analyse der Effekte der Ladung und der Clustergröße sind spekulativ. Es ist unumgänglich weitere Anstrengung in Experimenten, in Modellierung und high level *ab initio* Berechnungen zu investieren, um das Übergangsmetallcluster - Benzol - System vollständig zu verstehen. Es wurden erste temperaturabhängige Untersuchungen vorgenommen. Diese weisen eine noch unzureichende Themalisierung der Cluster - Ionen auf, um aus ihnen Aktivierungsenergien abschätzen zu können. Um eine bessere Themalisierung der Ionen zu erreichen, ist die gepulste Zugabe von thermalisiertem Helium als Stoßgas in die ICR - Zelle erforderlich.

Zusätzlich werden in dieser Arbeit auch Cobalt Legierungen mit Gold, Rhodium und Platin untersucht. Die Zugabe eines weiteren Übergangsmetalls zu den ionischen Cobaltclustern modifiziert die katalytische Aktivität dieser Cluster. Gemischte Cobalt - Gold Cluster zeigen keine Dehydrierungsprodukte in den Massenspektren und nur scheinbar intakte Adsorption von Benzol an den Cluster ist zu beobachten. In Cobalt - Rhodium - Clustern dagegen werden zwei Prozesse

## 6. Summary / Zusammenfassung

---

beobachtet: die scheinbar intakte Adsorption und die Dehydrierung von einem Wasserstoffmolekül. Dehydrierung wird auch in gemischten Cobalt - Platin - Clustern beobachtet. Hier findet zusätzlich auch die scheinbar intakte Anlagerung von Benzol statt. Effektive Dehydrierung findet in kleinen  $(n + m \leq 3)$   $Co_nPt_m^+$  Clustern statt. Ein einzelnes Platinatom fördert die Dehydrierung während weitere Cobaltatome sie dämpfen. Gemischte dreiatomige Cluster weisen einen kooperativen Effekt auf. Sie sind in der Lage sehr effektiv die Eliminierung eines einzelnen Wasserstoffmoleküls zu katalysieren. In allen untersuchten gemischten Clustern tritt ein inverser KIE auf und falls Dehydrierung beobachtet wird, überwiegt ein normaler DIE. Ein kinetisches Modell kann das Auftreten von inversem KIE und normalem DIE schlüssig erläutern. Der geplante Umbau des FT-ICR Massenspektrometers wird die Messung von kalten Metallcluster - Adsorbat - Komplexen ermöglichen. Dies erlaubt dann auch die Messung von hochaufgelösten IR-MPD Spektren, die zur Strukturaufklärung der Komplexe beitragen.

## 7. Publications and contributions to conferences

---

### 7. Publications and contributions to conferences / Publikationen und Konferenzbeiträge

#### Publications / Publikationen

*published / veröffentlicht:*

L. Barzen, M. Tombers, C. Merkert, J. Hewer, G. Niedner-Schatteburg, Benzene activation and H/D isotope effects in reactions of mixed cobalt platinum clusters: the influence of charge and of composition, *International Journal of Mass Spectrometry*, 330–332 (2012) 271–276.

*Submitted / eingereicht:*

C. Merkert, J. Mohrbach, L. Barzen, M. Tombers, M. Gaffga, G. Niedner-Schatteburg, H/D isotope effects in the reactions of benzene with Iron, Cobalt and Nickel cluster ions, *Physical Chemistry Chemical Physics*, submitted October 2013

*in preparation / in Vorbereitung:*

Christine Merkert, Anita Röthke, Lars Barzen, Gereon Niedner-Schatteburg, Philippe Maître; "Spectral fingerprints of proton delocalization in isolated dicarboxylic ions; *manuscript in preparation*.

C. Merkert, J. Mohrbach, L. Barzen, M. Tombers, G. Niedner-Schatteburg, H/D isotope effects in the reactions of benzene with Cobalt Gold and Cobalt Rhodium bimetallic cluster ions; *manuscript in preparation*.

#### Contributions to conferences / Konferenzbeiträge:

*Talks / Vorträge:*

M. Tombers, C. Merkert, L. Barzen, Gereon Niedner-Schatteburg, IRMPD- und ab initio-studie der homologen Reihe der Dicarbonsäuren, Bunsentagung, Saarbrücken, 2008.

*Posters / Poster:*

L. Barzen, B. Hofferberth, H. Kampschulte, C. Merkert, P. Maître, G. Niedner-Schatteburg, EPITOPES: Electrons Plus Infrared TO Probe and Elucidate Structures, Deutsch-Französisches Kooperations-treffen, Berlin, 2010.

M. Tombers, L. Barzen, C. Merkert, G. Niedner-Schatteburg, Charge, size and isotope effects within the reaction of ionic size selected cobalt-platinum clusters with C<sub>6</sub>H<sub>6</sub>/C<sub>6</sub>D<sub>6</sub> in the gas phase, Erste Gesamtkonferenz des Sonderforschungsbereichs SFB/TRR88 "3MET", Bad Bergzabern, 2011.

S. Jaberg, B. Pfeffer, L. Barzen, C. Merkert, G. Niedner-Schatteburg, C-H bond activation at the surface of isolated transition metal clusters, Symposium on Size Selected Clusters, Brand / Österreich, 2009

C. Merkert, M. Gaffga, M. Tombers, L. Barzen, A. Stamm, G. Niedner-Schatteburg, Normal and inverse H/D-isotope effects in the reactions of size selected transition metal cluster ions with aromatic hydrocarbon molecules



### 8. Acknowledgment

# Danke

... Prof. Gereon Niedner-Schatteburg für seine freundliche Betreuung, die gute Zusammenarbeit, die stete Diskussionsbereitschaft und den mir eingeräumten Freiraum.

... Prof. Markus Gerhards für die Übernahme des Zweitgutachtens und Prof. Werner Kubik für die Übernahme des Prüfungsvorsitzes.

... Prof. Christoph van Wüllen und Dr. Markus Mang aus der theoretischen Chemie die Betreuung der Rechencluster.

...Dr. Marc Proscenc für die wertvollen, wissenschaftlichen Diskussionen

... den Mitgliedern unseres Arbeitskreises die zur immer netten, hilfsbereiten und freundschaftlichen Atmosphäre des Arbeitskreises beitragen: Lars Barzen, Maximilian Gaffga, Joachim Hewer, Dr. Thomas Kolling, Johannes Lang, Jennifer Mohrbach, Matthias Tombers: Dimitri Imanbaew, Hans-Peter Mayer, Fabian Menges, Jennifer Meyer, Jonathan Meyer, Dr. Yevgeniy Nosenko, PD Dr. Christoph Riehn.

... allen ehemaligen Arbeitskreis-Kollegen für ihre herzliche Aufnahme und die Einführung im Arbeitskreis, sowie die Weitergabe ihres Wissens: Anita Röthke, Bernd Hofferberth, Stephanie Jaberg, Heinrich Kampschulte, und Britta Pfeffer.

... besonders allen, die sich mit mir nach Paris „getraut“ haben.

... Markus Becherer, Lukas Burkhardt, Sebastian Dillinger, Maximilian Gaffga, Joachim Hewer, Jennifer Meyer, Jennifer Mohrbach, Anke Stamm, Elvira Bohl und Matthias Tombers für ihre Forschungsarbeiten im Rahmen von Schwerpunktpraktika und Diplomarbeiten und ihre Unterstützung als wissenschaftliche Hilfskräfte.

... unseren guten Seelen Hilde Seelos, Sibylle Heieck und Inge Krull im Sekretariat der physikalischen und theoretischen Chemie und allen übrigen guten Seelen, die fast immer alles möglich machen.

... allen weiteren aktuellen und ehemaligen Mitgliedern der physikalischen und theoretischen Chemie für viele unterhaltsame Stunden und leckeren Kuchen im Kaffeezimmer.

... den Mitarbeitern der zentralen Metall- und Elektronikwerkstätten für viele beratende Gespräche und die Unterstützung, wenn's mal wieder eilig sein musste.

... der EU für die Finanzierung des Forschungsprojektes EPITOPES und der DFG für die Einrichtung des Sonderforschungsbereichs SFB/TRR 88 „3MET“ und die damit verbundene Finanzierung meiner Anstellung.

... allen meinen Freunden für ihre Geduld und Unterstützung

... meiner Familie, die immer für mich da war und ist.

**8. Acknowledgment**

---

### 9. Lebenslauf

#### Angaben zur Person:

Name: Christine Merkert  
Email: merkert@chemie.uni-kl.de

#### Schulische Ausbildung:

2000 Allgemeine Hochschulreife, St. Franziskus Gymnasium Kaiserslautern

#### Studium:

Studienrichtung: Chemie  
Schwerpunkt: Physikalische Chemie  
Erreichter Abschluss: Diplom, Titel: „Aufbau eines OPO-Lasersystems und dessen Kopplung mit einem FT-ICR-Massenspektrometer“  
Abschlussjahr: 2007  
Promotion: Doktorarbeit in Physikalischer Chemie: Wissenschaftlicher Mitarbeiter, TU Kaiserslautern, Titel: *“Metal cluster aggregates of the composition  $Fe_n^{+/-}$ ,  $Co_n^{+/-}$ ,  $Ni_n^{+/-}$  and  $[Co_nM_m]^{+/-}$  (M: Au, Rh and Pt) as model systems for catalytic C-H activation and structural determination of ionic dicarboxylic acids as model system for intramolecular hydrogen bonding”*  
Mdl. Abschlussprüfung: 27. März 2014





### **Eidesstattliche Erklärung**

Hiermit bestätige ich, Dipl.-Chem. Christine Merkert, dass die vorliegende Arbeit gemäß der Promotionsordnung des Fachbereichs Chemie der Technischen Universität Kaiserslautern selbständig und mit den angegebenen Hilfsmitteln und Quellen angefertigt wurde.

Kaiserslautern, im Februar 2014